NNT/NL : 2022AIXM0149/008ED353

THÈSE DE DOCTORAT

Soutenue à Aix-Marseille Université
le 29 mars 2022 par

Tristan JULIEN

Acoustic and Vibration Methods for the Phenomenological Study of Fuel Rod Cladding Failures in Nuclear Reactors

Discipline
Sciences pour l'Ingénieur

Spécialité
Acoustique

École doctorale
353 Sciences pour l'Ingénieur : Mécanique, Physique, Micro et Nanoélectronique

Laboratoire
CEA Cadarache, DES, IRESNE, DER, SPESI, LP2E

Composition du jury

Jean-Hugh THOMAS — Rapporteur
Laboratoire d'Acoustique de l'Université du Mans

Arris TIJSSELING — Rapporteur
Eindhoven University of Technology

Vegard AUNE — Examinateur
Norwegian University of Science and Technology

Jerome ANTONI — Président du jury
INSA Lyon, Laboratoire Vibrations Acoustiques

Guillaume RICCIARDI — Directeur de thèse
CEA Cadarache, Département de Technologie Nucléaire

Laurent PANTERA — Encadrant
CEA Cadarache, Département d'Etudes des Réacteurs

Emmanuelle SARROUY — Encadrante
École Centrale de Marseille, Laboratoire de Mécanique et d'Acoustique

Vincent FAUCHER — Invité
CEA Cadarache, Département de Technologie Nucléaire

Affidavit

Je soussigné, Tristan JULIEN, déclare par la présente que le travail présenté dans ce manuscrit est mon propre travail, réalisé sous la direction scientifique de Guillaume RICCIARDI, dans le respect des principes d'honnêteté, d'intégrité et de responsabilité inhérents à la mission de recherche. Les travaux de recherche et la rédaction de ce manuscrit ont été réalisés dans le respect à la fois de la charte nationale de déontologie des métiers de la recherche et de la charte d'Aix-Marseille Université relative à la lutte contre le plagiat.

Ce travail n'a pas été précédemment soumis en France ou à l'étranger dans une version identique ou similaire à un organisme examinateur.

Fait à Saint-Paul-Lez-Durance, le 24 janvier 2022.

List of publications and attended conferences

List of publications:

1. Under review, submitted on December 19, 2021: T. Julien, V. Faucher, L. Pantera, E. Sarrouy, G. Ricciardi, *Numerical Study of Coupled Fluid and Solid Wave Propagation Related to the Cladding Failure of a Nuclear Fuel Rod*, Applied Sciences.

2. Writing in progress: T. Julien, L. Pantera, E. Sarrouy, G. Ricciardi, *Processing of Experimental Acoustic Emission Signals for Detection and Localization of Failures during Hydraulic Tests*, Intended journal: International Journal of Pressure Vessels and Piping.

List of attended conferences and summer schools:

1. T. Julien, L. Pantera, E. Sarrouy, G. Ricciardi, *Design of an Experimental Mockup to Study the Possibilities of Acoustic Measurement for Nuclear Reactor Fuel Element Testing*, Xth Workshop “NDT in Progress", October 7-9, 2019, Prague, Czech Republic.

2. T. Julien, L. Pantera, E. Sarrouy, G. Ricciardi, *Design of Acoustic and Vibration Methods for the Phenomenological Study of Fuel Rod Cladding Failures in Nuclear Reactors*, Journées Jeunes Chercheurs en Acoustique, vibration et Bruit (JJCAB) 2021, November 18-19, 2021, Compiègne, France.

Résumé

Cette thèse porte sur l'étude des phénomènes d'interaction fluide-structure induits par une rupture de gaine d'un crayon de combustible dans un réacteur nucléaire. L'objectif principal est d'explorer les possibilités des méthodes acoustiques et vibratoires pour l'observation de cet évènement. La détection, la localisation et la caractérisation d'une rupture de gaine présentent un intérêt dans le cadre d'études sur le comportement du combustible menées dans les réacteurs de recherche, ainsi que pour l'optimisation du fonctionnement de réacteurs industriels. La rupture générant des ondes de pression dans le fluide entourant le crayon combustible et des vibrations dans le crayon et les structures environnantes, des méthodes acoustiques et vibratoires peuvent donc être utilisées pour l'étude de ce phénomène. De plus, la propagation de ces ondes à travers le système constitue un avantage de ces méthodes. Elle permet en effet des mesures avec des capteurs relativement éloignés de la source située dans le coeur du réacteur, où les possibilités d'instrumentation sont limitées (en raison du flux neutronique, des radiations, des hautes températures et de contraintes de place). Cependant, ces méthodes nécessitent des informations préalables sur les phénomènes de propagation des ondes dans le système et des potentielles autres sources qui peuvent exister. Ainsi, un premier objectif de cette thèse est d'améliorer la compréhension des phénomènes d'interaction fluide-structure induits par la rupture et le fluide autour du crayon. Un second objectif est d'identifier les méthodes les plus adaptées à l'étude de ces phénomènes avec une instrumentation acoustique ou vibratoire usuelle, telle que des accéléromètres, des jauges de déformation, des capteurs d'Emission Acoustique, ou des capteurs de pression. Le premier objectif est principalement atteint à l'aide de simulations numériques (réalisées avec le code EUROPLEXUS), tandis que le second objectif fait appel à des tests sur des dispositifs expérimentaux sur lesquels les phénomènes étudiés (rupture de gaine et écoulement du fluide environnant) sont reproduits sur un crayon combustible factice. Les résultats des simulations et des expériences sont comparés avec la théorie régissant les phénomènes étudiés. En plus de ces études numériques et expérimentales, le travail inclut également l'activité de conception des dispositifs expérimentaux et des chaînes de mesure.

Mots clés: Acoustique, Vibrations, Interaction fluide structure, Structural Health Monitoring

Abstract

This PhD consists of studying fluid-structure interaction phenomena related to fuel cladding failures in nuclear reactors. The primary aim is to explore the possibilities of acoustic and vibration methods for the observation of such events. Detection, localization and characterization of cladding failures are of interest for studies about fuel behavior in research reactors, as well as for optimizing the operation of industrial power plants. As cladding failures produce fuel rod vibrations and pressure waves in the fluid surrounding the rod, acoustic and vibration methods can be used to study such phenomena. Moreover, such waves can propagate over a relatively long distance. Therefore, an advantage of such methods is that the waves produced by the failure can be detected by sensors mounted relatively far from the source. This is beneficial since the fuel rods are located inside the reactor core, where instrumentation possibilities are restricted (because of neutron flux, radiation, high temperature, and available space). However, these methods require prior information about wave propagation phenomena and the different sources existing in the system. Thus, the first objective of the thesis is to better understand the fluid-structure interaction phenomena induced by the failure and the fluid around the rod. The second objective is to find suitable methods for the study of those effects with standard acoustic and vibration measurement devices such as pressure sensors, accelerometers, strain gauges, and acoustic emission sensors. The first objective is mainly achieved by numerical simulations (using the EUROPLEXUS code) and the second objective by tests on experimental mockups, where the phenomena of interest (cladding failure and surrounding fluid flow) are reproduced on a fake fuel rod. Both numerical and experimental results are compared to the underlying theory (using, for instance, an analytical water-hammer model). In addition to these numerical and experimental studies, the work also includes the design process of the experimental devices and of the instrumentation system.

Keywords: Acoustics, Vibration, Fluid Structure Interaction, Structural Health Monitoring, piping system

Acknowledgements

I wish to acknowledge the members of the jury, Pr. Jerome Antoni, Pr. Jean-Hugg Thomas, Dr. Arris Tijsseling, and Dr. Vegard Aune, for carefully reading my dissertation, attending my defense, and providing many interesting questions and suggestions.

Je tiens ensuite à remercier mon équipe encadrante. Guillaume, merci d'avoir accepté de diriger ma thèse, mais surtout, merci d'avoir toujours su reconnaître les moments où j'avais besoin d'aide, d'autonomie, de cadrage ou bien d'encouragements. Emmanuelle, merci d'avoir suivi avec patience et attention mon travail, et d'avoir toujours donné ton avis avec autant de franchise que de bienveillance. Laurent, merci de m'avoir accordé ta confiance pour ce projet et de m'avoir accompagné pour mes premiers pas dans ma carrière scientifique. En plus des mes trois encadrants, je suis aussi très reconnaissant envers Vincent Faucher pour son aide si précieuse, qui fut indispensable pour tout mon travail sur Europlexus. Votre accompagnement, à vous quatre, m'a évidemment permis de mener ma thèse à bien, mais il m'a surtout permis de progresser énormément sur le plan scientifique comme sur le plan humain.

Merci à tous les collègues du DER/SPESI et du DTN/STCP qui m'ont aidé dans la préparation de mes manips. Merci aux membres du LP2E pour ces quatre agréables années passées à vos côtés, pour ces nombreuses discussions sur des sujets divers et variés. De plus, je suis particulièrement reconnaissant envers Christine et Marie-Odile : merci pour tout le temps que vous m'avez accordé, sans lequel je n'aurais jamais pu mener à bien mon travail expérimental.

À tous les "co-thésards" du LP2E, du LDCI ou du LTHC, ce fut un plaisir de faire votre connaissance et de passer tous ces moments en votre compagnie. Merci Maxime de nous avoir régulièrement réunis, merci Mathieu de m'avoir fait me remettre à la trompette ! Julia, thank you for our many talks and all the pieces of personal advice you gave me.

Mes remerciements vont aussi à mes amis : ceux que j'ai rencontré avant ma thèse comme ceux que j'ai rencontrés pendant, ceux avec qui j'ai grimpé, fait de la musique, ou simplement passé du bon temps (karaoké inclus...). Quelque soit nos activités et la fréquence à laquelle nous avons pu nous revoir, votre présence a beaucoup compté pour moi.

Je remercie également toute ma famille et particulièrement mes parents, qui m'ont encouragé depuis le plus jeune âge à persévérer et m'épanouir, non seulement dans mes études, mais aussi dans mes différentes passions. C'est grâce à eux que j'ai pu arriver jusque là (et aussi un peu grâce à ma "soeur chérie que j'aime et que j'adore").

Enfin, merci Marie pour ta présence, ton écoute attentive et ton soutien permanent. Merci aussi pour tous ces merveilleux moments vécus en parallèle de ma thèse, en espérant qu'ils soient encore nombreux.

Contents

List of Figures

List of Tables

Acronyms

ADC Analog-to-Digital Conversion. 89, 90, 93, 94

AE Acoustic Emission. 3, 8–11, 71, 83–85, 89, 90, 93, 95, 98, 108, 113, 115, 122, 138, 143, 146, 155–157, 164, 168, 205, 208, 211, 215, 216

BP Band-Pass. 135, 138

CWT Continuous Wavelet Transform. 95, 99, 117, 120, 122, 128, 135, 138, 205, 208, 211, 213

DWT Discrete Wavelet Transform. 95, 117, 128, 131, 135, 138, 144, 157

EDC Expansion Due To Compression. 80

EMD Empirical Mode Decomposition. 95, 128, 131, 138, 148, 149, 157

EOS equation of state. 28, 36, 58

EPX Europlexus. 87

ESD Energy Spectral Density. 62, 94, 103, 108, 117, 120, 121, 213

FEM Finite Element Method. 39, 169

FFT Fast Fourier Transform. 94

FIV Flow-Induced Vibrations. 23, 72, 80, 111, 157

FSI Fluid-Structure Interaction. 11, 13, 26, 27, 35, 37, 38, 72, 159, 164, 169

HN Hsu-Nielsen. 98, 102, 103, 107

IEPE Integrated Electronics Piezo-Electric. 82, 83, 116, 122

IMF Intrinsic Mode Function. 95, 128, 131, 138, 148, 149, 197–199, 202

OMA Operational Modal Analysis. 107

PCMI Pellet-Cladding Mechanical Interaction. 10

PWR Pressurized Water Reactors. 4, 5, 7, 57, 72, 74

RIA Reactivity Initiated Accident. 6

SNR Signal-to-Noise Ratio. 82, 86, 93

STFT Short-Time Fourier Transform. 94, 99, 138, 210, 213

TDOA Time Difference Of Arrival. 51, 54, 55, 57, 94, 123, 124, 126–131, 138, 142, 146, 148–150, 155, 157

Zr-4 Zircaloy-4. 73, 161

List of Symbols

t	Time	$\underline{\underline{\boldsymbol{\sigma}}}$	Stress tensor
x	Axial coordinate	$\underline{\underline{\boldsymbol{\epsilon}}}$	Strain tensor
y	First transversal coordinate	$\boldsymbol{q}$	Structural displacement vector
z	Second transversal coordinate	ϕ	Scalar potential associated to longitudinal waves
r	Radial coordinate	$\boldsymbol{\psi}$	Vector potential associated to transversal waves
θ	Orthoradial coordinate	ω	Circular frequency
L	Length of the structure	k	Wave number
D	Characteristic diameter	q_{free}	Free response of a vibrating beam
R_{in}	Inner radius of the tube	q_p	Particular solution for the forced response of a vibrating beam
R_{out}	Outer radius of the tube	X	Space-dependent component of the free response of a vibrating beam
b	Tube's wall thickness	T	Time-dependent component of the free response of a vibrating beam
S	Cross-sectional area	Φ_n	Mode shape of the n^{th} mode
I	Quadratic moment of inertia around the transverse axis	Q_n	Displacement of the n^{th} mode in modal coordinates, for the particular solution of the forced response
ρ_s	Structure density	ω_{dn}	Damped natural circular frequency of the n^{th} mode
E	Young modulus	ξ_n	Modal damping rate of the n^{th} mode
ν	Poisson coefficient	F_n	Excitation in modal coordinates

c_T	Transverse structural wave velocity	c_{pm}	Velocity of water-hammer-induced primary wave
c_{L0}	Pure longitudinal structural wave velocity	c_{pc}	Velocity of water-hammer-induced precursor waves
c_L	Quasi-longitudinal structural wave velocity	$\boldsymbol{u}$	Fluid velocity vector
c_R	Rayleigh wave velocity	U	Average or characteristic velocity
ρ_f	Fluid density	p	Fluid pressure
K	Fluid bulk modulus	P	Average or characteristic fluid pressure
μ	Fluid kinematic viscosity	P_∞	Constant in the stiffened-gas equation of state, associated to the molecular attraction needed to represent liquids
κ	Fluid bulk viscosity	e	Internal energy
η	Dynamic viscosity	γ	Empirical constant in the stiffened-gas equation of state (equal to heat capacity ratio for a perfect gas)
c_{w0}	Wave velocity in an unrestrained volume of compressible water	Eu	Euler number
c_{w0b}	Wave velocity in incompressible water contained in an elastic tube	Re	Reynold number
c_f	Pressure wave velocity in a compressible fluid contained in an elastic tube	St	Strouhal number

Writing conventions:

$\overline{x}$: cross-section-average value,
$\dot{x}$: time derivative,
x_n: modal value associated to the n^{th} mode of vibration,
x_i, ($i = x,\ y,\ z,\ r$, or θ): component along direction i,
$\underline{\underline{x}}$: 2nd-order tensor (used for stress and strain tensors).

Introduction

Acoustic and vibration phenomena are widely used, in various ways, for the monitoring and inspection of industrial systems. They can provide information about different structural flaws, damage mechanisms, malfunctions, or other unwanted events. One class of acoustic and vibration methods, defined as *passive methods*, consists of recording the waves that are generated by the event to study. For another class of methods, referred as *active methods*, waves are artificially generated by the measurement apparatus. The response of the tested system to these artificial excitations is then analyzed to identify anomalies that affect the response.

Acoustic and vibration methods have several advantages compared to other testing methods, such as visual inspection, eddy current, and radiography. Some acoustic and vibration waves, especially guided waves, can propagate over long distances, through complex geometries, and multiple media. Thus, they can provide information from physically inaccessible areas. Moreover, when designed for passive methods, measuring devices can be relatively simple, robust, and small. Passive methods also offer great versatility, as they can provide information about various phenomena, depending on the choice of measuring devices and signal processing methods. For those reasons, passive acoustic and vibration methods are of particular interest for the monitoring of nuclear power plants. Indeed, some systems inside nuclear reactors are partially or totally inaccessible, due to safety confinement, radiation, and high temperatures. When installed on such systems, sensors are subjected to harsh conditions (high temperature and pressure, radiation that can damage materials, aggressive fluids leading to corrosion of metals), and radioactive contamination complicates their manipulation and maintenance. In addition, the place dedicated to such sensors in the reactor core is limited by the narrow available space, and by the need to avoid disturbing the neutron flux and coolant fluid flow. Furthermore, different phenomena having acoustic or vibration effects can occur in a reactor and, thus, can be observed by such measuring devices. This implies versatility, which can be considered as an advantage of passive methods, but also a drawback, as some *a priori* information is necessary to properly interpret the measurements from such complex environments.

Acoustic and vibration monitoring methods are commonly used for the monitoring and testing of different components of the fluid systems of nuclear power plants (such as pipes, heat exchangers, valves, and pumps or other rotating machinery), as shown in reviews like [1] or [2]. It seems that an application of such methods to the detection and localization of fuel rod cladding failures was seldom studied in the literature, although this would be of interest for the optimization of power plant operation, and the understanding of fuel behavior. Such an application is possible and suitable for the observation of a cladding failure, as this event generates different types of mechanical waves. Firstly, damage mechanisms in the cladding generate structural waves. This phenomenon, as well as the testing and monitoring methods using it, are known collectively as "Acoustic Emission" (AE). Secondly, failures can result in a significant release of the inner-rod pressure, thus resulting in a pressure surge in the coolant fluid surrounding the rod. These pressure changes and the associated fluid-structure interaction (FSI) induce pressure waves propagating through the fluid and structural waves propagating through the rod and outer structures. Such waves allow the use of methods based on structural vibration and fluid pressure measurements.

From a practical perspective, regarding AE methods, a correct understanding of the measurements requires accurate knowledge about material properties and fracture mechanisms at a micro-structural scale. Vibration and FSI phenomena also depend on material properties, but at a coarser scale. Thus, unlike AE, fluid and structural dynamic phenomena, with associated FSI, can be reproduced with some differences in the materials and the experimental conditions, without losing too much correlation to real in-reactor phenomena. Additionally, low frequency pressure and vibration measurements can be interpreted despite some uncertainties about material properties and experimental conditions. As a consequence, it was decided to focus the current work on the latter methods rather than AE methods. Nevertheless, it remains possible, as it will be shown, to use measurement tools initially designed for AE applications.

The methods that were ultimately chosen can provide information about different phenomena related to the dynamics of the rod and outer structure, as well as the dynamics of the fluid surrounding the rod. However, nuclear environments imply significant constraints, because of harsh conditions and safety rules. Some measurements are therefore impossible in real nuclear facilities. This results in a lack of information to fully understand the phenomenology associated to a cladding failure and improve measurement tools and methods. Furthermore, few references dealing with acoustic and vibration passive methods for rod cladding monitoring were found in the literature, and they focus on the application of AE methods only. In addition, no exhaustive study about the phenomenology that could generally affect fluid and structural dynamic measurements could be found. As a consequence, at a first stage, it is necessary to determine the ways the needed information can be obtained. This constitutes the main objective of this PhD, carried out at the French Commission for Atomic and Alternative Energies (*Commissariat aux Energies Atomiques et alternatives*, CEA).

To achieve this objective, it was decided to use both experimental and numerical methods, and to focus on the study of the phenomena induced by the failure and involving interaction between the coolant fluid and the structure. This PhD can be therefore considered as an exploratory work about the phenomenology and methods related to FSI, acoustic and vibration phenomena following cladding failure in a nuclear reactor.

The context and objectives of the current study are described in more depth in Chap. I. In this chapter, after brief descriptions of fuel rod and a cladding failure, the acoustic and vibration passive monitoring methods that have been used, or can be used, are introduced. It shows that, although such methods are widely used for various components of nuclear reactor piping systems, possible applications to the monitoring of fuel rod claddings have been seldom studied. This results in a lack of knowledge about the FSI, acoustic and vibration phenomenology, and about the possibilities of the identified methods. This allows the objectives of the current work to be clearly defined.

The theories that underlie the studied phenomena are described in Chap. II. The theoretical concepts related to structural waves (high frequency guided waves and low frequency structural vibrations) which allow for the interpretation of Acoustic Emission (AE) and vibration measurements are presented. Then, one-dimensional models designed for the study of water-hammer in piping systems are introduced. Such models allow a clear understanding of FSI phenomena occurring in the system after a cladding failure. In addition to water-hammer models, a different description of the fluid behavior and FSI using Euler equations is introduced, as it is the basis of the three-dimensional numerical simulations carried out in the current study.

Chap. III relays the analysis of the results of the numerical approach, using the EUROPLEXUS code for FSI simulations by Finite-Element-Methods (FEM). EUROPLEXUS was chosen because it is especially suitable for transient phenomena with FSI, such as a cladding failure. Moreover, as it is partially developed by CEA, human and software resources were easily available. The code already includes all the necessary features to simulate the studied phenomena. Thus, it was simply used without further development. Analyses of the results of these numerical simulations provide qualitative and quantitative information about the propagation of the failure-induced pressure surge. Qualitative information is useful for the phenomenological understanding, and quantitative information can help with the preparation and the interpretation of the experiments carried out in the experimental devices used in this PhD as well as in actual reactors. Moreover, the results also show that such three-dimensional simulations and classical one-dimensional water-hammer models can complement each other.

The experimental approach is described in Chap. IV. For this approach, the initial plan was to design, produce, and use a mockup that makes the reproduction of the cladding failure and the coolant fluid flow possible without radioactivity, to avoid the constraints inherent to nuclear facilities. Thus, its was intended to allow all the fluid pressure and structural vibration (both low frequency vibrations and high frequency guided waves) measurements that are necessary to understand the related phenomenology. However, it appeared that preliminary experiments on a simpler device were necessary to assess the feasibility of the initially proposed mockup and to define the safety obligations to consider. A preliminary device, called *RUPTUBE* (*RUPtures de TUBEs*, "tubes failures") was therefore designed. This device made it possible to validate a technical solution designed to produce failures in fake rod claddings, and to test tools and methods intended for structural measurements. This finally allowed for the design of the final mockup, *MAQAC* (*MAQuette pour l'étude du comportement Acoustique d'un Crayon combustible*, "Mockup for the study of the acoustical behavior of a fuel rod"). This device includes the reproduction of the fluid flow around the rod and the associated pressure measurement possibilities, in addition to the cladding failure and structural measurements. The relevant chapter presents the objectives of the experiments, the design of both devices, and the analysis of *RUPTUBE* experimental results, involving tests of different signal processing methods. As *MAQAC* was eventually delivered later than expected, the associated experiments are currently in progress. Hence, their results can not be included in this document.

I. Background and objectives

In the current chapter, the general context of the project is introduced. Previous works related to monitoring methods based on acoustics, vibration, or fluid-structure-interaction and applied to a similar context are briefly presented. Such a presentation allows the identification of a lack in the knowledge that is needed for the application of such methods to the monitoring of fuel rod cladding failure. The identification of this lack finally leads to the definition of the objectives of this PhD.

I.1. The cladding failure phenomenon

This work focuses on the monitoring of nuclear fuel rods and especially on the cladding failure phenomenon. The current section describes, firstly, the fuel rod and its environment. Secondly, causes and effects of a cladding failure are explained. Thirdly, previous works about the monitoring of fuel rods or similar elements are introduced.

I.1.1. Description of a fuel rod

The context of the current work is related to french industrial Pressurized Water Reactors (PWR). In such reactors, the fuel material consists of small pellets (about 8 mm diameter and 10 mm long) that are stacked in metallic tubes (about 4 m long, an outer diameter of 9.5 mm and a thickness of 0.57 mm). The tube is called "cladding", and the element constituted by the cladding and the pellets inside is called "fuel rod". The cladding is made of either Zircaloy-4 or M5 (both are zirconium-based alloys). Rods are gathered in assemblies (264 rods per assembly), that are vertically inserted in the core (see Fig. I.1). In total there are thousands of fuel rods in the core of an industrial reactor.

Around the rods, water flows from the bottom to the top at a velocity of 3.4 $m.s^{-1}$, with a pressure of 155 bar and a temperature of 280°C. This fluid has two purposes. The first one is related to the neutron moderation and does not need to be detailed for the understanding of the current work. The second one is to carry the heat out of the core, in order to transfer its energy, and to cool down the rods to prevent them to meld. For this reason, the water is usually referred to as the "coolant fluid".

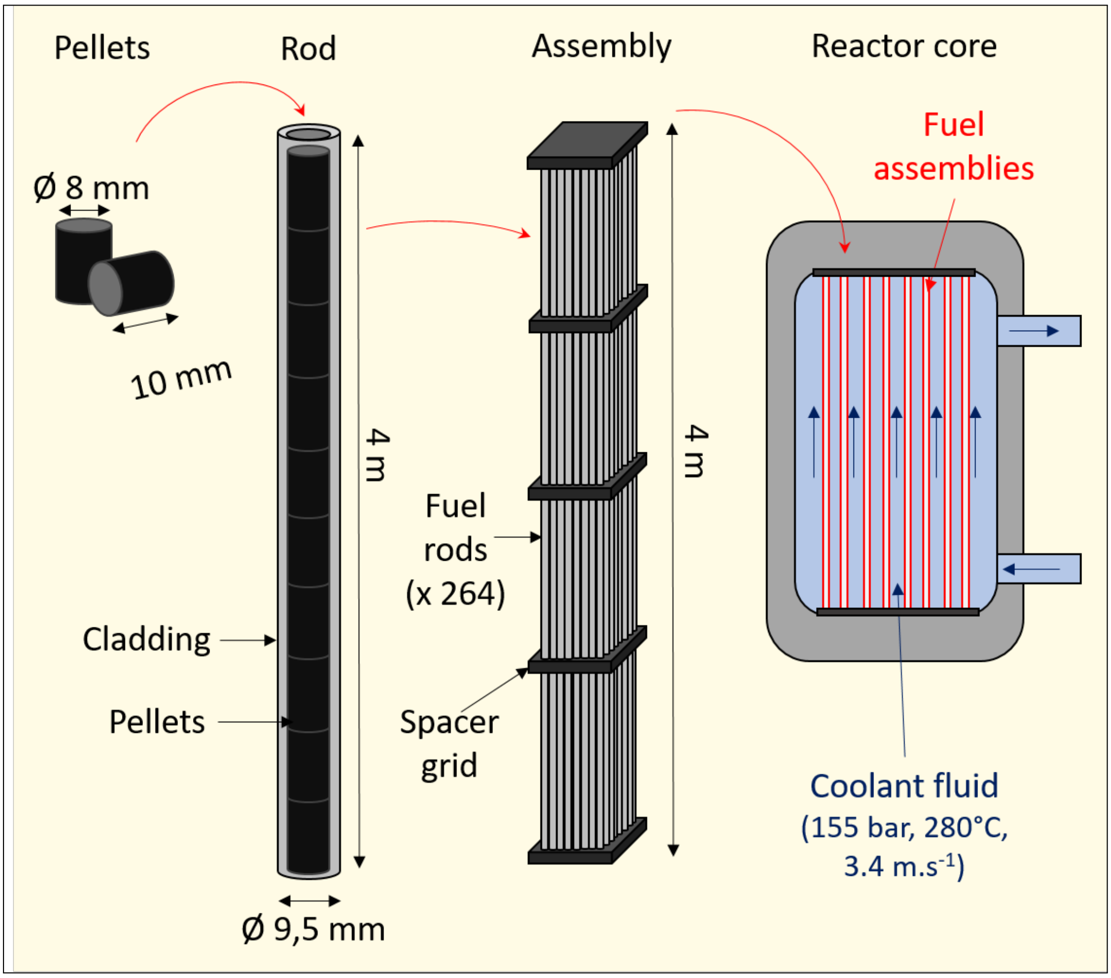

Figure I.1. *Explanatory drawings of the composition of PWR fuel elements.*

Some experiments dedicated to the study of fuel rod behavior are carried out in research reactors. In such cases (like in the REP-Na tests [3], the ISABELLE tests [4] or the forthcoming ADELINE tests [5]), the studied element consists most often of a single rod, of the same kind as industrial rods. This studied rod is often a sample extracted from a rod already used in an industrial reactor and cut into several pieces for research purpose. Hence, its length, about 60 cm, is smaller than a complete industrial rod. In such research reactors, the studied rod is subjected to various conditions that can be encountered in an industrial PWR. These conditions include accidental situations' ones. To reproduce both the desired neutronic and hydraulic conditions in a safe way and without damaging the whole core, the studied rod is placed in a closed device, which is placed in the reactor core and connected to a water loop independent from the coolant system of the core. The independent water loop reproduces the desired hydraulic conditions around the studied rod and the core generates the required neutron flux. The geometry of the test device, as described in Sec. III.1, forms an outer tube around the rod. The annular gap between the outer wall of the cladding and the inner wall of the outer tube is filled with the flowing water supplied by the water loop.

I.1.2. Causes and effects of a cladding failure

Because of combined effects of high temperature, radiation, chemical reaction between the cladding and the fission products, oxidation due to the coolant fluid, the cladding material is weakened during its use in a reactor. In addition to that, the cladding is subjected to various mechanical loads that can cause its failure. Different types of failures can be distinguished, depending on their causes. As explained in [6], some failures happen after a gradual wear (often because of fretting on the supports of the rod). Some other failures are more sudden and can be considered as bursts. Such failures can be generated by a phenomenon called Pellet-Cladding Mechanical Interaction (PCMI). This is caused by the swelling of the pellets that is generated by the nuclear reaction and can lead to important loads on the inner surface of the cladding. Sudden failures can also be due to an increase in the inner pressure due to fission gas (released by the pellets during the nuclear reaction) or the vaporization of water inside the rod because of an initial leakage that enables water to enter the rod [7].

Depending on causes and characteristics of the failure, various vibration or acoustic effects can be induced. The current work focuses on significant fluid-structure interaction phenomena related to the release of the initial pressure inside the rod and the generation of a pressure surge in the fluid surrounding the rod. The pressure surge in the surrounding fluid can be induced by the inner rod pressure release, a steam explosion (caused by a thermal interaction between ejected fuel particles and the coolant fluid), or both. Such phenomena are representative of either failures of waterlogged rods or failures in accidental situations, such as a Reactivity Initiated Accident (RIA). As shown in [8] and [9], because of the fast increase in temperature, failures during such accidents imply more likely a pressure surge than failures occurring in nominal operation, that are usually due to slow increase in the PCMI or gradual wear phenomena. Moreover, [7] explains that the release of high pressure steam or fission gas tends to eject fuel particles out of the rod, which increases the probability of fuel-coolant interaction leading to a steam explosion.

I.2. Cladding monitoring and failure detection

Possibilities to monitor rod claddings, and especially to detect and locate failures, have two main interests. The first one is an economical interest: when achieved in an industrial power plant, such a monitoring would be a way to optimize the reactor's operation, as failed rods reduce its efficiency. It would allow the operators to assess how many rods have to be changed and their position in the core. The second interest is the help it could provide with the understanding of fuel behavior. Position and time of occurrence of the failure can provide information about its causes and the state of the cladding or the fuel.

However the conditions inside a nuclear reactor (high temperature, radioactivity, narrow available space) imply some constraints on the sensors that can be mounted in the facility to use monitoring methods. The closer to the rod the sensor is, the higher temperature and neutron flux it has to withstand. Moreover, neither the neutron flux nor the coolant flow should be disturbed by the sensors. It is consequently practically impossible to mount sensors directly on, or around, the fissile part of the rod (which is the major part of the rod), where the neutron flux is generated and the heat is produced. Thus, sensors can be mounted either on the ends of a rod or on the outer structure. For this reason, acoustic and vibration methods are of interest. As a sudden cladding failure generates mechanical waves in the coolant fluid and in the cladding, and as such waves propagate along the system and can be transmitted to the outer structure, it is possible to measure them with sensors that are mounted relatively far from the failure. In addition to that, the required instrumentation for acoustics and vibration is relatively simple. Most common sensors are piezoelectric and piezoresistive sensors (those types of sensors are presented in Chap. IV). Those technologies are rather simple, commonly used in many fields and can withstand high temperatures and radioactivity. Their associated conditioning systems consist of simple analog amplifiers and filters (if needed) in addition to a Wheatstone bridge[1] for piezoresistive sensors.

Despite those interests, such methods require *a priori* information about the phenomenon to study, and the other phenomena that could disturb the measurements. It is necessary to know the effects of a failure regarding fluid dynamics, structural dynamics and fluid-structure interaction phenomena. For such methods, disturbances can be induced by the coolant fluid flow (which creates pressure fluctuations in the fluid and structural vibrations) or the noise from different components of the system (for instance, pumps of the water loop, or falls of the core's control rods [2]). The current work deals only with the first source (coolant fluid flow), which is similar in every system involving PWR hydraulic conditions and whose effects are relatively uniform along the whole system. The second one (external components' noise) should be addressed in studies specific to each case of application, as its characteristics depends on the configuration of the system. A second need for the application of such methods is the information about wave propagation. From the source to the sensors, waves travel through the system, in both fluid and solid media. This propagation can result in significant distortions of the signal, especially when dispersion is important. Generally, consequences of the propagation between the source and the sensors depend on the geometry and material characteristics of the fluid and the structure, and differ according to the frequency (for instance, dispersion is more significant at high frequency, when the wavelength is small compared to the characteristic transverse dimension of the system) and to the type of waves that are considered (propagation phenomena are not the same for fluid pressure wave and the different kinds of structural waves). In addition to distortions, reflections and attenuations, an important parameter to consider is the wave velocity. It firstly depends on the propagation medium and of the type of waves. When dispersion is considered, it depends therefore on the frequency, too. Knowing the wave velocity is essential for the localization of the source, and provides information about propagation phenomena.

[1] A Wheatstone bridge is an electrical circuit made of resistors. Its purpose is to measure the value of one of its constitutive resistors (the values of the other resistors are supposed to be known) and is therefore commonly used with resistive sensors, such as piezoresistive sensors, potentiometers, thermistors, etc.

[2] Control rods are rods made of a neutron-absorber material and are inserted in the core when a reduction of the nuclear reaction is needed. In accidental situations, control rods fall brutally in the core to stop the reaction as fast as possible. This may produce a shock sound.

I.2.1. General methods

In the current work, only passive acoustic or vibration methods are treated. Passive methods refer to methods that consist in recording the waves generated by either the evolution of the damages in the studied structure, or the response of the structure due to external environmental loads. The equipment associated to such methods does not include any source of excitation. On the other hand, active methods consist in recording the response of the studied structure to an excitation generated by the control apparatus. Most common sources are ultrasonic emitter and vibration shaker.

Passive methods have specific interests: by definition, they are not intrusive at all (except the presence of the sensor that may disturb the flow or the neutronic flux, depending on its position). Although some active methods, such as ultrasonic methods, can be considered as non-intrusive (the generated ultrasonic stresses or pressures are negligible regarding reactor's operation) and are able to detect and localize a failure, passive methods offer more versatility. Ultrasonic methods need a prior choice of the phenomenon to study, which determines the type of probes to use, their settings, their positions, etc. Passive methods that are described below can provide information about various phenomena with sensors of a single type. However, each passive method is more or less suited to the study of some phenomena, as it is explained below.

Ultrasonic methods are not treated in the current work. General information about such methods can be found in [10], and examples of application to nuclear reactors are presented in [2].

I.2.1.1. Acoustic Emission

Acoustic Emission refers to phenomena defined in ASTM E1316 standard [11] or in [12] as: "The class of phenomena whereby transient elastic waves are generated by the rapid release of energy from a localized source or sources within a material, or the transient wave(s) so generated." Similar definitions can be found in [13], [14], [15]. The term is extended to the non-destructive testing methods that use such phenomena, introduced in [16]. As explained in the latter reference, AE phenomena and the associated testing methods are closely related to fracture mechanisms in the microstructure of the material.

AE methods were mainly developed since the 1970's. They are used nowadays in various industrial fields for testing and monitoring a wide range of structures (pipes, pressure vessels, civil engineering structures, wires, bearings, vehicles, etc) and materials (metals, composite materials, polymers, wood) [12], [17]. They are also used in research because they provide a non-intrusive way to study the behavior of materials under loading.

I.2.1.2. Structural vibration methods

The frontier between vibration-based methods and AE methods is not clearly defined. From a purely physical point of view, AE waves are vibrations. However, in the context of engineering methods for structure testing or monitoring, AE and vibrations usually refer to two different classes of phenomena associated to specific methods and instrumentation.

AE is classically related to the waves that are generated inside the structure material, by internal damage mechanisms. Most often, such waves have relatively low amplitude and high frequency (typically, from 10 kHz to 1 MHz, depending on the material and the structure's geometry). Therefore, acoustic-emission sensors have to be very sensitive at high frequency. Vibrations usually refer to structural motion induced by external sources, for instance: flow around the structure, mechanical transmission in a motorized system, contact with another structure, etc. A structure has a specific response to the considered excitation, and this response can be affected by the state of the structure. For instance, cracks can change modal parameters, such as the natural frequencies, of a structure [18]. It is therefore possible to detect such cracks by comparing the results of modal analyses (either experimental modal analysis, with a controlled excitation source, or operational modal analysis with an excitation induced by operating conditions) carried out at different stages of the structure's life. Passive vibration methods are widely used for defect detection in rotating machinery. In such cases, the excitation is simply the normal operation of the machine. Its rotation characteristics implies strong periodic features in the induced vibrations, which are affected by shaft's imbalance or gear's and bearing's damages. This makes cyclostationary analyses methods (introduced for instance in [19]) especially suitable for rotating machinery monitoring.

Vibration methods focus on a lower frequency range than AE, typically from 0.1 Hz to 10 kHz. Such a frequency range includes the first modes of most of the structures to study, and modal identification is technically easier on lower modes than higher ones. The larger and heavier the structure is, the lower its natural frequencies are. Very large structures, such as bridges or buildings may have first natural frequencies around 1 or 0.1 Hz (for instance, the first mode of a 76-story tower occurs at 0.16 Hz [20]), while the smallest structures commonly controlled (for instance, computer hard-drive parts [21]) have first natural frequencies of the order of 1 kHz. In addition to that, as piezoelectric and piezoresistive accelerometers (which are the most common type of sensors for vibration analyses) are used below their resonance frequency, as explained in Chap. IV, the frequency range of the devices recording the studied vibrations is limited. According to [22], 20 kHz is a commonly accepted upper limit.

I.2.1.3. Pressure measurements methods

In the field of damage detection in industrial fluid systems, two types of methods using fluid pressure measurement can be considered and are commonly used. The first type is ultrasound and AE methods carried out with sensors in fluid media ([23], [24]). In such methods, the pressure changes of interest are of the acoustic pressure's order of magnitude, *i.e.* very low compared to the pressure changes related to the system's operation. It requires therefore suitable pressure sensors (with high sensitivity and, usually, high frequency range), that are referred to "hydrophones". Hydrophones have to be placed in the fluid and, hence, their positioning has to be taken into account in the initial design of the system. An underlying aim of the current work is to identify methods that can be easily implemented in existing research and industrial reactors. Therefore, the methods requiring hydrophones will not be further considered.

The second type is the methods consisting of detecting leakages from the induced pressure changes. For such methods, the pressure changes of interest are usually in the same range as the operation-related pressure changes. Measurements can be therefore carried out with field instrumentation (*i.e.* sensors that can be used for general system condition monitoring). In such cases, no additional and specific sensor is required, which is an advantage compared to the methods using hydrophones. Most often, the aim of such methods is a simple leakage detection, using the fact that a leakage induces a global pressure drop in the system. In some applications, pressure measurements are also used to localize the leakage. A first method is to detect the pressure transient generated when the leakage occurs. Such a method is used in pipeline monitoring applications and is described in [25]. Another method is to analyze the response of the system when subjected to a water hammer, whatever the cause of the event. An anomaly in the system may result in a modification of the response to a water hammer and this modification can be analyzed to get information about the anomaly [26]. Such methods are known as "transient-based leak detection methods" and are used, for instance, to detect leaks and illegal connections in water supply networks [27], [28]. Despite those possibilities and advantages, it seems that pressure-measurement-based methods are not commonly used for nuclear fuel element monitoring, although coolant systems are always equipped with pressure sensors to monitor thermo-hydraulic conditions.

I.2.2. State of the art regarding monitoring of fuel rods

Regarding in-service monitoring of nuclear fuel rods, the most commonly used passive methods are AE methods. Exemples of the use of AE for failure detection are presented in [29], [3] and [30]. The first two references present actual in-service monitoring of rods in research reactors, while the latter is about out-of-pile hydraulic tests without external fluid. Those references are the only ones that precisely describe AE applications related to a cladding failure and that could be found in the literature. As shown in [31], AE can also be used to detect water boiling on the cladding surface. Besides AE, some other applications of acoustic methods to fuel rod monitoring may provide useful information for the current work. [32] and [33] show that guided waves can be used to detect damages in the cladding, and introduce therefore the topic of guided waves in relation to fuel rod cladding. In [34], a method to analyze the inner gas composition to identify fission products is presented, as well as the associated instrumentation. [35] presents a way to detect cavitation around fuel elements in sodium-cooled reactors. [36] proposes a method to detect Pellet-Cladding Mechanical Interaction (PCMI) based on the identification of structural vibration mode, assuming that PCMI has a significant influence on modal parameters.

Although the results of those works are not directly applicable to the current work, they provide a useful overview about the possibilities of instrumenting fuel rods with acoustic or vibration sensors.

As explained in [16], or as shown by the various studies presented in [17], AE phenomena strongly depends on the material properties and the damage mechanisms at a microstructural scale. Therefore, to obtain meaningful conclusions about AE related to a cladding failure, the micro-structural phenomena that generate AE during real cladding failures in reactors should be accurately known, and the experimental conditions and material properties of the test samples should be perfectly controlled. This would require a substantial work about fracture mechanics, and heavy experimental resources to be able to reproduce the right conditions (material, loads, temperature, etc). Furthermore, validated numerical tools to model AE phenomena are not available yet. Design of such tools is still at a research stage (see for instance, [37]). Analysis of past tests in real reactors showed that Fluid-Structure Interaction (FSI) phenomena induced by the pressure surge in the coolant fluid has more significant effects on both fluid and structural measurements than proper AE phenomena. Such FSI phenomena are associated to low frequency (compared to typical AE frequency range) structural dynamics, and depend rather on macroscopic material properties. Such properties are easier to handle, or at least to estimate, during experiments. Generally, low frequency structural dynamics is less sensitive to small discrepancies in material properties and the effects of such discrepancies can be easily assessed by the theory or numerical computations.

Both topics – high-frequency AE with fracture mechanics issues and low frequency structural dynamics with FSI – should be taken into account. However, in the frame of this PhD, by considering constraints of the project (available time, human and material resources, safety obligations), it was decided to focus on FSI and structural dynamics. Such a choice made it possible to take advantage of the expertise in FSI, fluid dynamics and structural dynamics that is present in CEA, and of the various existing works and numerical tools related to such phenomena in nuclear reactors or similar systems.

I.3. Objectives of the work

The analyses of the context, the initial needs in cladding failure monitoring, the state of the art of suitable passive methods, and the available resources (human or material) enable the definition of objectives that are relevant, and achievable in the frame of this PhD. Those analyses show that passive acoustic and vibration methods can be of interest for the study of fuel behavior in nuclear environment, as they offer a rather simple and non-intrusive way to observe not only the cladding failure but some other phenomena related to the coolant fluid. Three types of passive methods were identified: AE, structural vibration measurements and pressure measurements. However, the necessary information to properly apply each of those methods and take advantage of all their possibilities is currently missing. While the application of AE methods requires an exhaustive study in material science and fracture mechanics, the missing information for structural vibration and pressure methods is mainly related to fluid-structure interaction issues. It was decided to focus the current PhD on such fluid-structure interaction issues. Thus, the following phenomena must be taken into account: the dynamic response of the structure due to the failure-induced shock, the propagation of the failure-induced pressure surge in the coolant fluid, and, more generally, the wave propagation in the fluid and the structure and the transmissions between the two media.

Before being able to obtain the necessary information, the ways to obtain it must be identified and the theoretical, numerical and experimental means must be implemented.

As several methods are already identified, and several phenomena have to be considered, it is necessary to evaluate which methods are the most efficient to get information about the failure, and how each phenomenon affects the results of the different methods. Those issues constitute the primary objective of the current work, which can be stated as the following question: What is the information provided by each of the identified methods, and how the different fluid-structure interaction and wave propagation phenomena can affect the quality of this information ? The work will therefore consist in exploring the possibilities of acoustic and vibration methods in the phenomenological understanding of a cladding failure in a nuclear reactor.

To reach this objective, the global phenomenology of the event must be understood. A clear understanding of each studied phenomenon will allow reliable assessment of the feasibility of the different methods and accurate conclusions concerning their respective advantages and limits.

Firstly, the phenomena that can be studied by all the methods, or that may influence their results, have to be identified. Secondly, those phenomena are studied by analytical and numerical models. Those studies aim to understand the global phenomenology, to help the design of future experimental approaches (either in real reactors or on experimental mockups), and to provide qualitative and quantitative information that will be useful for the interpretation of future experimental data. Thirdly, experimental studies can be carried out on a mockup, to definitely validate the methods before their applications in a real reactor. An experimental approach seems essential, as analytical and numerical models are necessarily simplified.

A secondary objective, which is more application-oriented, is to determine what information can be provided by the different kinds of sensors, and to find the best methods to process the measurements. For each type of sensor, the aims are to identify what phenomena can be observed by each sensor, and assess how the sensor positions affect the observation. Then, the set of sensors, their positions and the way to analyze the measurements that are the most suitable for failure detection and localization could be identified. Such practical issues can be solved by the same approaches as the main objective. Actually, choosing the right sensors, the right positions and the processing methods is included in the implementation of the experiments and the analyses of the results that are necessary to achieve the main objective about general phenomenology.

II. Theoretical descriptions of the underlying phenomena

The phenomena that are concerned can be divided into three categories: elastic guided waves, structural vibrations and fluid-structure interaction (FSI). Elastic guided waves are propagating elastic waves whose wavelength is relatively small compared to the typical transverse dimension of the structure (for instance, for the cladding, the typical transverse dimension is its thickness). As a consequence, longitudinal and transversal waves combine with each other and create specific propagation modes that are characterized by a specific displacement profile in the transverse plane (*i.e.* in the thickness) and a specific frequency-velocity relation (described by dispersion curves). Structural vibrations refer, in the current document, to waves of lower frequencies than guided waves and whose wavelength's order of magnitude is larger than the transverse dimension of the structure. As explained in Sec. II.2, the beam theory is used to describe such vibrations. In this theory, the displacement profile can be considered as uniform across the thickness of the structure. Structural mode vibrations are related to structural resonances in the main directions, that are, regarding beams, the longitudinal direction only[1]. Both elastic guided waves and structural vibration theories are of interest to interpret the experimental results of tests on tubes in the open air, presented in Chap. IV.

In the frame of the current work, the FSI category gathers all the phenomena involving fluid and structures excited by the failure-induced pressure surge. They are therefore useful for the numerical study, presented in Chap. III, which takes the coolant fluid into account. Additionally, effects of the surrounding flow will be studied in the frame of the experimental campaign with immersed tube and are also categorized in the FSI category.

The current chapter includes the description of four distinct theories. The first two introduced theories, namely the guided wave theory and the beam theory, are used for the interpretation of experimental results, presented in Chap. IV. Then, two different descriptions of FSI phenomena are introduced: water-hammer models, and Euler equations applied to FSI. The purpose of water-hammer models is to give a clear and easy understanding of the effects of a pressure surge, such as the one that can be generated by some cladding failures. Such models allow significant qualitative consequences to be understood, even without numerical resolutions. On the other-hand, Euler-equation approach constitutes the basis of the numerical simulations presented in Chap. III.

[1] Resonances are considered in the longitudinal direction, but the waves can be transversal (or flexural) waves as well as longitudinal waves.

II.1. Guided waves

In a solid medium, two fundamental types of waves can propagate: longitudinal waves (particle motion parallel to the propagation direction) and transversal waves (particle motion perpendicular to the propagation direction). Longitudinal waves are sometimes referred as compression waves, extensional waves, or dilatational waves (because of the induced Poisson effect), and transversal waves are sometimes referred as shear waves. According to the anisotropy of the medium and boundary conditions, the waves associated to the two fundamental types can combine in some specific ways and generate guided waves. According to the geometry of the propagation domain, different types of guided waves can be generated. In the current work, we focus on guided waves appearing in annular cylinder geometries (such as tubes and rod claddings). Contrary to structural vibrations, introduced in Sec. II.2, for which the displacement field depends on one dimension only, guided waves displacement fields are three-dimensional.

The current section introduces the theoretical background that is necessary to understand the propagation of high frequency structural waves in the studied structures. This introduction is based on [38], where the classical elastic wave theory is applied to the specific case of guided waves along a hollow cylinder.

II.1.1. Wave equation

In an isotropic and elastic material, wave propagation is described by the following wave equation (such an equation can be obtained from Newton's second law applied to an elementary particle of the material):

$$\mu\boldsymbol{\nabla}^{\mathbf{2}}(\boldsymbol{q}) + (\lambda+\mu)\,\mathrm{grad}(\mathrm{div}\boldsymbol{q}) = \rho_s\frac{\partial^2\boldsymbol{q}}{\partial t^2}, \tag{II.1}$$

with:

- $\boldsymbol{\nabla}^{\mathbf{2}}$: vector Laplacian operator,
- $\boldsymbol{q}$: displacement vector, depending on the three spatial coordinates (x, y, z),
- μ and λ: Lamé parameters,
- ρ_s: material density,
- t: time.

This equation can be solved by using Helmholtz's decomposition, which consists of expressing $\boldsymbol{q}$ as a sum of a scalar potential ϕ, associated to longitudinal waves, and a vector potential, $\boldsymbol{\psi}$, associated to transversal waves:

$$\boldsymbol{q} = \mathrm{grad}(\phi) + \mathrm{rot}(\boldsymbol{\psi}). \tag{II.2}$$

Such a decomposition allows Eq. (II.1) to be rewritten as two uncoupled equations related to longitudinal waves and transversal waves respectively:

$$\mathrm{div}(\mathrm{grad}\phi) - \frac{1}{c_L^2}\frac{\partial^2 \phi}{\partial t^2} = 0, \tag{II.3}$$

$$\boldsymbol{\nabla}^2 \boldsymbol{\psi} - \frac{1}{c_T^2}\frac{\partial^2 \boldsymbol{\psi}}{\partial t^2} = \boldsymbol{0}, \tag{II.4}$$

where $c_L = \sqrt{\frac{\lambda+2\mu}{\rho_s}}$ is the longitudinal wave velocity, and $c_T = \sqrt{\frac{\mu}{\rho_s}}$ is the transversal wave velocity. Those velocities can be equivalently expressed with Young modulus E and Poisson coefficient ν:

$$c_L = \sqrt{\frac{E}{\rho_s}}, \tag{II.5}$$

$$c_T = \sqrt{\frac{E}{2\rho_s\,(1+\nu)}}. \tag{II.6}$$

II.1.2. Solution for a hollow cylinder

The considered propagation domain is an elastic, isotropic cylinder, with an inner radius R_{in}, a thickness b and a length L. Cylindrical coordinates (r,θ,x) (radial, orthoradial and axial coordinates, respectively), depicted in Fig. II.1, are used. The displacement vector, $\boldsymbol{q}$, is constituted by three components (q_r, q_θ, q_x), which are the radial displacement, the orthoradial displacement and the axial displacement, respectively. Each component depends on the three cylindrical coordinates.

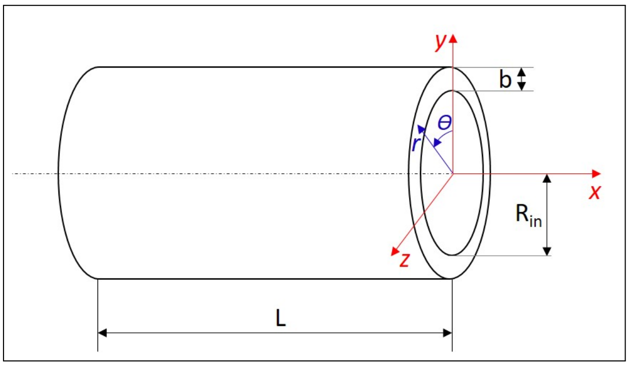

Figure II.1. *Propagation domain and cylindrical coordinates*

For such a configuration, components of the vector potential $\boldsymbol{\psi}$ can be written as $(\psi_r, \psi_\theta, \psi_x)$ and are respectively associated to particle motion in the radial direction, orthoradial direction and axial direction. All the waves propagate in the axial direction.

The solutions of the uncoupled Eq. (II.3) can be written in the following form:

$$\phi = f(r)\ \cos(n\theta)\ \cos(kx+\omega t), \tag{II.7}$$

$$\left\{\begin{array}{lcl} \psi_x & = & h_x(r)\ \sin(n\theta)\ \cos(kx+\omega t), \\ \psi_r & = & h_r(r)\ \sin(n\theta)\ \sin(kx+\omega t), \\ \psi_\theta & = & h_\theta(r)\ \cos(n\theta)\ \sin(kx+\omega t), \end{array}\right. \tag{II.8}$$

where k is the axial wave number.

By substituting those solutions into Eq. (II.3) and defining the operator $\Delta\cdot = \mathrm{div}(\mathrm{grad}\cdot)$, it yields:

$$\Delta\phi + \frac{\omega^2}{c_L^2}\phi = 0, \tag{II.9}$$

$$\left\{\begin{array}{r} \Delta\psi_x + \frac{\omega^2}{c_T^2}\psi_x = 0, \\ \Delta\psi_r - (\frac{1}{r^2} + \frac{\omega^2}{c_T^2})\psi_r - \frac{2}{r^2}\frac{\partial\psi_\theta}{\partial\theta} = 0, \\ \Delta\psi_\theta - (\frac{1}{r^2} + \frac{\omega^2}{c_T^2})\psi_\theta - \frac{2}{r^2}\frac{\partial\psi_r}{\partial\theta} = 0. \end{array}\right. \tag{II.10}$$

Solving such equations in cylindrical coordinates is a relatively long process, which is presented in details in [38]. This article shows that the solutions in terms of q_x, q_r, q_θ are combinations of modified Bessel functions, defined according to the ratios between the frequency and wave number. Taking into acount the boundary conditions (free outer and inner surface, in the article, as well as in the current work, implying null stresses on those surfaces) yields a set of 18 equations, which depend on the frequency, the wave number and the wave velocity. Those equations can be analytically solved in some particular cases only, which are treated in [38]. The article also shows that, in any case, the waves propagate as different types of modes, which are introduced in Sec. II.1.3.

II.1.3. Guided wave modes classification

Different conventions for the classification of guided waves modes can be found in the literature. In the current document, the convention used in [39] (among others) is adopted. According to this convention, guided waves modes can be divided into three families:

- Longitudinal modes, referred as "L": They are associated to a combination of axial and radial displacements forming an axi-symmetrical field,
- Flexural modes, referred as "F": They are associated to a combination of axial and radial displacements forming a non-axi-symmetrical field,
- Torsional modes, referred as "T": They are associated to an orthoradial displacement.

Each of those three families contains several modes. Each mode is referred by its family's letter (L, F or T) and the number of azimutal and radial nodes (a node is a position where the displacement is null). Thus, the modes are referred as L(0,m), F(n,m) or T(n,m), where n and m are the number of azimutal and radial nodes, respectively. One may notice that longitudinal modes do not have any azimutal node (the displacement field does not depend on θ), so n is always zero. This is specific to the adopted convention and may not be the case in other conventions.

A physical understanding of the three families of modes can be provided by Fig. II.2, which shows examples of guided wave modes in a cylinder. Only the displacement profile on the outer surface is shown, the number of radial nodes is therefore not visible.

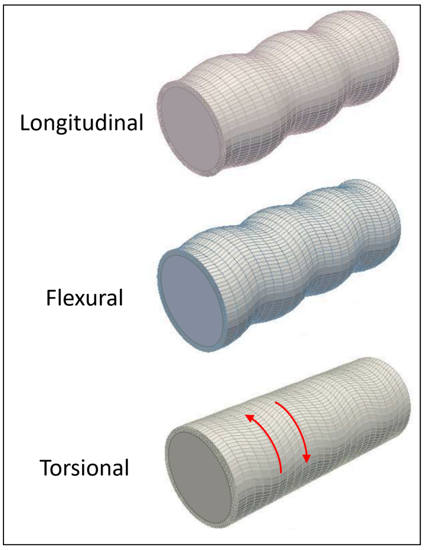

Figure II.2. *Drawings representing displacement profiles associated to the three families of guided wave modes in a cylinder [40].*

II.1.4. Boundary conditions at the ends

The conditions at the ends of the tube do not influence the generation and the properties of guided wave modes (they depend only on the conditions on the inner and outer surface of the tube) but influence the reflections of the waves. For each motion direction (axial, radial, orthoradial) and each fundamental type of waves (longitudinal or transversal), two types of conditions are classically considered: free or blocked. The free condition is expressed by:

$$\sigma_{ij}(x_b, r, \theta) = 0, \tag{II.11}$$

and the blocked condition is expressed by:

$$q_i(x_b, r, \theta) = 0, \tag{II.12}$$

where i and j refers to the direction (either x, r or θ) and $x_b = 0$ or L.

For the current work, the resolution of the problem described by Eq. (II.10) and by the boundary conditions described in Chap. IV, Sec. IV.3.4, is done through the CIVA software. The software is able to analytically compute the dispersion curves associated to every possible mode in the modeled structure, and can simulate the propagation of a signal generated by an emitter at a chosen position by Semi-Analytical-Finite-Element (SAFE) method, as explained in [41].

II.1.5. Additional information about guided waves

Longitudinal waves introduced in Sec. II.1.1, whose velocity is given by Eq. (II.5), correspond to tensile-compressive waves in a finite domain which is unrestrained at its boundaries. Hence, a dilatation in the direction perpendicular to the tensile-compression direction, known as "Poisson effect", is taken into account. This dilatation phenomenon slightly slows the waves down. Therefore, the longitudinal wave velocity in a finite (in lateral directions) and unrestrained solid domain is slightly lower than the velocity in an infinite domain, or in a finite domain with restrained lateral boundaries. The velocity in such a domain is given by:

$$c_{L0} = \sqrt{\frac{E}{\rho_s}\frac{(1-\nu)}{(1+\nu)(1-2\nu)}}. \tag{II.13}$$

The Poisson effect associated to tensile-compressive waves implies that such waves induce a motion in the direction perpendicular to the propagation direction, in addition to the main motion in the propagation direction. For that reason, such waves are sometimes referred as "quasi-longitudinal waves". In the current work, the studied structures are immersed in a fluid, so the outer-wall boundary can be considered as unrestrained. Moreover, the thickness of the structure is not large enough compared to the considered wavelengths to allow the structure domain to be considered as infinite. Therefore, Poisson effect can not be neglected and tensile-compressive waves are considered as quasi-longitudinal waves.

In semi-infinite solid domains, or, more practically, in structure whose thickness is large compared to the considered wavelength, another type of waves may be encountered, known as Rayleigh waves ([10]). Those waves are a combination of transverse and longitudinal waves that appear near the surface of a structure. The surface has to be free, or very lightly loaded, to allow Rayleigh waves to appear. The amplitude of such combined waves decreases with the distance from the free surface. However, when two free surfaces are close to each other (under a distance of the same order of magnitude as the wavelength), the waves combine into guided-wave modes, such as the ones described in Sec. II.1.3 for a cylinder, rather than Rayleigh waves. In the systems studied in the current work, *i.e.* test devices used in research reactors (described in Chap. III), Rayleigh waves can be found in the outer tube only, for the upper part of the considered frequency range (typically, about hundreds of kHz). In the considered frequency range, Rayleigh waves can not appear in the rod cladding, which is thinner than the outer tube.

Different approximations of Rayleigh wave velocity can be found in the literature, such as the following one, from [42], mentioned in [43]:

$$c_R = c_T\frac{0.87+1.12\nu}{1+\nu}. \tag{II.14}$$

II.2. Structural vibrations and beam theory

In structures whose transverse dimensions are small against the length, and when elastic waves whose wavelength is long compared to the typical transverse dimension of the structure are considered, the associated displacement profile can be assumed as constant across the cross-section. Therefore, such waves can be considered along one dimension only and the structure can be described by a beam model. Such a model is legitimate for the studied fuel rods and the experimental tube samples (described in Chap. IV, Sec. IV.4), as their outer diameter R_{out} (about 10 mm) is small compared to their length (about 600 mm). Moreover, as the displacements are supposed to be small, the beam can be modeled according to the Euler-Bernoulli theory. This theory, sometimes referred as "classical" beam theory, was likely firstly introduced around 1750 [44]. Since then, it has been extensively used, for both static and dynamic analyses, especially when powerful numerical tools did not exist, and is still commonly used nowadays when simplified models are necessary. Numerous books, lectures or articles present this theory and the associated resolution methods, such as [45], [46], [47].

In the current section, the Cartesian coordinate system shown in Fig. II.1 is used. The studied structure is a tubular beam of axis x, with a constant cross-sectional area S, a length L, an area moment of inertia around the transverse axis (y or z indifferently, as the cross section is circular), I. The constitutive material is isotropic and has a Young modulus E and a Poisson coefficient ν. The variables q_x, q_y and Θ represent the axial displacement, the transversal displacement, and the angular displacement about the x axis, respectively. External load distribution per unit length in the axial and transversal directions are referred as $f_x(x,t)$ and $f_y(x,t)$, respectively. The distribution of the loading moment around the x axis is referred as $M_t(x,t)$.

The Euler-Bernoulli theory consists of neglecting shear deformation and rotary inertia, which implies the following assumptions: the cross-section along the beam remains plane and perpendicular to the beam axis and is not distorted. Consequently, the beam is considered as a one-dimensional system, and displacements depend only on the axial position and the time.

Longitudinal, torsional and flexural vibrations are treated in the Sec. II.2.1, Sec. II.2.2, Sec. II.2.3. The resolution method is introduced for longitudinal vibrations only, but is similar for torsional and flexural vibrations.

II.2.1. Longitudinal vibrations

Longitudinal vibrations, or axial vibrations, are related to tensile-compressive stresses in the axial direction. Thus, in the current section, only longitudinal stresses are taken into account, and they are considered to be uniform over the cross-section. The resulting axial motion q_x is governed by the following wave equation:

$$-E\,S\,\frac{\partial^2 q_x}{\partial x^2} + \rho_s\,S\,\frac{\partial^2 q_x}{\partial t^2} = f_x(x,t). \tag{II.15}$$

The response of the system, q_x, which is the general solution of Eq. (II.15), is the superposition of the solutions of the homogeneous equation (*i.e.* Eq. (II.15) without the right hand term) and a particular solution of the equation with the right hand term. Therefore, the first step to find the response of the system is to solve the homogeneous equation. It can be shown that the space-dependent term of its solutions, called "mode shapes", are orthogonal with each other and can form a spatial basis, referred to as "modal basis". Every response of the system, whatever the initial conditions and the excitation, can be expressed on the modal basis. With a relevant truncation of the modal basis, it provides an interesting way to decompose the motion of the system on a finite basis.

II.2.1.1. Free response

After introducing the longitudinal wave velocity $c_L = \sqrt{\frac{E}{\rho_s}}$, the homogeneous equation reads:

$$-\frac{\partial^2 q_{free}}{\partial x^2} + \frac{1}{c_L^2}\frac{\partial^2 q_{free}}{\partial t^2} = 0. \tag{II.16}$$

This equation is written in terms of q_{free}, denoting its solution corresponds to the response of the system without excitation, called the *free response*. A solution can be obtained by the method of separation of the variables. It consists of expressing the solution as a product of a space-dependent function and a time-dependent function:

$$q_{free}(x,t) = X(x)\ T(t). \tag{II.17}$$

By substituting this form into Eq. (II.16), it yields:

$$-\frac{\partial^2 X(x)T(t)}{\partial x^2} + \frac{1}{c_L^2}\frac{\partial^2 X(x)T(t)}{\partial t^2} = 0, \tag{II.18}$$

which can be re-written as follows:

$$\frac{\partial^2 X(x)}{\partial x^2}\frac{1}{X(x)} = \frac{1}{c_L^2}\frac{\partial^2 T(t)}{\partial t^2}\frac{1}{T(t)}. \tag{II.19}$$

Considering that X and T are not constant, a constant k can be defined so that:

$$\frac{\partial^2 X(x)}{\partial x^2}\frac{1}{X(x)} = \frac{1}{c_L^2}\frac{\partial^2 T(t)}{\partial t^2}\frac{1}{T(t)} = -k^2, \tag{II.20}$$

$$k \neq 0. \tag{II.21}$$

k is referred to as the wave number. (The solution $k = 0$ is of no interest, as it would imply that there is no vibration.)

As a consequence, Eq. (II.16) yields two uncoupled equations:

$$\frac{\partial^2 X(x)}{\partial x^2} + k^2 X(x) = 0, \tag{II.22}$$

$$\frac{\partial^2 T(t)}{\partial t^2} + k^2 c_L^2 T(t) = 0. \tag{II.23}$$

The equations have an infinity of harmonic solutions, referred to as *modes*, that can be written as follows:

$$X_n(x) = A_n \cos(k_n x) + B_n \sin(k_n x), \tag{II.24}$$
$$T_n(t) = \alpha_n \cos(\omega_n t) + \beta_n \sin(\omega_n t), \tag{II.25}$$

where n is an integer, whose definition domain will be more precisely defined according to the boundary conditions, and ω_n is the circular natural frequency associated to the n^{th} mode, defined as:

$$c_L = \frac{\omega_n}{k_n}. \tag{II.26}$$

As the problem is linear, the free response of the structure can be written as a sum of those solutions:

$$q_{free}(x,t) = \sum_{n=1}^{\infty} X_n(x) T_n(t). \tag{II.27}$$

Coefficients A_n, B_n, and the constant k_n are determined according to the boundary and initial conditions. As it will be explained in Chap. IV, to accurately model the experimental devices, the exact boundary conditions should be experimentally estimated. In the current section, the example of a tube clamped at both ends is treated. The solutions for other boundary conditions can be found in [48]. With "clamped-clamped" conditions, the longitudinal motion on both ends is null, which yields:
At $x = 0$:

$$X_n(0) = 0, \tag{II.28}$$

By substituting Eq. (II.24) into the last equation, it finally yields:

$$A_n = 0. \tag{II.29}$$

Therefore,

$$X_n(x) = B_n \sin(k_n x), \tag{II.30}$$

Then, the condition at $x = L$ is used to define k_n:

$$X_n(L) = 0. \tag{II.31}$$

By using the last form of X_n given by Eq. (II.30), it yields:

$$\sin(k_n L) = 0,$$

which is equivalent to:

$$k_n = n\frac{\pi}{L}, \; n = 1, 2 \ldots +\infty. \tag{II.32}$$

As a consequence:

$$X_n(x) = B_n \sin\left(n\frac{\pi}{L}x\right). \tag{II.33}$$

Then, mode shapes can be defined, based on the expression of X_n:

$$\Phi_n(x) = \sin\left(n\frac{\pi}{L}x\right). \tag{II.34}$$

It can be noticed that every mode shape is orthogonal to each other (this is referred as the *mode orthogonality*):

$$\int_0^L \Phi_n \Phi_m \, dx = 0, \; \forall \; m \neq n. \tag{II.35}$$

By substitution the expression of k_n, Eq. (II.32), into Eq. (II.26), the circular frequency of the n^{th} mode can be written as:

$$\omega_n = c_L \, n \, \frac{\pi}{L}. \tag{II.36}$$

It is now possible to express the free response of the system, as the sum of all the solutions:

$$q_{free}(x,t) = \sum_{n=1}^{\infty} B_n \Phi_n(x) T_n(t) = \sum_{n=1}^{\infty} \sin\left(n\frac{\pi}{L}x\right)\left(\alpha_n \cos(\omega_n t) + \beta_n \sin(\omega_n t)\right). \tag{II.37}$$

Then, the left constants, α_n and β_n can be determined with the initial conditions and the mode orthogonality principle. For the current work, the natural circular frequencies and the mode shapes are the desired information, it is therefore not necessary to find the forced response. Nevertheless, in order to clearly show how the introduced equations and the information already obtained are related to the actual behavior of the tested rods or tubes, the full resolution method is briefly summarized in what follows. Although it was eventually not done in the frame of this work, the final solution can be used to build a more complete model to describe the experiments presented in Chap. IV and to take into account the effects of the flowing fluid on the structural response.

II.2.1.2. Modal damping

Before considering the initial conditions, damping can be added to the model, by introducing a modal damping term ξ_n in the time-dependent Eq. (II.23) which yields:

$$\frac{\partial^2 T_n(t)}{\partial t^2} + 2\xi_n \omega_n \frac{\partial T_n(t)}{\partial t} + \omega_n^2 T_n(t) = 0. \tag{II.38}$$

Therefore, the expression of T_n given by Eq. (II.25) can be replaced by:

$$T_n(t) = \left[\alpha_n \cos\left(\omega_n \sqrt{1-\xi_n^2}\; t\right) + \beta_n \sin\left(\omega_n \sqrt{1-\xi_n^2}\; t\right)\right] e^{-\xi_n \omega_n t}. \tag{II.39}$$

The effects of the damping on the free response is showed by the presence of the damping term in the sinusoidal components, and the addition of an exponential decay. The product of the term $\sqrt{1-\xi_n^2}$ and the circular natural frequency ω_n can be understood as a modified natural frequency, called "damped circular frequency":

$$\omega_{d\,n} = \omega_n \sqrt{1-\xi_n^2}. \tag{II.40}$$

The response of the experimental tube samples described in Chap. IV to a shock, such as a failure, can be modeled by the free damped response obtained by substituting the expression of T_n given by Eq. (II.39) into the expression of q_{free} given by Eq. (II.27), and by defining appropriate initial conditions on the velocity (a shock is represented by an initial imposed velocity at the source position).

II.2.1.3. Forced response

The general solution of Eq. (II.15), which corresponds to the forced response, is constituted by the free response q_{free}, previously determined, and a particular solution, q_p:

$$q_x(x,t) = q_{free}(x,t) + q_p(x,t). \tag{II.41}$$

q_p can be expressed on the previously defined modal basis and be written in the following form:

$$q_p(x,t) = \sum_{n=1}^{\infty} \Phi_n(x) Q_n(t). \tag{II.42}$$

By substituting this expression into the initial wave equation, Eq. (II.15), and by multiplying both terms of the equation by Φ_m, using the principle of mode orthogonality, and integrating along the beam's length, it yields a set of uncoupled equations of the form:

$$\frac{\partial^2 Q_n(t)}{\partial t^2} + 2\omega_n \xi_n \frac{\partial Q_n(t)}{\partial t} + \omega_n^2 Q_n(t) = \frac{F_n(t)}{m_n}, \tag{II.43}$$

where:

- m_n is the modal mass, defined by: $m_n = \int_0^L \rho_s S \Phi_n(x)^2 dx$, where S is the cross-sectional area,
- F_n is the excitation in modal coordinates: $F_n = \int_0^L f_x(x,t)\Phi_n(x)dx$.

Analytical solutions of Eq. (II.43) for different kinds of harmonic excitations can be found in [48]. For modeling the Flow-Induced Vibrations (FIV) in the case of a steady flow, harmonic solutions are appropriate. Otherwise, for arbitrary forces, a solution is provided by a *convolution integral*, which is defined as the convolution of the excitation and the impulse response h_n associated to the n^{th} mode ([48],[49]):

$$Q_n(t) = h_n(t) * F_n(t), \tag{II.44}$$

where $*$ denotes the convolution. The impulse response associated to the n^{th} mode, h_n is equivalent to a 1-degree-of-freedom system response and reads:

$$h_n(t) = \frac{1}{m_n\,\omega_{dn}} e^{-\xi_n \omega_n t} \sin(\omega_{dn} t). \tag{II.45}$$

Therefore:

$$Q_n = \frac{e^{-\xi_n \omega_n t}}{m_n\,\omega_{dn}} \int_0^t F_n(\tau) e^{+\xi_n \omega_n \tau} \sin\left(\omega_{dn}(t-\tau)\right)\, d\tau \tag{II.46}$$

The previous expression is sometimes called *Duhamel's integral*.

II.2.2. Torsional vibrations

Torsional vibrations are associated to the angular motion Θ about the beam axis and are governed by the following wave equation:

$$-G\,J\,\frac{\partial^2 \Theta}{\partial x^2} + \rho_s\,J\,\frac{\partial^2 \Theta}{\partial t^2} = M_t(x,t), \tag{II.47}$$

where M_t is the external load moment about x, G is the shear modulus, $G = \frac{E}{2(1+\nu)}$, J is the moment of inertia about x.

By introducing the torsional wave velocity $c_T = \sqrt{\frac{G}{\rho_s}}$, the equation can be rewritten as:

$$-\frac{\partial^2 \Theta}{\partial x^2} + \frac{1}{c_T^2}\frac{\partial^2 \Theta}{\partial t^2} = \frac{M_t(x,t)}{GJ}. \tag{II.48}$$

As the equation is of the same form as the longitudinal wave equation, Eq. (II.15), the resolution method and the form of the solutions are the same.

II.2.3. Flexural vibrations

Flexural vibrations are associated to motions along the beam's transverse axes, namely y and z. The governing equations, and hence the solution, are the same for both axes. In the current section, only the motion along y, q_y, is treated, but the method can be similarly applied to the motion along z.

Flexural (or bending) vibrations are described by a fourth-order partial differential equation:

$$EI\frac{\partial^4 q_y}{\partial x^4} + \rho_s S \frac{\partial^2 q_y}{\partial t^2} = f_y(x,t). \tag{II.49}$$

Although Eq. (II.49) has a different form than the longitudinal wave equation, the same resolution method can be applied. The separation of variables applied to the homogeneous equation provides mode shapes of the following form:

$$\Phi_n(x) = A_n \sin\left(k_{fn} x\right) + B_n \cos\left(k_{fn} x\right) + C_n \sinh\left(k_{fn} x\right) + D_n \cosh\left(k_{fn} x\right). \tag{II.50}$$

Relations between the constants A_n, B_n, C_n, D_n, and the wave number k_{fn} are determined by the boundary and initial conditions. (The wavenumber k_{fn} associated to flexural vibrations is different than the wavenumber k_n defined previously and associated to longitudinal vibrations.) The different solutions associated to all the fundamental boundary conditions can be found in [48]. For example, in the case of "pinned-pinned" conditions[2], the wave number is:

$$k_{fn} = n\frac{\pi}{L},\ n \geq 1, \tag{II.51}$$

and the mode shape is:

$$\Phi_n = \sin\left(n\frac{\pi}{L}x\right), \tag{II.52}$$

k_{fn} is related to the eigen-circular-frequency ω_n by the following expression:

$$\omega_n = k_{fn}^2\sqrt{\frac{EI}{\rho_s S}}. \tag{II.53}$$

It implies that the wave velocity depends on the frequency and is given by:

$$c_F = \frac{\omega_n}{k_{fn}} = \sqrt{\omega_n}\left(\frac{EI}{\rho_s S}\right)^{1/4}. \tag{II.54}$$

Hence, unlikely to longitudinal and torsional vibration waves, flexural vibration waves are dispersive.

Once mode shapes and eigenfrequencies are found, the resolution of the equation subjected to initial conditions and an excitation term is achieved with the same method as the one used for the longitudinal vibrations.

II.2.4. Elastic supports

As it will be explained in Chap. IV, Sec. IV.3.5.2, the fundamental boundary conditions (free, clamped and pinned conditions) did not accurately describe the real conditions encountered in the experiments. Flexural vibration modes were therefore computed by finite element methods in order to take into account elastic supports of the tube in a simple way. Such supports are modeled by adding rotational stiffness to the moment about the axis perpendicular to the longitudinal axis at both ends of the tube.

Those additional numerical computations were carried out on flexural vibrations only, as it was noticed that the measurements on the experimental setup allow the observation of the first flexural modes only.

The comparison between the results with elastic, clamped and pinned supports will be presented in Chap. IV.

[2] "pinned-pinned" conditions mean that, at both ends, the transversal displacement is blocked, but the rotation around the transversal axis is free.

II.3. Fluid-structure interaction

FSI related to the failure-induced pressure surge can be studied by two approaches. The first approach, presented in Sec. II.3.1, is based on the theory related to the phenomenon of "water-hammer". Many works have been carried out to study this phenomenon and resulted in several models. Some of those models offer an interesting and understandable physical description of the phenomena of propagation and FSI induced by a pressure surge in pipe-like structures. Moreover, thanks to one-dimensional approximation, some of them are also a fast computation tool to study such phenomena. The second approach is based on compressible Euler equation, which can be subjected to FSI conditions and solved by finite-element and finite-volume methods in three dimensions (results of such computations are presented in Chap. III). In such a case, the studied phenomena can be reproduced with great realism and by taking into account some specific properties of the system to consider.

II.3.1. Water-Hammer based approach

The water-hammer phenomenon can be understood as a pressure surge in a liquid conveying pipe. The surge is often induced by a sudden change in the velocity of the fluid flow (caused by a valve closure, for instance), but some other causes, such as the steam explosion or the high-pressure gas release associated to a fuel rod cladding failure, may produce the same effect. As it can cause severe damage to a wide range of industrial systems, the phenomenon was extensively studied. Therefore, different theories exist to describe the propagation of the pressure surge along the system. A very comprehensive review recounting the evolution of water-hammer theories from the 19^{th} century up to the late 20^{th} century is presented in [50]. Only the most significant references, relevant for the current work, are mentioned in what follows.

The first scientific considerations about water-hammer seem to arise in the late 17^{th} and the early 18^{th} centuries, with Montgolfier's work on hydraulic rams in 1803 [51], and Young's work on blood flow in 1808 [52]. First consistent theories of water-hammer are defined around 1860-1880, for instance by Menabrea [53], by Michaud [54] or by Kries [55]. In 1898, Joukowsky [56] proposed a relation between an instantaneous change in flow velocity and the induced pressure surge. Even though such a relation was found earlier by other authors, including Kries, it became known as the "Joukowksy equation". Lamb proposed in 1898 a general model for wave propagation in fluid-filled tubes that takes fluid-structure interaction into account (which was not the case in Joukowsky's work, where only the elasticity of the pipe is considered, without any inertia) [57]. In 1956, Skalak [58] proposes an extended model of Lamb's one, in addition to exhaustive physical considerations about Joukowsky's model's limits, the presence of precursor waves in addition to the main pressure wave, the effects of wall inertia and bending stiffness, the significance of dispersion. From the 1950s to the 1990s, numerous models have been either extended or built to take into account or neglect various phenomena (Poisson coupling, friction, radial inertia, etc) or consider specific conditions (pipe's bends or T-branches, for instance). Moreover, many works were also related to resolution methods, especially the Method of Characteristic [59], or to experimental validations, such as Bürmann's works mentioned in [50]. Recent works related to water-hammer focus rather on numerical resolution methods ([60]) or on the combination of several particular features - such as column separation, unsteady friction, viscoelasticity, anisotropic materials - in a single water-hammer model ([61], [62], [63], [64], [65]).

In the past thirty years, Tijsseling provided many resources (research articles [66], [67], discussions [68], [69], historical reviews [50], [55], [52]) about different topics related to water-hammers (for instance, column separation, water-hammer model in thin-walled pipes or thick-walled pipes, numerical resolution methods). The considerations about water-hammers that are presented in the current work are mainly based on articles of this author.

II.3.1.1. Four-equation model for a simple tube

The current paragraph summarizes the presentation of a water-hammer model given in [67]. However, some preliminary details are added regarding the original equations from which the final model stems. Those details can be found in the presentation of another water-hammer model in [70].

The model is valid for a straight and thick-walled tube, made of elastic and isotropic material, and with a constant circular cross-section. The inner fluid is a liquid considered as Newtonian (here, water is considered). Effects of the outer fluid are neglected, which is a reasonable assumption for a tube surrounded by a gas (it is the case for most of the test devices used in research reactor, where the tube containing the coolant fluid and the rod, is surrounded by a gaseous gap, as explained in Chap. III).

In the structure, radial inertia, bending stiffness and shear deformation are neglected. Damping is not considered, neither in the fluid nor the structure. Friction between the fluid and the structure is considered in the axial direction only. A perfect slip condition is assumed in the orthoradial direction. The model is valid when the flow velocity is significantly lower than the wave velocity, which is the case of the coolant fluid flow of a nuclear reactor. The flow-induced vibrations of the tube are not taken into account. Only the FSI directly related to the water hammer phenomenon are considered. The interaction can be caused by junction coupling, friction coupling and Poisson coupling, but friction coupling is disregarded in the current study.

A water-filled tube of inner radius R_{in}, thickness b and length L is considered. The inner fluid is governed by a continuity equation and a momentum equation. In [70], the momentum equations describing the water-hammer are derived from Navier-Stokes equations. For a fluid of density ρ_f, dynamic viscosity η and bulk viscosity κ, at a pressure p and flowing at a velocity $\boldsymbol{u}$, the basis equations read (in Eulerian form):

- Continuity equation:

$$\frac{\partial \rho_f}{\partial t} + \mathrm{div}(\rho_f \boldsymbol{u}) = 0. \tag{II.55}$$

- Momentum equation:

$$\rho_f \frac{\partial \boldsymbol{u}}{\partial t} + \mathrm{div}(\rho_f \boldsymbol{u}\boldsymbol{u}^T) = -\boldsymbol{\nabla} p + \eta \boldsymbol{\nabla}^2 \boldsymbol{u} + \left(\kappa + \frac{\eta}{3}\right) \boldsymbol{\nabla}(\mathrm{div}\boldsymbol{u}) + \boldsymbol{f}. \tag{II.56}$$

  The first right hand term, $\boldsymbol{\nabla} p$, represents the pressure force, the second and third terms, $\eta \boldsymbol{\nabla}^2 \boldsymbol{u} + (\kappa + \frac{\eta}{3}) \boldsymbol{\nabla}(\mathrm{div}\boldsymbol{u})$, are the viscous forces, and the last term $\boldsymbol{f}$ gathers all the possible body forces.

Considering cylindrical coordinates (with the coordinate system already used in Sec. II.1 and shown in Fig. II.1), the flow velocity can be divided into axial, radial and orthoradial components: $\boldsymbol{u} = (u_x, u_r, u_\theta)$. Thus, by neglecting orthoradial motion, as we consider the motion as axi-symmetrical, and by separating the momentum equation according to the radial and axial directions, the equations in cylindrical coordinates yield ([70]):

- Continuity equation:

$$\frac{\partial \rho_f}{\partial t} + u_x \frac{\partial \rho_f}{\partial x} + u_r \frac{\partial \rho_f}{\partial r} + \rho_f \frac{\partial u_x}{\partial x} + \frac{\rho_f}{r} \frac{\partial (r\, u_x)}{\partial r} = 0. \tag{II.57}$$

- Momentum equation in the axial direction:

$$\begin{aligned} \rho_f \frac{\partial u_x}{\partial t} + \rho_f u_x \frac{\partial u_x}{\partial x} + \rho_f u_r \frac{\partial u_x}{\partial r} + \frac{\partial p}{\partial x} &= \\ \left(\kappa + \frac{\eta}{3}\right) \frac{\partial}{\partial r} \left[\frac{\partial u_x}{\partial x} + \frac{1}{r} \frac{\partial (r u_r)}{\partial r} \right] &+ \eta \left[\frac{1}{r} \frac{\partial}{\partial r} \left(r \frac{\partial u_x}{\partial r} \right) + \frac{\partial^2 u_x}{\partial x^2} \right] + f_x. \end{aligned} \tag{II.58}$$

- Momentum equation in the radial direction:

$$\begin{aligned} \rho_f \frac{\partial u_r}{\partial t} + \rho_f u_x \frac{\partial u_r}{\partial x} + \rho_f u_r \frac{\partial u_r}{\partial r} + \frac{\partial p}{\partial r} &= \\ \left(\kappa + \frac{\eta}{3}\right) \frac{\partial}{\partial r} \left[\frac{\partial u_x}{\partial x} + \frac{1}{r} \frac{\partial (r u_r)}{\partial r} \right] &+ \eta \left[\frac{1}{r} \frac{\partial}{\partial r} \left(r \frac{\partial u_r}{\partial r} \right) - \frac{u_r}{r^2} + \frac{\partial^2 u_r}{\partial x^2} \right] + f_r. \end{aligned} \tag{II.59}$$

Those equations have to be completed by an equation of state (EOS). The following EOS, involving the bulk modulus K, is used:

$$\frac{\partial \rho_f}{\partial p} = \frac{\rho_f}{K}. \tag{II.60}$$

At this stage, several additional assumptions are made to simplify the equations. Firstly, isothermal conditions are assumed, which allows us to consider K and ρ_f as constant in Eq. (II.60). Then, gravity effects are neglected, the body forces f are therefore null. Moreover, convective and viscous terms in the right hand sides of Eq. (II.58) and Eq. (II.59) can be neglected [67]. By substituting the EOS, Eq. (II.60), into the continuity equation, Eq. (II.57), and by linearizing Eq. (II.57), Eq. (II.58) and Eq. (II.59) according to the mentioned assumptions, it finally yields:

- Continuity equation:

$$\frac{1}{K}\frac{\partial p}{\partial t}+\frac{\partial u_x}{\partial x}+\frac{1}{r}\frac{\partial (r u_r)}{\partial r}=0. \tag{II.61}$$

- Momentum equation in the axial direction:

$$\rho_f\frac{\partial u_x}{\partial t}+\frac{\partial p}{\partial x}=0. \tag{II.62}$$

- Momentum equation in the radial direction:

$$\rho_f\frac{\partial u_r}{\partial t}+\frac{\partial p}{\partial r}=0. \tag{II.63}$$

Equations are averaged over the cross section. The cross-section averaged velocity and pressure are U_x and P, respectively. It results in a one-dimensional model, which does not depend on r:

- 1D continuity equation:

$$\frac{1}{K}\frac{\partial P}{\partial t}+\frac{\partial U_x}{\partial x}+\frac{2}{R}u_r(R)=0, \tag{II.64}$$

- 1D momentum equation in axial direction:

$$\rho_f\frac{\partial U_x}{\partial t}+\frac{\partial P}{\partial x}=0, \tag{II.65}$$

- 1D momentum equation in radial direction:

$$\frac{1}{2}\rho_f R_{in}\frac{\partial u_r}{\partial t}|_{r=R_{in}}+p|_{r=R_{in}}-P=0, \tag{II.66}$$

with:

$$U_x=\frac{1}{\pi R_{in}^2}\int_0^{R_{in}} u_x(x,r,t)\,2\pi r\,dr, \tag{II.67}$$

$$P=\frac{1}{\pi R_{in}^2}\int_0^{R_{in}} p(x,r,t)\,2\pi r\,dr. \tag{II.68}$$

As explained in the original paper, [67], the first term in the simplified 1D momentum equation in radial direction, Eq. (II.66) is obtained by assuming that $r u_r = R_{in} u_r|_{r=R_{in}}$.

The structure, whose displacement is referred to as $\boldsymbol{q}=(q_r,q_\theta,q_x)$ and whose constitutive material has a density ρ_s, a Young modulus E and a Poisson coefficient ν, is governed by the following equation of motion:

$$\rho_s \frac{\partial^2 \boldsymbol{q}}{\partial t^2} = \mathrm{div}\underline{\underline{\boldsymbol{\sigma}}} + \boldsymbol{f_s}, \tag{II.69}$$

where $\underline{\underline{\boldsymbol{\sigma}}}$ is the stress tensor in the tube wall and $\boldsymbol{f_s}$ are the body forces exerting on the tube, which are assumed to be null in what follows.

Like for the fluid, the motion can be split into the axial and the radial motion, yielding two equations:
In the axial direction:

$$\rho_s \frac{\partial^2 q_x}{\partial t^2} - \frac{\partial \sigma_{xx}}{\partial x} = 0, \tag{II.70}$$

In the radial direction:

$$\rho_s \frac{\partial^2 q_r}{\partial t^2} - \frac{1}{r}\frac{\partial r \sigma_{rr}}{\partial r} + \frac{\sigma_{\theta\theta}}{r} = 0, \tag{II.71}$$

where σ_{xx}, σ_{rr} and $\sigma_{\theta\theta}$ are axial, radial and hoop stresses, respectively.

Some simplifications, introduced in [70], are necessary to obtain Eq. (II.70) and (II.71): the effects of bending stiffness, rotary inertia and transverse shear deformation are neglected, because of the long wavelength assumption, and deformations are considered to be small. In addition to the simplifications considered in this reference, an additional one is considered here; the shear stress induced by the fluid σ_{xr} on the inner wall (at $r = R_{in}$) and the outer wall (at $r = R_{in} + b$) are null, because friction is disregarded.

Again, the equations can be averaged over the cross-section, it finally yields:
In the axial direction:

$$\rho_s \frac{\partial^2 \overline{q_x}}{\partial t^2} - \frac{\partial \overline{\sigma_x}}{\partial x} = 0. \tag{II.72}$$

In the radial direction:

$$\rho_s \frac{\partial^2 \overline{q_r}}{\partial t^2} - \frac{R_{in} + b}{(R_{in} + b/2)b} \sigma_{rr}|_{r=R_{in}+b} + \frac{R_{in}}{(R_{in} + b/2)b} \sigma_{rr}|_{r=R_{in}} + \frac{1}{(R_{in} + b/2)b} \int_{R_{in}}^{R_{in}+b} \sigma_{\theta\theta} dr = 0, \tag{II.73}$$

where

$$\overline{q_x} = \frac{1}{2\pi b(R_{in} + b/2)} \int_{R_{in}}^{R_{in}+b} q_x(x, r, t)\, 2\pi r\, dr,$$
$$\overline{q_r} = \frac{1}{2\pi b(R_{in} + b/2)} \int_{R_{in}}^{R_{in}+b} q_r(x, r, t)\, 2\pi r\, dr,$$
$$\overline{\sigma_x} = \frac{1}{2\pi b(R_{in} + b/2)} \int_{R_{in}}^{R_{in}+b} \sigma_{xx}(x, r, t)\, 2\pi r\, dr.$$

In addition to that, the cross-sectional averages for σ_{rr} and $\sigma_{\theta\theta}$ are introduced:

$$\overline{\sigma_r} = \frac{1}{2\pi b(R_{in}+b/2)} \int_{R_{in}}^{R_{in}+b} \sigma_{rr}(x,r,t)\, 2\pi r\, dr,$$
$$\overline{\sigma_\theta} = \frac{1}{2\pi b(R_{in}+b/2)} \int_{R_{in}}^{R_{in}+b} \sigma_{\theta\theta}(x,r,t)\, 2\pi r\, dr.$$

As explained in details in [67], it is possible to relate stress components to velocity components by using Hooke's law (relation between stresses and strains) and the relation between the strains and the spatial derivatives of displacement. It finally yields the following expressions combining each displacement component with the stresses in three directions:

$$\frac{\partial \overline{\sigma_x}}{\partial t} = E\frac{\partial^2 \overline{q_x}}{\partial t \partial x} + \nu \frac{\partial \overline{\sigma_\theta}}{\partial t} + \nu \frac{\partial \overline{\sigma_r}}{\partial t}, \tag{II.74}$$

$$q_r = \frac{r}{E}\left(\sigma_{\theta\theta} - \nu(\sigma_{xx} + \sigma_{rr})\right), \tag{II.75}$$
$$\frac{\partial q_r}{\partial r} = \frac{1}{E}\left(\sigma_{rr} - \nu(\sigma_{xx} + \sigma_{\theta\theta})\right). \tag{II.76}$$

To simplify that set of equations and obtain the 4-equation model, boundary conditions have to be defined. To model the contact between the tube walls and the inner and outer fluids, the author imposes the equality between structural stress and fluid pressure and between structural velocity and flow velocity in the radial direction, on inner and outer walls:

$$\sigma_{rr}|_{r=R_{in}} = -p|_{r=R_{in}}, \tag{II.77}$$
$$\sigma_{rr}|_{r=R_{in}+b} = -P_{out}, \tag{II.78}$$
$$\frac{\partial q_r}{\partial t}|_{r=R_{in}} = u_r|_{r=R_{in}}, \tag{II.79}$$
$$\frac{\partial q_r}{\partial t}|_{r=R_{in}+b} = u_{r\ out}. \tag{II.80}$$

P_{out} and $u_{r\ out}$ are respectively the pressure and the velocity in the outer fluid. The last condition on the outer wall can not be used because $u_{r\ out}$ is not supposed to be known.

At this stage, the previous equations can be simplified not only by substituting the boundary conditions into them, but also by restricting the study to long wavelengths and assuming that, in such a case, radial inertia effects are negligible (which is also proposed by other authors, such as [58]). The long wavelength assumption allows us to consider that the hoop strain and, hence, the hoop stress, is only affected by a quasi-static relation with the inner pressure (as it is proved by the author).

Finally, by using the mentioned assumptions to simplify the presented equations, a 4-equation model is obtained. The model takes into account axial waves only. Such an approximation is reasonable for long wavelength and is commonly used in various water-hammer studies ([58], [70], [65]). It must be noticed however that the quasi-static relation between the radial stretching of the tube and the inner fluid pressure, and the Poisson effect (inducing radial dilatation associated to axial waves in the structure) are taken into account. In the current document, the structural axial waves generated by the water-hammer are referred as the "dynamic response" of the structure to the water-hammer, and the radial stretching of the tube around the mean pressure wave in the fluid is referred as the "quasi-static response".

The four equations are:

$$\begin{cases} \dfrac{\partial U_x}{\partial t} + \dfrac{1}{\rho_f}\dfrac{\partial P}{\partial x} = 0, \\[2ex] \dfrac{\partial U_x}{\partial x} + \left[\dfrac{1}{K} + \dfrac{2}{E}\left(\dfrac{R_{in}}{b} + \dfrac{1+\frac{b}{R_{in}}}{2+\frac{b}{R_{in}}} + \nu\right)\right]\dfrac{\partial P}{\partial t} - \dfrac{2\nu}{E}\dfrac{\partial \overline{\sigma_x}}{\partial t} = 0, \\[2ex] \dfrac{\partial^2 \overline{q_x}}{\partial t^2} - \dfrac{1}{\rho_s}\dfrac{\partial \overline{\sigma_x}}{\partial x} = 0, \\[2ex] \dfrac{\partial^2 \overline{q_x}}{\partial t \partial x} - \dfrac{1}{E}\dfrac{\partial \overline{\sigma_x}}{\partial t} + \dfrac{\nu}{E}\dfrac{R_{in}}{b}\dfrac{1}{1+\frac{b}{2R_{in}}}\dfrac{\partial P}{\partial t} = 0. \end{cases} \tag{II.81}$$

The set of equations can be written as a matrix equation:

$$\begin{bmatrix} 1 & 0 & 0 & 0 \\ 0 & \beta & \frac{-2\nu}{E} & 0 \\ 0 & 0 & 0 & 1 \\ 0 & \alpha & \frac{-1}{E} & 0 \end{bmatrix} \frac{\partial}{\partial t}\begin{pmatrix} U_x \\ P \\ \overline{\sigma_x} \\ \dot{\overline{q}}_x \end{pmatrix} + \begin{bmatrix} 0 & \frac{1}{\rho_f} & 0 & 0 \\ 1 & 0 & 0 & 0 \\ 0 & 0 & \frac{-1}{\rho_s} & 0 \\ 0 & 0 & 0 & 1 \end{bmatrix} \frac{\partial}{\partial x}\begin{pmatrix} U_x \\ P \\ \overline{\sigma_x} \\ \dot{\overline{q}}_x \end{pmatrix} = \mathbf{0} \tag{II.82}$$

$$\Leftrightarrow \boldsymbol{A}\frac{\partial \boldsymbol{\phi}(x,t)}{\partial t} + \boldsymbol{B}\frac{\partial \boldsymbol{\phi}(x,t)}{\partial x} = \mathbf{0}, \tag{II.83}$$

where $\alpha = \frac{\nu}{E}\frac{R_{in}}{b}\frac{1}{1+\frac{b}{2R_{in}}}$, $\beta = \frac{1}{K} + \frac{2}{E}(\frac{R_{in}}{b} + \frac{1+\frac{b}{R_{in}}}{2+\frac{b}{R_{in}}} + \nu)$ and the unknown variable $\boldsymbol{\phi}$:

$$\boldsymbol{\phi}(x,t) = \begin{pmatrix} U \\ P \\ \overline{\sigma}_x \\ \dot{\overline{q}}_x \end{pmatrix}$$

This equation has 4 eigenvalues c_i :

$$c_a = \sqrt{\frac{1}{2}\left(\Gamma^2 - \sqrt{\Gamma^4 - 4c_f^2 c_L^2}\right)}, \tag{II.84}$$

$$c_b = -\sqrt{\frac{1}{2}\left(\Gamma^2 - \sqrt{\Gamma^4 - 4c_f^2 c_L^2}\right)}, \tag{II.85}$$

$$c_c = \sqrt{\frac{1}{2}\left(\Gamma^2 + \sqrt{\Gamma^4 - 4c_f^2 c_L^2}\right)}, \tag{II.86}$$

$$c_d = -\sqrt{\frac{1}{2}\left(\Gamma^2 + \sqrt{\Gamma^4 - 4c_f^2 c_L^2}\right)}, \tag{II.87}$$

where $\Gamma^2 = \left(1 + 2\nu^2 \frac{\rho_f}{\rho_s} \frac{R_{in}}{E} \frac{1}{1+\frac{b}{2R_{in}}}\right) c_f^2 + c_L^2$.

c_L is the wave velocity of axial waves in a beam, which can be expressed by $c_L = \sqrt{\frac{E}{\rho_s}}$ (same formula as Eq. (II.5)). c_f is the typical wave velocity in a compressible fluid contained in an elastic pipe[3]. It is expressed by:

$$c_f = \sqrt{\rho_f \left[\frac{1}{K} + \frac{2}{E}\left(\frac{R_{in}}{b}(1 - \frac{\nu^2}{1+\frac{b}{2R_{in}}}) + \frac{1+\frac{b}{R_{in}}}{2+\frac{b}{R_{in}}} + \nu\right)\right]}^{\,-1}. \tag{II.88}$$

c_f can also be written as a combination of the wave velocity in an infinite volume of compressible fluid, $c_{w0} = \sqrt{K/\rho_f}$, and the wave velocity in an *in*compressible fluid contained in an elastic pipe,

$$c_{w0b} = \sqrt{\frac{2\rho_f}{E}\left(\frac{R_{in}}{b}(1 - \frac{\nu^2}{1+\frac{b}{2R_{in}}}) + \frac{1+\frac{b}{R_{in}}}{2+\frac{b}{R_{in}}} + \nu\right)}^{\,-1}.$$

Therefore, the expression reads (such an interpretation is given in [71] for a thin-walled pipe):

$$c_f = \sqrt{\frac{c_{w0}^2 c_{w0b}^2}{c_{w0}^2 + c_{w0b}^2}}. \tag{II.89}$$

The values c_i ($i = a,\ b,\ c$ or d) correspond to the velocities of the actual water-hammer related waves. As $c_b = -c_a$ and $c_d = -c_c$, those eigenvalues show that the waves travel in each direction at two different velocities. It can therefore be stated that two types of waves are generated by the water-hammer. c_a and c_b are associated to the main pressure wave, referred as the "primary wave", and are close to the typical wave velocity in fluid, c_f. c_c and c_d are close to the axial wave velocity in a beam, c_L, and are associated to axial waves, or quasi-longitudinal waves, propagating in the structure and radiating in the fluid, called "precursor waves". Such waves stem from the load exerted on the tube walls by the inner

[3]The variable c_f given by Eq. (II.88), unlike the variable c_a given by Eq. (II.84), does not include the effects of pipe vibrations on the wave speed in the inner fluid. It only takes in account the quasi-static wall stretching due to the pressure load, without any structural inertia.

pressure surge. The coupling between the inner pressure and axial waves is due to Poisson effect (ie. volume dilatation in the radial direction, induced by the axial compression of the tube wall) and junction coupling, which explains how the pressure inside a tube can generate axial waves and how axial waves can have an effect on the inner fluid pressure. In what follows, regarding structural waves, the term "quasi-longitudinal" waves is preferred to "axial" waves, as it emphasizes the Poisson effect (causing radial displacement), which is essential regarding the precursor wave phenomenon.

As a result, in the inner fluid of a pipe subjected to a water-hammer, small pressure disturbances induced by quasi-longitudinal structural waves travel ahead of the main pressure wavefront. The small pressure disturbances are referred to as precursor waves, and the main pressure wavefront is referred to as primary wave. In the current document, the terms of precursor and primary waves are used for the fluid pressure waves, while the structural waves are referred as the dynamic and the quasi-static responses, as previously explained.

II.3.1.2. Boundary and initial conditions

Boundary and initial conditions are presented with the aim of solving the matrix form of the four equation model, given by Eq. (II.82), by the method presented in [66]. In this article, the author presents an exact resolution method, with comprehensive and clear explanations, for the case of a thin-walled tube. It also provides an algorithm for the implementation of the method (the algorithm is written in Mathcad, but can be easily adjusted to other programming language, such as Python, Matlab, etc). With minor modification, the algorithm is suitable for thick-walled tubes.

Boundary conditions

Here, the term "boundary conditions" refers to the conditions at the ends of the tube. The conditions on the inner and outer walls of the tubes were previously introduced in Eq. (II.77-II.80).

End boundary conditions are defined by matrices $\boldsymbol{D_0}$ and $\boldsymbol{D_L}$, of dimension 2x4, and the excitation vectors $\boldsymbol{f_0}$ and $\boldsymbol{f_L}$, of dimension 2x1. $\boldsymbol{D}$ matrices and $\boldsymbol{f}$ vectors are related by:

$$\boldsymbol{D_{x_b}}(t)\,\boldsymbol{\phi}(x_b, t) = \boldsymbol{f_{x_b}}(t), \tag{II.90}$$

where $x_b = 0$ or L.

Composition of $\boldsymbol{D_0}$ and $\boldsymbol{D_L}$ depends on the configuration of the system (presence and positions of junctions, valves, dashpots, reservoirs, etc), as shown, for various systems, in [72] and [66].

Initial conditions

The initial state is given by $\boldsymbol{\phi}(x, t)$ at time $t = 0$. It is supposed to be known for all x. For an initial equilibrium state, all the components of $\boldsymbol{\phi}$ are constant over the whole length of the tube. Otherwise, each component can take arbitrary values to describe any particular situation, such as an initial localized over-pressure at a specific position.

II.3.1.3. Six-equation model for coaxial tubes

In [65], a six-equation model is proposed to describe a system consisting of two coaxial tubes, both thin-walled and filled with a fluid, subjected to a water-hammer in the fluid domain located between the two tubes.

Such a system is close to a typical test device used in research reactors, the inner tube corresponding to the fuel rod. Some differences should be noticed, though. A real fuel rod is not filled with fluid only, it also contains the fuel material, which consists of solid pellets. Moreover, although the rod cladding can be considered as a thin-walled tube, the outer tube of most test devices have thick walls (as shown in the description of the studied system in Chap. III). Including the effects of pellet-cladding interaction would be a complex task, as showed by some works especially related to such a topic [73], [74]. However, it could be easily attempted to adjust the model of [65] to make it valid for a thick-walled outer tube. Although the case of a fluid-filled inner tube is not perfectly representative of a real fuel rod, it is a realistic model of the experimental mockup designed in the frame of the current work and introduced in Chap. IV.

This model shows that the same FSI phenomena are observed in such an annular system than in the simple tube described by the 4-equation model. Like previously, the fluid pressure history exhibits precursor waves propagating at a velocity close to the quasi-longitudinal structural wave velocity and the primary wave propagating at a velocity close to the wave velocity in an unconfined fluid volume. As well as in the simple tube model, the structural response includes a dynamic part (quasi-longitudinal waves induced by Poisson coupling effect, in addition to possible junction coupling) and a quasi-static part which is the radial-stretching induced by the fluid primary wave. All types of waves reflect at the ends according to the boundary conditions, in the same ways as in the 4-equation model.

II.3.2. Euler equations approach

The current section introduces the theoretical basis of the numerical approach. Results of three-dimensional simulations based on the equations introduced in this section are presented in the Chap. III.

II.3.2.1. Fluid behavior

Here, a compressible, inviscid and adiabatic flow is considered. Such assumptions are reasonable, as we are interested in a fast transient phenomenon in water, involving relatively small displacements and a short duration (about some milliseconds). Therefore, there is no need to consider viscosity and conduction effects. Firstly, the equations governing the fluid motion are introduced. Then, the structure, consisting of isotropic and elastic materials, and its interaction with the fluid are described.

Considering a fluid corresponding to the mentioned assumptions, with a density ρ_f, moving at a velocity $\boldsymbol{u}$, and with a pressure p, the conservation of mass, momentum and energy yield the following equations, called Euler equations [75]. These equations are given in Eulerian form, as it is the form used for the final numerical computation in the fluid domain.

Continuity equation

$$\frac{\partial \rho_f}{\partial t} + \mathrm{div}(\rho_f \boldsymbol{u}) = 0. \tag{II.91}$$

Momentum conservation equation

$$\frac{\partial\, \rho_f \boldsymbol{u}}{\partial t} + \mathrm{div}\left(\rho_f\ \boldsymbol{u}\ \boldsymbol{u}^T\right)\ +\ \nabla p = \boldsymbol{f_{vol}^{flu}}, \tag{II.92}$$

where $\boldsymbol{f_{vol}^{flu}}$ is a vector containing the body forces. In that equation, the two first terms are related to the momentum variation, the third term represents the pressure force and the right hand term is the action of all the other forces (including gravity, which is however neglected in the current work).

Energy conservation equation

$$\frac{\partial\, \rho_f E_m}{\partial t} + \mathrm{div}\left((\rho_f E_m\ +\ p)\ \boldsymbol{u}\right) = 0, \tag{II.93}$$

where E_m is the total energy per unit mass, consisting of the internal energy and the kinetic energy:

$$E_m = e + \frac{|\boldsymbol{u}|^2}{2}, \tag{II.94}$$

where e is the internal energy, given by the EOS.

Stiffened-gas equation of state

The stiffened gas EOS is chosen, because of its suitability for a wide range of phenomena (including propagation of high pressure wavefront in gas, liquid or two-phase flows) combined with a mathematical simplicity, as explained in [76]. Such a simplicity implies both an easy physical understanding and an efficient numerical computation.

The definition of the stiffened gas EOS from the Grüneisen EOS is described in [77]. Practical applications of the equation are presented in [76], [78] or [75]. The stiffened gas EOS reads:

$$p = (\gamma - 1)\rho_f(e - e_f) - \gamma P_\infty, \tag{II.95}$$

where γ is an empirical constant (equal to heat capacity ratio for a perfect gas), e_f is the formation energy (we can simply take $e_f = 0$ because no phase change is considered in the current work, like in [76]), e is the internal energy, P_∞ is a constant associated to the molecular attraction needed to represent liquids such as water. The term $(\gamma-1)\rho_f$ is thus related, in this case, to the molecular repulsion effects, and γP_∞ represents fluid cohesion.

II.3.2.2. Application to a FSI problem

Euler equations describe what happens in the fluid only. Defining the structure behavior and the coupling conditions at the fluid-structure interface is necessary to take into account the motion of the structure and its interaction with the fluid.

Like in the previous approaches, the structure material is considered as isotropic and elastic. Neither plasticity nor fragmentation is taken into account. Therefore, the behavior of the structure can be described by the following equilibrium equation (given in the Lagrangian form, which is used for the numerical simulation in the structure):

$$\rho_s \frac{\partial^2 \boldsymbol{q}}{\partial t^2} + \mathrm{div}\left(\underline{\underline{\boldsymbol{\sigma}}}(\underline{\underline{\boldsymbol{\epsilon}}})\right) = \boldsymbol{f_{vol}^{str}}, \tag{II.96}$$

where ρ_s is the density of the structure material, $\underline{\underline{\boldsymbol{\sigma}}}$ is the stress tensor, $\underline{\underline{\boldsymbol{\epsilon}}}$ is the strain tensor, $\frac{\partial^2 \boldsymbol{q}}{\partial t^2}$ is the acceleration of the structure and $\boldsymbol{f_{vol}^{str}}$ contains the body forces exerted on the structure.

In the current work, a first condition at the fluid-structure interface can be referred to as a slip, or friction-less, condition. It means that the velocities of the structure and the fluid in the direction tangential to the interface are not related. However, another condition imposes the velocities of the structure and the fluid in the direction normal to the interface are imposed to be equal. Mathematically, it reads:

$$\boldsymbol{u}(\boldsymbol{M}) \cdot \boldsymbol{n_I} = \frac{d\boldsymbol{q}(\boldsymbol{M})}{dt} \cdot \boldsymbol{n_I}, \quad \forall\ \boldsymbol{M} \in I_{F-S}, \tag{II.97}$$

where $\frac{\partial \boldsymbol{q}}{\partial t}$ is the structure velocity, I_{F-S} is the interface between the fluid and the structure, $\boldsymbol{M}$ is a point located on the surface I_{F-S}, and $\boldsymbol{n_I}$ is the normal of the surface I_{F-S} at point $\boldsymbol{M}$.

Physically, it means that the fluid always stays connected to the structural wall, does not penetrate it, and can slide along it. As a consequence, considering a cylindrical geometry, such a condition implies that the orthoradial and axial motions of the structure have no direct influence on the fluid and reciprocally, but forces and motions in the radial directions can be transferred from one medium to the other. Actually, because of Poisson effect and the complex geometry of the system, axial and radial motions are however coupled and, hence, axial motions or forces of a medium can influence the other medium, as it is the case in water-hammer models with junction coupling and Poisson coupling, mentioned in Sec. II.3.1.

With this set of equations and conditions, all the motions of an inviscid and compressible flow together with an elastic structure can be described. However, the resolution of those equations can be numerical only. It is achieved with the EUROPLEXUS code, introduced in Chap. III, using Finite Element and Finite Volume methods associated to a time-explicit scheme. Finite element approach is used for the structural domain and for the momentum conservation equation in the fluid domain, while finite volumes are used for the mass and the energy conservation in the fluid domain. Chap. III focuses on the results of the numerical simulations rather than the computation methodology, which was simply used without further development in the frame of the current work. Details about this methodology can be found in [79], [80] and [81].

II.4. Conclusions of the theoretical descriptions of the underlying phenomena

The first two theoretical studies (about guided waves, in Sec. II.1, and structural vibrations, in Sec. II.2) aim at providing approximate quantitative information to help with the interpretation of measurements on structures, which are presented in Chap. IV. They are not intended to produce a model of the whole studied system. Indeed, they simply describe the parameters governing the response of a tubular structure to an undefined source, with a very partial description of the fluid effects (represented only as an added mass).

On the other hand, the objective of the two other approaches is to provide a description of the whole problem, and especially regarding fluid-structure interactions. The "water-hammer" approach (Sec. II.3.1) has two advantages. Firstly, it allows a more straightforward physical understanding of FSI and propagation phenomena (for instance, the actual velocities of the different types of waves and the relation between them are given by analytical expressions). Secondly, for simple systems, the equations can be solved rather easily and without requiring specialized computation tools (suitable algorithms can be easily implemented on classical programming tools such as Matlab or Python). However, the Euler equations are more general and can describe a very wide range of systems and phenomena with great accuracy, contrary to the water-hammer models, which focus on a specific phenomenon in pipe systems and require some approximation. Associated to suitable computation tools (for instance, finite volume or finite element codes), the Euler-equation based approach (Sec. II.3.2) is very versatile. It can be easily applied to accurate models of various complex systems with specific characteristics (materials, geometry). The main limits are computation costs. Compared to the "water-hammer" approach, the drawbacks are the need for suitable computation tools and resources, and a loss in the phenomenological understanding of the problem.

As it will be shown in Chap. III, the 1-D "water-hammer" approach and the 3-D Euler-equation-based approach can be made complementary. Some physical observations resulting from the water-hammer model will be used to better interpret numerical results obtained with a fluid-structure simulation involving a model described by the Euler equations and coupling conditions introduced in Sec. II.3.2.

III. Numerical approach

The current chapter presents the numerical approach, whose main objective is to provide the information that is necessary to understand the phenomenology associated to the propagation of waves generated by fuel rod cladding failures in test devices used in research reactors or experimental mockups. The approach consists of using Finite Element Method (FEM) to simulate the effects of a pressure surge generated in a three dimensional model representing a typical test device. In addition to a physical analysis of the results, failure localization methods are tested to prepare future applications in real reactors or experimental mockups.

III.1. Description of the studied system

The studied system is based on the typical geometry of experimental devices used in French research reactors for the study of a single rod's behavior (for instance, the REPNa devices in the CABRI reactor [3], GRIFFONOS and ISABELLE devices in the OSIRIS reactor [4], the forthcoming ADELINE device in the RJH [5]). Such a device contains a fluid channel where the tested rod sample is placed. The device is inserted in the reactor (usually a pool reactor) that generates a neutron flux representative of the one met by a rod in an industrial reactor. The channel containing the tested rod is connected to an independent water loop that recreates typical thermohydraulic conditions of industrial pressurized water reactors (water at 280°C and 155 bar, flowing at 3.4 m.s^{-1}).

Typical characteristics of such a device are:

- an overall length of several meters,
- a central section of about one meter, containing a fuel rod sample of about 60 cm and fixed to cylinder extensions,
- a structure mostly made of stainless steel and, in the central section, Zircaloy (because of its neutron-transparency property),
- various instrumentation downstream and upstream from the central section.

In the current study, only the central section and its inlet and outlet sections are considered. Typically, this part can be described as an annular structure with several coaxial layers. From the outside to the inside, these layers are: an external tube, an annular gap filled with gas, a second tube made of Zircaloy (called "channel tube" in Fig. III.1), an annular water channel, and the tested fuel rod. The gaseous gap is intended to mechanically and acoustically separate the inner channel from outside events. In this chapter, we focus on what happens inside the test device only and neglect the effects of the external layer. Thanks to the gaseous gap, these are realistic simplifications (it was verified in a real device that the sensors are almost insensitive to outside events). Thus, we consider only the part of the device including the channel tube, the water channel, and the fuel rod. Only that part is presented in Fig. III.1, which shows a simplified drawing of the studied part of the test device. In the following paragraphs, we refer to the channel tube as the "outer structure". From a longitudinal point of view, the section upstream from the rod is called the "inlet section", the section downstream the "outlet section", and the section containing the rod the "main section". The main section is separated from the inlet and outlet sections by short transition sections. In these transition sections, the channel cross-section is reduced to enable mechanical connection between the outer structure and the rod and extensions assembly. There, the channel cross section is not annular but consists of several holes. For the sake of understanding, an example of such a transition cross-section is shown in Fig. III.2.

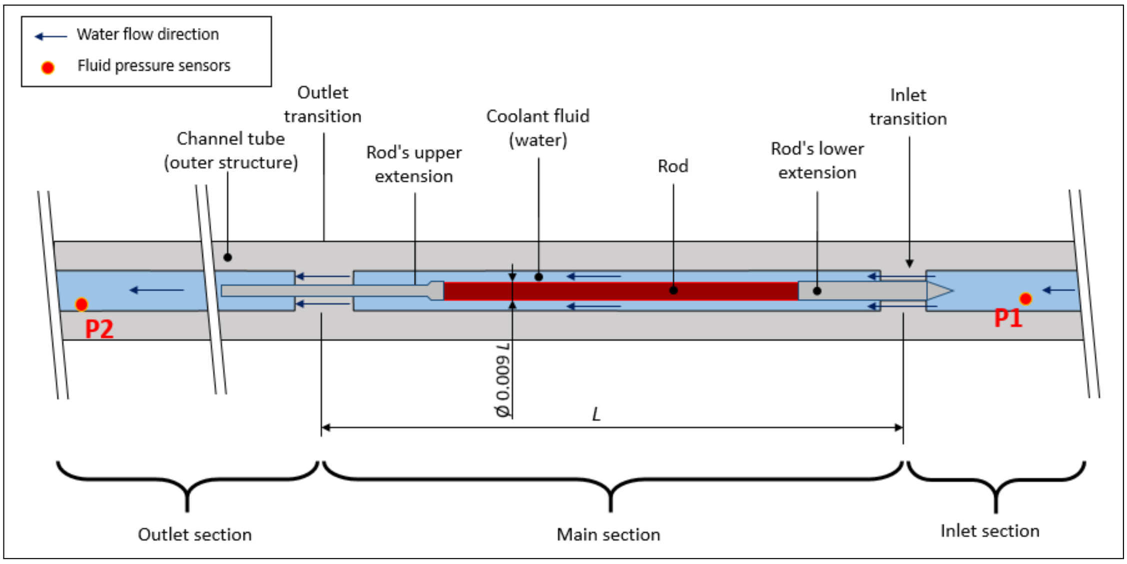

Figure III.1. *Simplified drawing of the test device (fuel rod in red, other structural parts in grey and fluid in blue). Dimensions are relative to the length of the main section, L ~ 1 m. The most external tube and the gaseous gap are not represented.*

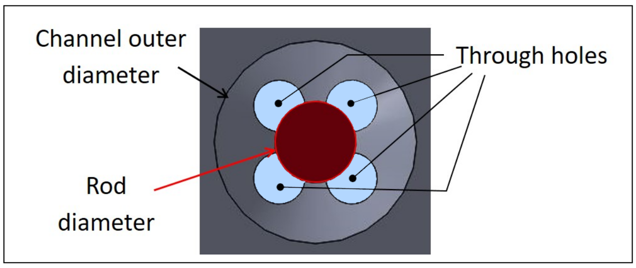

Figure III.2. *Exemple of a transition geometry with channel cross-section reduction.*

Several measurement points are considered in the system. Two of them, referred as P1 and P2, are located in the inlet and outlet sections and can be considered as realistic measurement points, as it is actually possible to place sensors at equivalent positions in a real device (see Fig. III.1). Therefore, they show the actual possibilities that can be expected from acoustic measurements in a real reactor. The other points, defined in Sec III.3.1, are located in the central section, or very close to it. They are used to get information for the understanding of the studied phenomena, but placing sensors on these positions in a real device is not assumed to be possible.

As it is the case in real devices, geometrical singularities of the channel lie between main section and the inlet and outlet sections, because of the mechanical supports of the rod and its extensions. The geometry is not symmetrical between the inlet side and the outlet side, which results in different wave paths between the source and the P1 and P2 sensors, as it is also the case in real devices.

Real devices are actually vertically inserted in the core, and water flows from the bottom to the top. In Fig. III.1, the inlet is on the right and the outlet on the left.

Because of non-disclosure obligation, physical values cannot be explicitly shown. Thus, length and pressure values are given in arbitrary units. The arbitrary unit of length, referred as A.U.L., is defined as the length of the main section of the device (see Fig. III.1). The order of magnitude of the A.U.L. is one meter. The arbitrary unit of pressure, referred as A.U.P., is defined as the maximum value measured by the pressure sensors. The order of magnitude of the A.U.P. is 100 bar.

III.2. Presentation of the EUROPLEXUS code and the model

A 3D model of the studied system was built. This model includes a partial description of the outer structure, of the test rod with its extensions, and of the fluid domain between them. It also includes a compressed gas bubble in a cavity inside the rod, expanding in the surrounding fluid through a small hole in the cladding. Here, we consider still water, because the actual flow speed (3.4 $m.s^{-1}$) is very low compared to the characteristic pressure wave speed (about 1100 $m.s^{-1}$ in water in the test conditions). However, simulating initially flowing water is straightforward and might be attempted in further study if needed. Numerical simulations are computed with EUROPLEXUS software (currently abbreviated EPX, [82]). It is a simulation software using finite-element and finite-volume methods for fluid-structure interaction problems. An explicit time integration algorithm makes the software especially suitable for fast transient phenomena, such as a fuel rod cladding failure. In the present study, computation in the structure and in the fluid domain are respectively performed with Lagrangian and Arbitrary Lagrange Euler representations, along with gas-water interface tracking in the fluid to produce sharp pressure loading (see [75]). Simulation duration is 2.5 ms. It is enough to observe the propagation of the relevant waves in both the structure and the fluid (assuming that the lowest wave speed is about 1100 $m.s^{-1}$ as mentioned above, which is a reasonable approximation for the wave speed in pressurized water at 280°C and confined in an elastic tube). Calculation time step is adaptive but the results are stored every 10^{-6} s. The full computation for approximately 400 000 elements requires about 230 000 s CPU (two days and a half) on a local workstation with limited parallel resources (see [79] for parallel framework in EPX).

III.2.1. Fluid model

Both fluid components (high-pressure gas and water) are modeled with the stiffened gas equation of state, introduced in Sec. II.3.2, Eq. (II.95), and reminded here:

$$p = (\gamma - 1)\rho_f(e - e_f) - \gamma P_\infty. \tag{III.1}$$

Damping in the fluid due to shock waves after the initial expansion of the compressed bubble is approximated by Neumann-Richtmyer artificial viscosity (introduced in [83]).

The average axial, radial and circumferential dimensions of a fluid element in the main section are respectively about 3 mm, 0.5 mm and 1 mm. Around geometrical singularities, the mesh is refined.

III.2.2. Geometry and structure

Dimensions of the model are based on the characteristics mentioned in Sec. III.1 and shown in Fig. III.1. Although real devices often contain some small asymmetrical parts, they have been neglected here so that the structure of the model is purely axisymmetrical, except at the transition sections, where the through holes are symmetrical with respect to a longitudinal plane. Neglected asymmetrical parts (mostly supports and fastenings for sensors and wires) are located on the outer surface of the structure. Therefore, they do not influence the behavior of the inner fluid. Thus, in order to reduce computation cost, and assuming the studied phenomena are axisymmetrical, only a half portion of the real system was modeled (from 0° to 180°). Therefore, while the real system has a cylindrical shape, the model has a semi-cylindrical shape. Symmetry conditions are applied on the cutting plane ($x - y$ plane, with x the longitudinal axis and y a transversal axis), by imposing the displacements normal to the plane to be zero.

In real devices, the different parts of the outer structure are welded. In the model, welded joints are modeled as simple planar interfaces with rigid connections. Connections between the rod and its extensions at both ends are rigid. Mechanical connections between the rod extension and the outer structure in the model are representative of real ones. The lower rod extension (on the right of Fig. III.1) is rigidly connected to the outer structure at the inlet transition and the upper rod extension (on the left) is pinned to the outer structure at the outlet transition.

The fuel model is simplified in a homogeneous solid volume instead of several stacked pellets. The cladding is modeled with shell elements (four nodes shell elements, based on [84], and referred as "$Q4GS$" in EPX, see [85]), the fuel cylinder and all the other structural parts are modeled with cubic elements ("$CUBE$" elements in EPX). The average axial, radial and circumferential dimensions of an element of the outer structure around the main section are respectively about 2.3 mm, 1.5 mm and 2 mm. Around geometrical singularities, the mesh is finer. Fig. III.3 shows views of the mesh around the inlet and the outlet transitions, where there are the most significant geometrical singularities.

Every structural part is modeled with its respective material (Zircaloy, Stainless steel, fuel material). Small pieces such as wires, screws or sensors are neglected.

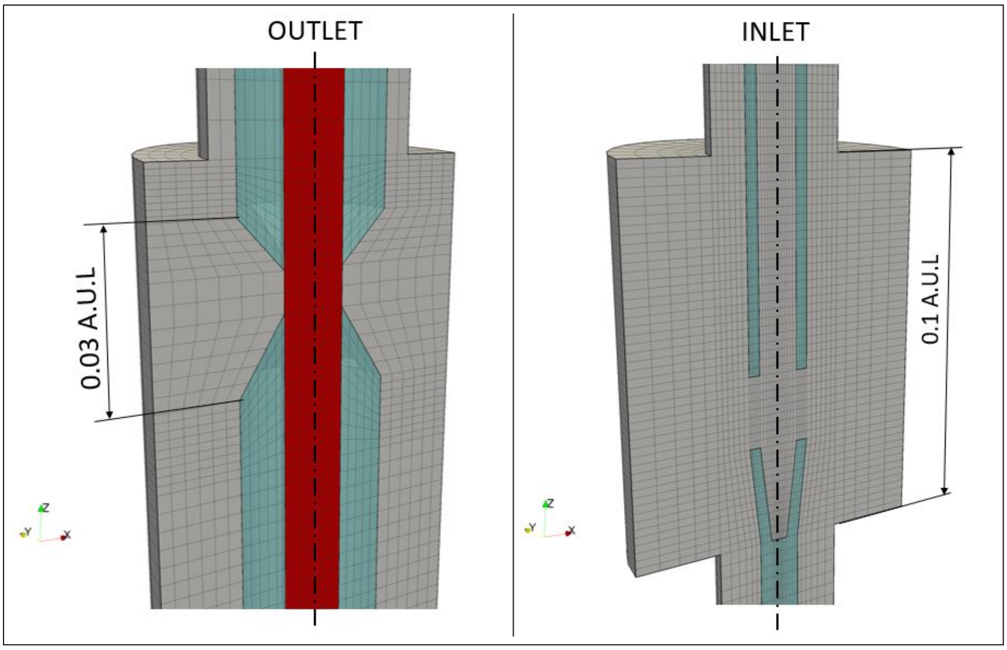

Figure III.3. *Cutaway views of the mesh around the inlet and the outlet transitions (stainless steel parts in grey, Zircaloy parts in red, fluid in blue).*

III.2.3. Material properties

Material properties used for the simulation are given in tables III.1 and III.2. They are approximated properties of the corresponding materials at 280°C and 155 bar, which are the average pressure and temperature in the test device and in industrial PWR. No damping is applied to the structure. Elastic deformation only is considered.

Material	**Density** ($kg.m^{-3}$)	**Young's modulus** (GPa)	**Poisson's ratio**
Steel	7830	176	0.3
Zircaloy	6560	78	0.4
Fuel	10500	80	0.37

Table III.1. *Structure materials' properties*

In a fluid represented by the stiffened gas equation of state, Eq.(III.1), the classical sound

Material	Density (kg.m^{-3})	P_∞ (Pa)	γ
Water (liquid)	764	4500	1.896
Water (gas)	1	0	1.4

Table III.2. *Fluid materials' properties*

speed c_{w0} in an infinite domain is given by ([76]):

$$c_{w0} = \sqrt{\frac{\gamma}{\rho_f}(P + P_\infty)} \tag{III.2}$$

Then, the sound speed in liquid water at 155 bar, 280°C, is $c_{w0} = 1075$ m.s^{-1}. This value refers to the speed of sound in an infinite volume of fluid, it does not take any structure into account. Sound speed in the gaseous phase (coming from the high-pressure cavity simulating the failure, as explained in Sec. III.2.4) has no practical importance here. Since no phase change is simulated, the volume of the gaseous phase remains very small compared to the liquid volume and stays concentrated around its initial location during the whole simulated time.

III.2.4. Simulation of the cladding failure effects

The objective of this study is not to achieve an accurate simulation of the failure itself, but to obtain information about wave propagation phenomena in the specific system corresponding to the test device. Hence, cladding failure is modeled in a rather simplified way. Neither material distortion nor fuel-coolant thermal interaction are simulated. We only reproduce the over-pressure resulting from these phenomena and propagating through the system. To reproduce this over-pressure, a cavity was created inside the rod. That cavity is initially filled with pressurized gas, at a higher pressure than the surrounding fluid pressure. That gas can represent pressurized fission gas, internal steam in case of a water-logged rod, or the pressure surge induced by fuel-coolant interaction. The contact area between the gas in the cavity and the surrounding fluid is obtained with an aperture in the cladding. At the beginning of the simulation, pressurized gas is instantaneously released in the surrounding fluid, creating a pressure wave that propagates along the system, in both directions (downstream and upstream). The cavity inside the rod is axisymmetrical but the aperture in the cladding stretches only over a reduced part of the cladding circumference and is not axisymmetrical. Thus, it results in an asymmetrical source and enables the observation of three-dimensional effects, which is necessary to estimate the validity of the plane wave assumption.

In the axial direction, the cavity and the cladding aperture in the model have the same length. The results that are presented in this chapter come from a simulation computed with an arbitrary failure position, set at $135.3 \cdot 10^{-3}$ A.U.L. from the lower end of the rod. In real experiments, the position of the failure depends on the initial state of the rod and the experimental conditions. The influence of the failure length in the model is discussed in Sec. III.3.1.1.

III.3. Analysis of the results and physical considerations

The results provided by the simulations can be divided in fluid-related data and structure-related data. Concerning the fluid, the useful data is the pressure in each volume of the domain. Concerning the structure, various values are of interest: the displacement, the velocity and the acceleration in each direction. All of them are available at each node of the structure domain.

Those results are intended to depict the evolution of the pressure field in the fluid and the vibration field (either displacement, velocity, or acceleration) in the structure, along the part of the device containing the tested fuel rod, with the final aim to be compared with future experimental results. However, unlike the simulation results, representing raw physical values, experimental results are affected by sensors' responses. While the response of commercial pressure sensors can be assumed to be flat up to 25% of their resonant frequency (usually given by the producer), and the output of such sensors can reliably be considered as the actual pressure (which is a simple scalar value), the interpretation of AE sensors' signals leads to some issues, as it will be further explained in Sec. IV.2. Firstly, most of AE sensors are intended to be used at their resonant frequency and have consequently a non-flat response. Secondly, the actual physical value measured by the sensor (displacement, velocity, acceleration) and the directivity are seldom known. Estimating the response of AE sensors is a recurrent problem that has been studied several times (for instance [86], [87], [88]). Results depend on the model of the sensor, and there is currently no simple solution to accurately estimate an AE sensor response. As a consequence, the interpretation of the raw physical values provided by the numerical simulation is suitable for signals measured by any model of fluid pressure sensors, but it might be unsuitable for AE sensors signals. Therefore, the current chapter focuses on the results related to pressure in the fluid. Some considerations about the structure-related data are nevertheless presented, although they will not be directly applicable to further experimental results. That is why the failure localization methods are tested with pressure results only.

III.3.1. Fluid pressure waves

III.3.1.1. Effects of the failure length

Before analyzing numerical results in details, preliminary observations regarding the length of the simulated failures are introduced.

It is assumed that the failure length influences the resulting pressure variation in the fluid, in both simulations and real situations. When numerical results are compared to experimental results from a failure test in a real reactor, the failure length in the model should be actually compared to the size of the reaction area where the over-pressure is produced in the real test and to the pressure profile in this area. However, the estimation of those characteristics is not simple. The most direct information that can be provided by tests in a real reactor are pressure histories in the inlet and the outlet section, given by sensors P1 and P2 (assuming that measurements closer to the failure are not possible). Depending on the possibilities in other kinds of measurements, some characteristics can be estimated afterwards. Visual examination of the rod after the experiment can give the approximate location of the failure but will not provide reliable information about the initial size of the reaction area, since we do not know the kinetics of the cladding failure and fuel ejection. Approximation of these parameters might be deduced from temperature and energy deposit, depending on the measurement possibilities, but it would require an extensive work that is far beyond the scope of the present study. Moreover, as shown in [8] and [9], these characteristics significantly depend on rod properties and are difficult to predict.

Given the large variability in the lengths of real failures, and since the accurate estimation of the actual over-pressure area might not be possible, the comparison between simulation results and future experimental results will likely require several simulation iterations with various failure lengths. To predict the effects of the failure length on the pressure that could be measured in the device, simulations with three different failure lengths (3 mm, 15 mm, and 30 mm) were performed. Fluid pressure histories in the outlet and inlet sections (at the "realizable" measurement points) obtained with the different failure lengths are presented in Fig. III.4. For the sake of readability, pressure variations around the initial pressure value of 155 bar are presented rather than absolute pressure values. Unless otherwise stated, it is the case for all pressure values in the present chapter.

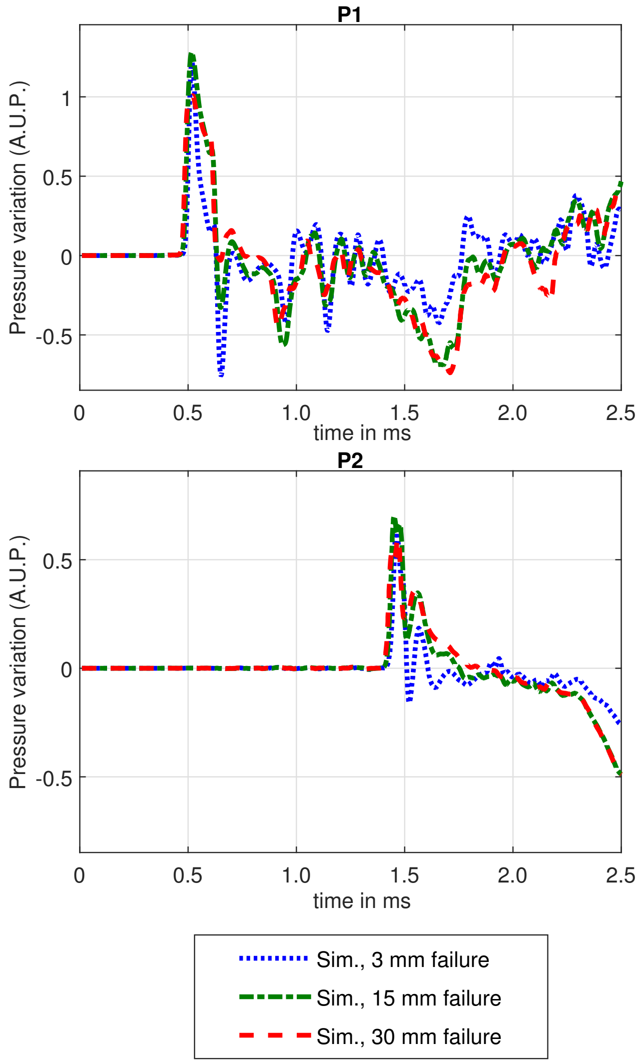

Figure III.4. *Simulated pressure at P1 and P2 for different simulated failure lengths.*

The effects of the differences in the failure length are clearly shown in Fig. III.4. The longer the failure is, the wider the first pressure peak on the signal is. In what follows, results obtained with a 30 mm are used. The choice is arbitrary, but, despite the noticeable difference in the signals, the analysis methodology and the physical interpretation is the same for any failure length.

III.3.1.2. Numerical results: Pressure history at different points

Signals used in this part are the average pressure over the cross section at defined axial positions. As the pressure field shows in Fig. III.5, III.6, and III.7, pressure waves can reasonably be considered as plane waves. It allows the use of the cross-section average pressure instead of the value at a point with specific angular and radial coordinates.

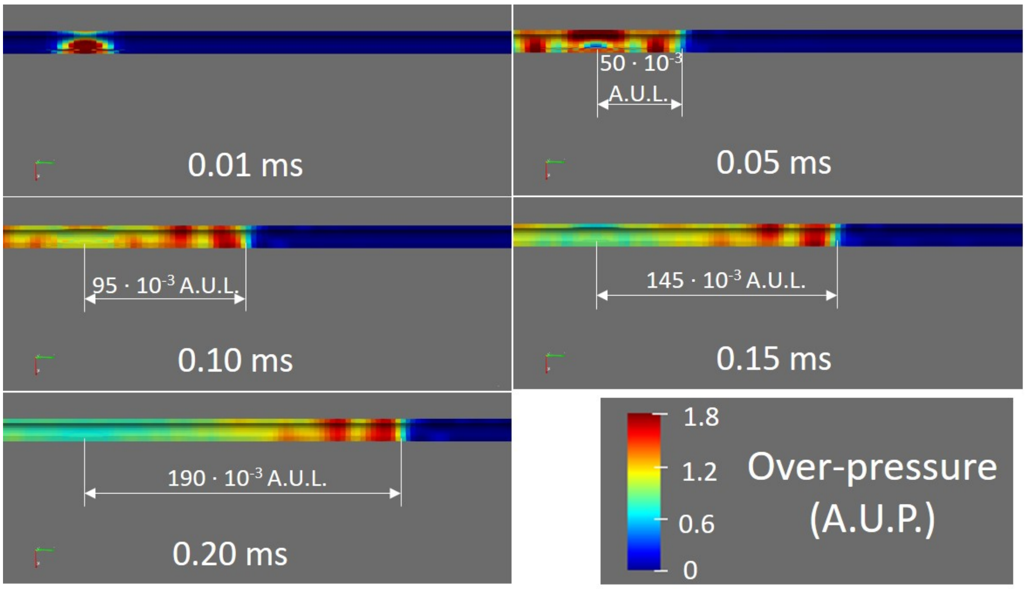

Figure III.5. *Representation of the fluid pressure field in the main section at different time steps. Approximate distances are indicated to show the figure scale. For the sake of clarity, the structure is not shown.*

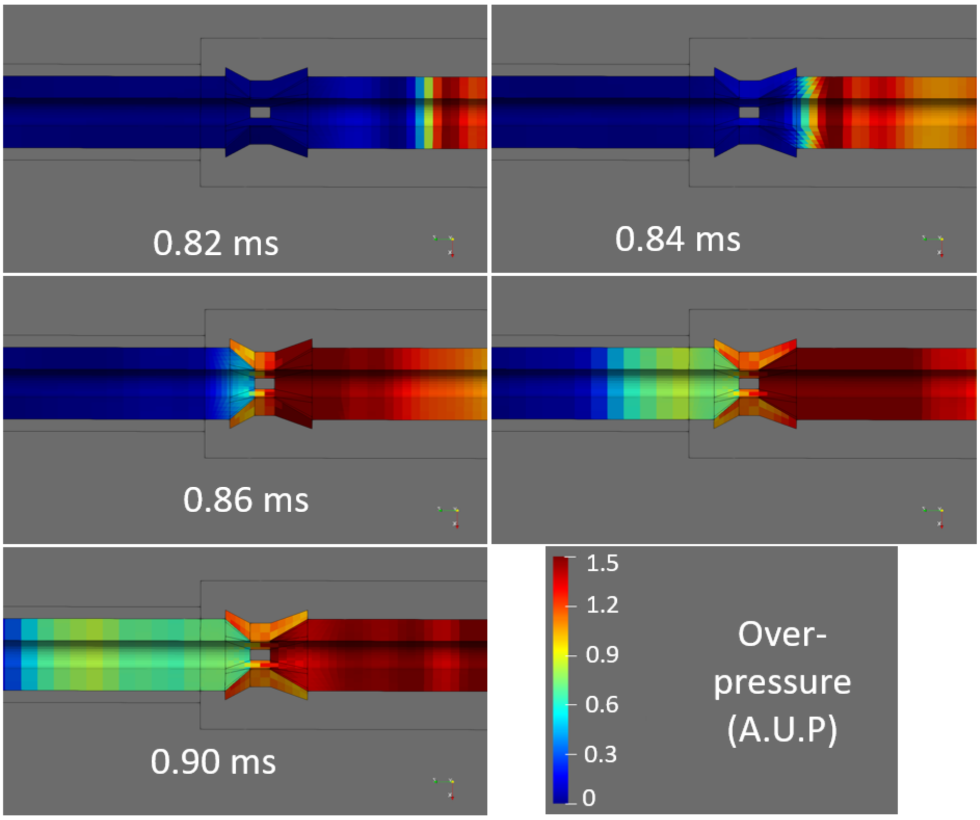

Figure III.6. *Representation of the fluid pressure field around the outlet transition at different time steps when the main pressure wavefront crosses the transition. For the sake of clarity, the structure is not shown.*

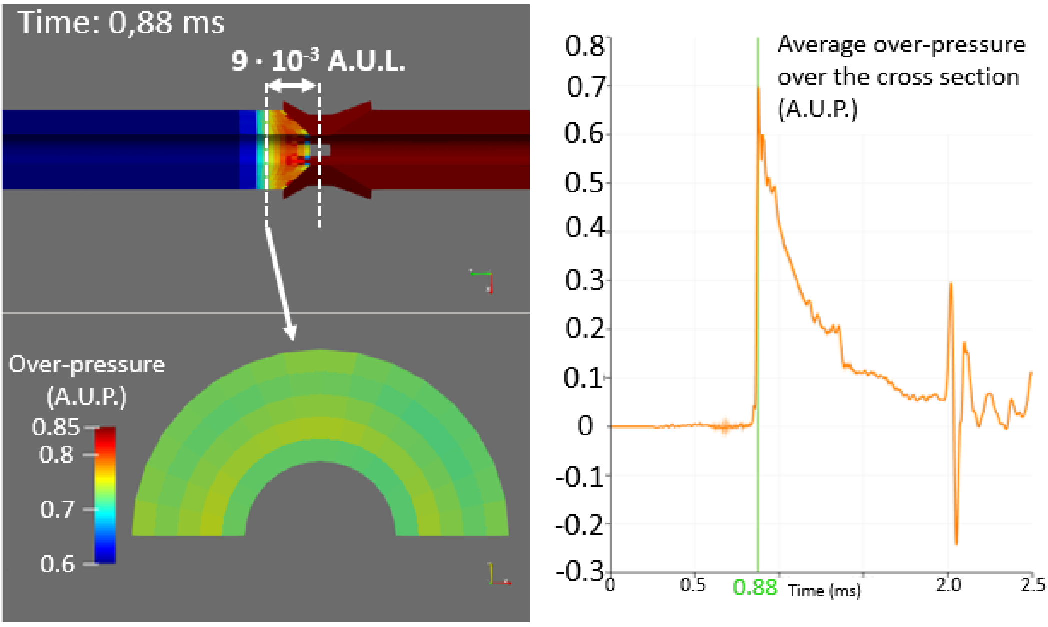

Figure III.7. *Representation of the fluid pressure field, at a distance of* $9 \cdot 10^{-3}$ *A.U.L. downstream from the center of the outlet transition, when the main wavefront reaches the section (at 0.88 ms).*

Fig. III.8 shows the pressure history at five different axial positions in the main channel. Fig. III.9 shows these positions.

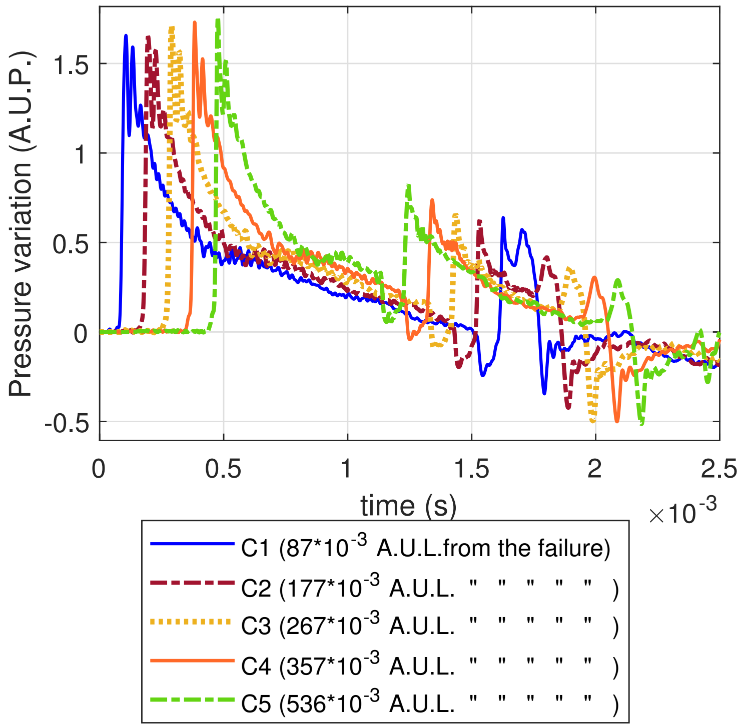

Figure III.8. *Simulated pressure at different positions in the main section.*

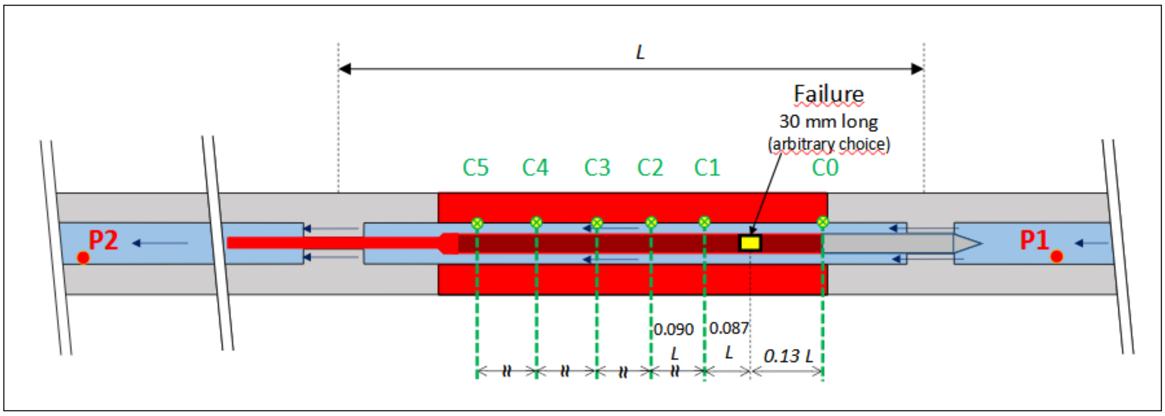

Figure III.9. *Positions of pressure history extraction points in the main section.*

Each signal in Fig. III.8 can be divided in four parts:

1. an empty part before signal arrival,
2. low amplitude waves (hardly visible on figure III.8, see figure III.10),
3. main wave front followed by slow pressure decrease,
4. first reflection followed by additional resonances.

The main wave front is assumed to be the primary wave (propagation of the pressure wave in water) and low amplitude waves appearing before the main wavefront are assumed to be precursor waves (structural waves induced by the fluid pressure load on the walls, propagating in the structure and radiating back into the fluid). An explanation of primary and precursor waves is given in Chap. II, Sec. II.3.1. Precursor waves are hardly visible in Fig. III.8, but we can clearly see them with a time magnification such as the example in Fig. III.10. They are also slightly noticeable on some frames in Fig. III.5 and III.6.

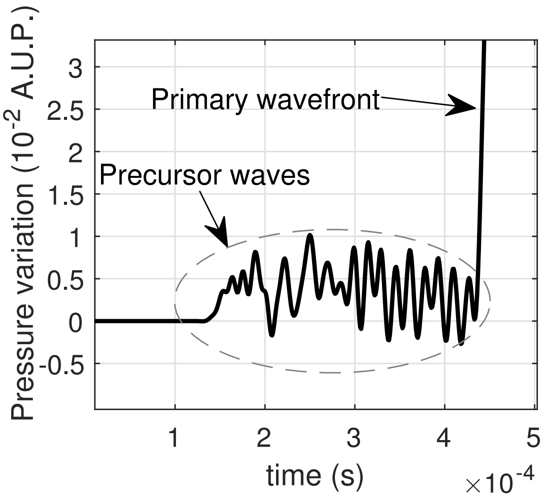

Figure III.10. *Example of precursor waves: Magnification around the precursor waves on the pressure history at point C5 (*$535.8 \cdot 10^{-3}$ *A.U.L. from the failure).*

To confirm that interpretation, velocities of the observed low amplitude waves and of the main wavefront are estimated, to be compared with theoretical values of precursor and primary waves. Considering a pair of signals i and j, the velocity is estimated by the following equation:

$$c = \frac{x_i - x_j}{\Delta t}, \tag{III.3}$$

where x_i and x_j are the axial positions of the sensor measuring the signal j and the sensor measuring the signal i respectively, and Δt is the Time Difference Of Arrival (TDOA) between the signals. The same formula is used for both the precursor waves and the primary wave. The velocities are estimated for each couple of signals (like the example in Fig. III.11), then the average value is computed. We obtain the following average values (with 95% confidence interval):

- For the early low amplitude waves (precursor waves): 3550 m.s^{-1} $\pm$ 132 m.s^{-1},
- For the main wave front: 1052 m.s^{-1} $\pm$ 9 m.s^{-1}.

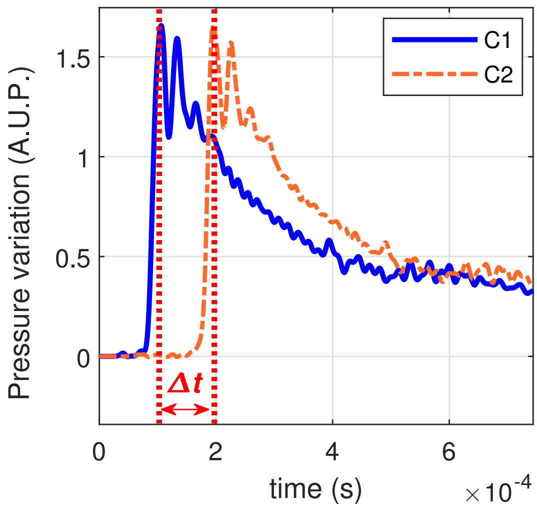

Figure III.11. *Example of TDOA estimation between two signals.*

These values are quite close to the values given by the simplified theoretical model (Sec. II.3.1) for precursor and primary waves, 3160 m.s^{-1} and 1062 m.s^{-1}, respectively. Our interpretation can therefore be confirmed.

The channel in the main section has a quasi-constant cross section (there is only a small and gradual increase of 40% of the cross-sectional area, upstream from the rod, due to a change in the upper extension's diameter). In that area, distortion of propagating wave is therefore very low, *i.e.* two pressure signals extracted at two different points in that section look very similar. In Fig. III.8, if we look at the first peak only, all the signals look quite similar and differ almost exclusively by time shifts (after the first peak, more significant differences arise because of reflections on channel ends). One may especially notice that the amplitude of that first peak is nearly constant over the six positions. At the transitions between the main section and the inlet or outlet sections however, there are strong and steep cross-section reductions. These reductions are necessary to make a mechanical connection between rod extensions and outer structure and thus to hold the rod, but they disrupt wave propagation, especially fluid pressure wave's one. Waves propagating from a source around the rod (such as a cladding-failure-induced pressure surge) to P1 or P2 sensors cross either the inlet or the outlet transition. Signals that are measured by these sensors are therefore affected by the perturbation due to these geometrical changes. Fig. III.13 shows pressure history at several positions around the outlet transition (the positions are shown in Fig. III.12). First peak amplitude on downstream positions is clearly lower than on upstream positions. That difference is due to the strong reflection at the upstream edge of the transition. Pressure histories at the two upstream positions clearly exhibit a second pressure peak which is related to the reflected pressure wave. It shows that, as the wave first travels through the system, a large part of its energy stays in the main section and does not enter the outlet sections. This phenomenon is also noticeable in Fig. III.6.

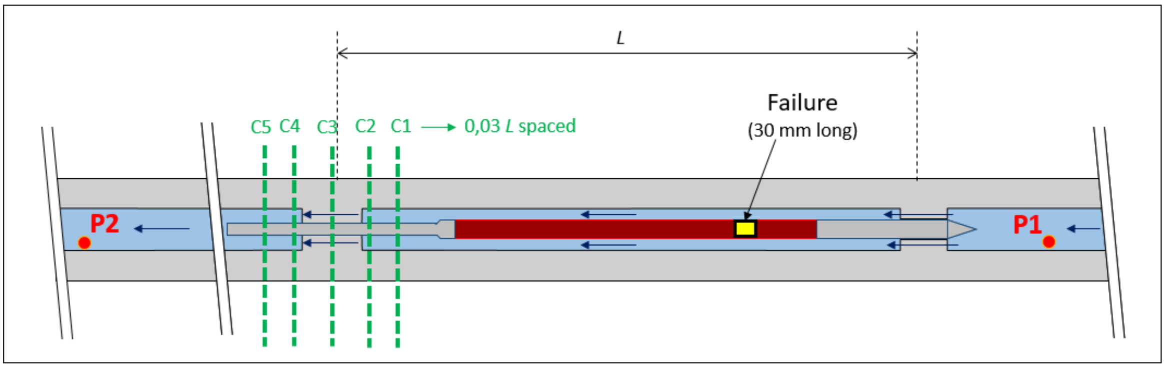

Figure III.12. *Positions of pressure history extraction positions around the outlet transition.*

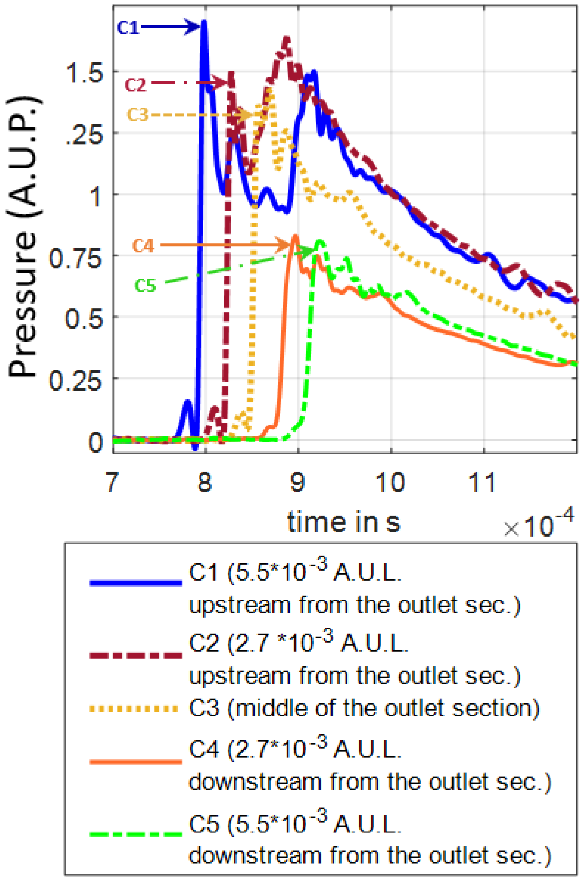

Figure III.13. *Pressure histories at several positions around the outlet transition.*

III.3.1.3. Application of failure localization methods to the pressure results

The simulated pressure histories are used to test some failure localization methods. To introduce the methods, we assume we know neither the failure position nor its occurrence time. In such a case, several simple methods to find the position are available with the current results:

1. Based on the TDOA of the primary wave between two points in the main section, one downstream and one upstream from the failure. Source position is estimated with the following expression:

$$x_s = \frac{(x_i + x_j - c_{pm}\Delta t)}{2} \tag{III.4}$$

   with x_i and x_j the axial positions of the two points from which pressure histories are extracted, Δt the TDOA between the two points, c_{pm} the primary wave speed.

2. Based on the TDOA of the primary wave between P1 and P2. Source position is given by the previous expression.

3. Based on the time delay between precursor waves and the primary wave at a single point (either a point in the main section, or P1, or P2). Assuming that precursor waves and the primary wave are created at the same point and at the same time, source position is deduced from:

$$d = (t_{pm} - t_{pc})\,\frac{c_{pm}\,c_{pc}}{c_{pc} - c_{pm}} \tag{III.5}$$

   with d the distance between the source and the point from which the pressure signal is extracted, c_{pm} the primary wave speed, c_{pc} the precursor wave speed, t_{pm} the arrival time of the primary wave and t_{pc} the arrival of the precursor waves.

These methods require either an assumption about wave velocities (we can use, for instance, the analytical formulae (II.84) and (II.86) or the average values deduced from our numerical results), or an additional point to estimate them by TDOA. In the latter case, the first two methods would require two points on one side of the failure and a third point on the other side. The third method would require two points on the same side of the failure.

Here, these methods are applied with assumed velocities (both with analytical ones and with the ones previously deduced from the numerical results). Hence, the first two methods require two sensors, they are therefore referred as “multi-sensor methods”, and the third requires a single sensor only and is called “single-sensor method”. Results obtained with the different methods are presented below. All positions are relative to the lower end of the rod.

Multi-sensor localization with points in the main section:
The TDOA is estimated between each of the points shown in Fig. III.8, which are downstream from the failure, and the point C0 which is upstream from the failure (the failure is quite close to the main section lower end, so only one upstream point is considered), as shown in Fig. III.9. Then, the source position is estimated with the Eq. (III.4). The average value is eventually calculated. Results are shown in table III.3.

Points	**Points' positions** (10^{-3} A.U.L.)	**TDOA** (μs)	**Assumed wave speed** (m.s^{-1})	**Resulting source position** (10^{-3} A.U.L.)
C0 ; C1	44.0 ; 222.9	-1.5 ± 2	1062 1052 ± 9	134.2 ± 2.8 134.2 ± 2.8
C0 ; C2	44.0 ; 312.7	87 ± 2	1062 1052 ± 9	136.0 ± 2.8 136.4 ± 3.5
C0 ; C3	44.0 ; 402.4	182 ± 2	1062 1052 ± 9	134.5 ± 2.8 135.4 ± 3.9
C0 ; C4	44.0 ; 592.1	275 ± 2	1062 1052 ± 9	134.1 ± 2.8 135.4 ± 4.3
C0 ; C5	44.0 ; 581.8	369 ± 2	1062 1052 ± 9	133.4 ± 2.8 135.1 ± 4.8
Average			1062 1052 ± 9	134.5 ± 2.8 135.3 ± 3.6

Table III.3. *Multi-sensor localization with points in the main section - results*
(Actual source position: $135.3 \cdot 10^{-3}$ *A.U.L.)*

Multi-sensor localization with P1 and P2:
The TDOA is estimated between P1 and P2 and source position is deduced with eq. (III.4). Results are given in Tab. III.4.

Points	**Points' positions** (10^{-3} A.U.L.)	**TDOA** (μs)	**Assumed wave speed** (m.s^{-1})	**Resulting source position** (10^{-3} A.U.L.)
P1 ; P2	-324.8 ; 1490.0	919.6 ± 4	1062 1052 ± 9	134.7 ± 3.9 138.8 ± 7.7

Table III.4. *Multi-sensor localization with P1 and P2 - results*
(Actual source position: $135.3 \cdot 10^{-3}$ *A.U.L.)*

Single-sensor localization
Localization results with the pressure history at different points in the main section[1] are given in Tab. III.5.

Localization results with the pressure history at P1 or P2 are given in Tab. III.6.

Fig. III.14 shows the localization results with the different methods, except the inconsistent value of the single-sensor localization with P2 and numerically estimated velocities (last row of Tab. III.6).

[1] C1 is not used here because it is close to the failure and the time delay between precursor and primary waves is therefore too short to yield an accurate result.

Point	Point's position (10^{-3} A.U.L.)	Time delay precursor-primary waves (μs)	Assumed wave speed (m.s^{-1}) c_{pm} | c_{pc}	Resulting source position (10^{-3} A.U.L.)
C2	312.6	87 ± 3	1062 | 3160 1052 ± 9 |3550 ± 132	150.5 ± 4.4 161.1 ± 8.3
C3	402.4	182 ± 3	1062 | 3160 1052 ± 9 |3550 ± 132	143.4 ± 4.4 160.3 ± 10.9
C4	492.1	275 ± 3	1062 | 3160 1052 ± 9 |3550 ± 132	133.3 ± 4.4 156.8 ± 13.5
C5	581.8	369 ± 3	1062 | 3160 1052 ± 9 |3550 ± 132	122.5 ± 4.4 152.5 ± 16.1
Aver.			1062 | 3160 1052 ± 9 |3550 ± 132	137.4 ± 4.4 157.7 ± 12.2

Table III.5. *Single-sensor localization with points in the main section - results (Actual source position:* $135.3 \cdot 10^{-3}$ *A.U.L.)*

Point	Point's position (10^{-3} A.U.L.)	Time delay precursor-primary waves (μs)	Assumed wave speed (m.s^{-1}) c_{pm} | c_{pc}	Resulting source position (10^{-3} A.U.L.)
P1	607.3	325 ± 3	1062 | 3160 1052 ± 9|3550 ± 132	152.2 ± 7.3 121.0 ± 19.3
P2	1874	4000 ± 3	1062 | 3160 1052 ± 9|3550 ± 132	6.2 ± 7.3 103.2 ± 45.5

Table III.6. *Single-sensor localization with P1 or P2 - results (Actual source position:* $135.3 \cdot 10^{-3}$ *A.U.L.)*

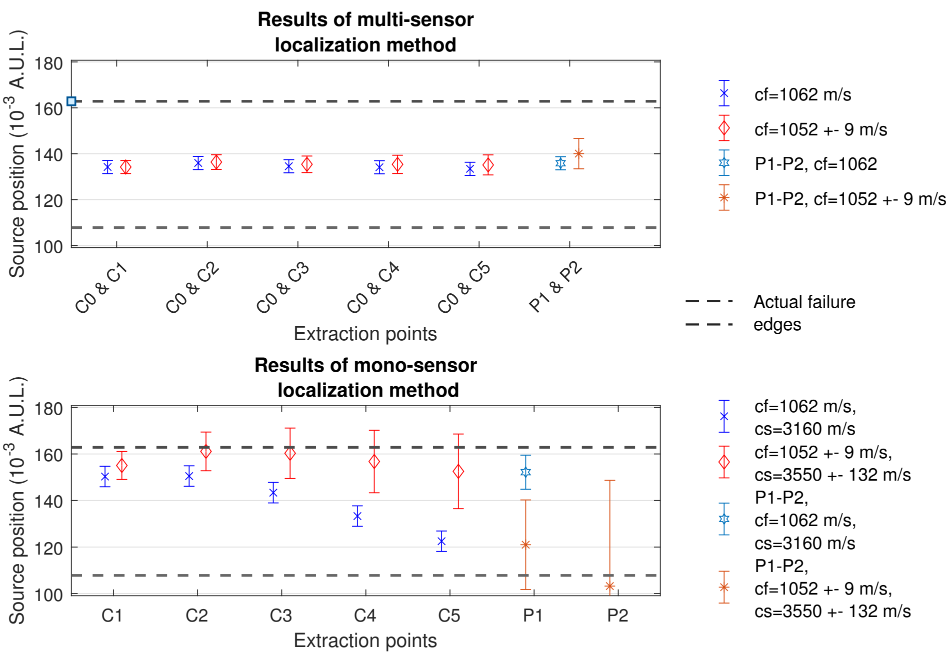

Figure III.14. *Results of the different methods for source localization (source position in arbitrary unit of length, defined as the length of the device main section).*

Here, using analytical velocities provides smaller uncertainties than using values deduced from TDOA on numerical results. Actually, there is no uncertainty on the analytical wave speeds because we could use the exact same material properties for the determination of analytical velocities and for the numerical computation. However, in an experimental context, there are uncertainties on material properties and consequently on the analytical estimation of the wave speed. Depending on these uncertainties, using analytical velocities may not be more reliable than estimating them by measurements with additional sensors.

III.3.2. Additional results

III.3.2.1. Additional study with a rigid structure model

An additional simulation was carried out to confirm more reliably the precursor and primary waves interpretation, the assumption about the influence of fluid-structure interaction on the wave velocity, and to determine if the transmission loss through the geometrical singularities is mainly due to reflections or to the transmission to the structure. For this simulation, the elastic structure is replaced by a perfectly rigid one. Thus, the model includes simply the fluid domain with perfectly rigid boundaries. Any effect of the structure response, whether dynamic or quasi-static, is therefore canceled.

This model is actually derived from a preparatory version that was parameterized for a temperature of 20°C, unlike the final model used in the previous sections (Sec. III.3.1), which reproduced PWR conditions, *i.e.* 280°C. Elastic structure model's results presented in the current section for comparisons are therefore those obtained with the preparatory version, with a temperature of 20°C. For this temperature, the sound velocity was set at 1500 m.s^{-1}.

Firstly, a pressure signal extracted from the rigid structure simulation is compared to the one of the elastic structure model, at the same position (438 mm from the failure). The superimposition of the signals is shown on Fig. III.15. A magnification on the beginning of event is shown in Fig. III.16 and highlights the fact that precursor waves do not exist when the structure is rigid. It proves that they are actually due to the structure response and are not artifacts induced by the numerical computation.

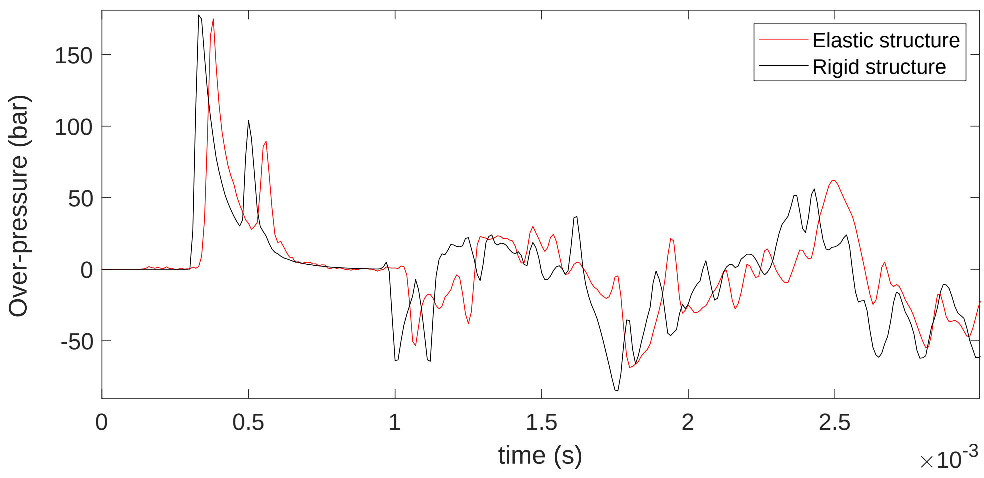

Figure III.15. *Comparison of pressure histories at 438 mm from the failure for an elastic structure and a rigid structure.*

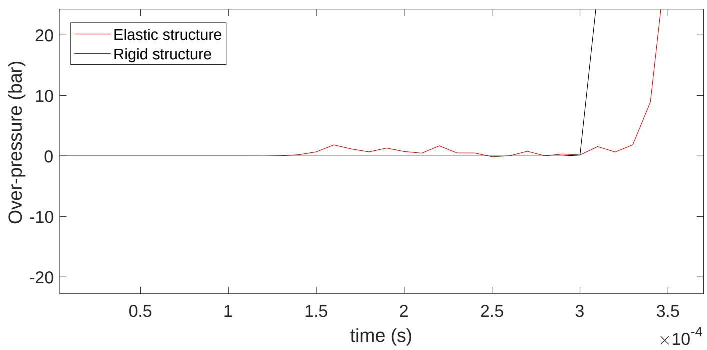

Figure III.16. *Comparison of pressure histories at 438 mm from the failure for an elastic structure and a rigid structure - Time magnification on the precursor waves.*

Secondly, the primary wave velocity is calculated (by the method introduced in Sec. III.3.1.2) for both the elastic and the rigid structure models. An average value of 1258 m.s^{-1} is obtained for the elastic structure model, and an average value of 1500 m.s^{-1} for the rigid structure model. The first value is lower than the one obtained with Eq. (II.84) (introduced in Sec II.3.1), 1410 m.s^{-1}, with material properties corresponding to a temperature of 20°C. The second value is equal to the theoretical sound velocity parameterized in the simulation inputs[2]. Qualitatively, it also means that the primary wave velocity is lower with a surrounding elastic structure than with rigid boundaries. This is consistent with the theory presented in Sec II.3.1. This qualitative observation is also shown by Fig. III.16, where the main wavefront arrives earlier in the rigid-structure simulation (in both simulations, the source signal is generated at time $t = 0$ and at the same position).

[2]More accurately, the inputs given to the Europlexus software are the parameters involved in the stiffened gas EOS (introduced in Sec. II.3.2). Since those parameters are directly related to the sound velocity by the linear formula given by Eq. (III.2), the sound velocity can be considered as an input.

Thirdly, the evolution of the pressure profile through the outlet transition is studied to check the geometry-related effects of the propagation through this singularity. To this aim, the spatial evolution of the pressure profile is analyzed. To depict this evolution, the pressure field around the transition is shown in Fig. III.17 and the pressure histories at different positions in the area are shown in Fig. III.18. The positions are the same as the ones used in Sec. III.3.1.2 and shown in Fig. III.12.

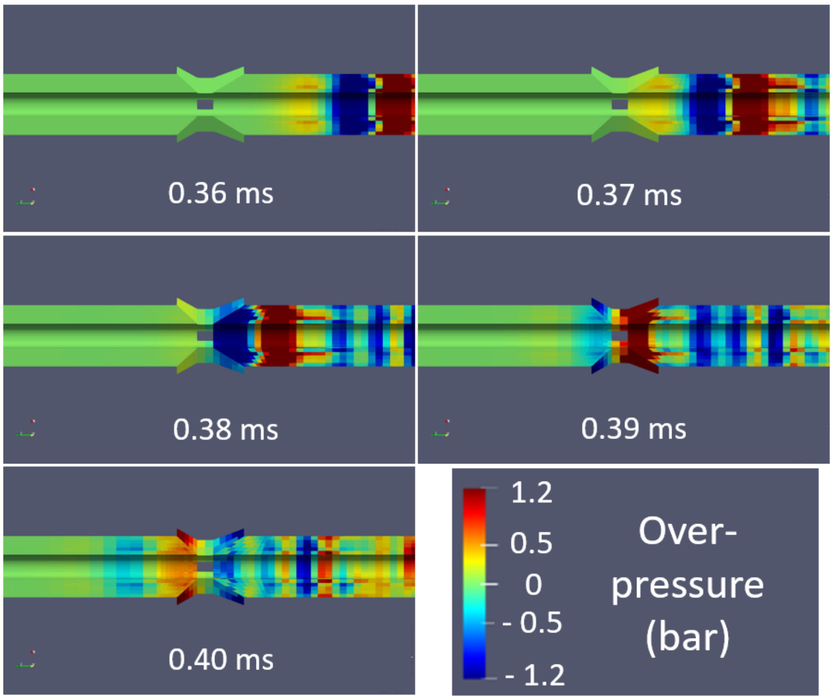

Figure III.17. *Evolution of pressure field around the outlet transition (rigid structure).*

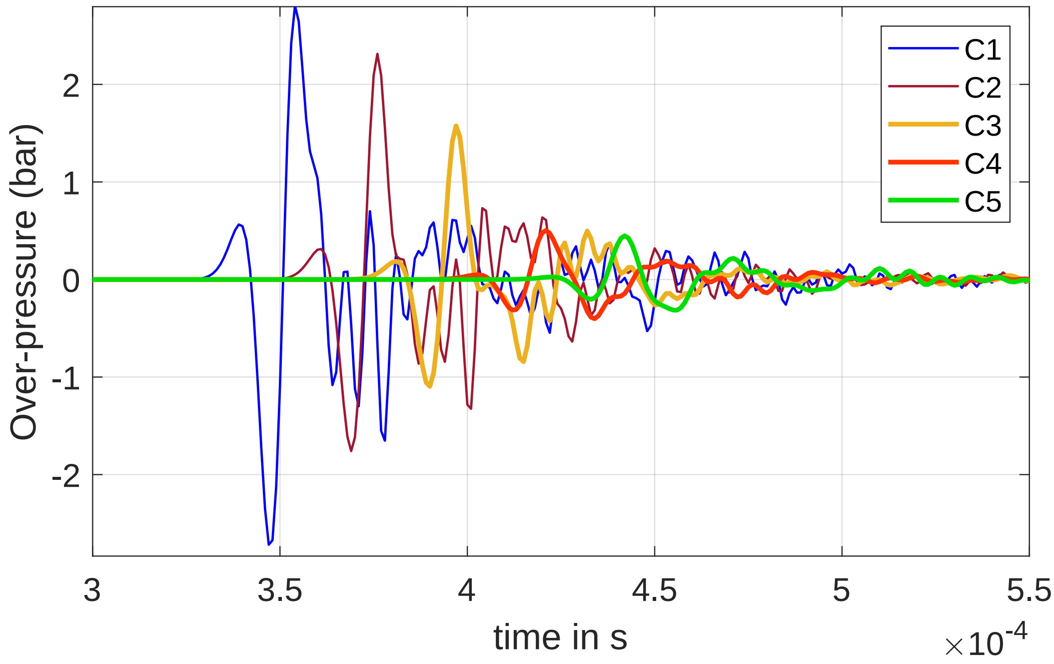

Figure III.18. *Pressure histories at different postions around the outlet transition.*

Those representations show that the main wavefront tends to decrease throughout its propagation (its amplitude decreases with the distance from the source), but the effect of the geometrical singularity is not significant. To analyse it more accurately, the variations in the signal energy between each section are calculated for the elastic structure and the rigid structure and are plotted in Fig. III.19. The signal energy is defined, for a numerical signal $x(n)$ of size N, as[3]:

$$E = \sum_{n=1}^{N} |x(n)|^2 \tag{III.6}$$

[3]The definition of numerical signal energy does not exactly correspond to physical energy. However, here, the comparison is simply performed on ratios between signals of the same size, of the same sampling rate and related to the same physical data. Therefore, the comparison is physically meaningful.

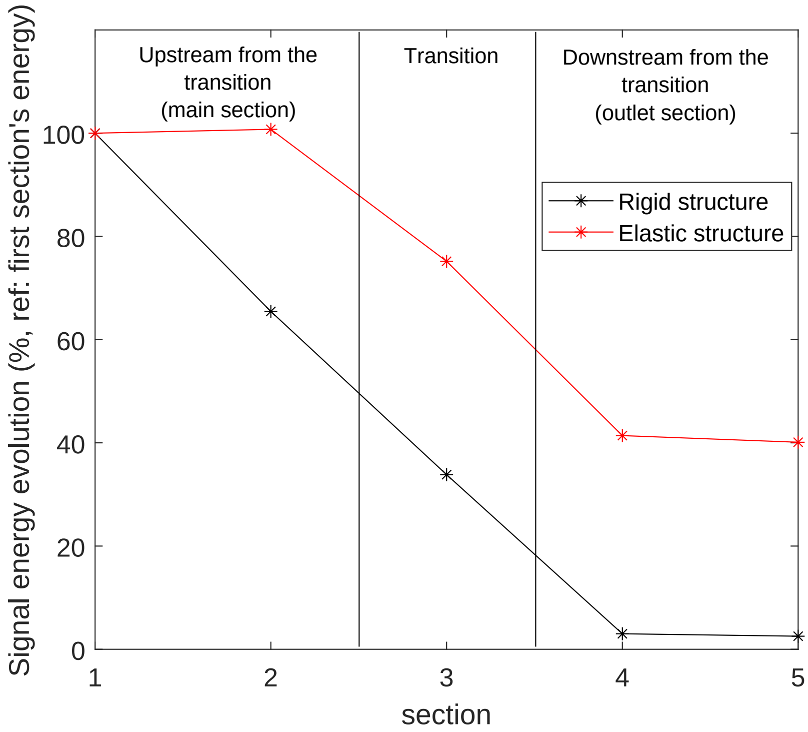

Figure III.19. *Evolution of signal energies between different points around the outlet transition, for an elastic structure and a rigid structure.*

In both cases, the energy significantly decreases with the distance from the source. However, while in case of the elastic structure the decrease seems to be induced by the transition, in the case of the rigid structure, the decrease starts before the transition and stops downstream.

In addition to that, it can be noticed that for positions far enough from the source, the pressure histories in the fluid with rigid boundaries tend to exhibit an oscillatory characteristic, unlike the pressure histories from the elastic structure simulations that keep the same characteristic all along the system (a high peak with exponential decay followed by random-like resonances). This difference is due to the fact that rigid boundaries implies a total reflection of the waves in the radial direction, which spread out all along the channel as high frequency modes with relatively high energy. On the contrary, with the response of the elastic structure, radial reflections are attenuated and most of the emitted energy concentrates in the main wavefront that propagates in the axial direction as a plane wave.

In the case of the rigid boundaries, the oscillatory characteristic allows to study the effects of the propagation through the geometrical singularity in the frequency domain. To this aim, frequency transfer functions between each section were computed. The frequency transfer function between two points, i and j is defined as:

$$H_{i,j} = \frac{S_j(f)}{S_i(f)}, \tag{III.7}$$

where S_i and S_j are the Fourier transforms of the signals measured at points i and j. Fig. III.20 shows the transfer function between sections 1 and 2, between sections 2 and 4, between sections 4 and 5, and between sections 1 and 5. They respectively depict the distortion due to the propagation downstream from the transition geometry, the effects of the propagation through the transition, the distortion upstream from the transition, and the global distortion between a point upstream and a point downstream from the transition. They are displayed on the frequency range of [0; 200] kHz, above which the energy is very low. The most significant effect of the transition geometry is the attenuation over 140 kHz. It can be considered that, in the ideal case of a perfectly rigid bounded fluid, the transition geometry acts like a low-pass filter for the pressure waves.

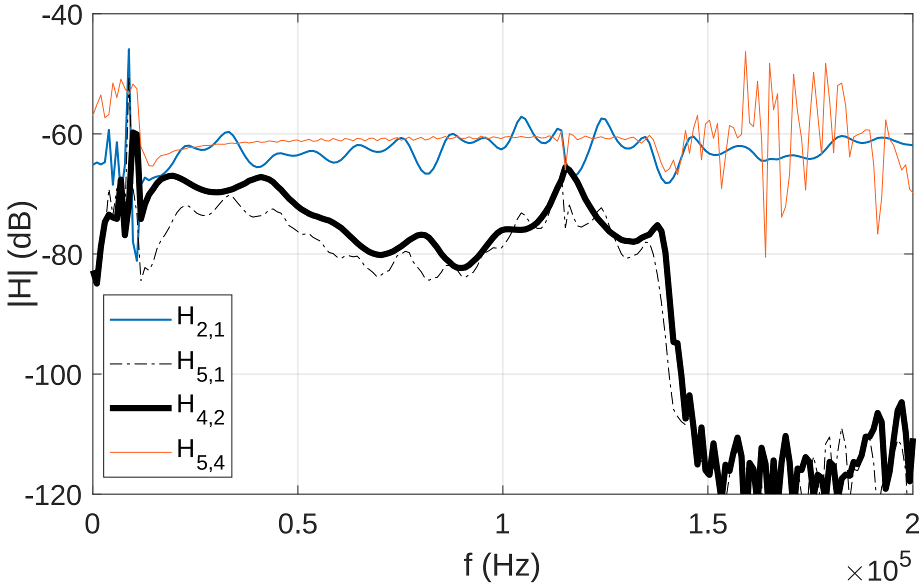

Figure III.20. *Transfer functions between different positions around the outlet transition, for a rigid structure. $H_{i,j}$ is the transfer function between position j and position i, with i and j corresponding to the positions presented in Fig. III.13.*

The oscillations above 150 kHz, especially noticeable in the $H_{5,4}$ transfer function, are due to the lack of energy of $C4$ and $C5$ signals in those frequency ranges, as shown by the Energy Spectral Density (ESD) in Fig. III.21. The figure also highlights the difference in the signal energy over 150 kHz between $C1$ and $C2$ on one hand, and $C4$ and $C5$ on the other hand.

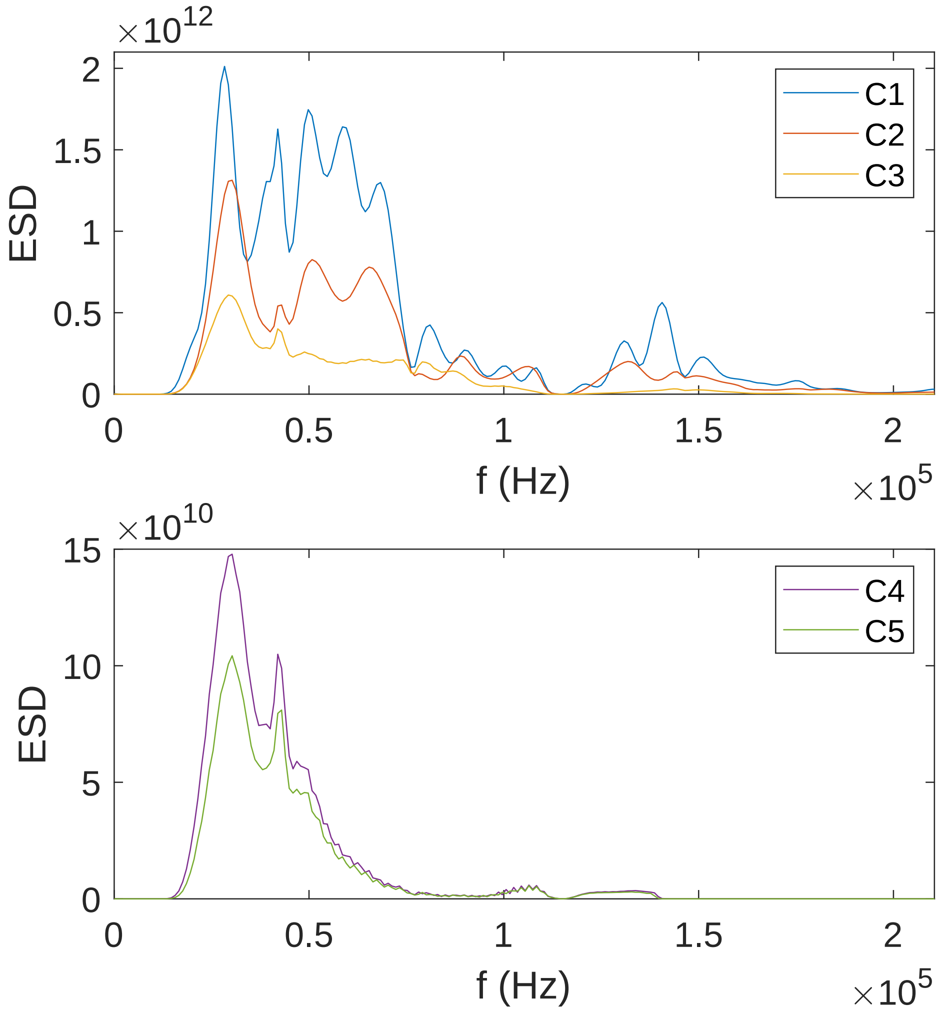

Figure III.21. *ESD of the pressure histories at different positions around the outlet transition.*

Such a frequency analysis is unfortunately not possible on the elastic structure models' results because of the absence of oscillations in the frequency range of interest, considering this range corresponds to the oscillations due to reflections of pressure waves on the lateral walls.

As a partial conclusion of this additional study, it can be stated that both the fluid boundaries' geometry and the structure response have an effect on the propagation of pressure waves through geometrical singularities in the channel. The most significant effect of the geometry can be depicted as a low-pass-filter of the pressure waves, while the presence of an elastic structure results in a significant transmission loss in the pressure waves between the upstream and the downstream of the geometrical singularities. However, the propagation in an ideal rigidly bounded fluid domain results in signals of a different nature than those obtained when the fluid is surrounded by an elastic structure. As a consequence, accurately estimating the respective effects of the geometry and the structure interaction would require further and extensive investigations.

III.3.2.2. Results in the structure domain

For the reasons mentioned in the introduction of Sec. III.3, the analysis of the numerical results focuses on the fluid pressure data. Nevertheless, the results related to the elastic waves in the structure are presented in the current section.

Firstly, histories of all the motion components (displacement, velocity and acceleration in the three directions) at a point in the main section (772 mm from the failure) are shown in Fig. III.22, III.23 and III.24. All the histories are superimposed to the pressure at the same position, in order to highlight the effects of fluid-structure interaction. The results at only one point are presented, but several points in the main section were studied as well and led to the same observations.

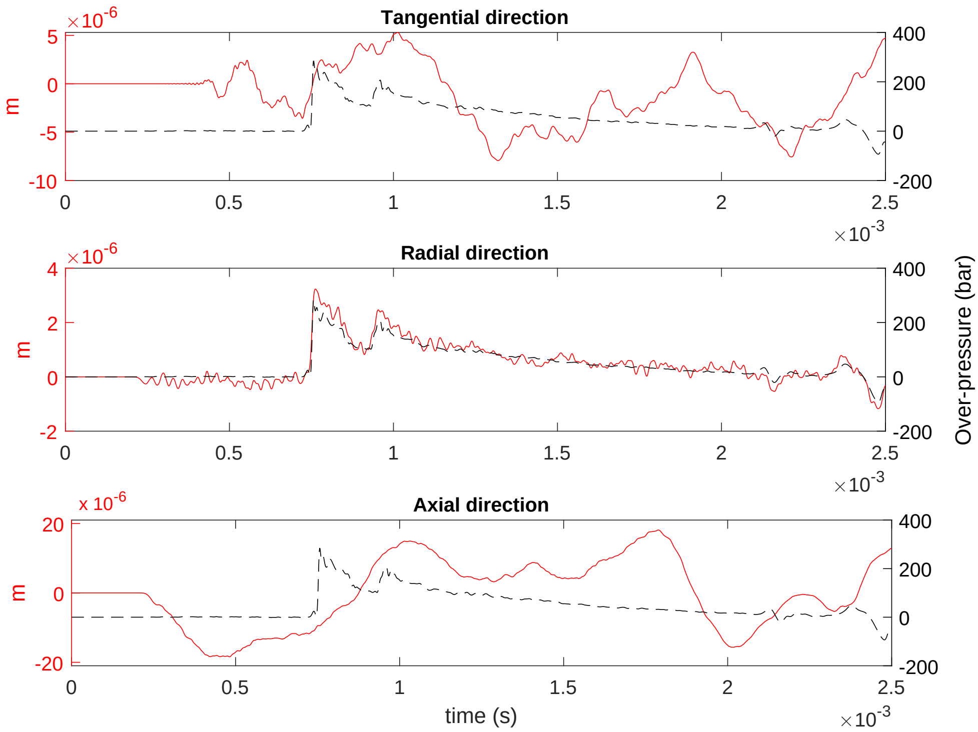

Figure III.22. *Structural displacement on the outer surface of the outer structure, at 772 mm from the failure.*

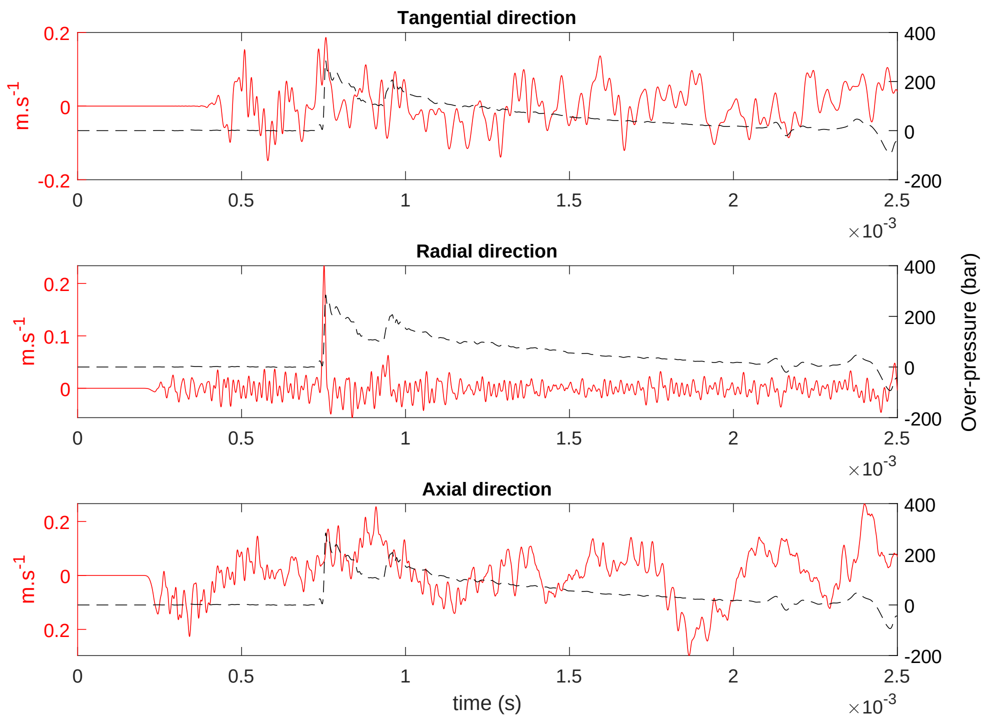

Figure III.23. *Structural velocity on the outer surface of the outer structure, at 772 mm from the failure.*

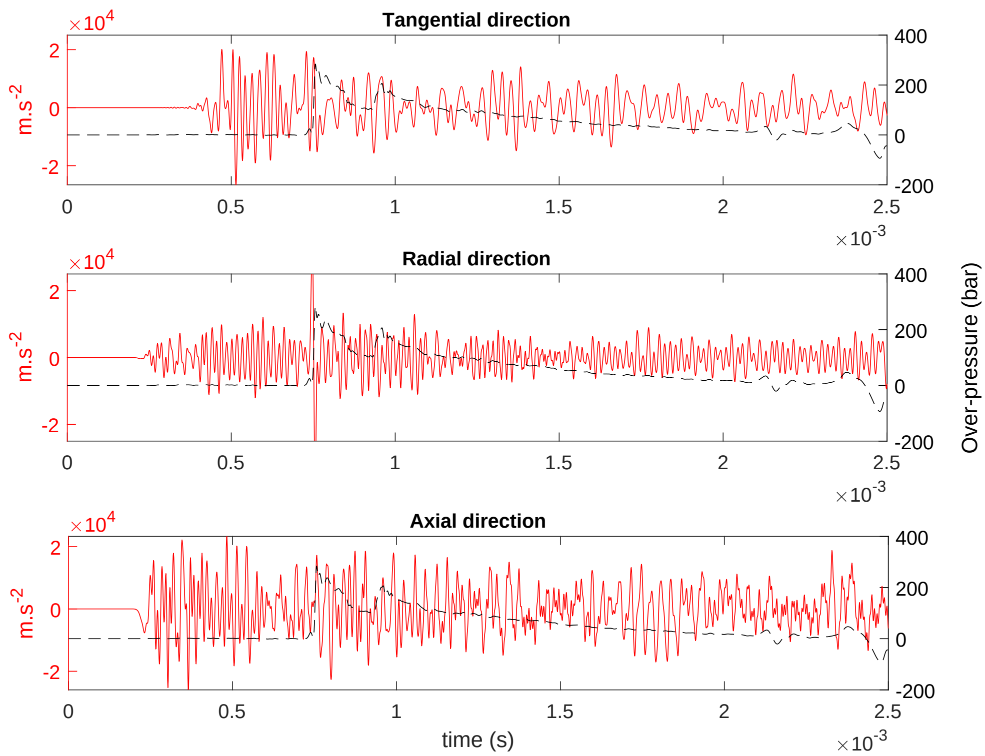

Figure III.24. *Structural acceleration on the outer surface of the outer structure, at 772 mm from the failure.*

The early oscillations exhibited by ortho-radial motion components are related to transversal waves, and the ones exhibited by radial and axial motions components are related to quasi-longitudinal (also called "dilatational waves"), according to the terminology introduced in Sec. II.1. Those waves depict the dynamic response of the structure, which includes the effects of structural inertia, as explained in Sec. II.3.1. In the radial components' histories, the effects of the main fluid pressure wavefront (ie. primary wave), which arrives after the quasi-longitudinal waves, is also noticeable. On the radial displacement especially, a high amplitude peak correlates with the primary pressure wave and shows how the tube is radially stretched by the inner pressure surge. This is referred as the quasi-static response of the structure, which is related to the elastic distortion of the tube induced by the pressure surge but is not influenced by the structure inertia, as explained in Sec. II.3.1. The quasi-static response is less significant in the velocity history, and even less significant in the acceleration. This is explained by the fact that the quasi-static response (radial stretching) has a lower frequency than the axial structural waves, and that time differentiation tends to emphasize high frequency variations compared to low frequency ones.

Secondly, the same analysis is carried out on results from a point on the outlet section and a point on the inlet sections, considered as "realizable" measurement points. They are also located on the outer wall of the outer structure, where sensors could be actually mounted. Only the motion components in the radial direction are presented, because they exhibit both the quasi-static and the dynamic response of the structure, and the intended measurements on a real device are assumed to be especially related to radial motions. Histories of the three components are shown in Fig. III.25 and Fig. III.26.

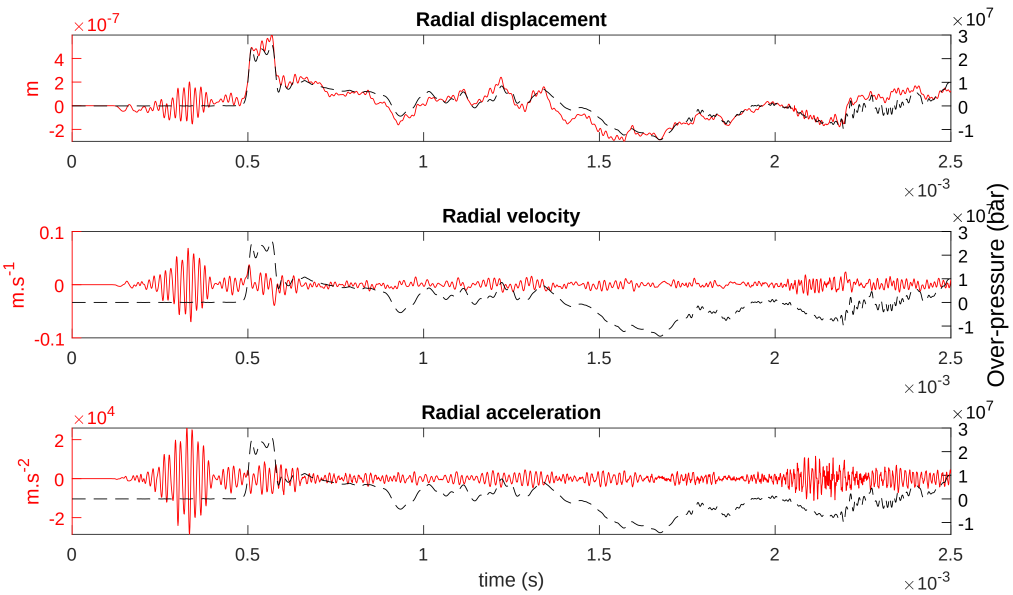

Figure III.25. *Radial motion components at a point on the inlet section, on the outer structure.*

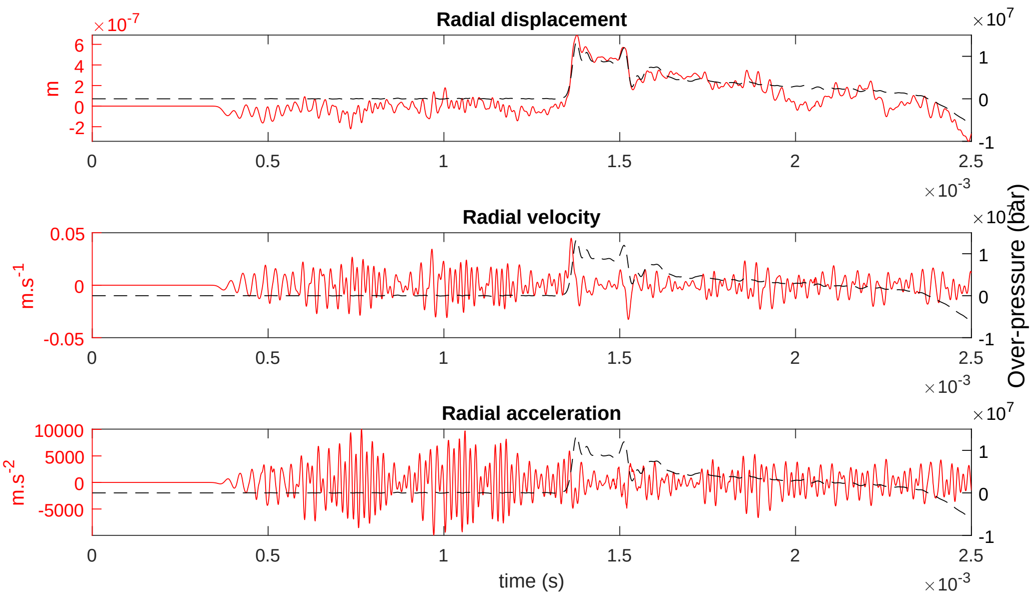

Figure III.26. *Radial motion components at a point on the outlet section, on the outer structure.*

In velocity and acceleration in the external sections, the quasi-static response is hardly visible. However, it can be detected in time-frequency representations, as shown by the continuous wavelet transforms (CWT) of the velocity histories (the CWT is introduced in Sec. IV.3.3.2 and detailed in App. B) in Fig. III.27 and III.28.

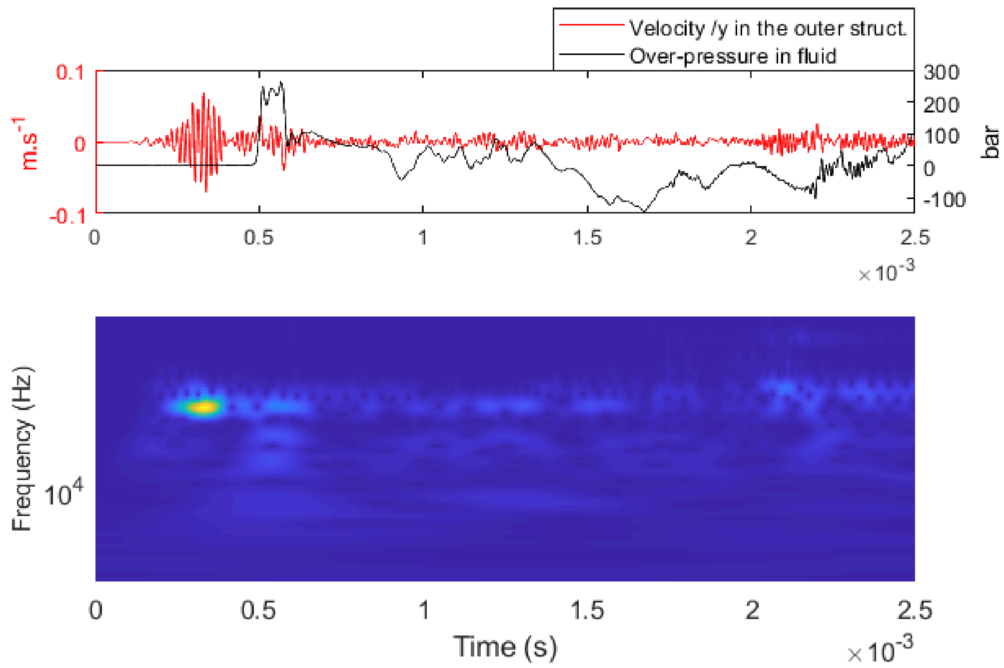

Figure III.27. *CWT of the radial velocity of a point on the inlet section, on the outer structure.*

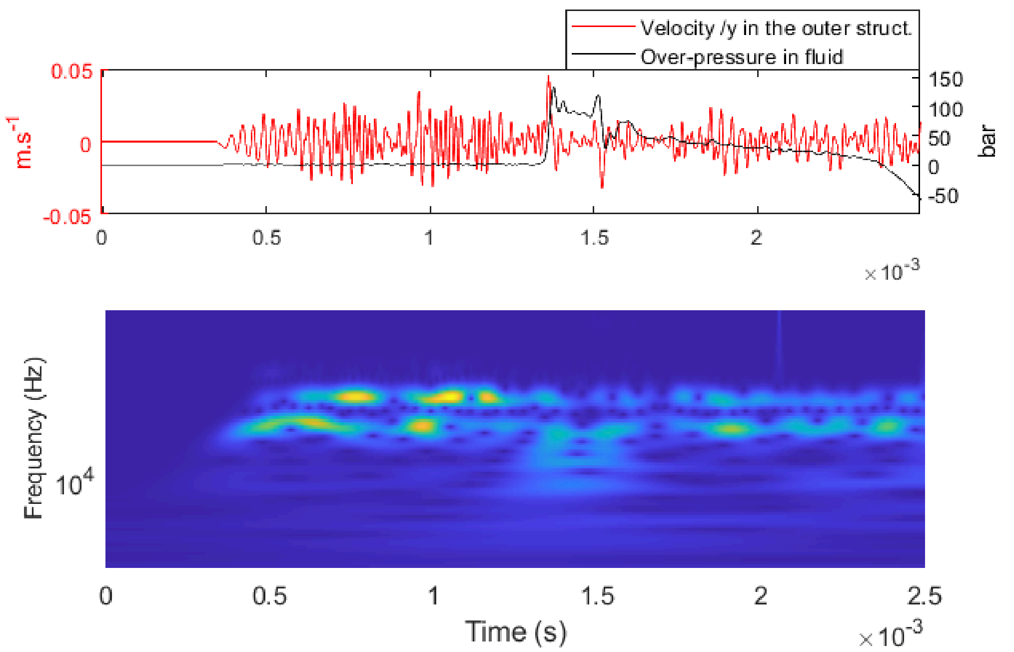

Figure III.28. *CWT of the radial velocity of a point on the outlet section, on the outer structure.*

Although the detection is not obvious, it should be reminded that no structural damping was implemented in the presented simulations (adding Rayleigh damping was attempted but it led to an excessive computational cost). Therefore, in real experiments, an attenuation of the precursor waves according to the distance from the source is expected. On the other hand, as fluid damping is already implemented in the presented model, the primary wave amplitude is not expected to be significantly lower in the experiments. Thus, the dynamic response at positions far from the source would likely be less significant, compared to the quasi-static one, in experimental results than in the current numerical results.

III.4. Conclusion of the numerical simulation results

Numerical simulations were computed with the EUROPLEXUS code to improve the understanding of fluid-structure interaction phenomena related to fuel cladding failure in a nuclear reactor and, thus, to design a failure localization method based on pressure signals analysis. Different models were used to observe the influence of some parameters, such as the failure length, the elasticity of the structure, and material properties.

These simulations allow for the confirmation of several phenomenological assumptions. The observation of the spatial evolution of the pressure profile proves that the plane wave assumption is valid. It also shows that a geometrical singularity in the channel leads to reflections of the pressure waves and, consequently, transmission loss between the two sides of the singularity. Moreover, the time evolution of the pressure at different points of the system exhibits two kinds of waves, referred to as precursor and primary waves, according to the terminology used in water-hammer studies. Histories of the motion components (displacement, velocity and acceleration) in different directions allow to observe two types of structural waves (quasi-longitudinal and transversal), which compose the dynamic response of the structure due to the excitation induced by the fluid pressure surge. The motion in the radial direction also exhibits the radial stretching of the structure generated by the inner fluid pressure surge, referred as the quasi-static response of the tube. As a consequence, in both the fluid and the structure, the propagation of structural waves and the propagation of the pressure surge in the fluid can be observed. This information also shows that the approach based on three-dimensional simulations using EUROPLEXUS, and an approach based on classical one-dimensional water-hammer models can be considered as complementary. Indeed, on the one hand, some information provided by the water-hammer theory (appearance of precursor and primary waves, wave velocity values, etc) can help with the interpretation of EUROPLEXUS results, on the other hand, EUROPLEXUS results show which simplification inherent to water-hammer models, such as the plane wave assumption, is acceptable.

These simulations also bring quantitative information about the velocities of precursor and primary waves, which can be estimated from the simulated signals. They were compared to analytically determinated values and proved to be consistent with them. This quantitative information can be of interest for the analysis of experimental results, since the measurements that are necessary to estimate wave velocities may not be possible in a real reactor.

From a practical perspective, simulations show that precursor and primary waves appearing in pressure signals can be used to detect and locate the failure. Thus, detections and localizations can be achieved with a single sensor, using the time difference of arrival (TDOA) between the two kinds of waves, although using the TDOA between the primary waves of two different sensors' signals provides more accurate results. Moreover, precursor waves have a small amplitude compared to the primary waves, and, although they are detectable in noiseless simulated signals, they might be hidden by noise in experimental signals.

Despite the useful information provided by the simulations, some limits of the current numerical model have been identified:

- Simulated phenomena are simplified: only the transient over-pressure due to the failure is simulated. Material failure or distortion, fuel pieces ejection are not simulated, even though they might happen in reality. This simplification is related to the reproduction of the excitation phenomenon, but is independent from the results related to propagation phenomena,
- Coolant fluid vaporization is not reproduced, although it affects the wave propagation. Nevertheless, such a phenomenon does not occur at every failure,
- No structural damping is implemented, which can result in an over-estimation of the amplitude of structural waves away from the failure.

Furthermore, the numerical model still needs to be validated by comparisons with experimental results. To this aim, an experimental mockup was designed and experiments are currently being carried out. This device is introduced in Sec. IV.5. In this mockup, failure of fake fuel rods are reproduced and resulting fluid pressure waves and vibrations are recorded at several positions of the system. Thus, the fluid pressure profile evolution along the system will be compared to the numerical results to validate the model presented in the current chapter. Measurements related to elastic waves in the structure, carried out with AE sensors, strain gauges and accelerometers, will be compared to the numerical results in order to estimate the bias induced by the response of those sensors.

After this validation, the numerical model can be used according to the presented methodology for the interpretation of experimental results from tests in a real reactor. In such a case, it will be necessary to adjust some parameters, such as the failure length and position, to make the simulation representative of the specific test being analyzed.

IV. Experimental approach

The experimental approach is a major part of the work presented in this thesis. This approach consists of reproducing in a mockup some mechanical phenomena of interest in order to study their effects by using methods and tools that are not available in a real nuclear reactor. Two different experimental devices were designed and used in the frame of this work. The first device, named RUPTUBE, was intended to test solutions for generating tube failures (representing fuel rod cladding failures) and measuring structural vibration effects of the failures. Results brought by that device helped the design of the second device, named MAQAC, in which surrounding fluid flow and measurements in the fluid were added to the tube failure system and the structural measurements. Design of the experiments and the instrumentation systems are presented in Sec. IV.1 and Sec. IV.2. The RUPTUBE device and experimental results are presented in Sec. IV.3 and Sec. IV.4, and the MAQAC device is introduced in Sec. IV.5.

IV.1. Objectives, constraints and technical solutions related to the experimental approach

Performing tests in a real nuclear reactor implies a very expensive, long and complex preparation. Moreover, high temperature and radioactivity, which are inherent conditions in a working reactor, prevent the use of most acoustical and vibration sensors. As a consequence, it was not possible to carry out the experimental work intended in this PhD in a real reactor. Therefore, it was intended to make and use a mockup of the test device used in a research reactor. The first purpose of this mockup is to reproduce the mechanical phenomena of interest: the cladding failure, the coolant fluid flow, and the coolant fluid boiling. The aim is to reproduce them in a controlled way, to be able to independently study their respective effects and mutual interactions, and without radioactivity nor high temperature, to minimize the restrictions on sensors that can be used and on their positions in the mockup. The second purpose is to make all the necessary measurements possible to study acoustic and vibration effects of a tube failure with accuracy. It should be possible to measure structural waves (low frequency vibrations and high frequency guided waves) directly on the surface of the tube with either optical devices, such as a laser Doppler vibrometer or a high-speed camera, or contact sensors such as accelerometers, strain gauges, and AE sensors. Structural waves measurements should also be possible on the outer structure. Fluid pressure wave measurements in the flowing water have to be available around the rod as well as downstream and upstream from the rod.

Those measurements are supposed to provide signals that are slightly distorted by the propagation between the source and the measurement point. Then, by processing those signals, it should be possible to accurately and reliably localize the source, to estimate the ratio of energy transmitted to the structure and to the fluid, and get information about wave propagation through the cladding, the surrounding fluid, and the outer structure. The desired information is the displacement and pressure fields, the wave velocities in the different media, and the effects of the propagation through the mechanical connections between the rod and the outer structure and through geometrical singularities in the fluid channel.

In addition to those objectives, the device must be simple, intrinsically safe, and easy to use, so that a person can design and use it alone and with limited safety obligations. It must also comply with the European pressure equipment directive ([89]).

The current section introduces the global objectives and constraints of the experimental approach.

IV.1.1. Reproduction of the coolant fluid flow

The coolant fluid flow around the rod has several effects. The most significant ones are the added mass and added damping, which have an impact on the vibration, rod's FIV (structure vibrations due to the dynamic load of the fluid on the structure), and noise produced by flow disturbances (eddies, cavitation, bubbles, pressure surges). Moreover, the fluid is a propagation medium for the waves that are created either in the fluid itself, or waves in the structure that radiate into the fluid.

The fluid is therefore a propagation media as well as an acoustic or vibration source, and a parameter impacting structure vibrations. That is why it has to be taken into account in our study and reproduced in the experimental mockup. Like in a real research reactor, the mockup rod is coaxially inserted in a cylindrical channel, where water flows in the axial direction. However, several important discrepancies in materials, geometry, and hydraulic parameters are imposed, for the reasons explained below.

The coolant fluid flow is reproduced by installing the experimental device in a water loop. A water loop is a water system consisting of a circulation pump, instrumentation to monitor the system (such as flow-meters, pressure sensors, temperature sensors) and, if necessary, a cooler. That loop provides a water flow to the experimental device, whose properties depend on the loop's characteristics and settings.

The test section intended for this work is installed in an existing water loop that was initially designed for the work presented in [36]. This loop works in ambient temperature and can provide a maximum flow rate of 5 $m^3.h^{-1}$ at a pressure of 5 bar (the pressure is imposed by the flow rate, otherwise, cavitation may occur). Temperature and pressure conditions in a real system (*i.e.* typical french PWR), are respectively 280°C and 155 bar. Water properties are therefore different in a real system and the mockup.

Geometry and constitutive materials of the mockup structure, which can influence some FSI and vibration phenomena, are imposed by the various technical functions of the device. Concerning the outer tube, a transparent material is required for optical measurements and PMMA was chosen. Its inner diameter (*i.e.* the diameter of the channel) is imposed by the size of the sensors that should be mounted on the test tube, in order to prevent any contact between sensors and the wall of the channel. This results in an inner diameter of 21 mm. Concerning the test tube representing the rod, using real Zircaloy-4 (Zr-4) claddings in the mockup was not possible because of costs and difficulty to obtain. Material and dimensions of that tube will be imposed by constraints related to the failure generation, as it will be explained in Sec. IV.1.2, and the ease of supply. At the time of the mockup's design phase, neither the test tube diameter nor the test tube material was definitely settled on. A 8 mm or 10 mm diameter, and stainless steel or aluminium were the likeliest choices. The tube thickness is 0.5 mm. Thus, four possible designs of the test section were considered and analyzed. The different considered designs are:

- Case 1: channel diameter = 25 mm; tube outer diameter = 10 mm, stainless steel tube,
- Case 2: channel diameter = 25 mm; tube outer diameter = 8 mm, stainless steel tube,
- Case 3: channel diameter = 25 mm; tube outer diameter = 10 mm, aluminium tube,
- Case 4: channel diameter = 25 mm; tube outer diameter = 8 mm, aluminium tube.

All those constraints result in the imposed variables regarding dimensions, material properties and water loop characteristics that are presented in Tab. IV.1, for the four design cases. This table also presents the corresponding variables in a real system and shows the differences between the reality and the mockup possibilities.

	Real case (standard PWR)	**Case 1** (Stainless steel, 10 mm diameter)	**Case 2** (Stainless steel, 8 mm diameter)	**Case 3** (Aluminium, 10 mm diameter)	**Case 4** (Aluminium, 8 mm diameter)
Pressure P (bar)	155	up to 5	up to 5	up to 5	up to 5
Water density ρ_f (kg.m^{-3})	747 [90]	1000	1000	1000	1000
Water dynamic viscosity μ (Pa.s)	$808 \cdot 10^{-5}$ [91]	$1.1 \cdot 10^{-3}$	$1.1 \cdot 10^{-3}$	$1.1 \cdot 10^{-3}$	$1.1 \cdot 10^{-3}$
Speed of sound in water c (m.s^{-1})	1075	1500	1500	1500	1500
Characteristic diameter D (mm)	*Confidential*	15	17	15	17
Channel cross section (mm^2)	*Confidential*	412	441	412	441
Characteristic length L_f (mm)	*Confidential*	1047	1047	1047	1047
Flow rate (m^3.h^{-1})	*Confidential*	5	5	5	5
Aver. flow velocity u (m.s^{-1})	5.0	3.37	3.15	3.37	3.15

Table IV.1. *Dimensional analysis: variables imposed by the systems.*

In order to estimate the effects of such differences, a dimensional analysis of the studied problem is necessary. Generally, a dimensional analysis helps designers of a mockup to achieve the optimal similarity between the mockup and a real system. Here, because of the mentioned constraints, the main purpose of the dimensional analysis is rather to predict and understand the discrepancies that are expected between the experimental results and the real situation in a PWR reactor. The theoretical background for dimensional analysis can be found in [92] or [93]. The current application is inspired from the one presented in [94].

The following dimensional analysis was related to flow parameters and flow-induced vibrations. Phenomena related to acoustics, failure-induced waves and water-hammer were not regarded in this analysis.

The studied flow is a closed-conduit flow. In the main section (*i.e.* the section containing the rod), the flow is confined between the outer wall of the rod (including its extensions) and the inner wall of the external tube. At the inlet and outlet of the main section, geometric singularities induce flow disturbances. The following dimensional analysis is only applied to the area of the main section where steady state can be assumed. In the inlet and outlet section, only the geometric similarity is considered.

Fluid flow analysis

In a steady state closed-conduit flow, physical values to be considered are:

- fluid velocity at the point of interest: u,
- characteristic velocity: U,
- characteristic diameter: D,
- fluid density: ρ_f,
- characteristic pressure: P,
- dynamic viscosity: μ,
- characteristic time: t,
- characteristic length: L_f.

Every value has to be considered at comparable points in the real system and in the mockup. Density and dynamic viscosity are assumed to be constant in the whole system. The characteristic velocity U and pressure P are respectively chosen as the mean flow velocity and the mean static pressure at the inlet of the main section. Those values will be estimated from flow rate and pressure settings of the circulation pump. The characteristic length L_f is the main section's length (distance between the two rod-external structure connections) and the characteristic diameter is the hydraulic diameter in the main section. For an annular channel, the hydraulic diameter is defined by: $D = D_o - D_i$, where D_o and D_i are respectively the outer and the inner diameter. The characteristic time t is chosen as the inverse of the vortex-shedding frequency (see Strouhal number's definition below).

The dimensional analysis is carried out, using Buckingham's theorem (also called Pi theorem), defined in [92]. The system is described by eight values. All those values can be expressed with three fundamental units (distance, time and mass). According to Buckingham's theorem, the system can be described by 8-3=5 independent parameters. There are several possible parameter combinations, but, here, a very common one is chosen. With this combination, it yields:

$$\frac{u}{U} = \Phi\left(\frac{P}{\rho U^2}, \frac{\rho U D}{\mu}, \frac{D}{U\,t}, \frac{L_f}{D}\right) \tag{IV.1}$$

The terms appearing in that expression are usual dimensionless parameters used in fluid mechanics. They are described in the following paragraphs.

Euler number, $\mathrm{Eu} = \frac{P}{\rho U^2}$**:** The Euler number can be considered as the ratio between pressure force (P) and inertia force ($\frac{1}{2}\rho U^2$). Euler number can depict the pressure loss due to friction in a duct when P is chosen as the pressure drop between two points in the duct.

Reynolds number, $\mathrm{Re} = \frac{\rho U D}{\mu}$**:** The Reynolds number is related to the ratio between viscous forces and inertial forces. It depicts the state of the flow. When $\mathrm{Re} > 5 \cdot 10^3$, the flow can be considered as fully turbulent.

Strouhal number, $\mathrm{St} = \frac{D}{U\,t}$**:** The Strouhal number gives information about oscillating flow mechanisms induced by structure obstacles encountered by a flowing fluid. It can be used to determine vortex-shedding frequency according to flow speed and geometry of the obstacle. In such a case, the time t is equal to the period of a vortex and, since the vortex frequency $f = 1/t$, Strouhal number can be expressed as $\mathrm{St} = \frac{f\,D}{U}$. Strouhal number depends on Reynolds number. It is close to 0.2 over a large range of Reynolds, but the limit of that range and the relation between Strouhal and Reynolds numbers out of this range depends on the system. An investigation of this relation in a system rather similar to the studied one (axial flow in a pipe with inner obstacles) is presented in [95]. This article gives an empirical formula to calculate Strouhal number as a function of geometry and Reynolds number:

$$\mathrm{St} = 0.2420\left(1 + \frac{31.69}{\sqrt{\mathrm{Re}}} - 0.0657\frac{D}{D-d}\right), \tag{IV.2}$$

where d is the dimension of an circular orifice placed in a channel of diameter D. This formula is used in the current work to predict the Strouhal number and, hence, the vortex shedding frequency, which will be experimentally verified afterward.

Geometry coefficient $\frac{L_f}{D}$**:** ratio between the characteristic length in the axial direction (for instance, we can use the length of the main section) and the hydraulic diameter.

The following criterion is not part of the dimensional analysis, but it should be checked beforehand, to ensure that the fluid can be considered as incompressible.
Mach number, $M = \frac{U}{c}$**:** The Mach number is the ratio between the flow velocity and the speed of sound in the considered fluid, c. It indicates whether the flow is subsonic ($M < 1$), sonic ($M \approx 1$), or supersonic ($M > 1$). When M is low enough, the flow can be considered as incompressible[1]. It is commonly stated that compressibility can be neglected when $M < 0.3$ (for instance, in [92]). Moreover, a low Mach number also implies that the flow velocity is neglictible with respect to acoustical velocities [96].

Structure vibrations analysis

Structure vibrations are depicted by the following variables:

- resting position: x_0,
- displacement about the resting position: x,
- Young modulus of the material: E,
- Poisson coefficient of the material: ν_s,
- material density: ρ_s,

[1] Compressibility can be disregarded when analyzing the flow only. This approximation is not possible for the analysis of pressure wave propagation or other acoustic phenomena.

- gravitational acceleration: g,
- characteristic time: t,
- characteristic length: L,
- characteristic diameter: D.

For characteristic time and length, we use the same references as for the flow analysis. For the characteristic diameter, we choose the rod's outer diameter. Concerning the resting position, we can simply decide that $x_0 = 0$.

Like for the flow analysis, Buckingham's theorem is used to describe the system with dimensionless parameters. Once again, commonly used dimensionless parameters are preferred. At the end, it yields:

$$\frac{x}{L} = \Phi_s\left(\frac{L\rho_s g}{E}, \frac{t\sqrt{E/\rho_s}}{L}, \nu_s, \frac{x_0}{L}, \frac{L}{D}\right) \tag{IV.3}$$

Those parameters are described below:

- $\frac{L\rho_s g}{E}$: ratio between volume forces (here, as we consider the structure only, the single volume force is the weight) and elastic forces. In the current case, gravity effects can be neglected, so the whole term can be as well,
- $\frac{t\sqrt{E/\rho_s}}{L}$: time similitude criterion, which is the ratio between the characteristic time and the time for elastic waves to travel the length L,
- ν_s: the Poisson coefficient, which is a property of the material. In the present study, it is considered constant in time and space,
- $\frac{x_0}{L}$: initial distortion. Here, it is null because we consider the initial position x_0 as the null position, *i.e.* $x_0 = 0$,
- $\frac{L}{D}$: geometry coefficient, which depicts the slenderness of the structure.

Fluid-structure analysis

After separate dimensional analyses of the fluid flow and of the structure vibrations, a coupled analysis is carried out. Now, the variables defined in both the flow and the structure analyses are taken into account. Application of Buckingham's theorem yields:

$$\begin{aligned} \frac{u}{U} &= \Phi_c\left(\frac{\rho_f UD}{\mu}, \frac{D}{Ut}, \frac{P}{\rho_f U^2}, \frac{L}{D}, \nu, \frac{x_0}{L}, \frac{t\sqrt{E/\rho_s}}{L}, \frac{\rho_f}{\rho_s}\right) \\ &= \Phi_c\left(\text{Re, St, Eu}, \frac{L}{D}, \nu, \frac{t\sqrt{E/\rho_s}}{L}, \frac{\rho_f}{\rho_s}\right) \end{aligned} \tag{IV.4}$$

Since the initial distortion is null, the term $\frac{x_0}{L}$ can be removed. The previously defined parameters are finally obtained, and an additional one, $\frac{\rho_f}{\rho_s}$, called the "mass ratio" is introduced.

Similarity of vibration amplitudes with Burgreen's correlation

Other methods can be used to compare flow induced vibration phenomena. Some correlations were especially defined for the study of axial flow induced vibrations (some of them are discussed in [97]), such as Burgreen's correlation (the original reference [98] could not be obtained, but the expression can be found in other articles, such as [99]). That correlation was defined, and is commonly used, to study nuclear fuel rod in turbulent flow. The reference system to scale is a cylinder with a Young modulus E_R and a mass M_R, subjected to an axial flow of velocity U_R, density ρ_R and dynamic viscosity μ_R. The mockup reproducing the reference system has Young modulus E_M and a mass M_M and is subjected to a flow of velocity U_M, density ρ_M and dynamic viscosity μ_M. Vibration amplitudes in the real system and in the mockup are the same if the following equation is satisfied:

$$\frac{U_M}{U_R} = \frac{\rho_R^{0.5}\mu_R^{-0.33}E_R^{-0.33}M_R^{0.165}}{\rho_M^{0.5}\mu_M^{-0.33}E_M^{-0.33}M_M^{0.165}} \tag{IV.5}$$

In practice, that equation allows for instance to express the velocity in the mockup, U_M, that is needed to get the same vibration amplitudes as in the real system, as a function of the real velocity U_R and all the mentioned parameters.

Tab. IV.2 presents the values of the dimensionless parameters for the real case and the different mockup design cases. Concerning the mockup design cases, parameters are calculated with the maximum flow rate of the pump ($5m^3.h^{-1}$).

	Real case	Case 1 (Stainless steel, 10 mm diameter)	Case 2 (Stainless steel, 8 mm diameter)	Case 3 (Aluminium, 10 mm diameter)	Case 4 (Aluminium, 8 mm diameter)
Aver. flow velocity (m.s^{-1})	5.0	3.37	3.15	3.37	3.15
Mach	$4.6 \cdot 10^{-3}$	$2.2 \cdot 10^{-3}$	$2.1 \cdot 10^{-3}$	$2.2 \cdot 10^{-3}$	$2.1 \cdot 10^{-3}$
Eu	830	35	40	35	40
Re	$2,3 \cdot 10^{5}$	$5.1 \cdot 10^{4}$	$5.4 \cdot 10^{4}$	$5.1 \cdot 10^{4}$	$5.4 \cdot 10^{4}$
St	0,24	0,22	0,21	0,22	0,21
Vortex frequency, from S_t (Hz)	215	49	39	49	39
Character -istic time (s)	$4.7 \cdot 10^{-3}$	$2.1 \cdot 10^{-2}$	$2.6 \cdot 10^{-2}$	$2.1 \cdot 10^{-2}$	$2.6 \cdot 10^{-2}$
Geometry coefficient	148	54	48	54	48
ν	0,32	0,30	0,30	0,33	0,33
Mass ratio	$7 \cdot 10^{-2}$	$10 \cdot 10^{-2}$	$10 \cdot 10^{-2}$	$10 \cdot 10^{-2}$	$10 \cdot 10^{-2}$

Table IV.2. *Dimensional analysis: dimensionless parameters.*

Table IV.3 presents the targeted and the actual ratio between the flow velocity in the mockup (U_M) and the one in the real case (U_R). The targeted ratio is the ratio given by Burgreen's correlation. If this ratio was achieved, vibration amplitudes in the mockup and in the real case would be similar. The actual ratio is the ratio obtained considering technical constraints of the system, such as the flow rate limit of the pump or the required 25 mm diameter channel to install sensors on the test tube.

Case	Targeted U_M/U_R according to Burgreen's correlation	Actual U_M/U_R
1	2,41	0,93
2	2,55	0,84
3	1,80	0,93
4	1,84	0,84

Table IV.3. *Ratio between flow velocities in the mockup and in the real case.*

Burgreen's correlation is therefore not achieved. However, in such a phenomenological study, Reynolds number can be considered as the most important parameter. If Reynolds numbers are of the same order of magnitude, it means that flows are in similar states. Here, all considered flows are turbulent, since $\text{Re} > 5 \cdot 10^3$ in every case (see Tab.IV.2). Furthermore, those Reynolds numbers imply close Strouhal numbers as well. Oscillation mechanisms are therefore comparable.

It would be better to have close Euler numbers, but the high pressure applied in the real case makes it practically impossible, given safety restrictions. Regarding the mass ratio, it is important to have the same order of magnitude in the real system and the mockup, which is achieved in the four design cases.

The analysis above allows to identify factors that induce most discrepancies between the mockup and the reality: the flow velocity, which is too low, and the channel diameter, which is too large. Increasing the velocity in the mockup would imply higher Reynolds number and higher vortex frequencies (equivalently, smaller characteristic time). However, increasing the velocity needs to increase the flow rate, thus, to change the pump currently installed on the water loop. Reducing the channel diameter would increase the velocity without necessity of a higher flow rate, as well as increasing geometry coefficient, but, as previously stated, it would prevent to mount sensors on the test tube. Making a second channel tube with a smaller diameter or changing the pump can be considered for further experiments, although it is not possible for the first experimental campaign.

In addition to those analyses, some interesting orders of magnitude regarding flow-induced vibrations' amplitude or spectra can be found in the literature. In [97], it is stated that the ratio between vibration amplitudes and structure diameter is "typically less than 10^{-3}" and "rarely exceeds 10^{-1}". Those values can help to predict the amplitude and frequency content of the noise we are supposed to measure during experiments with flow. In the same article, the author says (by using several anterior works) that analytical models of the excitation produced by axial flow do not provide reliable results, except in the case of a perfectly quiet flow. He therefore recommends to characterize exciting pressure field by real *in situ* measurements. In [100], a dimensionless spectrum of the drag force exerted on a rod by a turbulent axial flow is displayed, giving an order of magnitude for the expected frequency range of FIV excitation. Based on that, an excitation up to 340 Hz is expected in the mockup.

In addition to those predicted FIV, it should be also noticed that the pump rotation may induce some noise at a specific frequency. At the maximum flow rate of the circulation pump, its rotation speed is 2800 rpm. Therefore, noise at 47 Hz and its harmonics may appear in the measurements.

IV.1.2. Reproduction of the cladding failure

The objective is to generate the failure of the test tube with a pressure that remains below 100 bar, for safety reasons. Moreover, the test tube must have dimensions close to real fuel cladding's dimensions (*i.e.* 9.5 mm outer diameter and 0.6 mm thickness). The closest dimensions that are easily available on the market are 10 mm outer diameter and 0.5 mm thickness.

Several methods can be used to generate a tube failure. The failure can be obtained with a constant inner relative pressure by heating the tube to decrease material strength until it fails. The use of that method is presented in [101] (in french). Since high temperature has to be avoided in our situation, such a method cannot be used. The failure can also be obtained by increasing the mechanical load applied to the tube. It can be achieved by the method called Expansion Due To Compression (EDC), described in [102], or by filling the tested tube with water and freezing it to increase the volume ([103]), or by increasing the pressure of an inner fluid. The latter is the most commonly used technique (for instance, [104], [105], [106]).

To reduce the failure pressure, an initial crack is machined on every test tube. The aim is to generate a failure by crack growth, hence a pressure failure lower than the failure pressure in case of a simple overload on a flawless tube (for an explanation, the reader may refer to [107]). The initial crack also offers the possibility to choose and predict the failure location, because the tube will fail where it is the weakest: at the crack position.

A method to analytically estimate the failure pressure of a cracked tube was found in [108] and is presented in App. C. This method allows to estimate failure pressure as a function of the material properties (fracture toughness, whose definition can be found in [109], and Poisson coefficient), the dimensions of the tube and the dimensions of the initial crack. The results show that a failure under 100 bar with stainless steel or aluminium is possible only with specific dimensional configurations. For instance, for a 10 mm outer diameter and 0.5 mm thickness tube, made of a standard stainless steel (the average fracture toughness of common use stainless steel is 154 MPa), and an initial crack with a depth of half the tube wall thickness, the calculated failure pressure is slightly more than 80 bar.

For safety reasons, it was decided to use water as pressurization fluid. Water is nearly incompressible, thus, it limits energy release and whipping when the failure occurs compared to a compressible fluid such as air. Moreover, water is easily available. It also makes possible to use a pump intended for piping hydraulic tests, which is cheaper and simpler to use and maintain than a gas pump. The chosen model is a manual pump providing a maximum pressure of 110 bar.

IV.1.3. Reproduction of the coolant fluid boiling

To reproduce coolant fluid boiling that is realistic enough to obtain interesting results, heating the rod cladding would be necessary. A feasibility study was carried out and is presented in App. D. Combining a heating system with the cladding failure system and the water loop would result in an exceedingly complex device. Moreover, it would imply safety constraints because of hot water. Since the boiling crisis was only an incidental topic in the frame of this work, it was finally decided not to study it.

IV.2. Description of the instrumentation systems

One of the objectives of the experimental approach is to identify the most suitable measurement devices for the observation of vibration or acoustical phenomena induced by a cladding failure. To this end, various sensors and instruments were tested. These sensors and the associated instruments are described in the current section.

IV.2.1. Accelerometers

Generality about accelerometers

Accelerometers provide a signal related to their own acceleration in a given direction. If correctly mounted on the studied structure, their own acceleration is equivalent to the acceleration of the structure at the sensor position. Single axis and multi axis accelerometers exist. They respectively provide acceleration signal in a single direction and in several directions.

Regarding the current study, accelerometers can be mounted on the test tube and on the outer structure. They can therefore provide direct information about the vibrations of the test tube and the outer structure induced either by the flow, the failure or the fluid pressure wave following the failure. They can also be used to study vibration transmissions between the rod and the outer structure. That phenomenon is of importance regarding the use of such sensors in nuclear environment. Indeed common accelerometers cannot be directly mounted on a real fuel rod in a working reactor, because of radioactivity and high temperature.

There are several technologies of accelerometers, such as piezoelectric, piezoresistive, capacitive or MEMS. The most commonly used is the piezoelectric type. Piezoelectric type was chosen it this work because it offers the best compromise between size, bandwidth and strength. Because the studied structure is small and light, and the available space is narrow, the sensors should also be small and light (otherwise, they significantly influence the response of the structure). The main phenomenon of interest, the failure, is a transient phenomenon. Studying such a phenomenon requires high frequency measurements. Failure tests are destructive tests. Therefore, sensors have to be removed from the failed tube and mounted on the next one for every test. Thus, they have to be strong enough to withstand the repeated dismountings.

Piezoelectric accelerometers consist of a piezoelectric material cell and a damped spring-mass system, both housed in a casing, as depicted in Fig. IV.1. As a consequence, such a sensor has a resonant frequency, which can be tuned by adjusting mass and spring properties. The spring-mass system is designed in a way that the sensor is especially sensitive to a chosen direction (multiaxis accelerometers contain several spring-mass systems). Usually, it is considered that the response of such a sensor is nearly flat up to 20% of the resonant frequency. Over that limit, the effect of resonance on the sensor's response becomes too significant and causes measurement errors. Therefore, a low pass filter should be used to cut the resonant part away and to keep the flat part only. It is recommended to use an analog filter before the amplifier instead of a post-processing numerical filter. Otherwise, amplifier's gain is limited by the level at the resonant frequency, which unnecessarily reduces the level over the frequency range of interest (*i.e.* the flat part of the response) and may cause the Signal-to-Noise Ratio (SNR) to be too low.

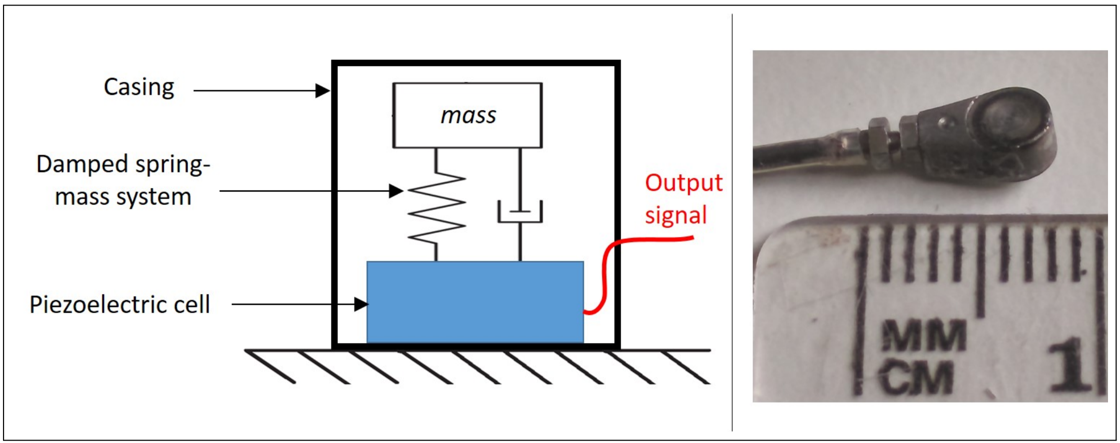

Figure IV.1. *Schematic view of a piezoelectric accelerometer and picture of a A/128/V1 miniature accelerometer by DJB Instruments.*

Piezoelectric accelerometers can work either with Integrated Electronics Piezo-Electric (IEPE), or in charge mode. IEPE sensors contains a charge to voltage converter, so that the charge signal coming from the high impedance output of the piezoelectric cell is transformed into a voltage signal coming from the low impedance output of the integrated electronics. A voltage signal generated by a low impedance source is less distorted by transmission over long and low quality wires, through dirty connectors, and in noisy environment. The drawback of IEPE sensors, in addition to a more complex manufacturing, is that the sensitivity and the full-scale are imposed by the integrated electronics. Another drawback is the impossibility to use such sensors under high temperature, but it is not a concern in the current work. Moreover, the integrated electronics needs power. Power is supplied as constant current by the conditioner and is carried on the same wire as the measured signal. Constant current results in a voltage offset (called "bias voltage"), and the sensor output signal oscillates around this offset. IEPE conditioning instruments include a coupling capacitor to remove the continuous component due to the bias voltage before the amplification of the signal. As a consequence, IEPE instruments cannot measure continuous signals, which cannot be differentiated from the bias voltage[2]. In charge mode, the charge output of the piezoelectric cell is directly connected to the conditioning system. The conversion to a voltage signal, which is necessary for the final acquisition, is achieved by a charge amplifier included in the conditioner. The dynamics of the measurement is limited by the charge amplifier, and not by an integrated electronics like in IEPE sensors. An external charge amplifier usually offers an adjustable dynamics, which is not the case of IEPE circuits. However, in addition to be more sensitive to electromagnetic noise, charge mode amplifiers response depends on wire resistivity and can be distorted by long wires or dirty connectors.

For more information about accelerometers, the reader may refer to [110].

[2]The impossibility to measure continuous signals with IEPE is actually not a major drawback. Indeed, a static or nearly static load applied to a piezoelectric cell induces a drift in the output signal. Although drift can be removed by a proper signal conditioning or processing, other types of sensors, such as piezoresistive sensors, are usually preferred for quasi-static measurements.

Details about the used system

In this work, miniature IEPE accelerometers (A/128/V1 from DjB Instruments [111]) were chosen. Their bandwidth goes up to 10 kHz, which is the highest that could be found on miniature accelerometers market. A four-channels analog IEPE conditioner was used (LHP/4/10 from DjB Instruments), including programmable amplifiers, high- and low-pass filters. This system has an overall bandwidth of 0.1 Hz to 98 kHz. The output of the conditioner is analog signal. Thus, it was connected to the USB oscilloscope described in Sec. IV.2.5.

IV.2.2. Acoustic Emission

Generality on AE sensors

Several types of sensors are available to measure AE waves ([112]). The most common type, which is the one used in the present work, is piezoelectric sensors. Piezoelectric AE sensors are relatively similar to accelerometers. The main difference is that, in AE sensors, the piezoelectric cell is not fixed to a damped spring-mass system. There is only an homogeneous material, called backing, fixed to the back of the cell and filling the cavity, in order to damp resonances of the sensor's cavity and of the cell (see Fig. IV.2).

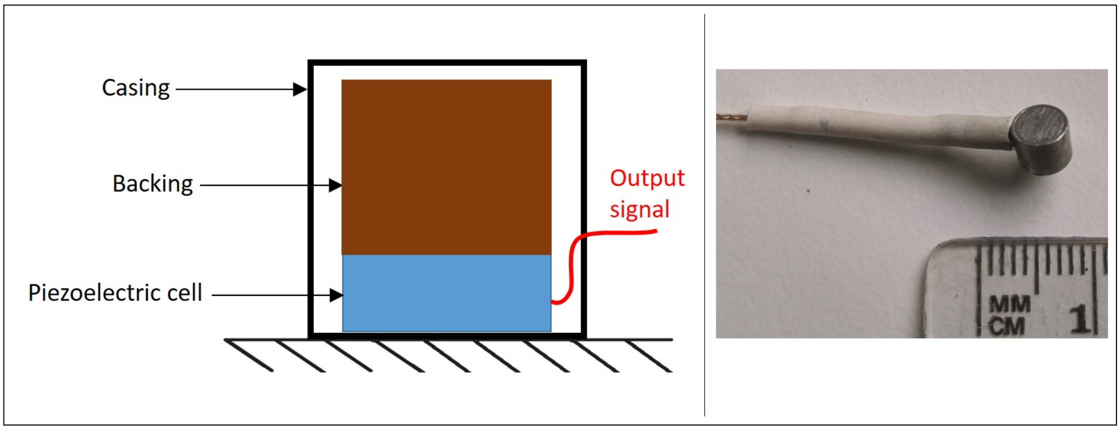

Figure IV.2. *Schematic view of an AE sensor and picture of a PICO sensor by Physical Acoustics.*

Contrary to accelerometers, AE sensors are intended to be used in the resonant frequency range. For some applications, when the objective is simply to detect a specific phenomenon, resonance of the sensor is wanted because it can improve the sensor's sensitivity to that phenomenon (if the resonant frequency is chosen accordingly with the spectrum of the phenomenon). In such cases, so-called "resonant sensors" are used. In some other cases, the sensor response is wanted to be as flat and as wide as possible, to obtain a signal representative of the waves that actually reached the sensor and to be able to observe different phenomena with various spectra. For that purpose, so-called "broadband sensors" have been designed so that their response is relatively flat even in the resonant frequency range.

A significant drawback of AE sensors is the lack of accurate and meaningful calibration. Even though standards related to calibration methods exist ([113]), it remains unclear what physical value an AE sensor actually measures (displacement, velocity, or acceleration) and to which kind of waves (longitudinal or transverse) a given sensor model is sensitive. Those problems were studied in [86], and some alternative calibration methods were developed ([88], [87]). However, this topic is beyond the scope of this work and neither material nor time resources necessary to attempt alternative calibration methods were available.

Details about the used system

In this work, broadband sensors (Pico from Physical Acoustics - Mistras [114]) have been mainly used. A resonant sensor (D9215 from Physical Acoustics - Mistras, [115]), similar to the sensors used in a real research reactor was also used in some tests. The obtained measurements were actually processed as high dynamic motion measurements rather than proper AE signals. If we consider AE in its initial definition (*i.e.* small energy release during micro-structural changes inside the material, as explained in Sec. I.2.1.1), no AE could be clearly observed during the tests. The main observed phenomena is related to the dynamic response of the tube to external excitation, induced by the inner fluid pressure release and inner fluid ejection when the failure occurred. AE waves might be superimposed to external excitation response, but AE waves magnitude is very low compared to the one of the waves induced by external excitation. Thus, signals from AE sensors were processed with general methods (presented in the following section, IV.3.3). Usual AE parameters, such as hit count rate, hit duration or rise time, were not used since they are closely related to the source phenomena, *i.e.* micro-structural changes. However, methods referred as "Modal Acoustic Emission methods" ([116]), using guided waves specificity, are closer to the methods used in this work.

During the first experiments, only one amplifier specifically designed for AE measurements was available. This amplifier (2/4/6 amplifier from Physical Acoustics - Mistras, [117]) included a high pass filter and an anti-aliasing analog filter, with respective cutoff frequencies of 20 kHz and 1 MHz. To perform measurements with four sensors, generic instrumentation amplifiers were used (USB-BP-S1 from Alligator Technology, [118]). Those included a pass-band filter with an overall bandwidth of 1 Hz to 200 kHz. Gain and filter were fully programmable. In this document, specific AE amplifiers are referred as High Frequency (HF) amplifiers, and generic instrumentation amplifiers as Low Frequency (LF) amplifiers, although 200 kHz is a rather high frequency compared to usual measurement methods in the field of structural dynamics.

At the very end of the first experimental campaign, four additional HF amplifiers could be purchased. Therefore, a single test was performed on the first experimental device with several HF amplifiers, to compare it with the previous tests done with LF amplifiers. Tests with the LF amplifiers showed that enough information is contained under 200 kHz. However, HF amplifiers showed a significant amount of energy between 200 and 500 kHz. Over 500 kHz, the energy is negligible. As shown in Sec. IV.4.3, HF amplifiers seem to offer slightly better results in source localization.

IV.2.3. Strain gauges

Generality about strain gauges

Strain gauges are used to measure strain on a surface, by using piezoresistive effects. A strain gauge consists of a thin metallic foil, fixed on a flexible substrate. When the foil is strained, its electrical resistivity varies. Thus, by connecting the foil to a system that measures its resistivity, and by bonding the substrate to an object, it is possible to measure strains on the object. To efficiently measure the resistivity value of the gauge, it is connected to a Wheatstone bridge. One or several branches of the Wheatstone bridge can consist in gauges, and the other are simple electrical resistors. While Wheatstone bridge circuit is the most commonly used, other gauge measurement techniques exist. Further details and explanations can be found in [119].

Although strain gauges were initially designed for static measurement, they are commonly used for dynamic measurements ([65], [120], [121], [35]). The bandwidth of a strain gauge depends on its grid length (the grid refers to the measuring area of the gauge). A strain gauge can theoretically detect wavelength down to two times its grid length. Under that limit, a part of the grid is compressed while the other is elongated and, as a consequence, resistivity variation of the gauge does not provide reliable information anymore. Practically, some additional phenomena occur and make the accurate estimation of a gauge response more complex. This topic is investigated in [122]. An important conclusion of that work is that a 3 mm grid gauge can be used up to 300 kHz.

Strain gauges have a lot of advantages: they are relatively cheap (compared to accelerometers for instance), they are technologically simple, they have a wide bandwidth and a flat response. If correctly applied, they can give reliable information about the measured phenomena (direction of the strain or types of waves, for instance), they are flexible and can therefore be applied on structures with particular shapes (such as small diameter tubes). However, they also have drawbacks: they are very sensitive to temperature changes, they are not as strong as metal-housed sensors, the measured signal is a differential voltage, and the resistivity variation of the gauge and the voltage output of the Wheatstone bridge are usually quite low (of the order of some mV). As a consequence, great care must be provided to the instrumentation: the Wheatstone bridge should be regularly balanced to compensate temperature effects, excitation voltage should be carefully adjusted because a too high voltage can heat the gauge and even make it melt, low-noise wires and instruments should be used to protect the low voltage signal, instruments with differential inputs are necessary. An additional drawback is that strain gauge bonding is a complex operation, and, once bonded, a gauge cannot be removed and applied to another surface. This drawback is of importance in the case of repeated destructive tests.

Details about the used system

Two sizes of strain gauges were tested: 6 mm and 0.8 mm. A homemade Wheatstone bridge, with integrated power supply, was built and connected to analog filters and amplifiers. Later, a full conditioner and ADC system with built-in Wheatstone bridge (SIRIUS from DeweSoft) was purchased. The advantage of the homemade system was its bandwidth up to 500 kHz. The commercial system reaches 100 kHz. However the resulting

SNR with the homemade system was quite low compared to the one obtained with the full commercial system. If necessary, some improvements of the homemade system may enable it to provide less noisy signals, such as the use of shielded and differential connectors and wires (currently, BNC connectors are used), higher quality resistors, and a properly manufactured printed-circuit board instead of a prototype printed board.

IV.2.4. Fluid pressure sensors

Most common types of pressure sensors, for the pressure range of interest in this work (from 1 to 100 bar), are piezoelectric and piezoresistive. The main practical differences between piezoelectric and piezoresistive pressure sensors are related to the bandwidth. Generally, piezoelectric sensors have a wider bandwidth than piezoresistive. However, piezoelectric sensors are less suitable than piezoresistive sensors for static or quasi-static measurements, for the same reason as the one mentioned in Sec. IV.2.1 about accelerometers. As a consequence, piezoelectric pressure sensors are rather used to study transient or oscillating phenomena, and piezoresistive sensors are preferred when a constant or slowly varying pressure has to be measured.

In the presented work, both types of sensors are used. Piezoelectric sensors are used to measure pressure fluctuations in the surrounding flow and a piezoresistive is used to measure the pressure inside the test tube.

An important aspect of pressure sensors mounting should be noticed. To measure the wall pressure inside a pipe, pressure sensors are usually screwed to the outer wall of the pipe, with the sensor head pointing toward the inner wall and the sensor body staying outside (see Fig. IV.3). Recessed-mounting and flush-mounting are possible. In the first case, the sensor head is placed in a cavity between the inner and the outer wall of the pipe, it is recessed from the inner wall. A small orifice connects the sensor cavity to the inner fluid. In the second case, the head reaches the inner wall and should be aligned as perfectly as possible to avoid flow disturbance. Flush-mounting is more suitable for dynamic measurements because recessed mounting induces resonance effects of the orifice and the cavity, which form a Helmholtz resonator, as explained in [123].

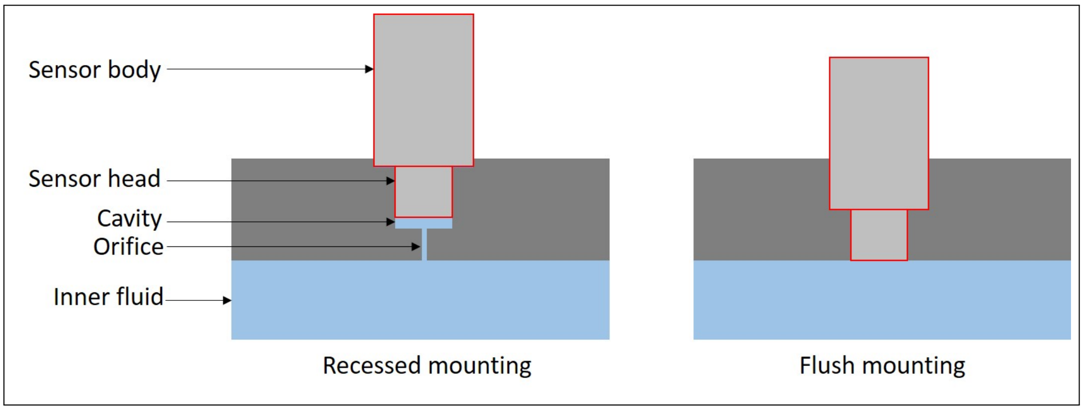

Figure IV.3. *Pressure sensor mountings.*

Details on the used piezoelectric pressure sensors

The aim of these sensors are to analyse the transient effects of the cladding failure. It is expected to detect precursor waves (this phenomenon is described in Sec II.3.1), primary waves and their reflections. Large dynamics is necessary to detect primary waves and not to saturate at primary waves arrival. A wise choice would be to use a sensor whose highest admissible pressure is the highest pressure that can be found in the whole system (*i.e.* the failure pressure of the test tube). The absolute pressure limit is therefore 110 bar, considering a maximum relative failure pressure of 100 bar (estimation based on RUPTUBE results, presented in Sec IV.4.1), surrounding water pressure at 5 bar and an additional safety margin of 5 bar. That sensor should also have a good enough sensitivity to detect precursor waves, and a wide bandwidth to have a good description of transient phenomena. A simulation was performed using a model of the mockup and the computation code Europlexus (EPX) (with the method presented in Chap. III) to obtain spectra of pressure signals at some points in the system and estimate the frequency range of interest. It showed that a bandwidth from 0.1 to 100 kHz would be relevant. In addition to that, the sensor head has to be small enough to be flush-mounted on the external tube of the mockup without troubling the flow. Resulting specifications are presented in Tab. IV.4.

Full scale (bar)	Resolution (bar)	Bandwidth (kHz)	Max. head diameter (mm)
0-110	0.01	0-100	10

Table IV.4. *Initial specifications of piezoelectric pressure sensors.*

Six models from three different producers were identified. Although those models are the closest to the specifications, they do not reach all of them. Their technical characteristics are given in Tab. IV.5.

Producer	Model ref.	Full scale (bar)	Sensitivity (mV/bar)	Resolution (equivalent electronic noise in bar)	Bandwidth (kHz)	Head diameter (mm)
Dytran	2300V5	0-345	14	$5 \cdot 10^{-3}$	100	9.6
Dytran	2300V4	0-70	71	$1 \cdot 10^{-3}$	100	9.6
Kistler	603CBA00350	0-345	14	unknown	100	9.6
Kistler	603CBA00070	0-70	71	unknown	100	9.6
PCB Piezotronics	102B22	0-345	71	$1.4 \cdot 10^{-3}$	100	9.6
PCB Piezotronics	102B04	0-70	71	$1.4 \cdot 10^{-3}$	100	9.6

Table IV.5. *Characteristics of the pressure sensors available on the market.*

No producer offers a sensor with a full scale close to 0-110 bar. Appropriate available ranges are either 0-70 bar or 0-345 bar. With a 0-345 bar full scale, there is obviously no risk of saturation. However, 0-345 bar sensors resolution is not as good as 0-70 bar sensors[3]. EPX simulation results were therefore used to determine with more accuracy the expected pressure range at sensors' positions. They showed that the order of magnitude of precursor waves is 0.01 bar, and that the primary wave peak is between 50 and 60 bar for the different sensor positions.

According to those results, sensitivity of the 0-345 bar sensors is too close to precursor waves amplitude. Measuring such waves might be impossible with those sensors. However, the results also show no risk of crossing the 70 bar limit at the different sensors positions. For those reasons, it was finally decided to use 0-70 bar full-scale sensors.

Details on the used piezoresistive pressure sensors

To measure the average pressure inside the test tube, high frequency response or high sensitivity are not necessary. However, the sensor has to be able to correctly measure static signals. The full scale of the sensor should be at least 0 to 110 bar. Common industrial sensors with built-in electronics are suitable for those needs. For practical reasons, a voltage mode transducer was preferred to a 4-20 mA loop (for explanation about 4-20 mA loop, the reader may refer to [124]). The piezoresistive sensor XMEP3K0PT730 from Schneider Electric was selected. It was powered by a ordinary AC-to-DC power supply. Such an apparatus provides a rather noisy signal and a poor frequency response, but it is enough to get wanted information about failure pressure.

IV.2.5. Choice of the acquisition system

The choice of the Analog-to-Digital Conversion (ADC) system depends on the number and the characteristics of the different measurement devices (sensors and instruments), summarized in Tab. IV.6.

[3]The resolution of the pressure sensors is considered as the smallest pressure fluctuation that can be measured. It is deduced from the electrical noise and the sensitivity, which are given by the producer.

Type of sensors	Bandwidth	Output range of the sensor	Output range of the analog conditionner	Needed resolution	Number of channels	Specific needs
AE	0-1 MHz	± 5 V	± 12 V	14 bit	5	External constant current power supply for the preamplifier
Accelerometers	0-10 kHz	± 5 V	± 12 V	14 bit	4	IEPE instrument
Test tube inner pressure sensor	Not specicified	unknown	0-10 V	8 bit	1	External constant voltage power supply
Pressure fluctuation sensors	0-100 kHz	± 5 V for IEPE sensors, ± 5000 pC for charge sensors	± 12 V	16 bit	6	IEPE or charge instrument
Strain gauges	0-300 kHz	~ 10 mV	± 5 V	16 bit	2	Differential voltage measurement

Table IV.6. *Acquisition needs*

Two types of ADC were chosen. The first type is a general use oscilloscope (HS6 USB oscilloscope from TiePie) and could be used with AE, accelerometers instruments and the piezoresistive pressure sensors for the test tube inner pressure. This system was selected for its great versatility, its relatively good resolution (14 bits) and sampling rate (100 MHz), its low cost, and the possibility to synchronize several systems together. Since this oscilloscope provides four measurement channels, two of them were necessary to get an eight-channel system, which is necessary for the RUPTUBE campaign tests involving AE sensors, accelerometers and the piezoresistive sensor for the test tube inner pressure.

To use strain gauges and piezoelectric pressure sensors, another system was necessary. A full system, including an analog conditioner and an ADC, was chosen. This system (SIRIUS, from DeweSoft) can be used with IEPE or charge mode piezoelectric sensors and also includes built-in Wheatstone bridges for measurements with strain gauges and piezoresistive sensors. It can measure simple voltage as well. Despite its versatility, its bandwidth is limited to 100 kHz, which is smaller than the theoretical bandwidth of the strain gauges, but still appropriate for the pressure sensors. The system has a resolution of 24 bits.

IV.3. RUPTUBE: characterization of the setup

The RUPTUBE experimental device was designed prior to the final mockup, as a tool to test and validate choices related to failure generation technique and instrumentation. Experiments carried out on that device consisted basically in generating tube failure and recording the vibration effects with several sensors installed on the device.

IV.3.1. Introduction

The first objective of the RUPTUBE (*RUPtures de TUBEs*, "tubes failures" in english) experimental campaign is to check the feasibility of the technical solution for tube failure generation, and experimentally estimate the failure pressure of tubes of various materials (aluminium, stainless steel, PMMA) and dimensions. The considered technical solution for failure generation is an inner pressurization of the tube. Details about this solution were given in Sec IV.1.2.

A second objective is to test different acoustic or vibration instrumentation systems to detect and localize the failure. The experimental campaign was also the occasion to record vibration and AE signatures of failures on various tube samples, which can be useful in the frame of the current study as well as in further works.

Two series of tests were carried out, the first one focused on the failure pressure estimation objective and the second one on the instrumentation tests. The current section presents the design of the RUPTUBE device, the experimental plans and protocols, and the results.

IV.3.2. The device

Technical specifications of the RUPTUBE device are to hold the tested tube and to allow filling and pressurization of the fluid inside the tube. It has to enable the operator to physically access the outer surface of the tube to install different kinds of sensors (before or after the pressurization and the failure; the physical access during pressurization is not necessary). Moreover, the surface must be visible to enable optical measurements with a laser vibrometer and a high-speed camera. It also includes a protection of the surrounding instruments and operators from water projection, tube pieces projection and tube whipping.

The device consists in two flanges (made of stainless steel blocks), linked by four threaded rods. The tested tube is mounted between the two flanges and connected to them by various size adaptors. Different adaptors allow the use of tubes of different diameters and ensure water tightness of the connections. On one flange, called "inlet flange", a fitting is mounted to allow connection with the pump. A pressure sensor is placed between the pump and the inlet flange to record the pressure in the pressurization system. A degassing valve is mounted on the other flange, called "outlet flange". The flanges are designed so that fluid can go from the pump into the tube and then to the degassing valve. That valve is necessary to evacuate the air from the system before the pressurization and to avoid the risk related to compressible fluids. The whole system is designed to be totally tight under an inner pressure up to 110 bar (assuming an outer pressure of 1 bar). The device's structure allows physical access to the tube, however, during pressurization, transparent PMMA shields are placed around the device, making it physically inaccessible.

Fig. IV.4 shows a global view of the device. Fig. IV.5 shows a cutaway view of the connections between a flange, an adaptor and the tube. A picture of the setup with the device, the pump and the assembled transparent shields is given in Fig. IV.6.

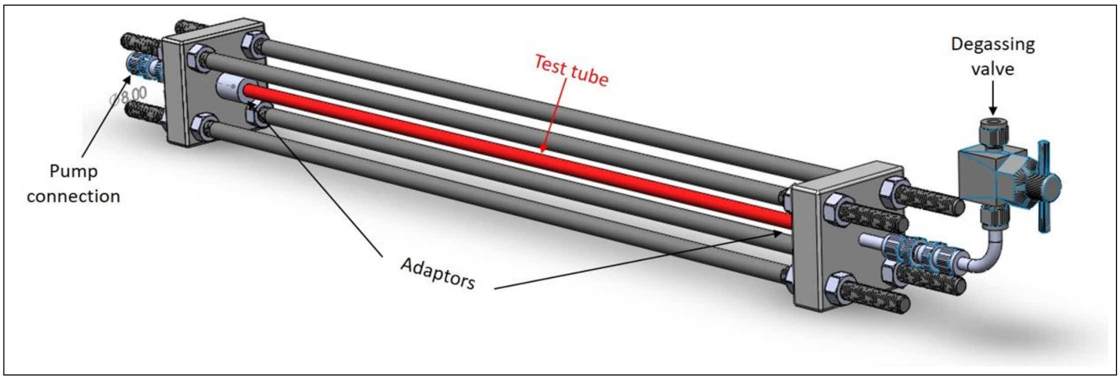

Figure IV.4. *View of the RUPTUBE device*

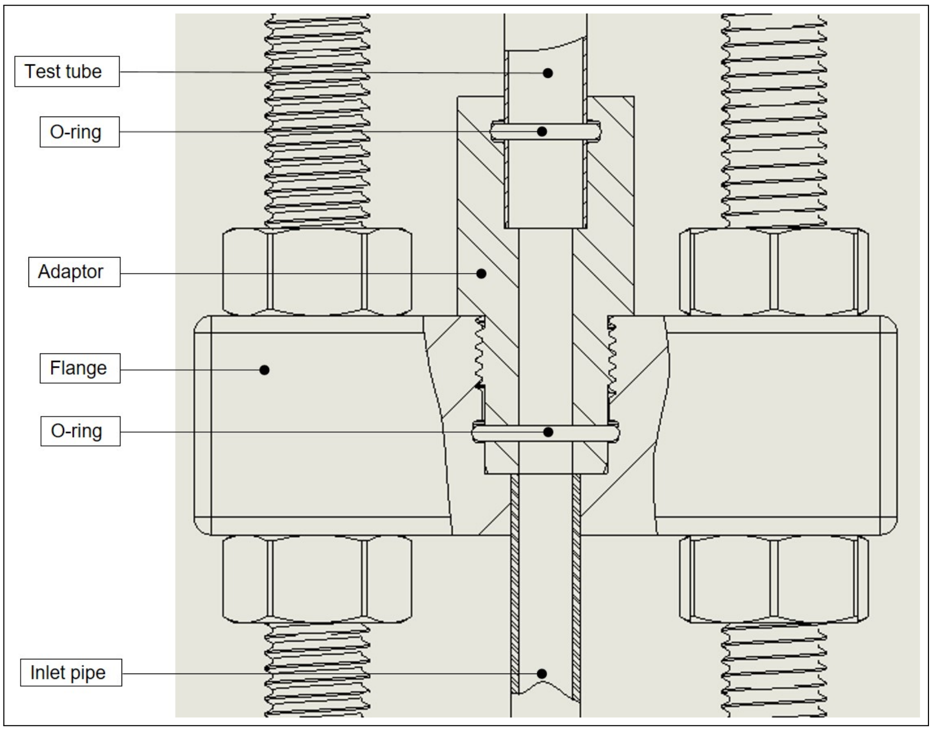

Figure IV.5. *Cutaway view of a flange with an adaptor and an end of the tested tube*

Figure IV.6. *Picture of the setup, from the foreground to the background: the device, the pump, the transparent shields assembled by an aluminium structure.*

Allowed dimensions for the tested tube are 6, 8, 10 or 12 mm external diameter, and a length from 30 to 800 mm. There is no restriction on the inner diameter and the material.

Technical drawings of every part of the device can be found in App. K. A complete technical description of the device is given in the specifications [125] (in french).

IV.3.3. Signal measurement, acquisition and processing methodology

IV.3.3.1. Measurement and acquisition parameters

In order to get usable signals, measurement and acquisition parameters must be carefully chosen. Before the acquisition, signals are processed by the analog conditioning system. This system includes filter(s) and amplifier(s). Analog filters have two purposes: reducing the signal level of unwanted frequency ranges (to remove noise or sensor resonance, for instance), and reducing the signal above the so-called Nyquist frequency [4]. In the first case, the filter can be a band-pass, high-pass or low-pass filter, depending on its actual purpose. In the second case, it is generally a low-pass filter, although it can be a band-pass filter. The purpose of an amplifier is mainly to enhance the SNR, by amplifying the measured signal. The amplifier enhances the SNR only in regard to electronic, electromagnetic and quantification noises that appear after the amplifier. The noise that is already present in the signal as it reaches the amplifier will be amplified as well as the wanted part of the signal. Another purpose of an amplifier is to provide an impedance adaptation between the sensor output and the acquisition system input.

[4]The Nyquist frequency, f_N is equal to the half of the sampling frequency, f_S. It is the highest frequency of a numerical signal sampled at the frequency f_s. If an analog signal containing frequencies higher than $f_N = f_S/2$ is sampled at f_s, it will result in an aliasing phenomenon, so a distortion of the signal.

Resolution and sampling rate are the main parameters of the ADC system. Resolution is the number of bits used to digitize the signal. The more bits are used, the larger the dynamic range is (the dynamic range is the ratio between the highest and the smallest signal amplitude). Several types of quantification method exist and exhibit specific relations between resolution and dynamic range, but this topic is out of scope of the present study. Especially when measuring shock phenomena, it is wise to use the best resolution available. TiePie's HS6 USB oscilloscope offers a maximum resolution of 14 bit. That resolution was used for all the measurements performed with this ADC.

The sampling rate determines the highest frequency of the signal, as previously explained. Therefore, the spectrum of the signal of interest must be predicted beforehand. If reliable prediction is impossible, a too high sampling rate is better than a too low sampling rate. If the initial sampling rate is too high, the signal can be down-sampled afterward. If it was too low, lost information cannot be retrieved. However, a high sampling rate also implies larger file size. In any case, the sampling frequency must be higher than twice the highest frequency of the signal to acquire to satisfy the Nyquist-Shannon condition. To have an accurate description of transient phenomena, a higher frequency is more appropriate.

Failure-induced signals are broadband and cover the whole bandwidth of the different analog conditioners. That is why sampling frequencies are chosen according to the conditioners' bandwidths. The highest frequency of the AE amplifiers is 1 MHz, so the sampling frequency should be of at least 2 MHz. A sampling frequency of 5 MHz is finally chosen, because it is more appropriate to have an accurate description of the studied transient phenomena. When accelerometers are used alone, without AE sensors, the sampling frequency is reduced to 1 MHz (ten times the highest frequency of the accelerometer conditioner, which is 100 kHz). Such a sampling frequency is very high compared to the Nyquist-Shannon condition applied to the 100 kHz bandwidth of the conditioner but, given the relative short length of the measurements, the size of the signals sampled at that frequency still complies with the available memory space.

The high-speed camera has its own conditioner and ADC. Selecting its sampling rate and resolution is a completely different process than with the ADC used for the sensors. Regarding cameras, the term "resolution" refers to the number of pixels in the pictures. Considering a constant size of the filmed area, increasing the resolution results in a better spatial accuracy. Considering a constant spatial accuracy, increasing the resolution results in a wider filmed area. With the used system, only predefined combinations of resolution-sampling rate are available. In those combinations, the higher the sampling rate, the lower the resolution. As a practical consequence, with the RUPTUBE setup, a sampling rate of 11 kHz allows a filmed area of approximately 1 cm^2 and a spatial accuracy of the order of 0.1 mm^2.

IV.3.3.2. Post-processing methods

In this section, the different post-processing methods that are used are briefly introduced. Details on their implementation and their results are presented in details in Sec. IV.4 and in App. J.

Time domain

In this work, time domain analyses are mainly used for the estimation of TDOA between sensors, in order to localize the source of interest (such as the tube failure). Different methods have been tried: the threshold crossing method and the time-domain cross-correlation. Other methods were identified, but the needed time to implement them was not available. Those methods are the semblance methods ([126]), the cumulative Shannon entropy methods ([127]), and the Akaike Information Criterion (AIC, [128]).

Spectrum (frequency domain)

Since the studied events are transient, Energy Spectral Density (ESD) is used to analyze their spectra, following the recommendations given in [129]. Fourier transforms, which are necessary to compute the ESD, are computed by a Fast Fourier Transform (FFT) algorithm.

Time-frequency domain

Time-frequency visualization tools that have been used are Short-Time Fourier Transform (STFT), smoothed Wigner-Ville distribution (classical Wigner-Ville was tried but exhibited a lot of interference when signals contained several transients) and wavelets scalogram. All these tools are presented in [130]. STFT was used for quick previews of the signals, but not for accurate analyses because it does not allow to have good resolutions in both frequency and time domains, which is necessary for studying such non-stationary signals. Smoothed Wigner-Ville distribution is computationally expensive and was therefore seldom used, although it provided an accurate time-frequency representation of the signals. Finally, wavelet transform was the main tool used for time-frequency visualization. Wavelets scalograms were generated using the Continuous Wavelet Transform (CWT) implemented in Matlab [131]. Because of redundancy of the CWT, it provides overcomplete data. However, as it is used for visualization purpose only, that property is not a problem. To separate specific signal components and denoise signals, Discrete Wavelet Transform (DWT) is used.

Empirical Mode Decomposition (EMD) method (described in [132], briefly introduced in App. A) is also used to extract signal components. This method decomposes a signal in a set of independent functions, called Intrinsic Mode Function (IMF). In some cases, IMF are related to different events or to different modes (structural vibration modes as well as guided wave propagation modes) related to a single event. Here, it is expected that EMD performed on AE sensor signals (in high frequency range) exhibit different guided wave modes and EMD performed on accelerometer signals depict structural vibration modes, both excited by the failure.

Prony analysis were also tried. This method can help to determine eigenfrequencies and modal damping of structure vibration modes excited by a pulse-like source (*i.e.* when the free response is measured). That method was tested with our results. It provided modes that could be related to first flexural modes which were identified by both theory and other experimental data processing methods (introduced in Sec. IV.3.5.2), but also a large amount of other modes whose frequencies did match neither theoretical natural frequencies nor peak frequencies observed in measured signal spectra. Thus, since results of that method have to be validated by a complementary method, it was finally not actually used in this work. However, it could be useful for further studies (especially regarding accelerometers measurements). It can be especially useful when it is necessary to know damping and amplitudes of the excited modes in addition to their eigenfrequencies, or when the system response has to be synthesized. Such objectives are nevertheless beyond the scope of the current work.

IV.3.4. Preliminary guided wave simulations

Some simple simulations were carried out, with the CIVA software [133] (which solves the guided-wave-related equations introduced in Sec. II.1), to get prior information about guided waves propagation through the tested tubes. The objectives are mainly to check some qualitative assumptions and to get dispersion curves giving wave velocities of the different propagation modes according to the frequency. The first assumption to be checked is that the fastest waves travel with a maximum velocity equal to the theoretical quasi-longitudinal, given by Eq. (II.5) (introduced in Sec. II.1). The second assumption is that dispersion effects imply important discrepancies between displacement histories of different points along the tube. Consequently, displacement histories (or any displacement-related value, such as the velocity or the acceleration) at two different points should not exhibit a similar pattern that is simply shifted in time.

Dispersion curves of a water-filled aluminium tube of 10 mm outer diameter and 0.5 mm thickness are computed. Fig IV.7 shows the group velocities as a function of the frequency of the first guided waves modes. Moreover, the non-dispersive first torsional mode is clearly visible, with a constant velocity of 3100 m.s^{-1}, which is the transversal wave velocity according to Eq. (II.5).

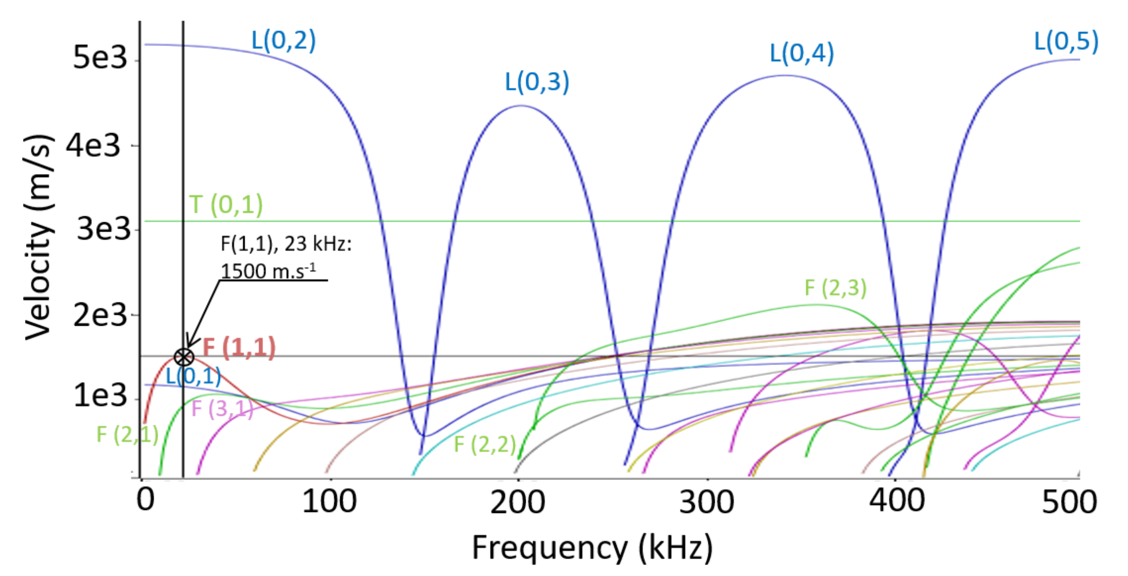

Figure IV.7. *Guided waves simulation: group velocities of the first guided wave modes as functions of the frequency in a water-filled aluminium tube of 10 mm outer diameter and 0.5 mm thickness. L(0,n), T(m,n) and F(m,n) refer respectively to the longitudinal, torsional and flexural guided wave modes, following the terminology introduced in Sec. II.1.*

To check the second assumption, a simulation of wave propagation was carried out, considering a source at 180 mm from the end of the tube. To accurately model the boundary conditions at the end of the tube, which have effects on the wave reflections in the axial direction, as explained in Chap. II, Sec. II.1, it would be necessary to consider the mechanical connections between the tube and the O-rings placed between the tube and the adaptors (as shown in Fig. IV.5), with specific stiffness and damping according to the directions. However, such characteristics are difficult to estimate. Compared to classical conditions (blocked or free), it would add significant complexity to the model, which could not be dealt with by CIVA. Therefore, the following assumptions are made:

- The O-rings are considered as perfectly rigid and the contact area between the O-rings and the circumference of the tube is a line located at the very end of the tube. Therefore, regarding radial direction, the tube can be considered as pinned at both ends,
- The O-rings are greased enough to allow the tube to slide and rotate, therefore, the condition in the axial and orthoradial directions can be considered as perfect sliding connections.

In terms of boundary conditions, those assumptions can defined as follows: $\forall\ \theta$:

$$q_r(x_b, R_{out}, \theta) = 0,$$
$$\sigma_{rr}(0, R_{in}, \theta) = 0.$$

$\forall\ \theta$ and $\forall\ r$:

$$\sigma_{ij}(0, r, \theta) = \sigma_{ij}(L, r, \theta) = 0,\ \forall\ (i, j) \neq (r, r).$$

Since the real source signal induced by a failure is unknown, an arbitrary source signal must be chosen. It was chosen in order to be a pulse-like signal. To this aim, a Hanning shape was used, as shown in Fig. IV.8. The source is punctual and the mechanical load applies in the radial direction only. Fig. IV.9 shows radial displacement histories at 160 mm and 360 mm from the source. As assumed, the signals look different, although some common patterns can be identified, such as the first wave group or the highest peak. The traveling velocity of those two patterns were found to be respectively about 2600 m.s^{-1} and 1410 m.s^{-1}, which indicates that the first one is related to the first torsional mode and the second one is related to the first flexural mode F(1,1).

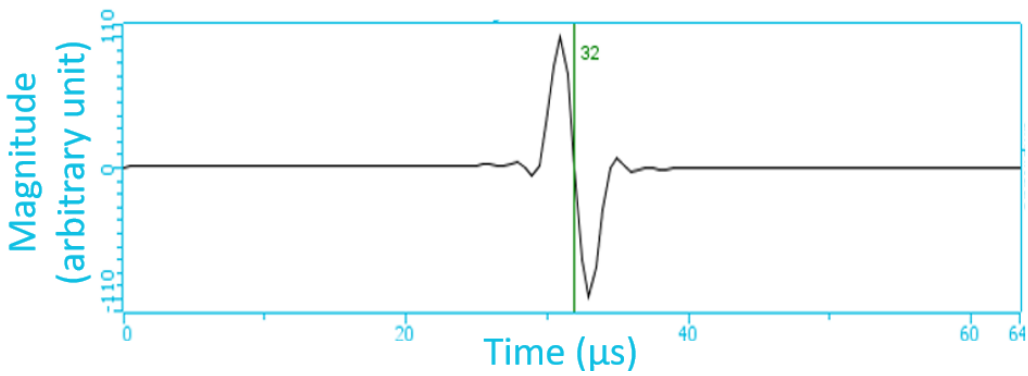

Figure IV.8. *Guided waves simulation: shape of the source signal (CIVA software screenshot).*

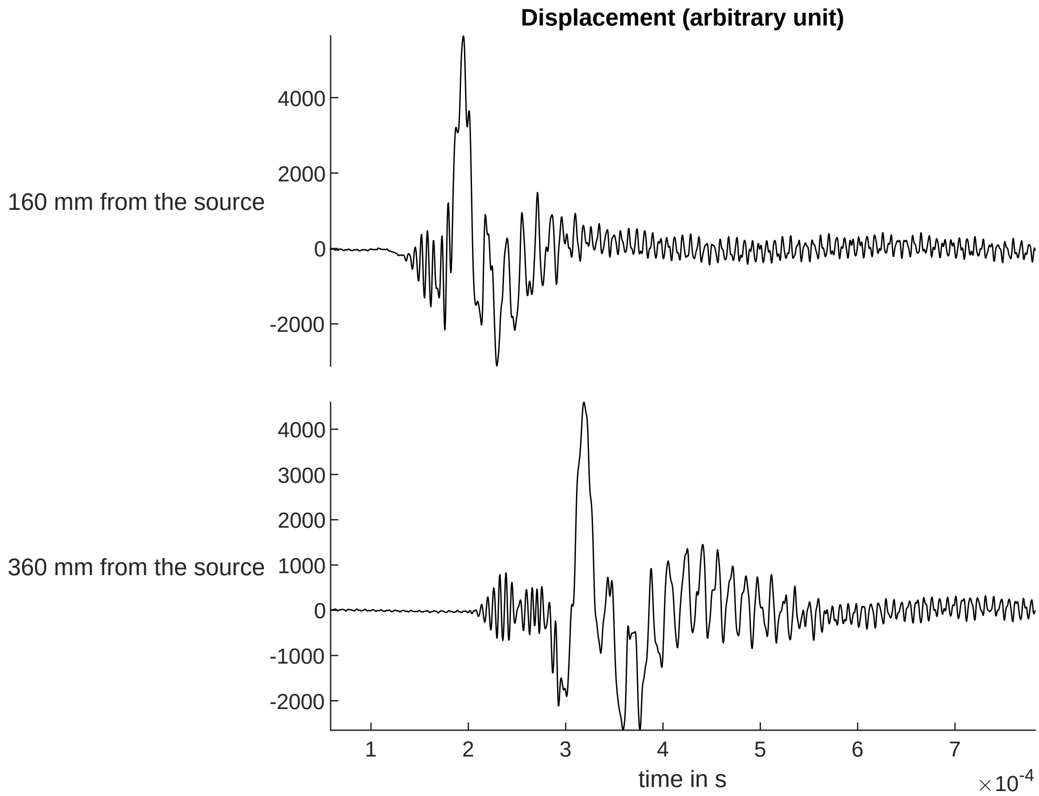

Figure IV.9. *Guided waves simulation: radial displacement histories at 160 mm and 360 mm from the source.*

While the dispersion curve is inherent to the tube's geometry and material and does depend neither on the source properties nor the measurement point, the simulated displacement histories depend on the source signal, the source position and the measurement points. Therefore, dispersion curve provides quantitative information that can be used for the experimental results analysis (although the real tubes properties may differ from the ideal ones considered for the calculations), but the simulated displacements allow only qualitative conclusions, because neither the real source properties nor the effects of the sensor response on the measured signals could be modeled.

IV.3.5. Preliminary tests

IV.3.5.1. Hsu-Nielsen (HN) source characterization

HN source is an artificial source commonly used to check the operation of AE sensors or study AE waves propagation in a structure. It consists in a pencil lead break, with a specific pencil whose shape is defined by standards (in France, the applicable standard is NF EN 1330-9 [134]). As shown in Fig. IV.10, the lead is broken on the surface of the studied structure and forms with that surface an angle determined by the shape of the pencil's end. Such a tool should result in a good repeatability. However, because using this tool on small diameter metal tubes is a delicate task (the lead tends to slip on the tube surface), it was preferred to check the actual repeatability. To this end, several lead breaks were successively done on the same tube, at the same position and recorded with the same sensor, which was not dismounted between the different tests. These signals are recorded with a broadband *Pico* sensor and a HF amplifier and sampled at 5 MHz.

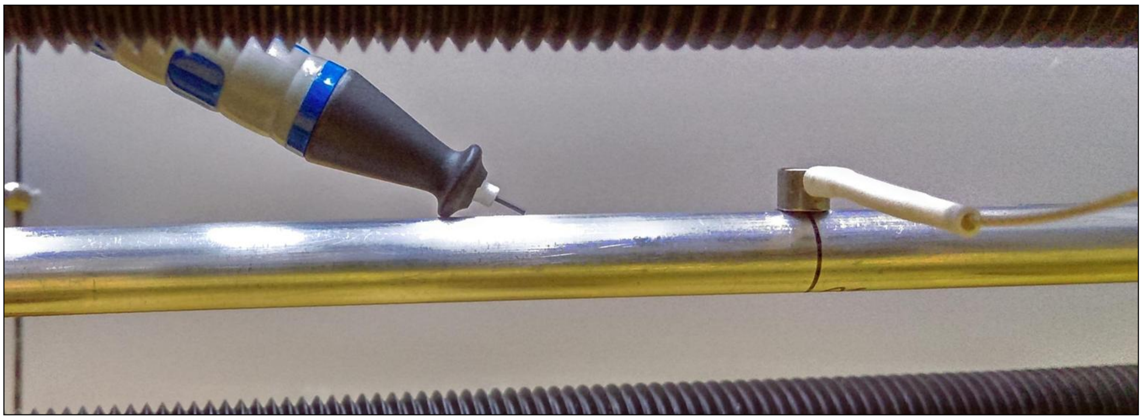

Figure IV.10. *A standardized HN source next to an AE sensor.*

Time domain and time-frequency domain representations of four different recorded signals are analyzed and respectively shown in Fig. IV.11 and IV.12. Here, STFT are used for the frequency analysis, rather than Wavelet analysis, as it provides a clearer overview of the global frequency content of the event and the good resolution provided by CWT is not currently necessary. In addition to that, a comparison in frequency domain is performed with the coherence function, which depicts the degree of linear relationship between the spectra of two signals. One coherence can be computed for each pair of signals (so with four signals, it yields six coherences). For the sake of clarity, only the average of the six coherences is shown in Fig. IV.13.

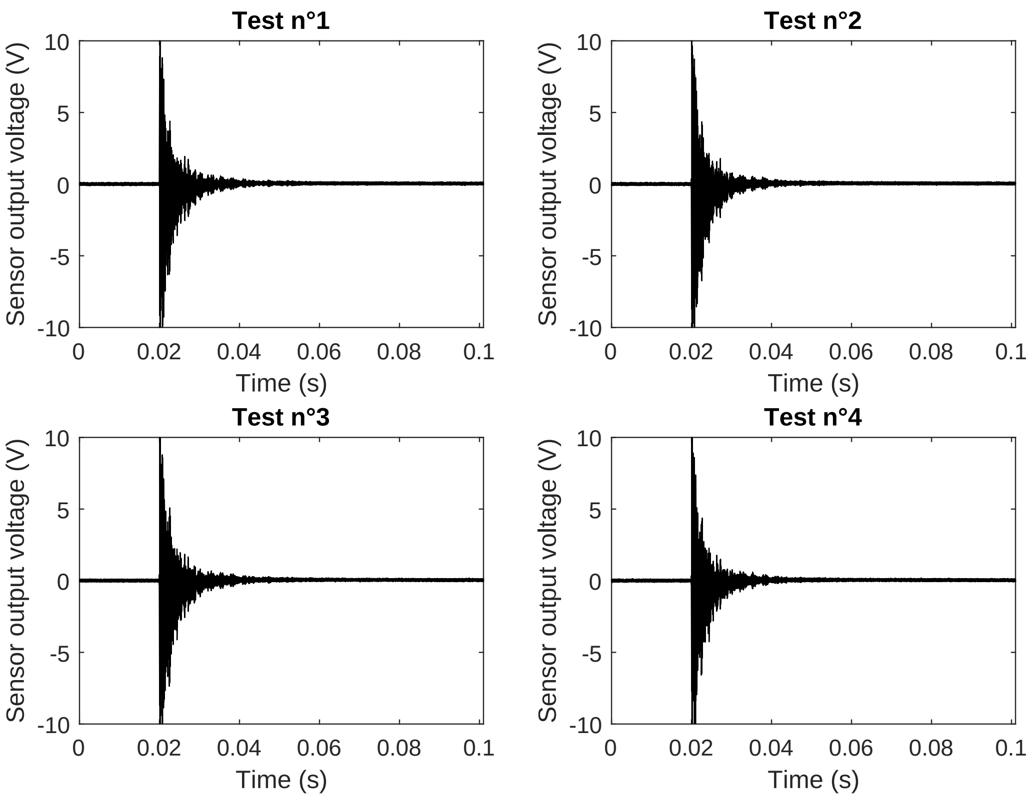

Figure IV.11. *RUPTUBE - HN source repeatability: AE signals of four different tests.*

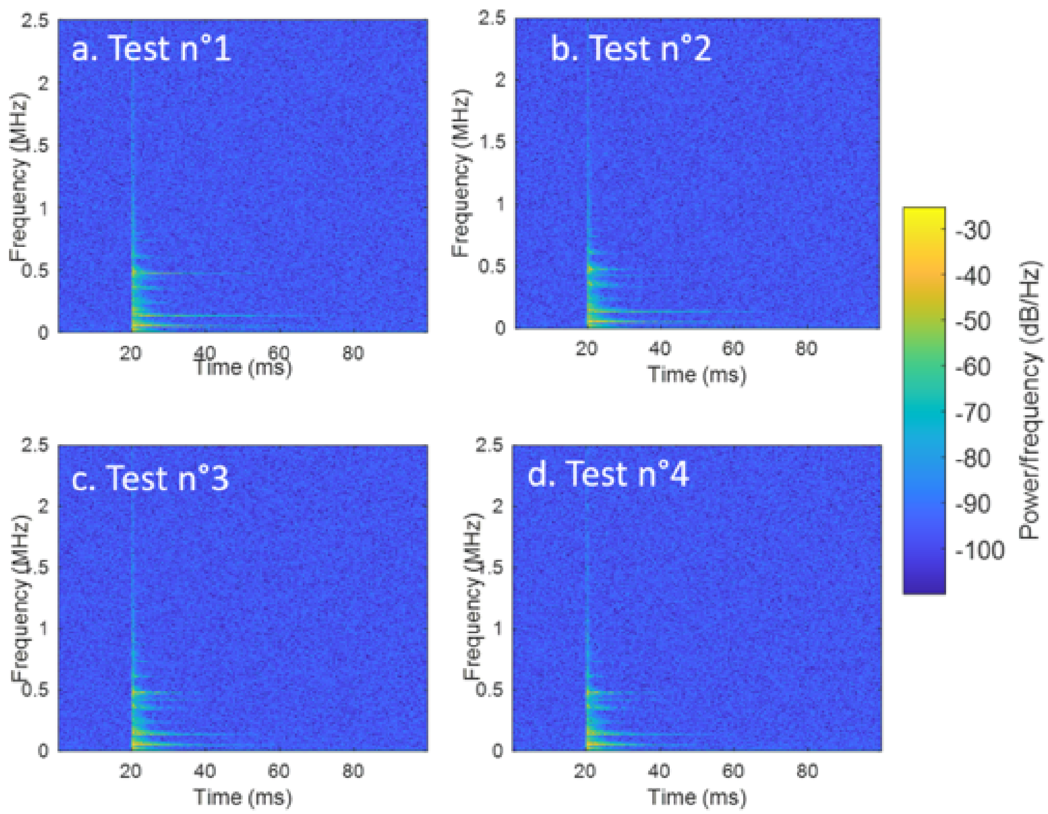

Figure IV.12. *RUPTUBE - HN source repeatability: spectrogram of four different tests.*

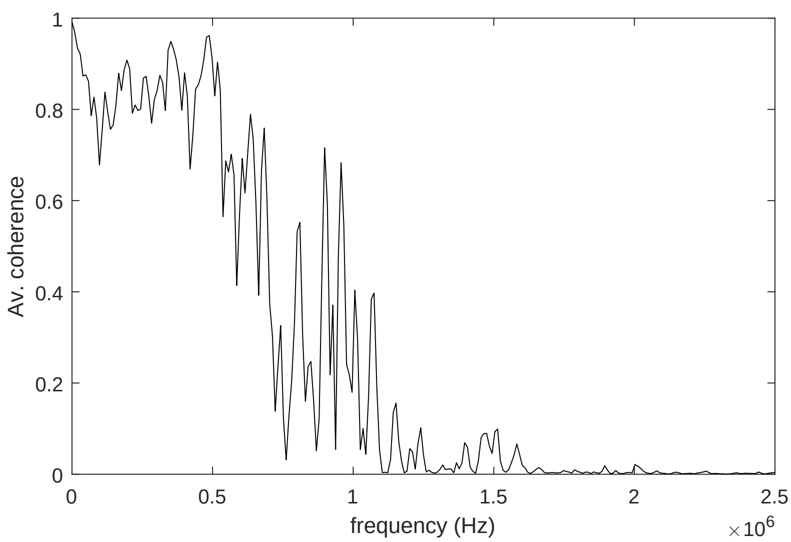

Figure IV.13. *RUPTUBE - HN source repeatability: average coherence between the AE sensor signal of four different tests with the same HN source position.*

Those analyses exhibit a great similarity between the different records. The average coherence is close to 1 up to 500 kHz, decreases between 500 kHz and 1 MHz and becomes very low above 1 MHz. It shows that spectra of the different signals are relatively similar to each other within the sensor bandwidth (up to 750 kHz). A low coherence outside the sensor bandwidth is normal. As shown by the superposition of the signals in Fig. IV.14 (the signals are synchronized, using the maximum value of the cross-correlation between Test 1 and every other test), time history of the signals are almost perfectly overlaid on each other. For those reasons, HN on the test tubes source can be considered as repeatable.

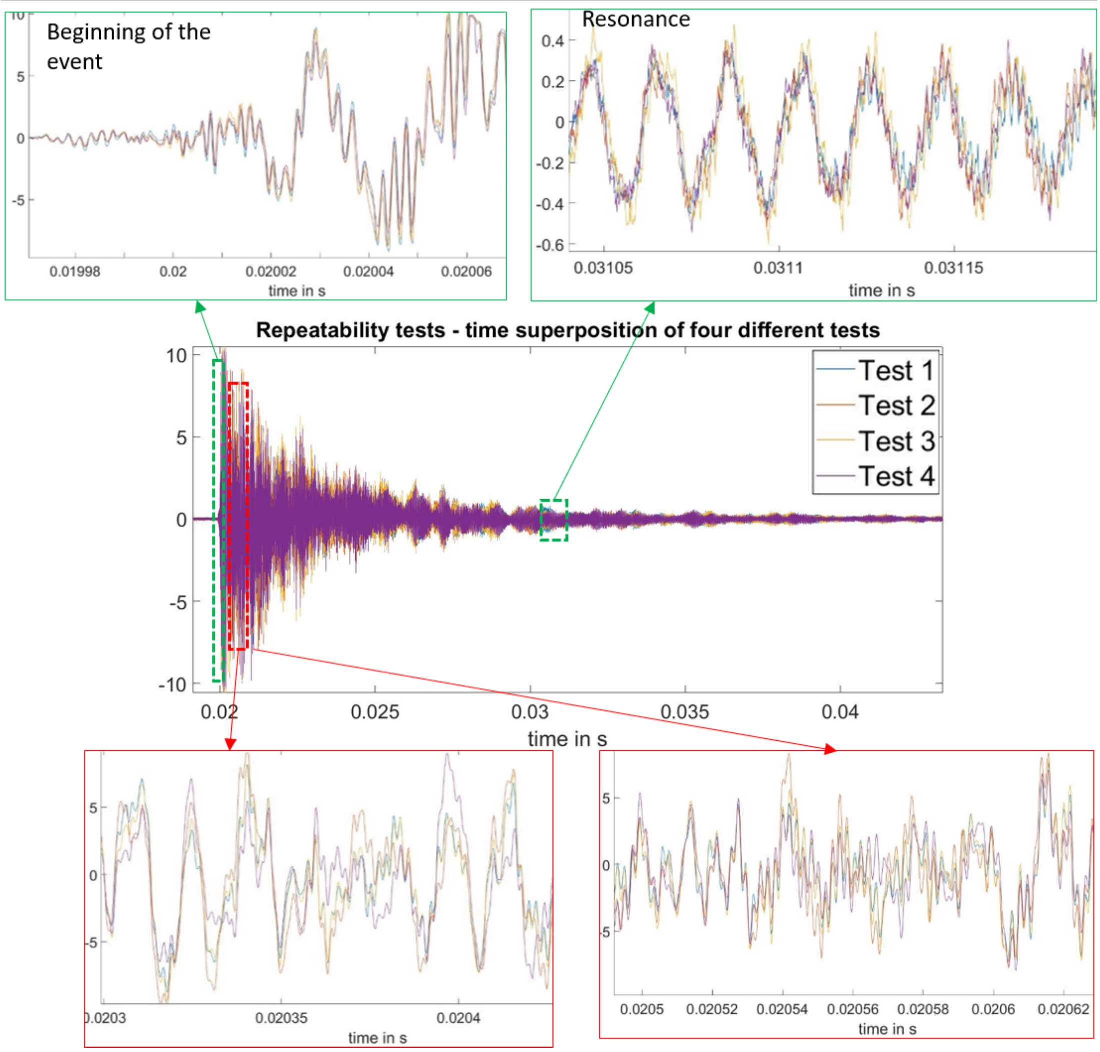

Figure IV.14. *RUPTUBE - HN source repeatability: superimposition of signal histories and magnification views.*

Spectrograms in Fig. IV.12 also provide information about the frequency content of a HN-induced signal. It shows that, even though the initial shock covers the whole available bandwidth, most of the information is contained under 500 kHz. Moreover, high-amplitude and lightly-damped resonances are under 250 kHz. More precisely, in every signal, significant resonance lines are observed at 26, 52, 135, 360 and 470 kHz. It is reminded that the amplifier contains a high-pass filter with 20 kHz cutoff frequency, that is why no significant components are observed under 26 kHz.

Since it was proved that HN source is repeatable, it can be checked if the direction of the pencil has an impact on the measured signal. Given the geometry of the structure, the pencil direction can only be parallel to the tube axis, pointing either in the direction of the sensor (like in Fig. IV.10), or in the opposite direction. It is impossible to produce a lead break when the pencil is not parallel to the tube axis. If the source is perfectly bidirectional, *i.e.* the measured signals are the same whenever the pencil is oriented toward the sensor or in the opposite way, it is possible to estimate the symmetricity of the propagation by breaking a lead in the center of the tube and measuring the propagated signals with two sensors mounted on both sides. To check the directivity of the source, a test is performed with the pencil pointing toward the sensor, and another test with the pencil in the opposite way. Several tests were performed for each lead direction, despite the good repeatability that was already proved. Fig. IV.16 shows these average ESD. Fig. IV.15 shows a time magnification on the superimposition of the signals associated to all the performed tests. It shows a good consistency, whichever the lead direction. Such a consistency can be observed along the whole signals. To compare the spectra, ESD was computed for the signal associated to each test, and average ESD were finally calculated for the two lead directions. Fig. IV.16 shows these average ESD. In addition to that, coherence was calculated for each pair of signals associated to different lead directions. The average of all the coherences is shown in Fig. IV.17 (for the sake of readability, it is displayed in a reduced frequency range from 5 to 10^3 kHz).

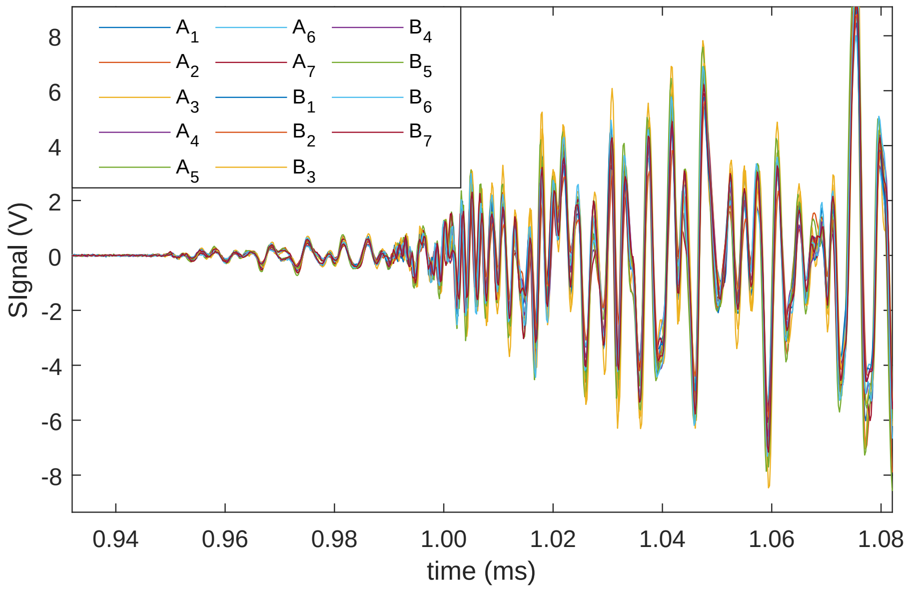

Figure IV.15. *RUPTUBE - HN source directivity: AE sensor signals associated to the two lead positions. Signals from all the tests, with both lead positions, are plotted together. Each color corresponds to a test.*

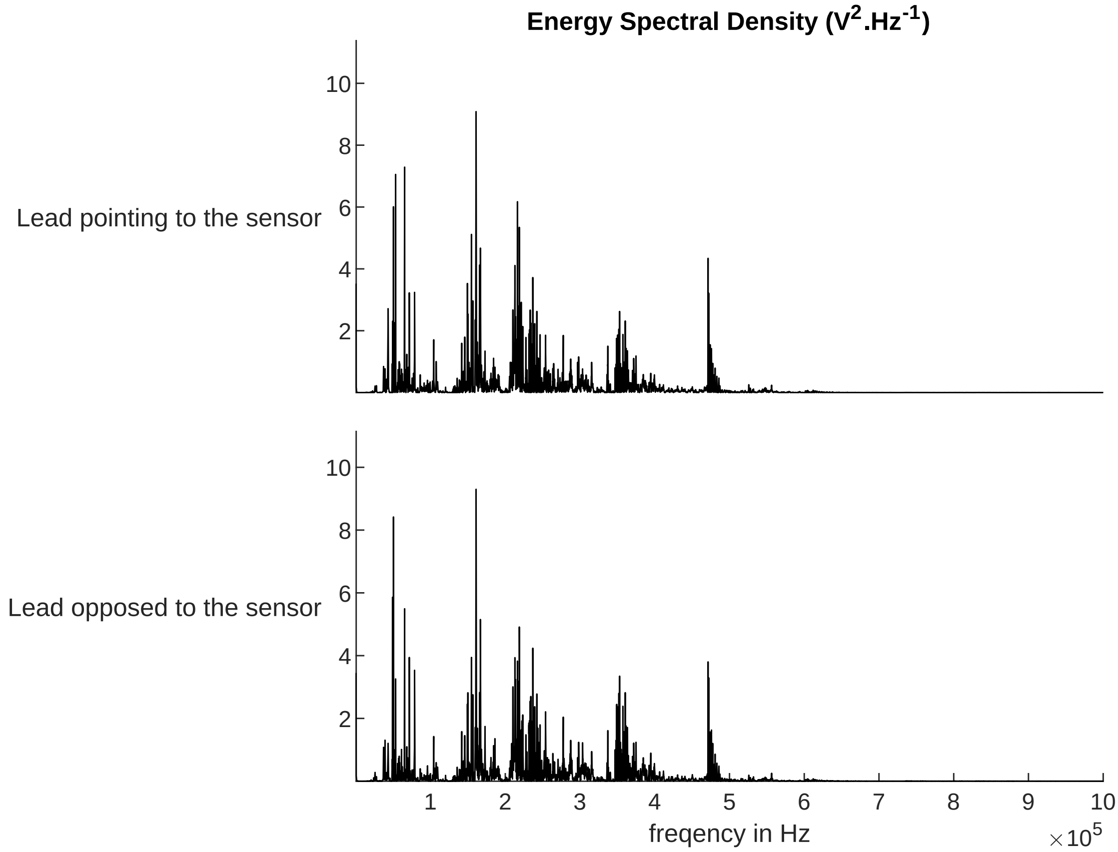

Figure IV.16. *RUPTUBE - HN source directivity: average ESD of the AE sensor signals for each lead position.*

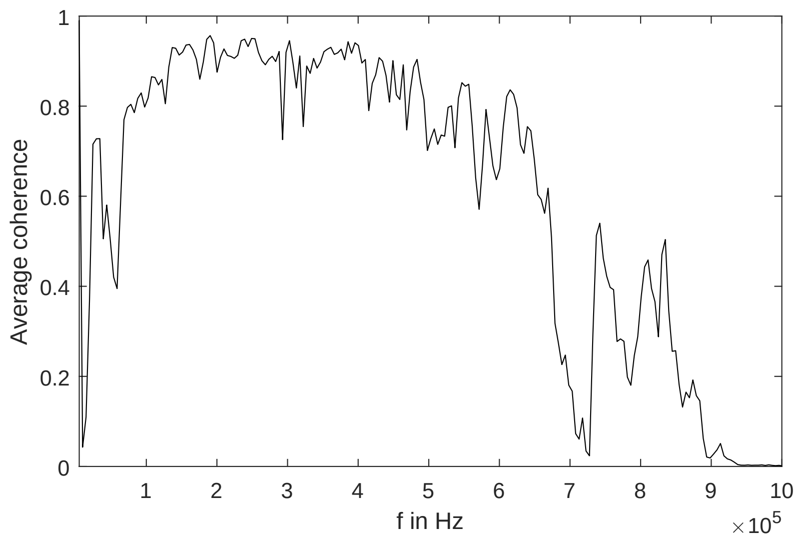

Figure IV.17. *RUPTUBE - HN source directivity: average coherence between AE sensor signals associated to different lead directions*

Those figures show that the direction of lead in relation to the sensors has a negligible influence on the measured signals. The difference between a signal measured when the lead is pointing the sensor and a signal measured when the lead is in the opposite direction is of the same order as the difference between two signals measured with the same lead's direction.

Now, the symmetricity of the propagation can be checked. A lead is broken at the center of the tube instrumented with four sensors, as shown in Fig. IV.18. The signals are shown in Fig. IV.19. They clearly show great discrepancies. Those discrepancies can be due to imperfection in the sensor mounting and, more likely, in-homogeneity in the tube properties, which troubles waves propagation. Therefore, propagation-induced distortion of the signals cannot be accurately determined, because they depend on imperfections in the sensor mounting or in the tube properties that cannot be characterized in the frame of this work. As a consequence, this prevents not only to determine the failure-related source directivity, but also to characterize accurately the source signal.

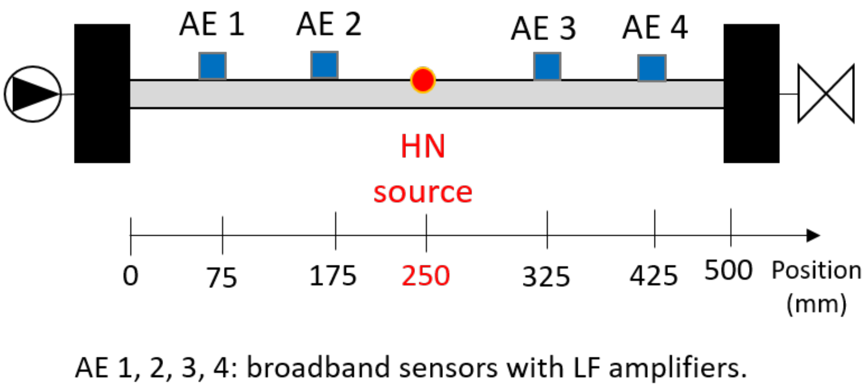

Figure IV.18. *RUPTUBE - Preliminary study on propagation's symmetricity: test configuration.*

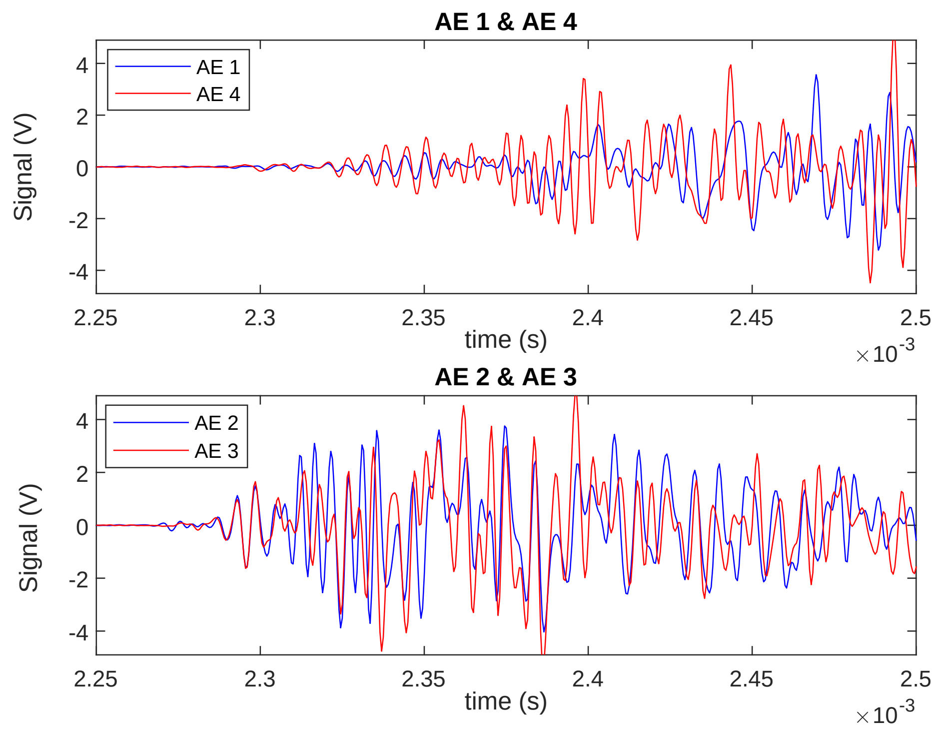

Figure IV.19. *RUPTUBE - Preliminary study on propagation's symmetricity: AE sensor signals.*

IV.3.5.2. Modal analysis

It is considered as necessary to know at least the eigenfrequencies and approximated modal shapes of the first modes of the test tube, prior to the processing of failure tests results. Then, it is expected that the identification of specific modes excited by the failure is possible. Such an identification could provide information about the excitation induced by the failure. For instance, if flexural modes are highly excited, it can show that the failure induces a load in the transverse direction. Identifying the different mode families (longitudinal, flexural, torsional) indicates which propagation phenomena have to be considered and, hence, which wave velocity should be used for source localization. Comparing the resulting amplitudes at the different eigenfrequencies also brings information about the source position, because the excitation of a mode is low if the source is near a node of the mode shape, or high if it is near an anti-node. For the same reason, it would also allow to predict the frequency content of a signal according to sensor positions (the measured amplitude at an eigenfrequency is low if the sensor is near a node of the mode shape and high if it is near an anti-node). Moreover, knowing which mode is excited by the failure before starting the second experimental campaign is of importance to predict how the fluid flow around the rod that will be reproduced in the second campaign can affect failure-induced signal.

In addition to that, some preliminary information about modal parameters could be useful for solving inverse problems for the accurate excitation identification, in the frame of a possible further study.

Generally, modal parameters of a structure are estimated by exciting the structure with a known input source, either a shaker or an instrumented impact hammer. However, during RUPTUBE campaign, neither shaker nor suitable impact hammer was available. An impact hammer was available and tested, but it turned to be unsuitable for the kind of structure tested here. The hammer was too big and heavy, implying many double impacts and a poor coherence in the measurements and finally, unusable data. Therefore, a kind of Operational Modal Analysis (OMA) was attempted. The technique consisted in lightly impacting the tube with a small metal blunt object (a 3 mm Allen key was used). Like in the classical "roving hammer" method, impacts are generated at several points of the structure. The response is measured by four accelerometers distributed along the tube length and mounted in the same azimuth direction. For classical OMA processing methods, such as the ones described in [135], the excitation has to be close to a random signal and uniformly distributed over the structure. In the current case, the source is a punctual impact. The impact is generated at different points, but it is not repeatable, contrary to the HN (which cannot be used for the modal analysis because its low frequency content is too low). Because of its non-repeatability, it is impossible to gather the measurements corresponding to the various impact positions and consider it is equivalent to a uniformly distributed excitation. Indeed, the impact generated at some positions can be stronger than in other positions. As a consequence, another processing method should be employed. Since only the eigenfrequencies and one-dimensional mode shapes are wanted, the processing can be simpler than classical algorithm which are intended to give modal damping and multi-dimensional shapes. Nevertheless, the method has to take into account the non-repeatability of the source that can cause unbalance between the measurements related to the different impact positions.

Before defining the methods, two assumptions must be introduced. Firstly, the impacts differ from each other only in the energy they inject in the tube. The duration and the direction of the impacts are assumed to be always the same. Secondly, the relation between the impact energy and the tube response is linear. A consequence of those assumptions is that for two impacts generated at the same position, the only difference in the spectra of the measured signals will be the total energy. The main idea of the method is to consider a value of the total energy measured by the sensors for each impact and considering that this value depicts the energy injected by the impact. Then, for every impact position, the spectrum of each signal is normalized by the total measured energy. Thus, the effects of the difference in the injected energy are canceled and measurements associated to different impacts can be compared.

For the mathematical description of the method, let's consider four signals $x_j(t)$ ($j = 1, 2, 3,$ or 4) measured by the sensors mounted on the tube during a test (a test corresponds to the generation of an impact at a given position). The total measured energy of the test, E_{tot}, is considered as the sum of each sensor's signal energy, E_j:

$$E_{tot} = \sum_{j=1}^{4} E_j, \tag{IV.6}$$

where E_j is theoretically the integral of the ESD:

$$E_j = \int_0^{f_{max}} |X_j(f)|^2 df, \tag{IV.7}$$

where $X_j(f)$ is the Fourier transform of the signal $x_j(t)$ of the sensor j, theoretically given by:

$$X_j(f) = \int_{-\infty}^{\infty} e^{-i2\pi f t} x_j(t) dt. \tag{IV.8}$$

Practically, with numerical signals of size N, E_j is approximated by:

$$E_j = \frac{1}{N} \sum_{f_{n=0}}^{f_{max}} |X_{dj}(f_n)|^2, \tag{IV.9}$$

X_{dj} is the discrete Fourier transform computed by a "Fast Fourier Transform" algorithm (by the Matlab function "fft" [136], based on the FFTW library [137]). For better reliability, each test should be repeated several times, and thus, X_{dj} in the expression above should be replaced by its average. Here, each test was repeated five times.

Finally, for each test, every sensor's energy is divided by the total measured energy of the test:

$$\tilde{E}_j = \frac{E_j}{E_{tot}}. \tag{IV.10}$$

Therefore, the results of different tests can be compared to each other.

Actually, such a method would be valid if the sensors were uniformly distributed along the tube, which is not the case here (the sensors were deliberately placed in unregular positions so that they do not all fall on the nodes of some mode shapes). In the current configuration, in addition to the sensors on the middle of the tube (at 250 mm from both ends), two sensors are mounted on a half (at 50 and 150 mm from the inlet end) of the tube while only one is mounted on the other half (at 400 mm from the inlet end).

This modal characterization focuses on the [1-10] kHz frequency range. That is why it was carried out with accelerometers only, and without AE sensor.

The tested tube had an outer diameter of 10 mm, a thickness of 0.5 mm and a length of 500 mm. Positions of each impact points and of the four accelerometers are shown in Fig. IV.20.

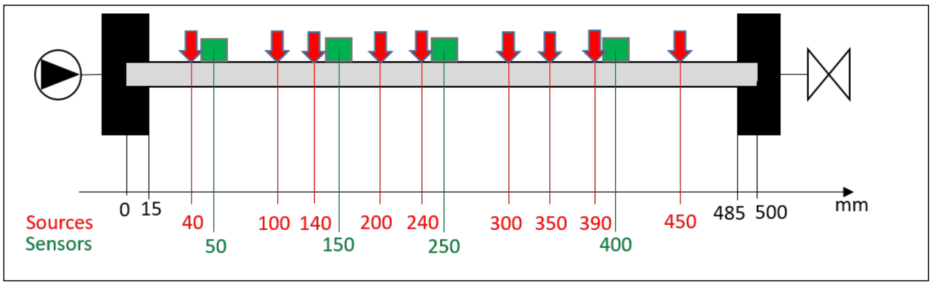

Figure IV.20. *RUPTUBE - Modal analysis: configuration.*

Fig. IV.21 shows all the normalized spectra. For each sensor, the spectra obtained with the different impact positions are plotted according to those positions. It allows to observe the spatial distribution of different frequency peaks featured in the spectra. It can be noticed that those distributions seem to be correlated with the first modes' shapes (up to the fifth modes). Above 2 kHz, the number of points does not offer a good enough spatial resolution to identify the next mode shapes.

To confirm this interpretation, theoretical eigenfrequencies of first flexural modes are calculated for various boundary conditions and are compared to the frequencies of the observed peaks. Initially, theoretical frequencies were analytically estimated, using beam theory applied to the case of a clamped-clamped tube and a pinned-pinned tube (with the formula given in [48]). It was noticed that experimental frequencies seems to be between these two cases. Thus, flexural stiffness at the tube boundaries was considered and the natural frequencies were computed by Finite Element methods. Fig. IV.22 allows the comparison of the calculated natural frequencies and the measured spectra. The spectrum plotted in this figure is actually the average of all the normalized spectra obtained with the described method. Its only purpose is to show all the spectral peaks measured at different positions and with different source positions while keeping the figure clear. The calculated frequencies are given in Tab. IV.7). It shows that, with a specific value of stiffness, the model with elastic boundaries can fit very well the experimental data. The aim of the current work is not to build an exact model of the experimental system, so this track is not further investigated, but the first results highlight the fact that the real boundary conditions neither correspond to exact clamped supports nor exact pinned supports.

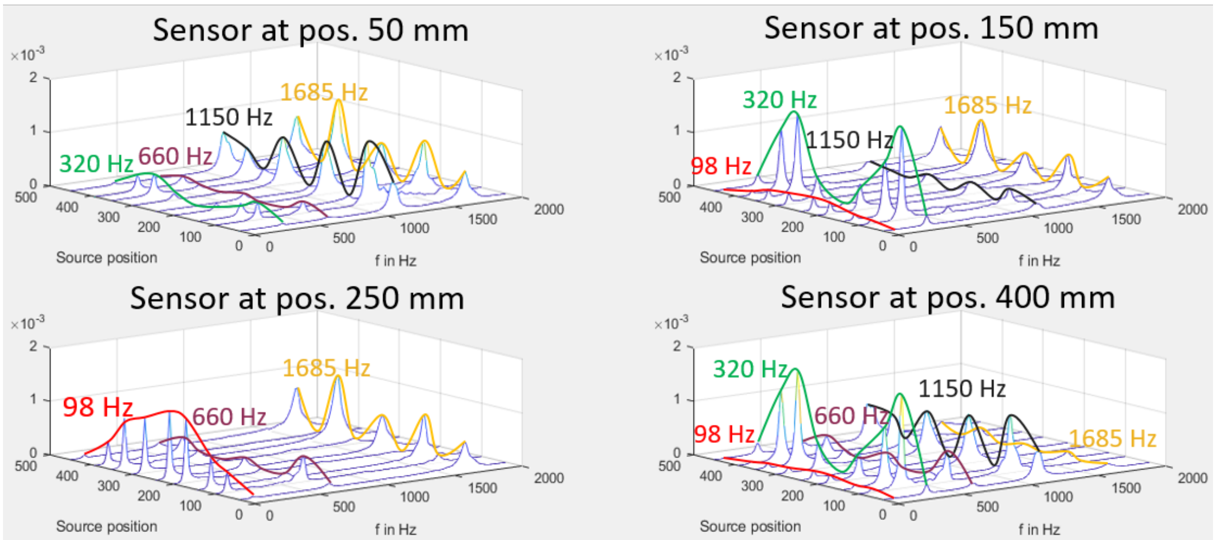

Figure IV.21. *RUPTUBE - Modal analysis: plots of the normalized spectrum received by each sensor for each impact position, over a [0; 2] kHz frequency range.*

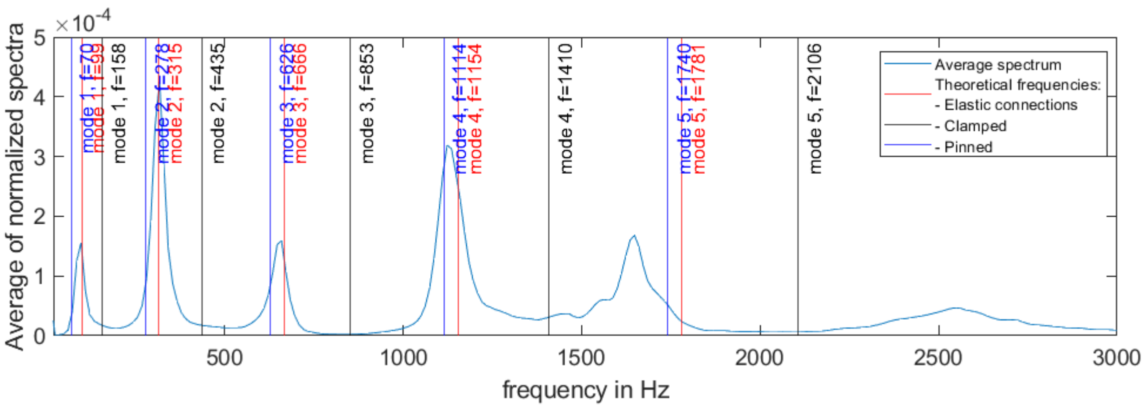

Figure IV.22. *RUPTUBE - Modal analysis: comparison of the experimental results and the calculated natural frequencies of first flexural vibration modes for different boundary conditions.*

Mode	**Frequency for a clamped-clamped tube** (Hz)	**Frequency for a pinned-pinned tube** (Hz)	**Frequency for elastic connections** (Hz)	**Measured natural frequency** (Hz)
1	158	70	99	98
2	435	278	315	320
3	853	626	666	660
4	1409	1114	1154	1150
5	2106	1740	1781	1685

Table IV.7. *Eigenfrequencies of the first flexural modes calculated for different boundary conditions.*

Impact response measurements were also performed on other tubes. It was noticed that peaks' frequencies could differ between the tests, even though the tubes were in the same material and had the same dimensions. Differences are too large to be attributed to temperature changes only. Spectral peaks were extracted from the signals of the different tests and their frequency distribution was plotted in a histogram, in Fig. IV.23. To plot this histogram, the frequency bandwidth of interest (0-2 kHz, in order to include the five first flexural modes that could be previously identified) was discretized in bands with a width of $\Delta f = 20$ Hz. Theoretical eigenfrequencies are also displayed on the graph in order to compare them with the experimental results. The resonances measured in the different tests seems to fall between the three theoretical models. That is likely due to inconsistency in the tube-to-outer-structure connection. To be properly inserted in the outer structure adaptors, tubes' ends had to be machined, which was done by hand tools, implying inconsistency in the final geometry. Because of the design of the connection between the adaptor and the tube (shown in Fig. IV.5), its stiffness is directly related to the tube outer diameter.

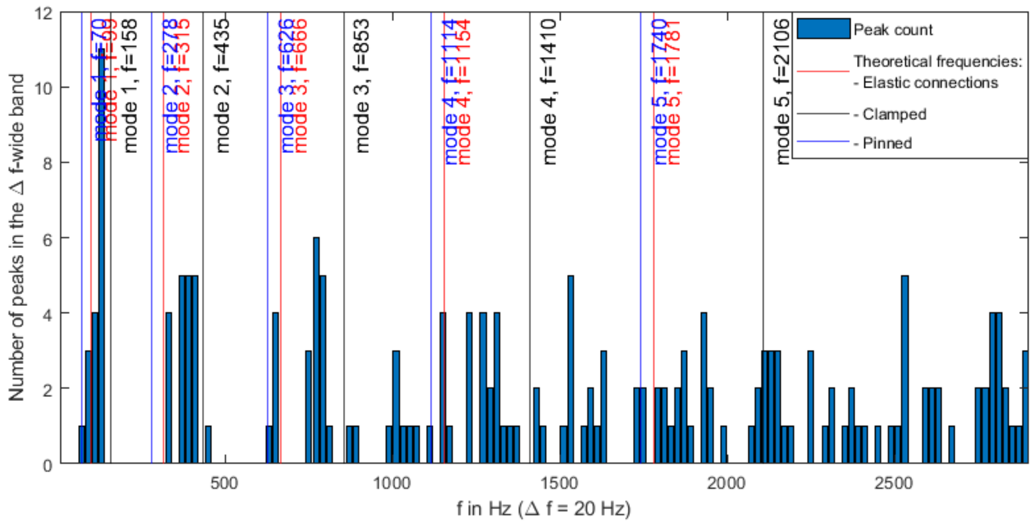

Figure IV.23. *RUPTUBE - Modal analysis: Distribution of the spectral peaks contained in signals from different impact tests (20 tests, on seven different tubes).*

As a conclusion, the described modal analysis allowed us to find actual flexural modes whose frequencies are rather close to the theoretically expected ones, but with a relative discrepancy due to inconsistency in the boundary conditions. For the second experimental device (MAQAC, described in Sec IV.5), that problem will be taken into account and a corrective element will be added to the system in order to ensure rigid connections between the tube and the outer structure, independently of the tube's ends geometry.

However, modes can be reliably identified and the influence of the source position on the spectra of the measured signals is clearly visible. Thus, this influence could be used to get information about the source position when it is unknown and has to be determined. Moreover, the modal identification can also be useful to characterize the FIV in the experiments on the second device (the first one does not reproduce external flow).

IV.4. Failure tests on RUPTUBE

IV.4.1. Design of experiments and experimental protocol

A first design of experiments was defined, by Taguchi's method (presented in App. E), with the aim of experimentally validating the failure pressure calculations. Thus, this first design focused more on pressure failure related parameters than considerations related to wave propagation or structure vibrations. The final goal was to reliably determine what material and what initial crack dimensions to choose in order to be able to generate a failure on a 10 mm outer diameter and 0.5 mm thickness tube.

Eventually, that experimental campaign did not validate the model and exhibited failure pressure significantly higher than the predicted ones. Most of the stainless steel tubes could not be failed because of a too high failure pressure, which exceeded the maximum pressure provided by the pump. Finally, the small number of obtained failures allows to deduce neither an empirical model nor a reliable tendency. However, it showed that aluminium tubes can fail at a reasonable pressure (between 80 and 100 bar) with a crack depth of approximately half of the tube thickness and a crack width of about 2 mm. The exact initial crack depths of failed tubes cannot be known because all the cracks that made a failure possible were made deeper by hand, in a way that does not allow to estimate the resulting depth. Among original cracks made by electro-discharge, only one made a failure possible (0.375 mm deep and 15 mm long crack on a 6 mm diameter, 0.5 mm thickness aluminium tube). Tab. IV.8 shows the obtained failure pressure in the first test series with the single original crack made by electro-discharge and the cracks modified by hand.

Since failure pressure estimation is not the main objective of the work, that problem was not further investigated. However, two likely reasons that could explain the gap between the calculation results and the experiments were identified: firstly, the initial article presenting the calculation method, [108], deals with pipes with a "diameter/thickness" ratio significantly higher than the currently tested tubes (about 80 in the article and 20 in the current work). Although it is not stated in the article, the model might be unsuitable for such small diameter tubes. Secondly, the fracture toughness of the tested tubes' materials could not be estimated, because it would require specific devices and skills that were not available. The considered values were an average of different values found in various literature references. It is therefore possible that those values do not correspond to the effective property of the tested tubes. An error on fracture toughness value is identified as a common source of issues in failure mechanics studies, according to [107].

Tube diameter (mm)	**Tube thickness** (mm)	**Initial crack depth** (approx., mm)	**Initial crack width** (mm, uncertainty of ± 0.5 mm)	**Initial crack length** (mm, uncertainty of ± 4 mm))	**Failure pressure** (bar, uncertainty of ± 1 bar)
12	1.0	> 0.5	1	50	143
10	1.0	> 0.5	1	50	74
10	0.5	> 0.25	1	50	29
10	0.5	> 0.25	1	50	71
8	0.5	> 0.25	1	50	88
6	0.5	0.375 ± 0.01 (original crack by electro-discharge)	0.2 ± 0.01	15 ± 0.1	61

Table IV.8. *Failure pressure in the first RUPTUBE test series with aluminium tubes.*

Even though the failure pressure model was not validated, it was confirmed that 10 mm outer diameter and 0.5 mm thickness aluminium tubes could easily fail with less than 100 bar of relative inner pressure, as shown in Tab. IV.8. Thus, a second series of tests could be carried out with an emphasis on acoustic and vibration phenomena study. The first objective was to test various types of acoustic or vibration measurement devices with the aim of failure detection and localization, and wave characterization (*i.e.* identifying the kind of waves that are generated by the failure and the modes that are excited, regarding both high frequency guided waves and low frequency structural vibrations). Moreover, those tests also allowed to gather several vibration and AE signals induced by failures in tubes of various dimensions or at various positions. Thus, signal processing technique could be developed to study such signals and get information about wave propagation in a tube without effects of a surrounding fluid flow.

To reach these objectives, an experimental plan was designed and is presented in Fig. IV.24.

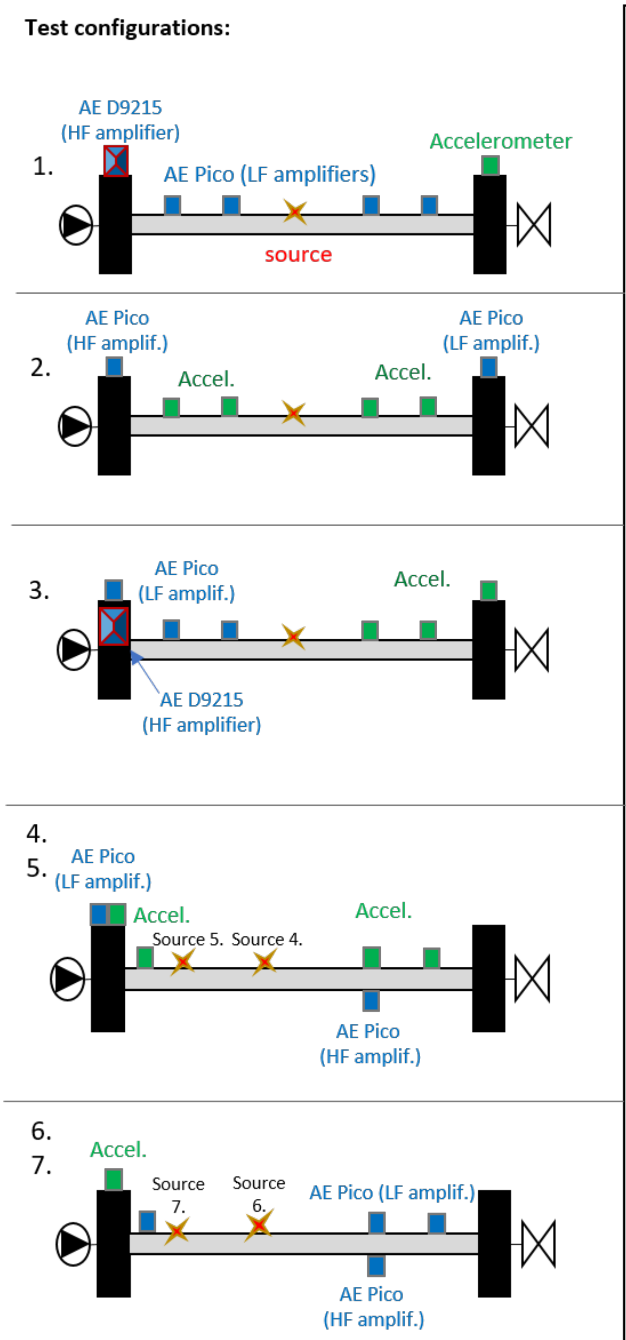

Objectives:

Test 1:
- Failure detection with accelerometer on the outer structure,
- Failure detection with resonant AE sensor on the outer structure,
- Information about guided wave propagation along the tube and attempt to localize the source with AE sensors on the tube.

Test 2:
- Comparison between HF and LF amplifiers for AE sensors on the outer structure,
- Information about vibration response of the tube and attempt to localize the source with accelerometers on the tube.

Test 3:
- Comparison between AE and accelerometers,
- Information about the transmission from the tube to the outer structure,
- Comparison between broadband sensors (with LF amplif.) and resonant sensor (with HF amplif.).

Tests 4 and 5:
- Failure localization with accelerometers,
- Recording signals with broadband AE sensor and HF amplif.,
- Information about the transmission from the tube to the outer structure,
- Failure detection with an AE sensor with LF amplif. on the outer structure.

Tests 6 and 7:
- Failure localization with AE sensors,
- Recording signals with broadband AE sensor and HF amplif.,
- Failure detection with an accelerometer on the outer structure.

Figure IV.24. *RUPTUBE - Second experimental campaign.*

Each test follows this procedure:

1. Sensors mounting (structural sensors on the tube and/or the external structure, pressure sensor on the inlet flange),
2. Check of the acoustic or vibration sensors, with a HN source (for AE sensors) or a hammer impact (for accelerometers),
3. Shields installation,
4. Filling and degassing,
5. Increasing the pressure up to 10 bar and releasing it to check the pressure sensor,
6. Start of the acquisition,
7. Increasing the pressure until the failure,
8. Stop of the acquisition some seconds after the failure.

When high-speed camera is used, the activation signal is sent to the device immediately after the failure. The device has to be configured so that it can store some seconds of images in the appropriate number of buffers and then sends to the computer the images that precede the activation signal. The activation signal is sent manually [5]. The maximum delay between the failure and the activation signal has to be determined according to the sampling rate and the number of available buffers, which depends on the image resolution.

Unless otherwise stated, the tests presented here were carried out on tubes with a diameter of 10 mm, a thickness of 0.5 mm and a length of 500 mm.

IV.4.2. Data processing methodologies

In this section, processing methodologies are firstly presented in details with a test example, for each kind of measurement device (accelerometers, AE sensors with LF amplifiers, with HF amplifiers, high speed camera and strain gauges). Then, results of the different tests introduced in the experimental plan (in Sec. IV.4.1) are presented and analyzed according to the objectives introduced in Fig. IV.24. The analysis focuses on two elements: wave velocities estimation, and source position estimation. The wave velocity is not only required for the source position estimation, but it also provides information about the kind of waves that are generated by the failure (longitudinal, torsional, flexural waves). That information can be useful for several reasons. In the frame of the current work, it can help to improve the choice of the sensors and their locations. It could also be used in further studies, to determine how a surrounding flow can influence the measured signals, to characterize the source signal and to study accurately the transmission between the tube and the outer structure. The source position estimation is useful to determine which

[5] Simple electronic circuits can be built to automatically send the activation signal to the camera when the pressure signal falls down, indicating a failure. It would make the operation easier and prevent a late activation. However, since the camera was used only few times during this study, building such a system was not considered as valuable.

sensors are the most relevant to localize a failure, which is one of the main objectives of the final application in nuclear reactors, and also allows to validate the propagation wave velocity estimation, when the real source position is already known.

IV.4.2.1. Accelerometers

It came out that the available accelerometers are too sensitive to measure the response of the tube to the generated failures. As a consequence, most of the accelerometer signals recorded during failure tests exhibit saturation when they are directly mounted on the tube. This saturation is due to the IEPE circuitry. Indeed, the voltage did not cross the conditioner's range, there is therefore no reason for it to saturate, and the limits of the piezoelectric element are much higher than the IEPE circuitry's ones. The upper limit of the piezoelectric element's range is about 10^4 g while the one of IEPE circuitry's range is about 410 g. Thus, the limit of the whole device is imposed by the IEPE circuitry's ones. Moreover, an overload of the piezoelectric element would result in a non-linear output signal but would not produce such a saturation pattern.

Nevertheless, one clean signal was acquired in one of the tests with an accelerometer on the tube. This signal was measured during Test 3. Therefore, this test is presented here, to introduce methods for the processing of accelerometers signals.

The configuration of this test is shown in Fig. IV.25.

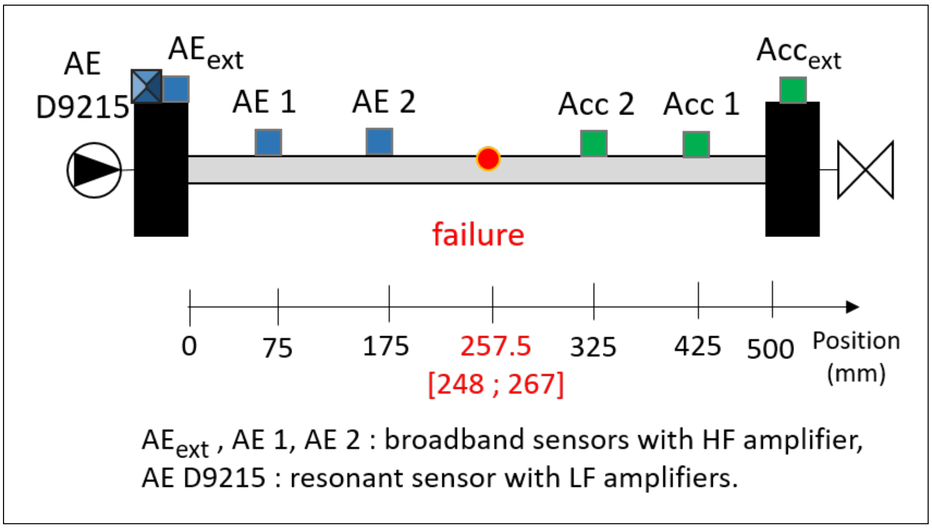

Figure IV.25. *RUPTUBE - 2nd campaign, test 3: configuration.*

This test was carried out on a 12 mm outer diameter, 0.5 mm thickness tube. Moreover, accelerometers were mounted at an azimuth of 90° from the failure, with the aim of reducing the acceleration level and avoiding sensor saturation. Eventually, the accelerometer 1 did not saturate, but the accelerometer 2 did slightly. The accelerometer on the outer structure did not but has a poor SNR. The raw signals are shown in Fig. IV.26.

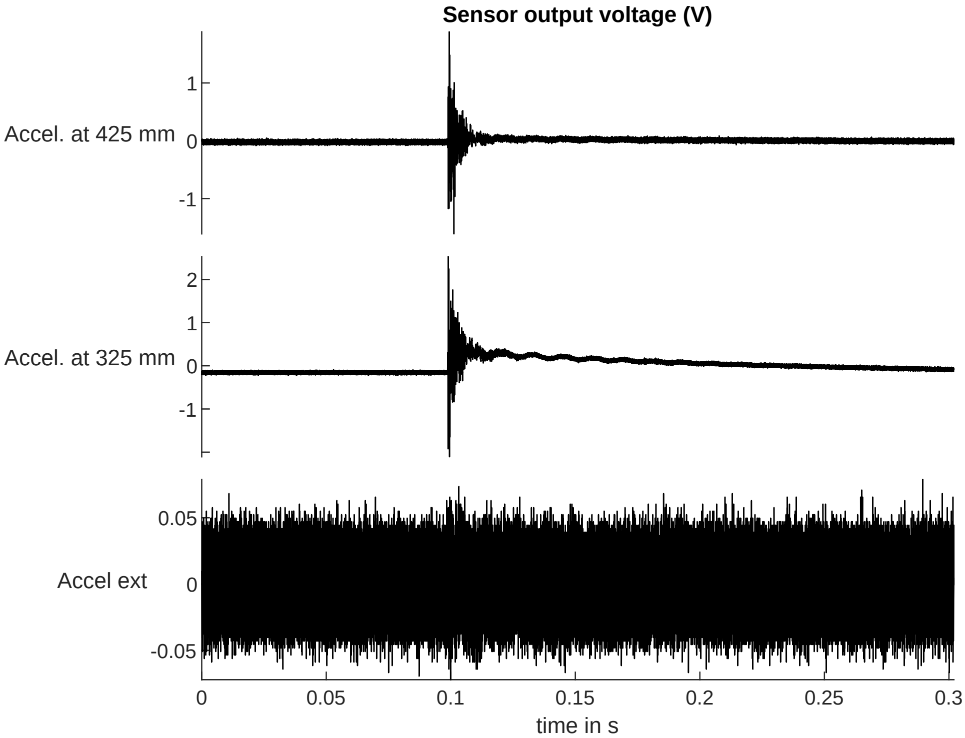

Figure IV.26. *RUPTUBE - 2nd campaign, test 3: time domain view of the accelerometers' signals.*

As shown by the DWT (Fig. IV.27) of the signal of the accelerometer on the outer structure, the first detail coefficients contain only noise. The failure signal appears from level 8. Thus, the signal is denoised by a wavelet thresholding. To have an homogeneous process on all the signals, the other two signals are also denoised by the same technique, although their SNR was high enough. A high-pass filter is also applied to the signals in order to remove the potential 50 Hz noise and the low-frequency drift in the signal of Acc. 2 induced by the saturation. Processed signals are shown in Fig. IV.28, and their CWT on Fig. IV.29. Fig. IV.30 shows the superimposition of their ESD. It allows to see the spectral distortion between the signal measured on the tube and the one measured on the outer structure. In this figure, the ESD have been normalized because the absolute energy of the signal measured on the outer structure is very low compared to the ones of the signals measured on the tube.

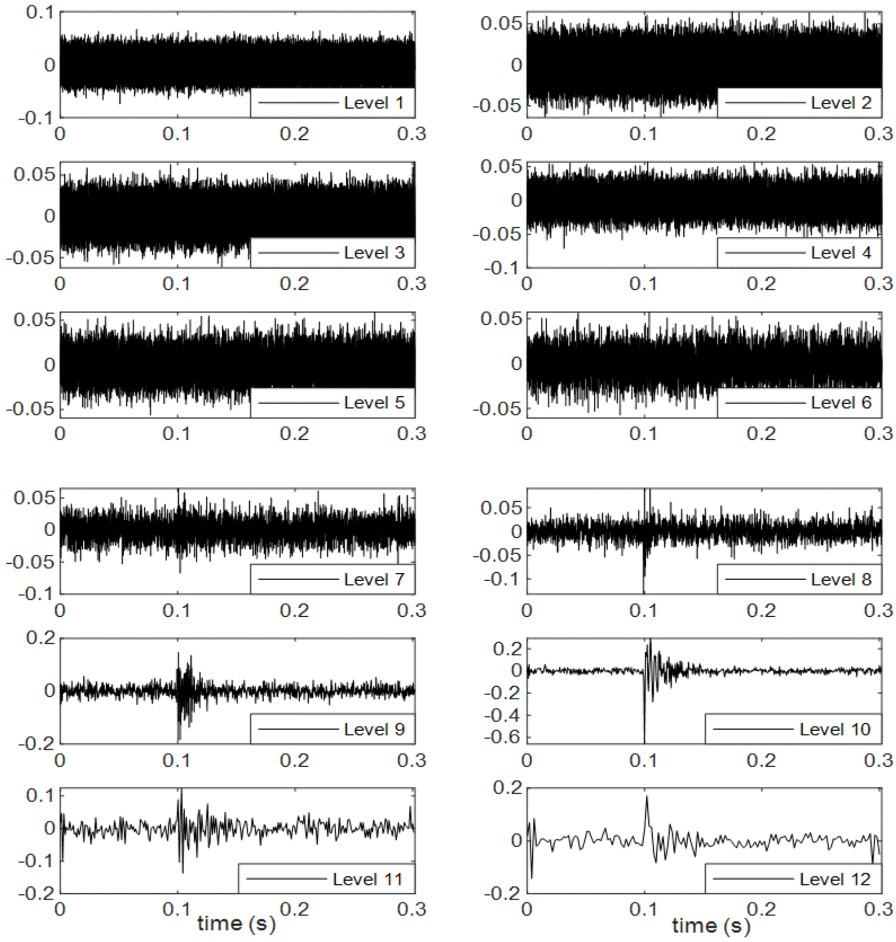

Figure IV.27. *RUPTUBE - 2nd campaign, test 3: detail coefficients from the DWT of the outer accelerometer signal.*

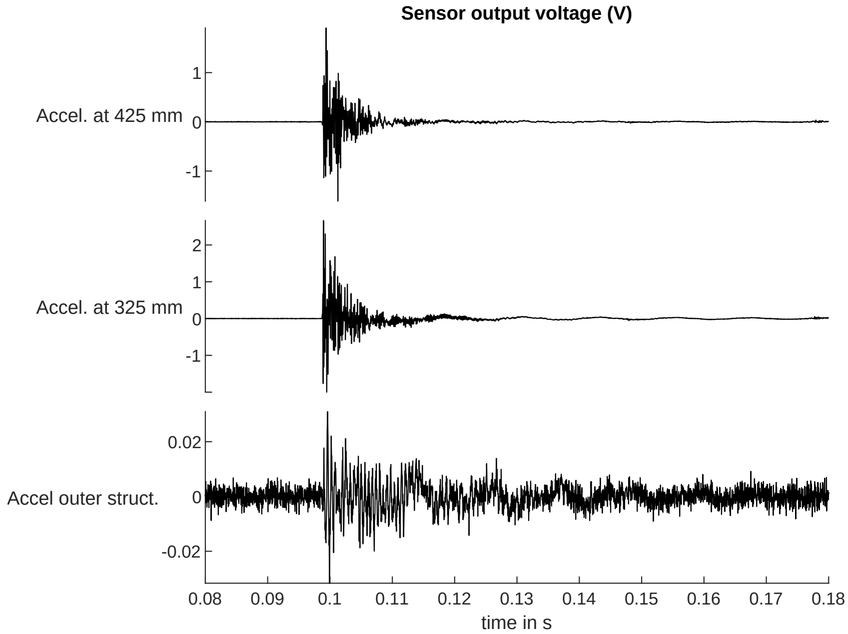

Figure IV.28. *RUPTUBE - 2nd campaign, test 3: accelerometers' signals after processing.*

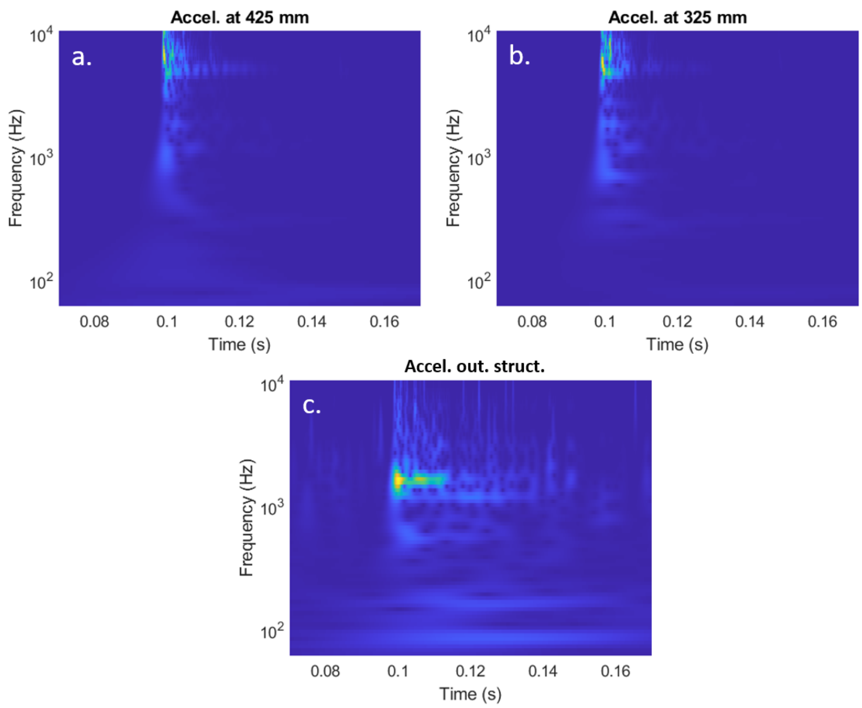

Figure IV.29. *RUPTUBE - 2nd campaign, test 3: CWT (with Morse wavelets) of accelerometers' signals.*

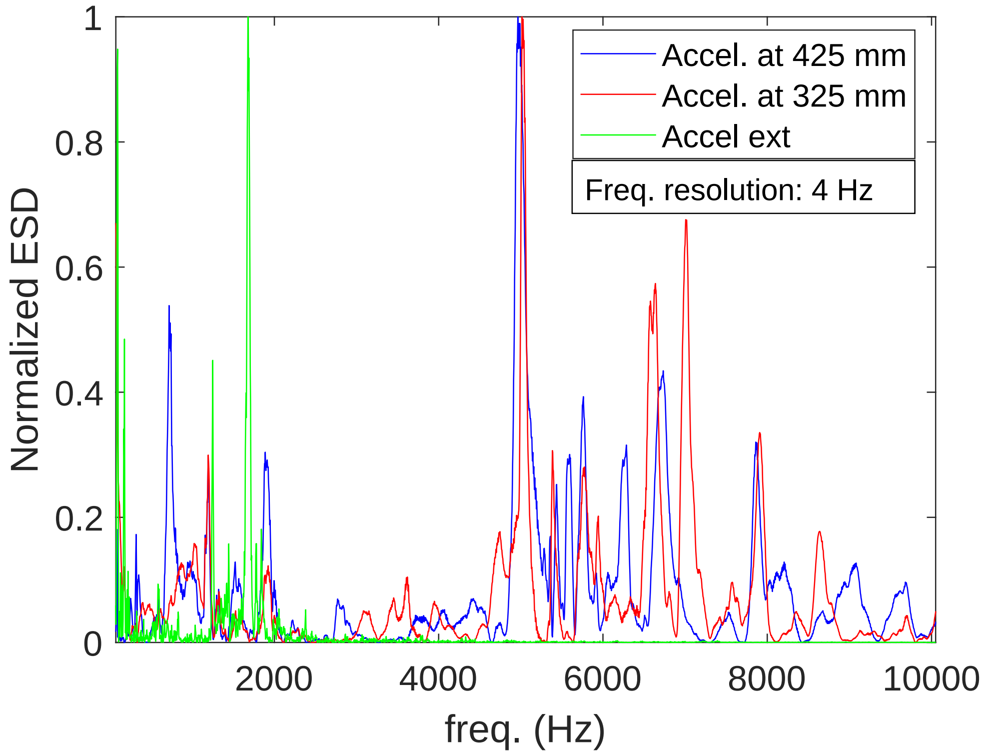

Figure IV.30. *RUPTUBE - 2^{nd} campaign, test 3: superimposition of the normalized ESD.*

The ESD superimposition shows that, while the signals measured on the tube have a significant amount of energy between 5 and 8 kHz, the signal measured on the outer structure concentrates under 2 kHz. It can be assumed that the loss due to the transmission from the tube to the outer structure is more important in the high frequency range.

The signals of the accelerometers on the tube exhibit a resonance after the main wavefront (they are highlighted by the magnification on the CWT in Fig. IV.31), at a frequency of 87 $\pm$4 Hz, which is close to the theoretical frequency of the first flexural mode (85 Hz, according to the method presented in Sec. II.2). Therefore, it can be reasonably considered that the failure significantly excited the first flexural mode. The consistency between the theoretical natural frequencies and the spectral peaks eventually observed were verified in details with a 10 mm diameter and 0.5 mm thick tube (this verification is presented in Sec. IV.3.5.2), and was more quickly verified, with only an impact test with the tube filled with air instead of water, on the 12 mm diameter and 0.5 mm tube used in this test. The theoretical eigenfrequency of the first flexural mode for such a tube filled with air is 144 Hz. The impact test showed a resonant frequency at 131 $\pm$27 Hz (the uncertainty is due to the variation in the frequency of the peak observed among several repetitions of the impact test).

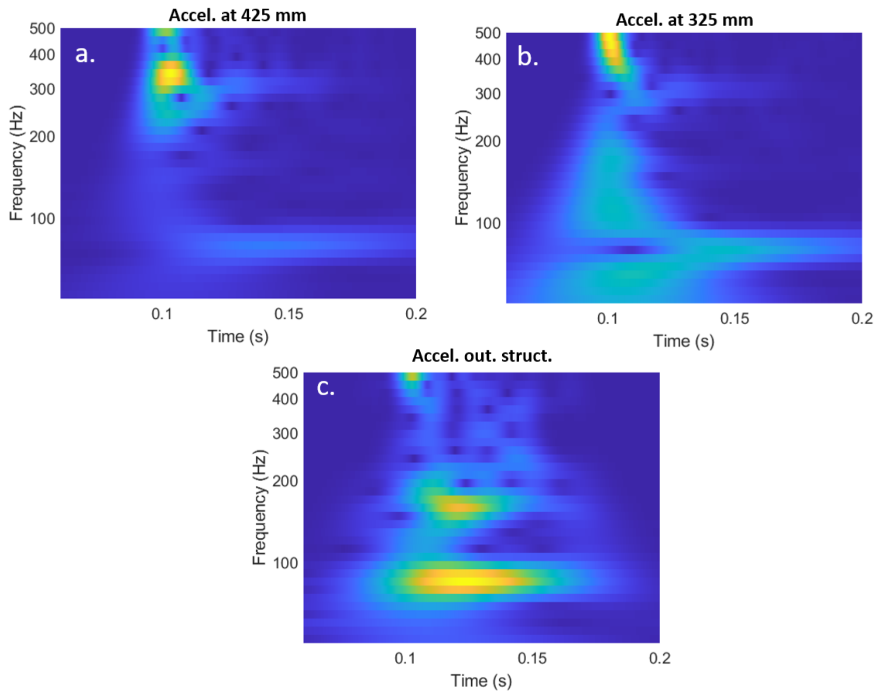

Figure IV.31. *RUPTUBE - 2nd campaign, test 3: time and frequency magnification on the CWT (with Morse wavelets) of accelerometers' signals.*

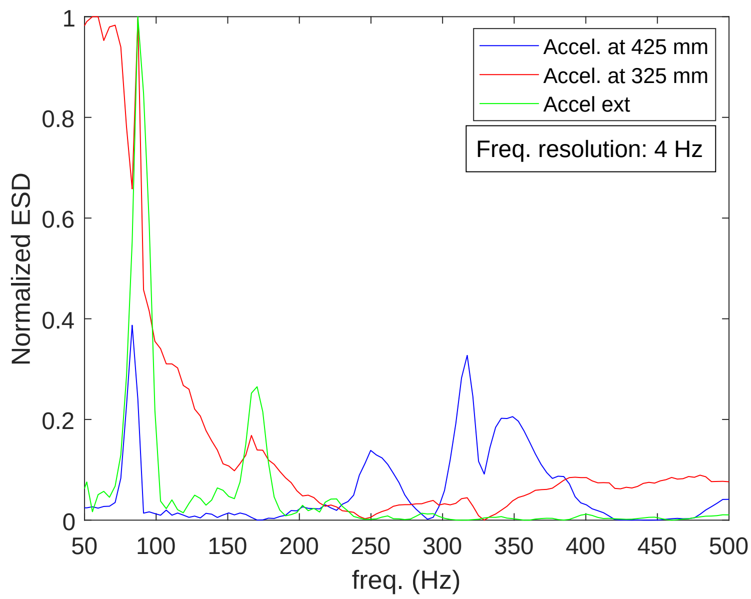

Figure IV.32. *RUPTUBE - 2nd campaign, test 3: frequency magnification of the normalized ESD.*

As shown by the superimposition of the ESD in Fig. IV.30, and the low frequency magnification in Fig. IV.32, the first flexural vibration mode's contribution is measured by all the sensors. One may notice that the spectrum of the accelerometer at 325 mm from the tube's end show a peak around 175 Hz (which is close to the theoretical frequency of the second flexural mode), while the ones of the accelerometer at 425 mm does not have any peak at this frequency. This is consistent with the relation between the mode shape and the position of the sensor explained in Sec. IV.3.5.2. Indeed, the sensor at 425 mm is near a node of the second flexural mode shape while the sensor at 325 mm is near an anti-node.

It should be noticed that in the other tests involving accelerometers on the tube, all the signals saturated but, during the IEPE system release following the overload, oscillations at the first flexural mode's frequency can be observed. As explained in Sec. IV.4.2.4, it was checked with the high-speed camera that those oscillations correspond to actual physical resonance of the tube and are not a consequence of the overload of the electronics.

IV.4.2.2. Acoustic Emission sensors

With low frequency amplifiers

As examples, results of test n°6 are presented in details. The whole recorded signals last about 60 s. Only a reduced part focusing around the failure time is actually shown. AE sensor signals are shown in time domain (Fig. IV.34) and time-frequency domain (CWT in Fig. IV.35). The reference number and the position of each sensor is given in Fig. IV.33.

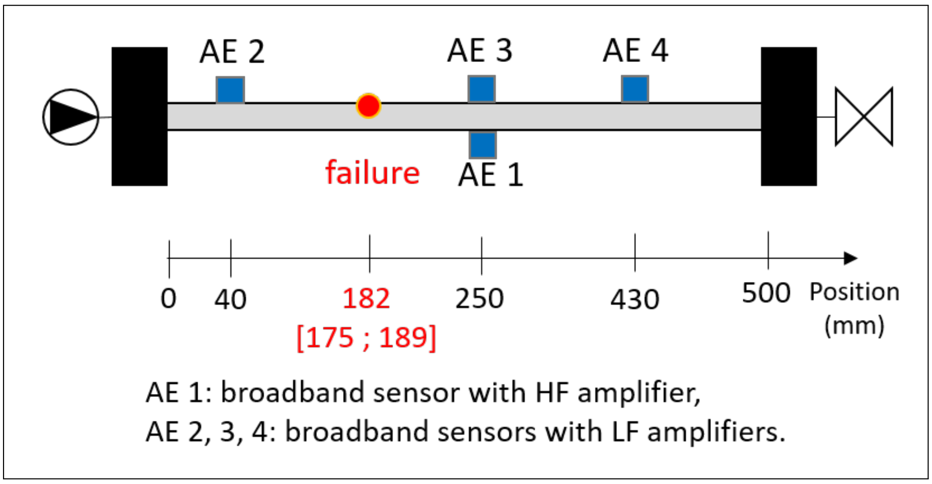

Figure IV.33. *RUPTUBE - 2nd campaign, test 6: configuration.*

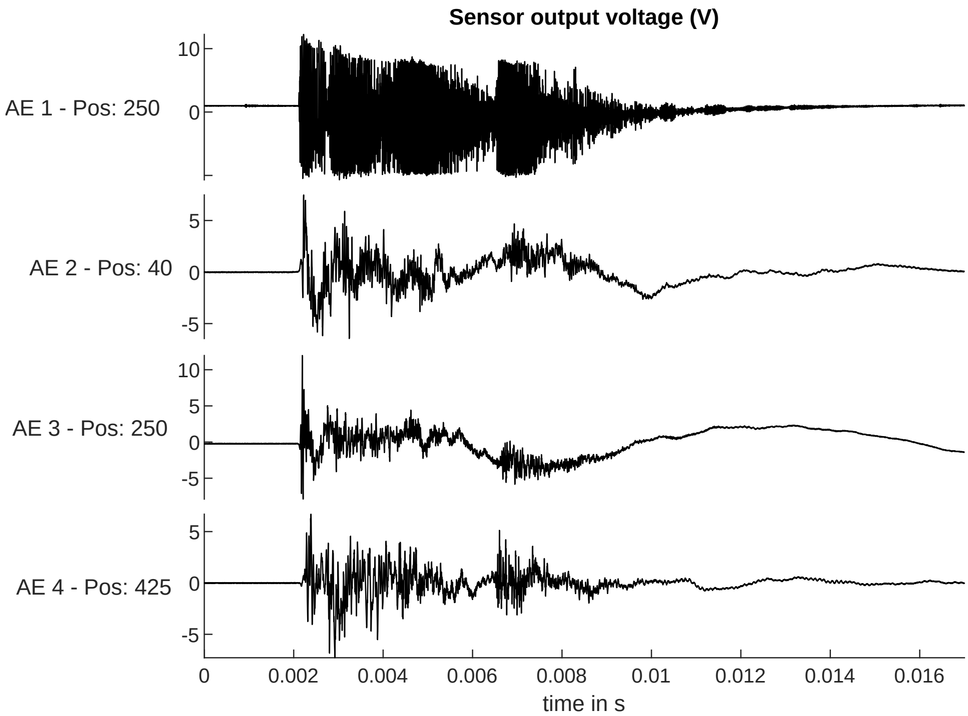

Figure IV.34. *RUPTUBE - 2nd campaign, test 6: time domain view of the AE sensors' signals.*

Since AE 1 signal is saturated and was recorded with a different amplifier than the other signals, it is not considered in the first step of the analysis. The other time domain views show that the signals look different from each other. They do not exhibit a similar pattern that would simply be shifted in time. These discrepancies are due to wave dispersion and to imperfection in sensors mounting [6]. It is also assumed that the tube material is not perfectly homogeneous, inducing unpredictable propagation distortion between the different sensors. Despite those uncertainties, the time of arrival of the failure-induced waves on each sensor can be approximated. Then, the estimation of the failure position is possible. To this end, different techniques, usually referred as TDOA, can be attempted.

[6]Despite the care accorded to the mounting, the coupling between such a sensor, which has a planar interface, and a curved surface of small radius is indeed prone to imperfection, since the contact area between the planar sensor and the curved surface is small. Effects of such imperfections cannot be accurately determinate.

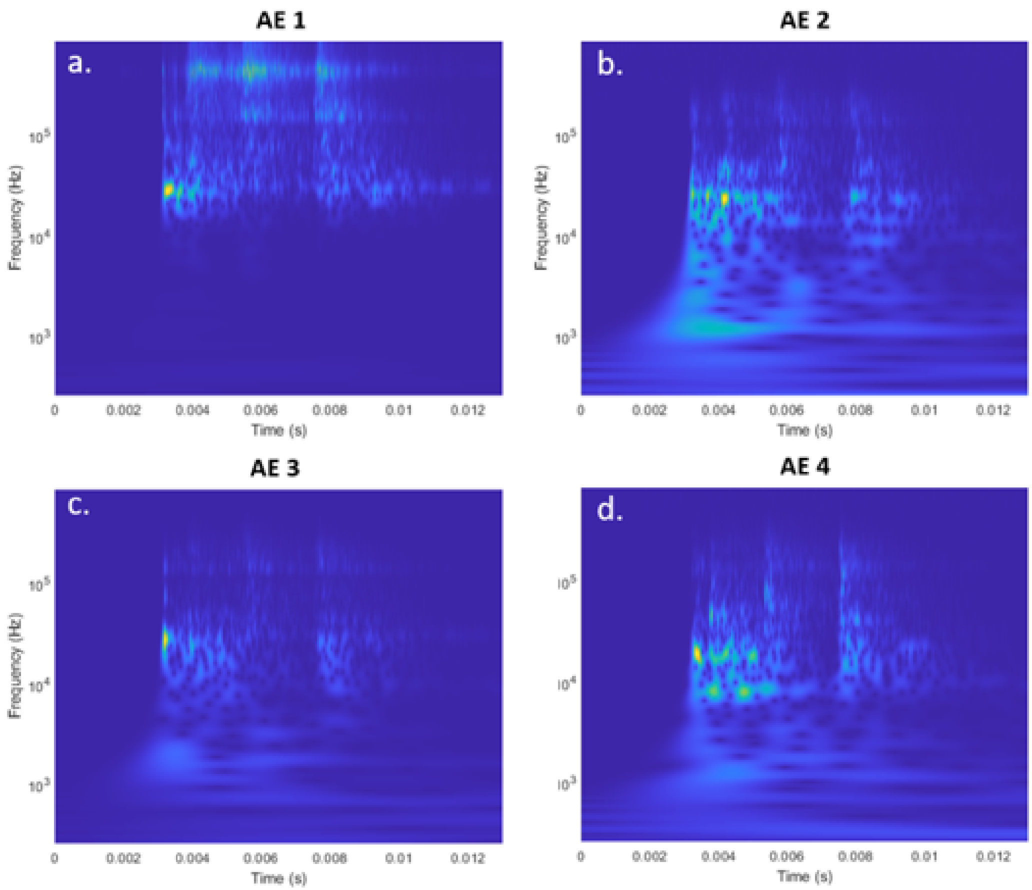

Figure IV.35. *RUPTUBE - 2nd campaign, test 6: time-frequency views of the AE sensors' signals. CWT by Morse wavelets. a.: sensor 1, b.: sensor 2, c.: sensor 3, d.: sensor 4.*

Time-frequency views show that the different signals have similar spectra. They especially exhibit a peak of energy between 20-30 kHz at the beginning of the event. Such a feature can be used to improve TDOA estimation, as explained below.

TDOA estimation was first attempted by threshold crossing with the raw signals. As shown by the time magnifications in Fig. IV.36, low frequency components prevent an accurate localization of the event beginning because they make the wavefront too smooth. Thus, the threshold crossing detection was attempted on filtered signals. The applied filter was a High-Pass 2nd order Butterworth filter, with a cut-off frequency of 20 kHz. As shown by the time magnification of the filtered signals in Fig. IV.37, such a cut-off frequency makes an accurate localization of the event beginning possible. Moreover, it is also the same cut-off frequency as the built-in analog filters of the HF amplifiers. It makes therefore the results obtained with LF amplifiers more comparable with the ones obtained with HF amplifiers.

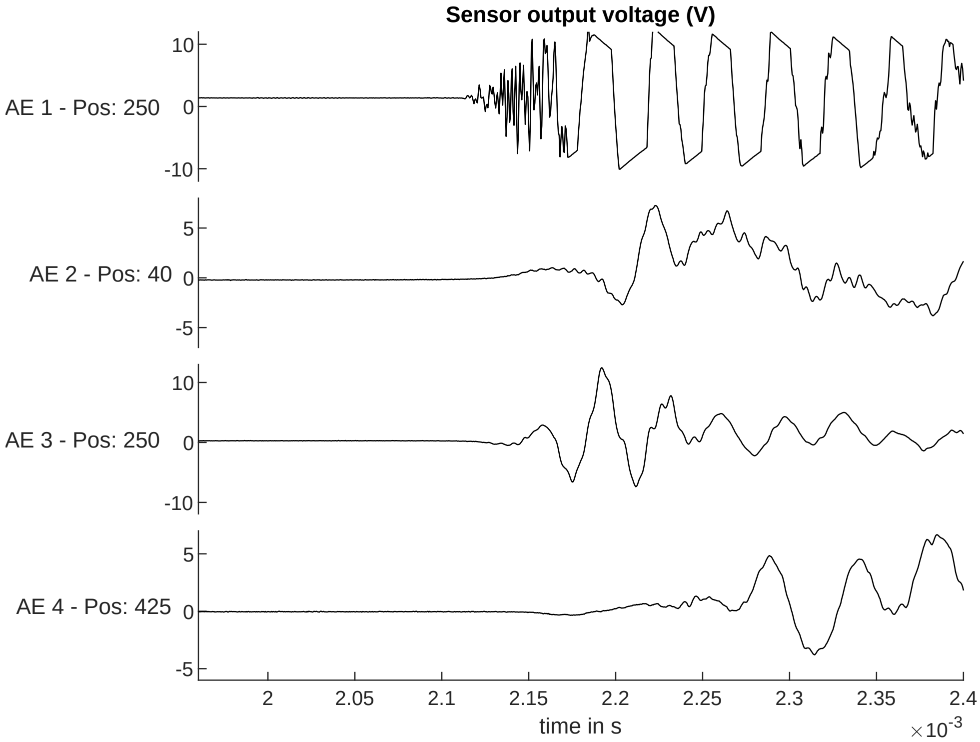

Figure IV.36. *RUPTUBE - 2^{nd} campaign, test 6: time and amplitude magnification around the beginning of the event on raw signals.*

Fig. IV.36 also shows that the HF amplifier of the sensor AE 1 started to saturate only $5 \cdot 10^{-5}$ s after the first waves arrival. Therefore, the very beginning of the signal is usable, especially for the estimation of first waves arrival time.

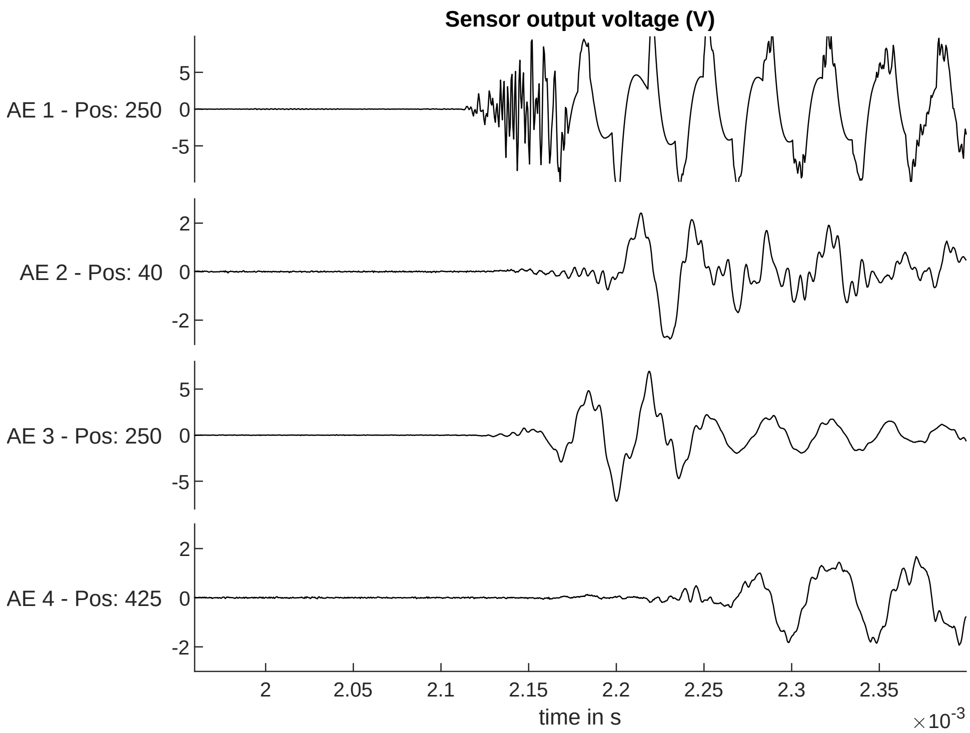

Figure IV.37. *RUPTUBE - 2^{nd} campaign, test 6: time and amplitude magnification around the beginning of the event on filtered signals (2^{nd} order Butterworth High-Pass filter at 20 kHz).*

Fig. IV.38 shows, for example, how two filtered signals overlay when one is time-shifted by the value of the TDOA obtained by threshold crossing method. Such plots allow to check that thresholds are correctly adjusted. Here, the threshold was adjusted so that it detects the very first disruptions in the signal. Those disruptions are related to the fastest traveling waves, which have a velocity of about 5090 m.s^{-1} (theoretical quasi-longitudinal wave velocity according to Eq. (II.5), introduced in Sec. II.1, and considering Young's modulus $E = 70$ GPa, Poisson coefficient $\nu = 0.34$, and density $\rho = 2700$ kg.m^{-3}).

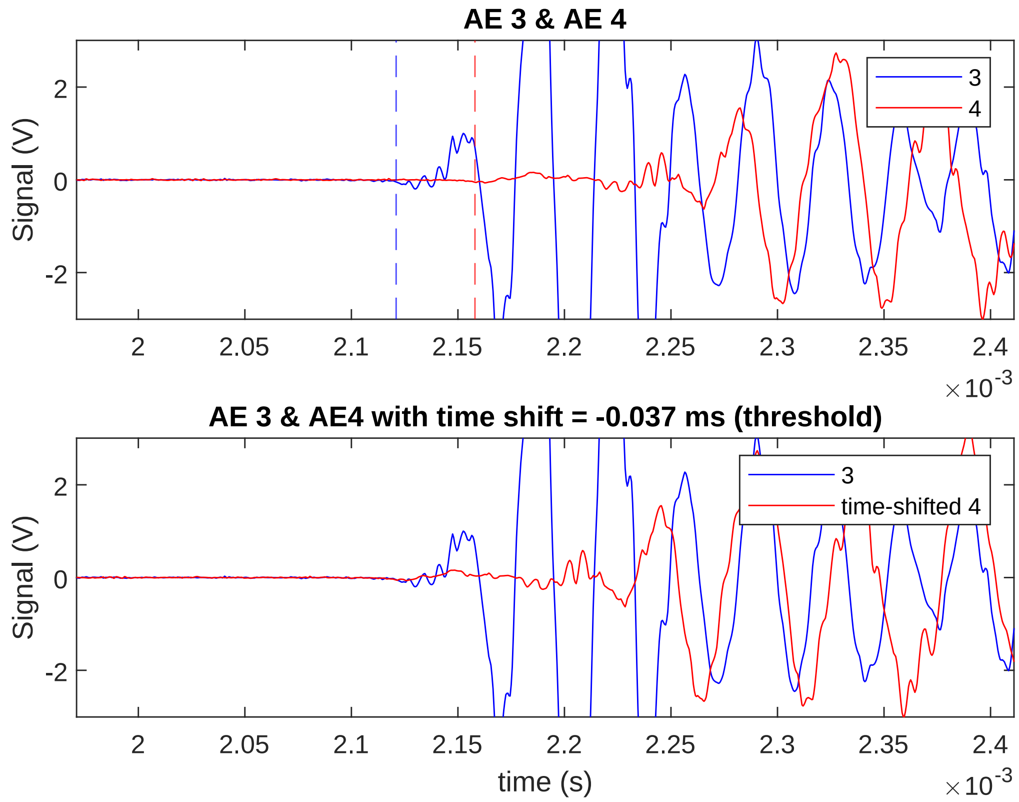

Figure IV.38. *RUPTUBE - 2nd campaign, test 6: verification of the TDOA obtained by threshold crossing method on AE 3 and AE 4 signals (with 20 kHz HP filter).*

Applying the method to sensors AE 3 and AE 4 provides an estimation of the wave speed between the two corresponding sensors, with the expression: $c = |\frac{x_4 - x_3}{\Delta t}|$, where x_4 and x_3 are the axial positions of the sensors and Δt the TDOA. The obtained value is 4865 ± 600 m.s^{-1}, which is close to the expected theoretical velocity of quasi-longitudinal wave speed in aluminium (5090 m.s^{-1}). In any case, the velocity value used for the next step of the analysis is the experimentally estimated one. It is assumed that this speed is constant along the tube and can therefore be used to find the source position with the TDOA between either AE 2 and AE 1, or AE 2 and AE 3, or AE 2 and AE 4. The source position, x_S, as a function of the TDOA, Δt, is given by:

$$x_s = \frac{(x_i + x_j - c\,\Delta t)}{2}, \tag{IV.11}$$

where c is the previously estimated wave speed, x_i and x_j the positions of the two considered sensors. The uncertainties on input parameters (position of the sensors and time of arrival) used for the estimation of the velocity and the source position are $\delta t_i = \pm 5 \cdot 10^{-6}$ s for the time of arrival on each signal, and $\delta x_i = \pm 1$ mm for the position of each sensor. Uncertainty on the velocity is given by: $\delta c = \pm\, (|\frac{(x_j - x_i)}{\Delta t^2}\, 2|\, \delta t_i + |\frac{2}{\Delta t}| \delta x_i)$. Uncertainty on the source position is given by: $\delta x_s = \pm\, (|\frac{\Delta t}{2}| \delta c + |c|\, \delta t_i + \delta x_i)$.

The positions estimated with the three sensor pairs are presented in Fig IV.39.

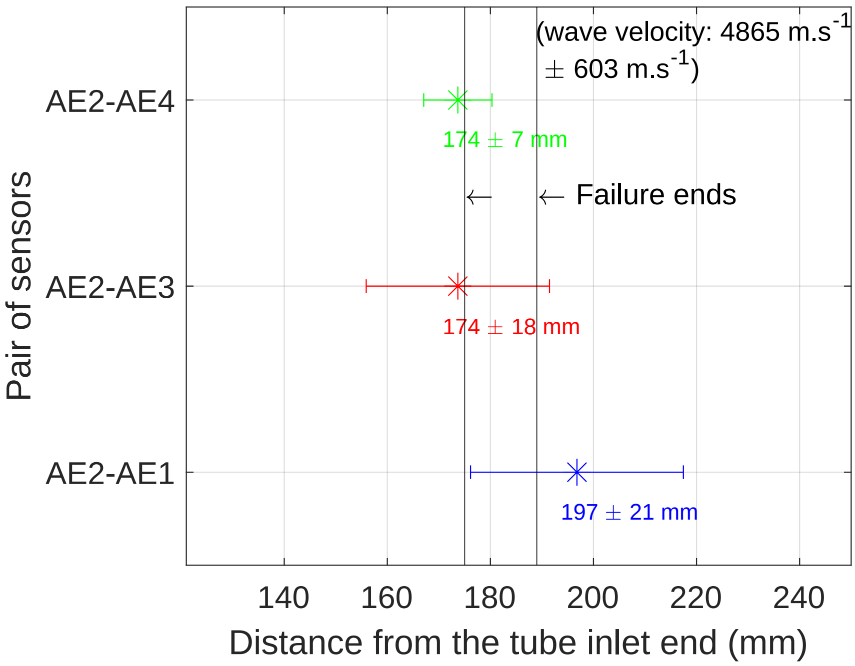

Figure IV.39. *RUPTUBE - 2nd campaign, test 6: source positions obtained by threshold crossing method with 20 kHz LP filtered signals. Indicated failure ends are observed after the test.*

TDOA estimation was also attempted by cross-correlation. However, since time evolution of the signals look quite different, especially at the beginning of the transient phase, which is the most important for time localization, cross-correlation is not efficient on raw signals. The method is tested on extracted components only. The underlying assumption is that the components separated by DWT (referred as "detail coefficients") or EMD (referred as IMF) correspond to physical guided wave modes. Considering signals from two different sensors, it is assumed that, if extracted components share a similar spectrum, those components correspond to the same propagation mode measured by the different sensors. Waves related to a single mode are theoretically not distorted by dispersion and the cross-correlation can therefore be efficient in estimating TDOA with this isolated mode. The EMD of signals AE 3 and AE 4 are given in App. F and App. G. Each IMF is plotted with its Fourier transform. It can be noticed that the corresponding IMF of both signals have close mean and maximum frequencies, but generally, the spectra of all the IMF spread over a relatively wide frequency range. Therefore, it seems that in the current situation, the EMD does not allow to extract components with a narrow bandwidth. However, it can be noticed that IMF n°2 of both signals have relatively similar spectra. They correspond to the peak of energy that can be observed on the CWT (Fig. IV.35) between 20 and 30 kHz. Thus, the cross-correlation between those two extracted components is computed and shown in Fig. IV.40. It is assumed that the position of one of the maxima of the cross-correlation corresponds to the TDOA. A time-shift equal to the estimated TDOA is applied to signal 2 in order to verify the superposition of the signals, as shown in Fig. IV.41. This procedure is applied to each pair of signals in order to deduce wave velocity (with the TDOA between sensor 3 and sensor 4) and the source position, with the TDOA between sensors 2-3 and 2-4 (sensor 1 is not used here because its frequency response is not the same as the others).

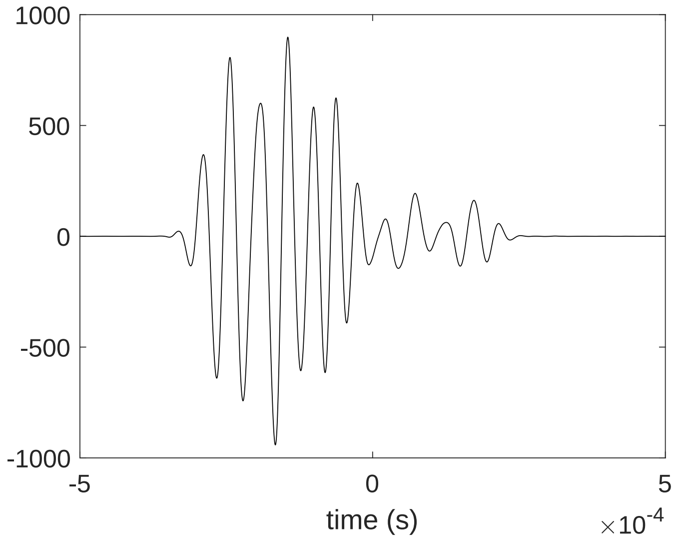

Figure IV.40. *RUPTUBE - 2^{nd} campaign, test 6: cross-correlation between the IMF 2 of signals AE 3 and AE 4.*

The selected time-shift is the second maximum of the cross-correlation (-0.145 ms). After verification, it turned out that with a time shift equal to the first maximum (-0.166 ms), the signals do not overlay well. The same verification was done with the first five maxima of the cross-correlation. Finally, the selected value yields a wave velocity of $1241 \pm 57 \mathrm{m.s}^{-1}$. This value is close to both the guided wave velocity of the first flexural mode, F(1,1), around 25 kHz and the pressure wave velocity in water.

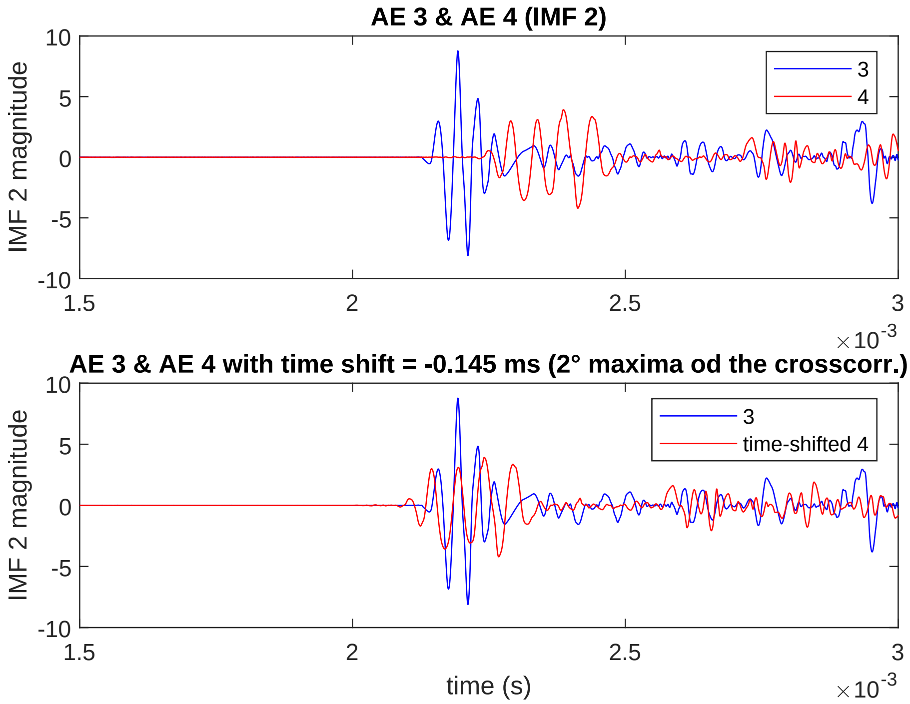

Figure IV.41. *RUPTUBE - 2nd campaign, test 6: verification of the estimated TDOA between the IMF 2 of signals AE 3 and AE 4.*

Considering the estimated velocity, the source position obtained with the TDOA between the signals AE2 and AE3, and signals AE2-AE4 are shown in Fig. IV.42.

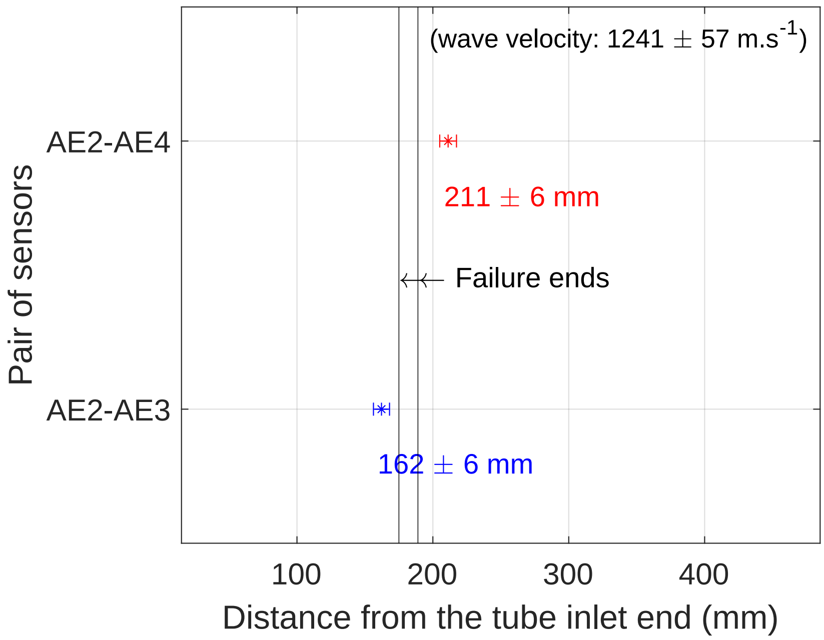

Figure IV.42. *RUPTUBE - 2^{nd} campaign, test 6: source positions obtained by cross-correlation method applied on the IMF 2 from the EMD of the AE sensors' signals.*

The error on the estimated source positions are about 20 mm. As a conclusion, compared to the threshold crossing method applied to simply denoised signals, the cross-correlation method applied to IMF from EMD failed at estimating the source position.

The same procedure is applied to DWT-extracted components. The fifth detail coefficient is selected, as it corresponds to the noticed component between 20 and 30 kHz. At the fifth level of the DWT, the sampling rate is 63.8 kHz (in DWT, the sampling rate is divided by two at each level of the decomposition). Results of the DWT are shown in Fig. IV.43, Fig. IV.44. The superimposition of the selected detail coefficient is shown in Fig. IV.46. The time shift is obtained by the cross-correlation shown in Fig. IV.45. The obtained wave speed is 1276 $\pm$581 m.s^{-1} and resulting source positions are presented in Fig. IV.47. As it can be noticed in that figure, the uncertainty is quite higher than with other methods. This is due to the lower time resolution, implying greater uncertainty on the TDOA.

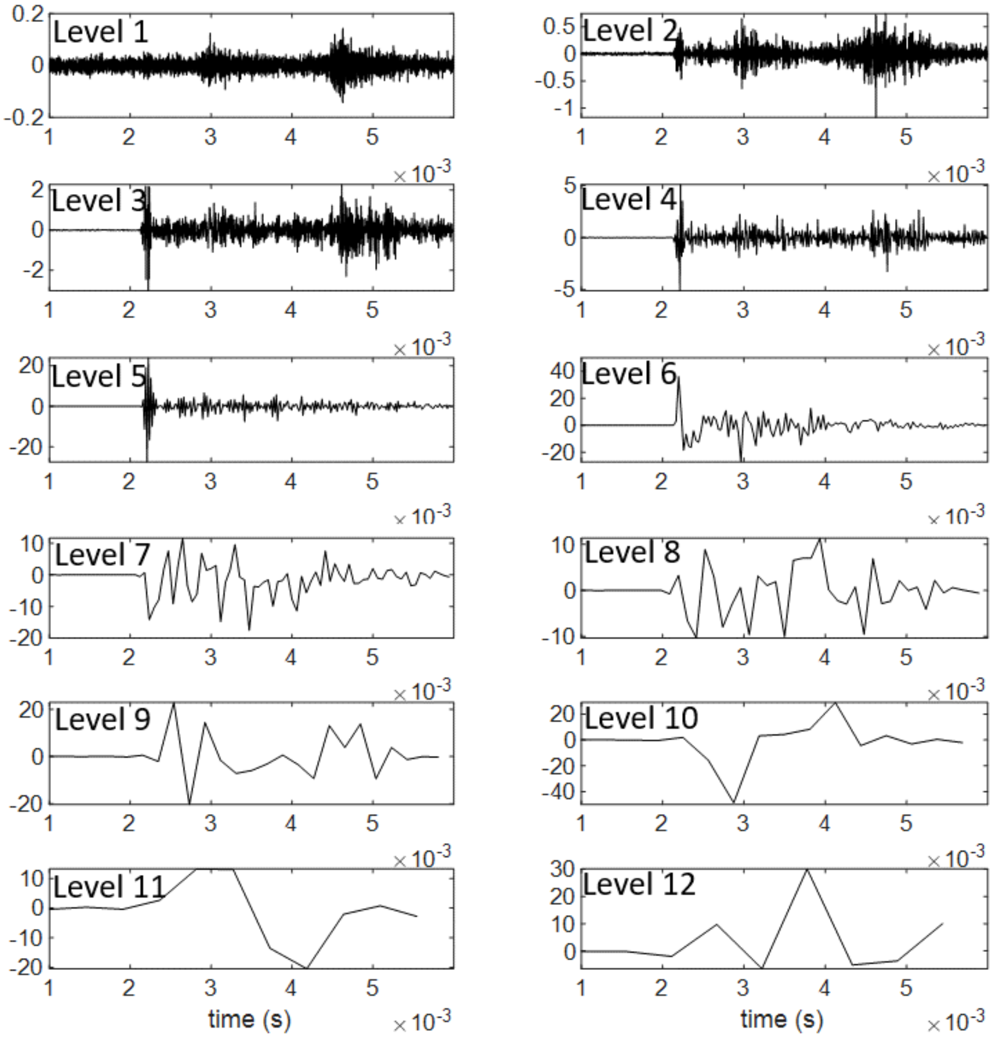

Figure IV.43. *RUPTUBE - 2^{nd} campaign, test 6: detail coefficients of a 12-levels DWT of signal AE 3.*

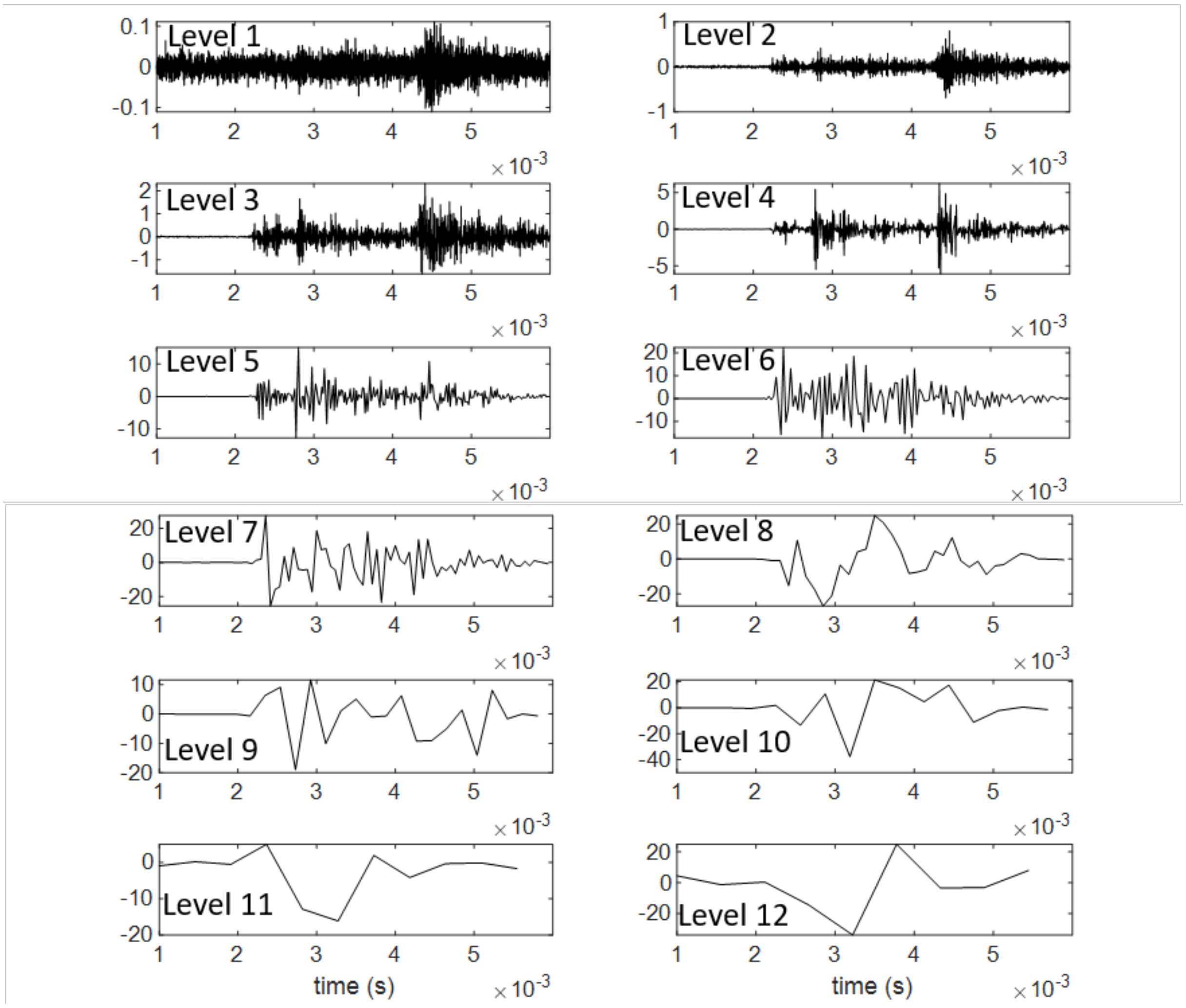

Figure IV.44. *RUPTUBE - 2nd campaign, test 6: detail coefficients of a 12-levels DWT of signal AE 4.*

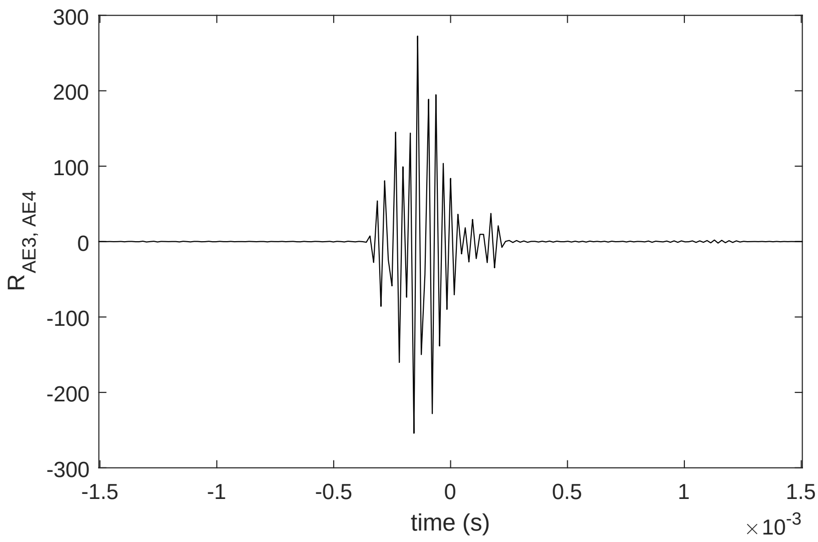

Figure IV.45. *RUPTUBE - 2nd campaign, test 6: cross-correlation between the wavelet detail coefficient 5 of signals AE 3 and AE 4.*

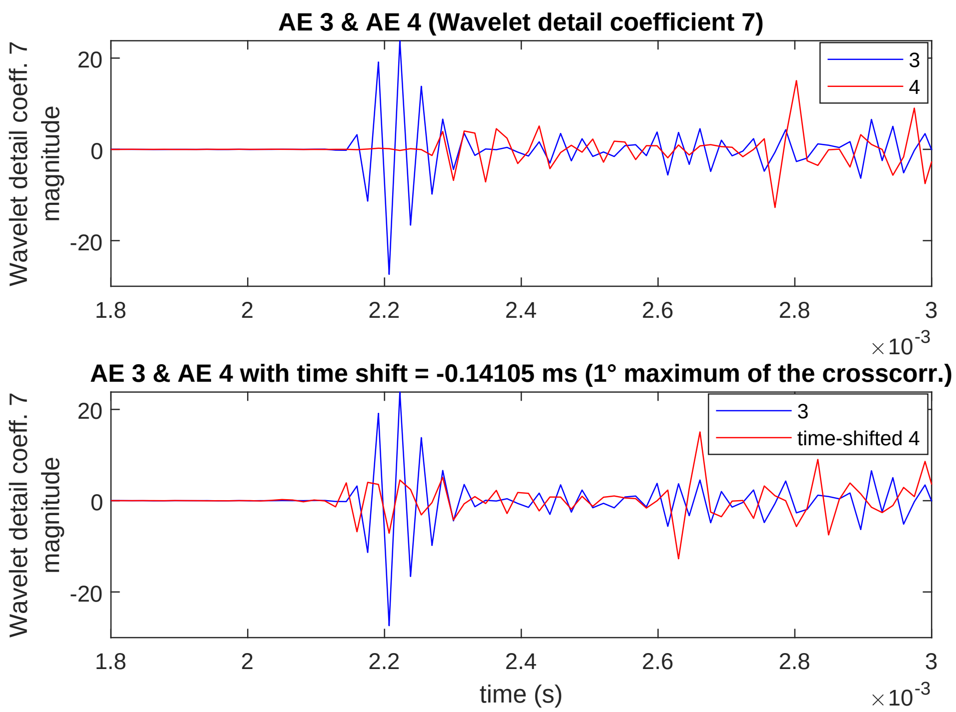

Figure IV.46. *RUPTUBE - 2nd campaign, test 6: verification of the estimated TDOA between the wavelet detail coefficient 5 of signals AE 3 and AE 4.*

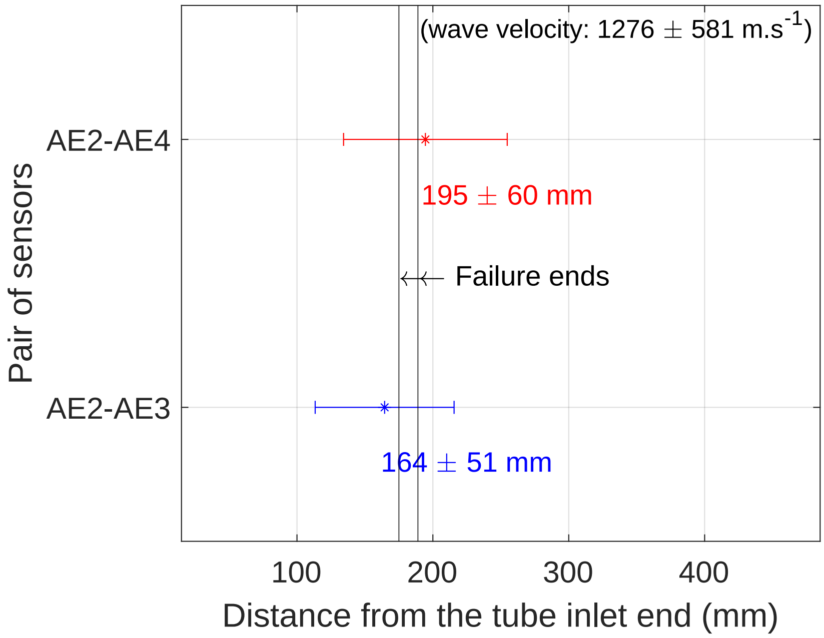

Figure IV.47. *RUPTUBE - 2nd campaign, test 6: source positions obtained by cross-correlation method applied on the wavelet detail coefficient 5 of AE sensors' signals.*

The error on the source position obtained with DWT-based method is slightly lower than the one of the EMD method results, but the EMD offers better accuracy. The two methods are anyway less efficient than the threshold crossing method results.

The same procedure is applied again, on band-pass filtered signals. The applied Band-Pass (BP) filter, on the frequency range [20;30] kHz, with the aim to isolate the common energy peak observed with the CWT views. As for the other extraction methods, results are presented in Fig. IV.48, IV.49, IV.50, and IV.51.

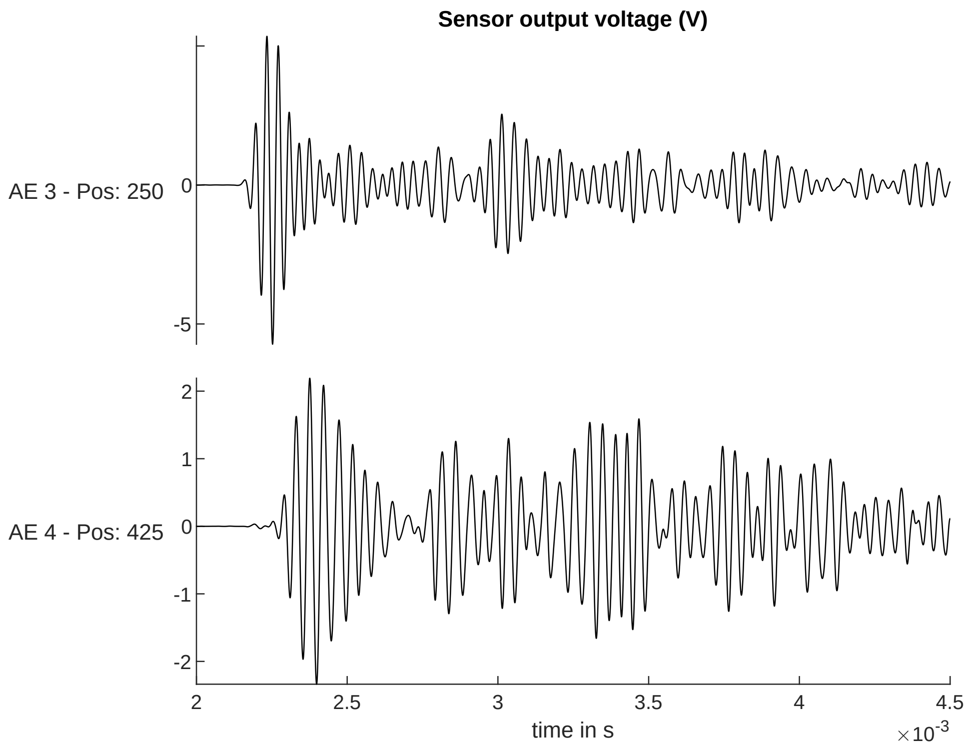

Figure IV.48. *RUPTUBE - 2^{nd} campaign, test 6: signals AE 3 and AE 4 after band-pass filtering.*

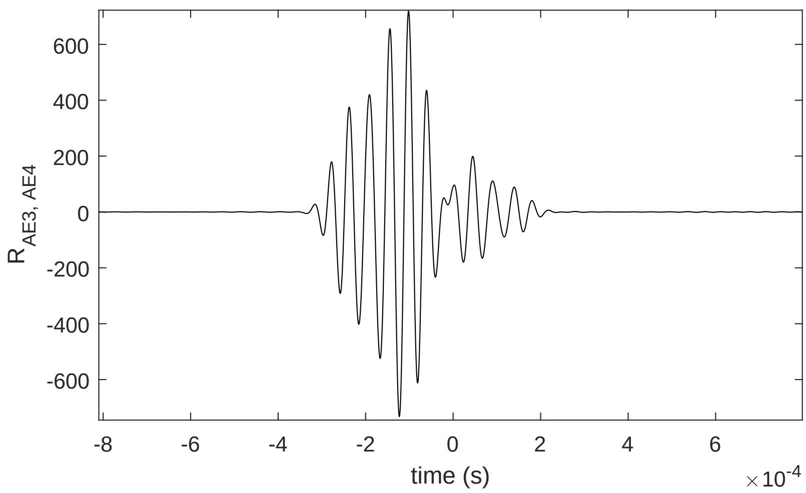

Figure IV.49. *RUPTUBE - 2^{nd} campaign, test 6: cross-correlation between the BP-filtered signals AE 3 and AE 4.*

The third maximum of the cross-correlation is the one corresponding to the most realistic time-shift.

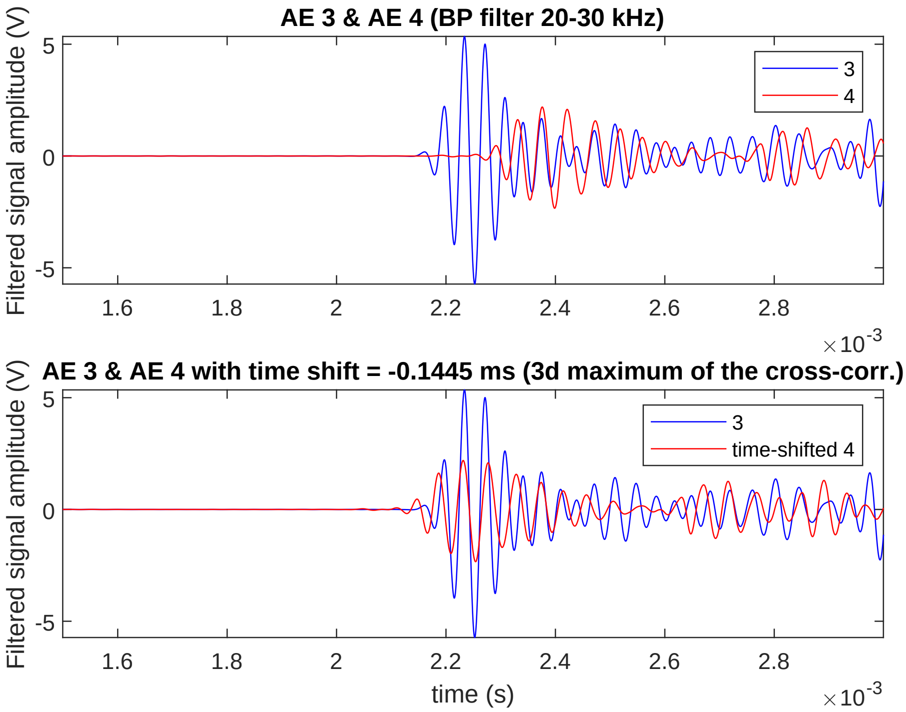

Figure IV.50. *RUPTUBE - 2nd campaign, test 6: verification of the estimated TDOA between the BP-filtered signals AE 3 and AE 4.*

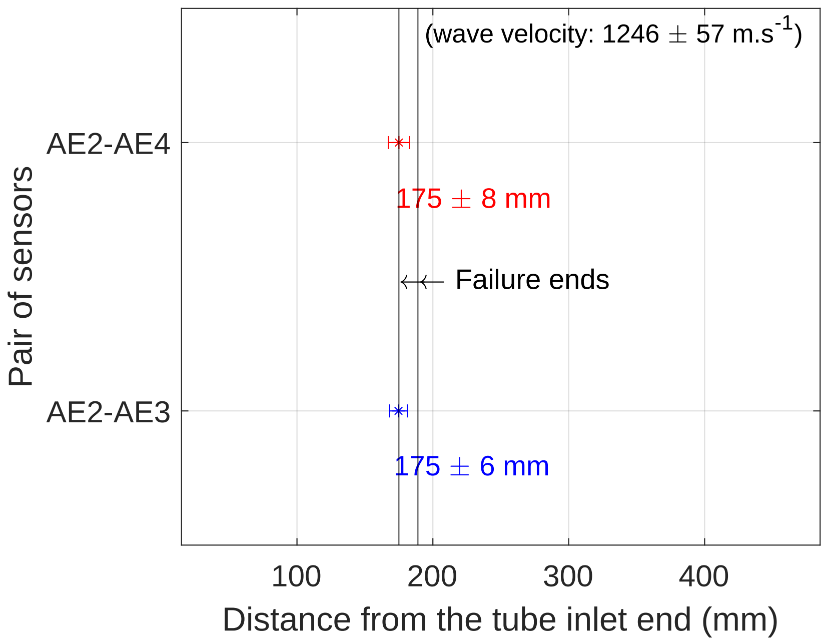

Figure IV.51. *RUPTUBE - 2nd campaign, test 6: source positions obtained by cross-correlation method applied to the BP-filtered signals.*

For source localization with AE sensors, the extraction of the components of interest by band-pass filter provides better results than the extraction by EMD or DWT. The reason is that the EMD of the AE sensors provide IMF with wide band spectra. Contrary to the expectation, each IMF seems to contain several propagation modes. Therefore, dispersion effects still have influence and cross-correlation does not give good results, although those effects are lower than on raw signals. Concerning the DWT, detail coefficients have also relatively wide band spectra (less than IMF from EMD, though) and in addition to that, the time resolution is lower than the initial signal's one, hence providing less accuracy on the TDOA.

As a conclusion, the efficiency of the methods consisting of extracting approximately monofrequency components and using the cross-correlation to determine the TDOA depends on several considerations: when using EMD or DWT for the extraction, the narrower the spectrum of the selected component, the less significant the dispersion effects, and thus, the more efficient the cross-correlation. Moreover, high frequency components should be preferred as they offer more time accuracy, especially with the DWT, where the time resolution of the detail coefficients decreases with the level of the decomposition. If a component of interest could be identified (by looking at a CWT or a STFT, for instance) and the EMD or the DWT do not provide a corresponding IMF or detail coefficient with a narrow band spectrum, a simple BP filter might be more efficient to extract that component. Nevertheless, the EMD and the DWT can actually allow to identify the component of interest beforehand, as it shows the amplitude and the time evolution of each component. Finally, concerning the cross-correlation, it was observed that the actual physical time-shift between two signals does not always correspond to the absolute maximum of the cross-correlation. Sometimes, a secondary maximum is actually related to the real time-shift. Therefore, care must be given to the choice of the cross-correlation maximum to consider to estimate the TDOA.

Actually, such methods are assumed to be more useful when first wavefronts are not steep enough to be accurately localized by threshold crossing, or when the background noise prevents to detect the first oscillations. They are not of major interest for RUPTUBE experiments, where the threshold crossing method works relatively well. However, testing them was useful to anticipate the potential needs in the experiments on the second device or in real reactors, where the surrounding flow may damp failure-induced waves and add significant noise in the measurements.

With high frequency amplifiers

During RUPTUBE experimental campaign, only one HF amplifier was available. Four additional amplifiers were later purchased. An additional test was performed on the RUPTUBE device with four broadband AE sensors and four HF amplifiers. The sensors were mounted on the tube as shown in Fig. IV.52.

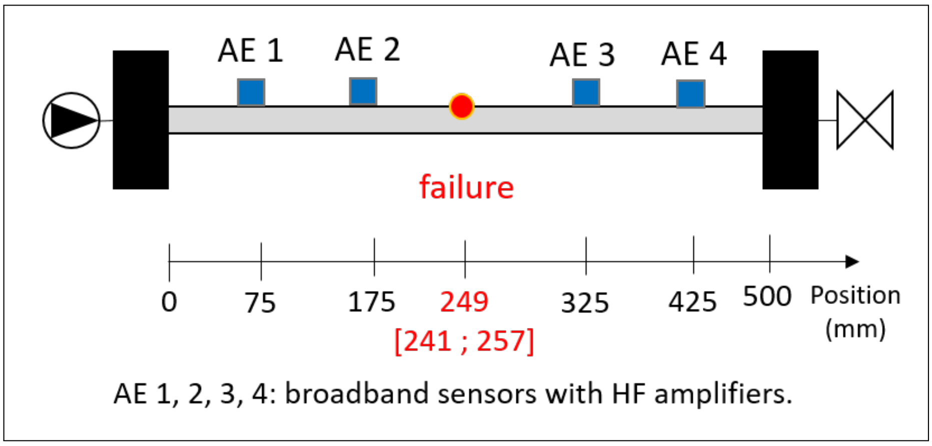

Figure IV.52. *RUPTUBE - 2nd campaign, HF amplifiers test: configuration.*

Time domain view of the obtained signals are shown in Fig. IV.53 and time-frequency domain view is depicted in Fig. IV.54.

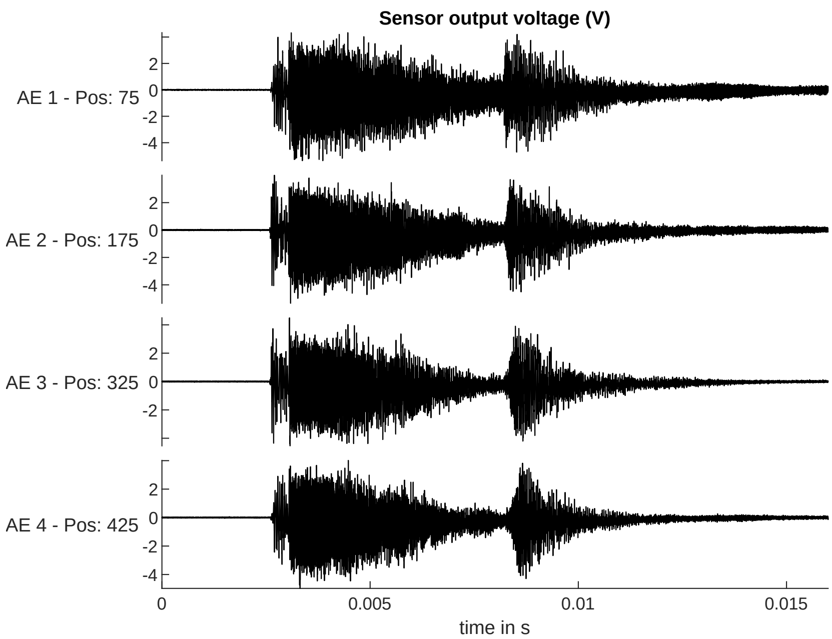

Figure IV.53. *RUPTUBE - 2nd campaign, HF amplifiers test: time domain view of the AE sensors' signals.*

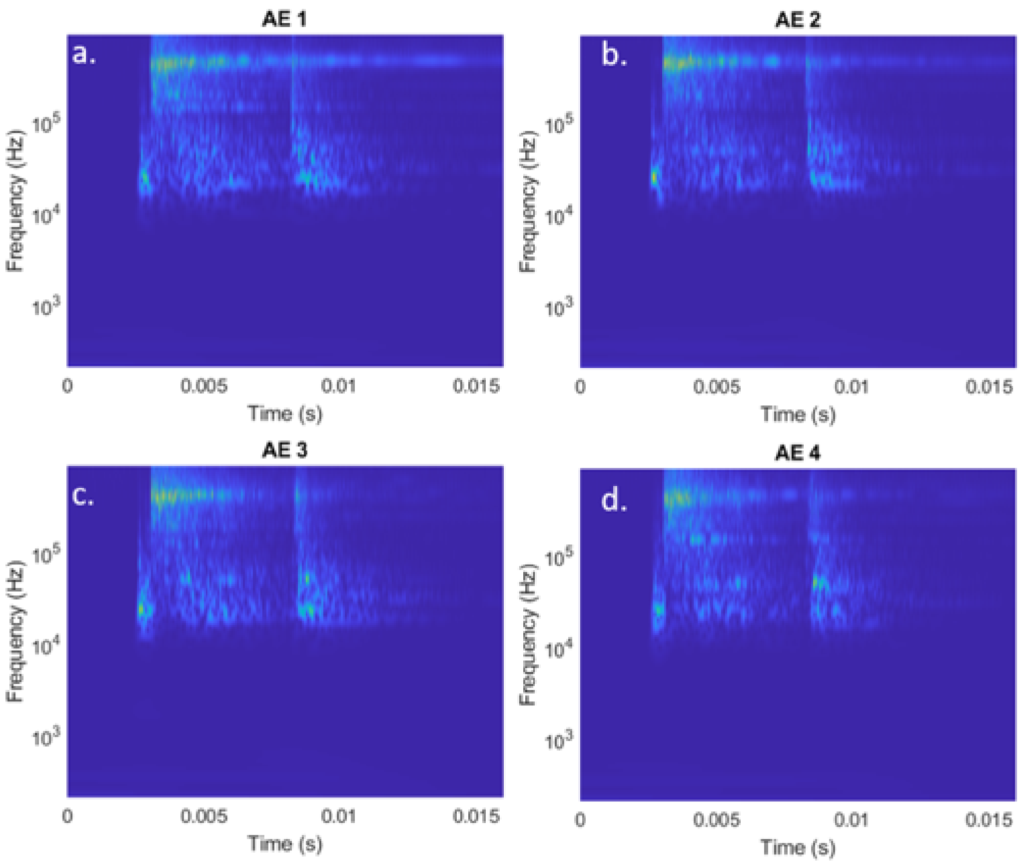

Figure IV.54. *RUPTUBE - 2nd campaign, HF amplifiers test: time-frequency views of the AE sensors' signals. CWT by Morse wavelets. a.: sensor 1, b.: sensor 2, c.: sensor 3, d.: sensor 4.*

Two peaks can be observed on each signals. The second peak, at about 8 ms is likely due to a second part of the failure. As it is shown in the picture of the failure after the tests, Fig. IV.56, it seems that the failure is divided in two parts. Unfortunately, the second peak is not steep enough to achieve an accurate localization of the associated source. Thus, only the first peak is treated here. A time and frequency magnification around this peak is shown in Fig. IV.55.

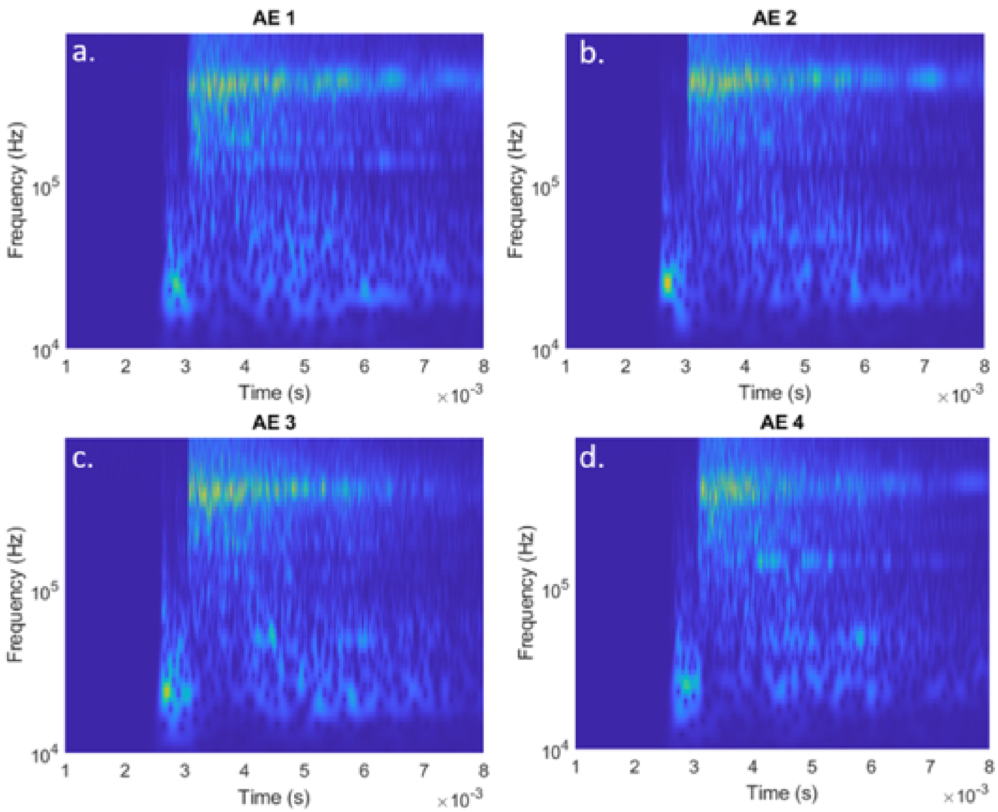

Figure IV.55. *RUPTUBE - 2nd campaign, HF amplifiers test: time-frequency views of the AE sensors' signals, magnification around the first peak. CWT by Morse wavelets. a.: sensor 1, b.: sensor 2, c.: sensor 3, d.: sensor 4.*

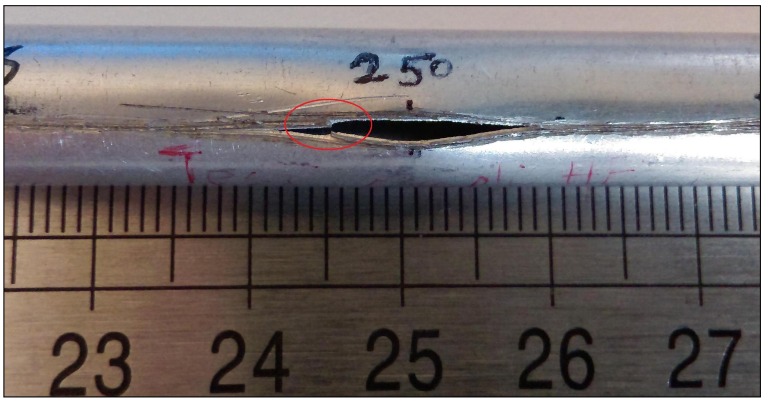

Figure IV.56. *RUPTUBE - 2nd campaign, HF amplifiers test: picture of the failure after the test.*

As observed in the measurements with LF amplifiers, the first detected waves exhibit a frequency peak around 25 kHz. With HF amplifiers, a later component can be observed around 460 kHz, which cannot be observed with LF amplifiers because of their bandwidth (0-200 kHz).

Firstly, the threshold crossing technique is directly applied on the raw signals which are already filtered by the 20 kHz HP analog filter included in the amplifiers. The aim is to achieve the detection of first arriving waves, with the same method as the one previously introduced (Sec. IV.4.2.2). Fig. IV.57 presents the verification of the TDOA estimated between sensors AE 1 and AE 2, which yields a wave velocity of 4762 $\pm$1229 m.s^{-1}. Fig. IV.58 shows the resulting source positions. If the wave velocity is estimated with AE 3 and AE 4 sensors, the obtained value is 5000 $\pm$ 1350 m.s^{-1} and the resulting source positions are shown in Fig. IV.59. Both velocity values are close to the theoretical quasi-longitudinal waves velocity (5090 m.s^{-1}).

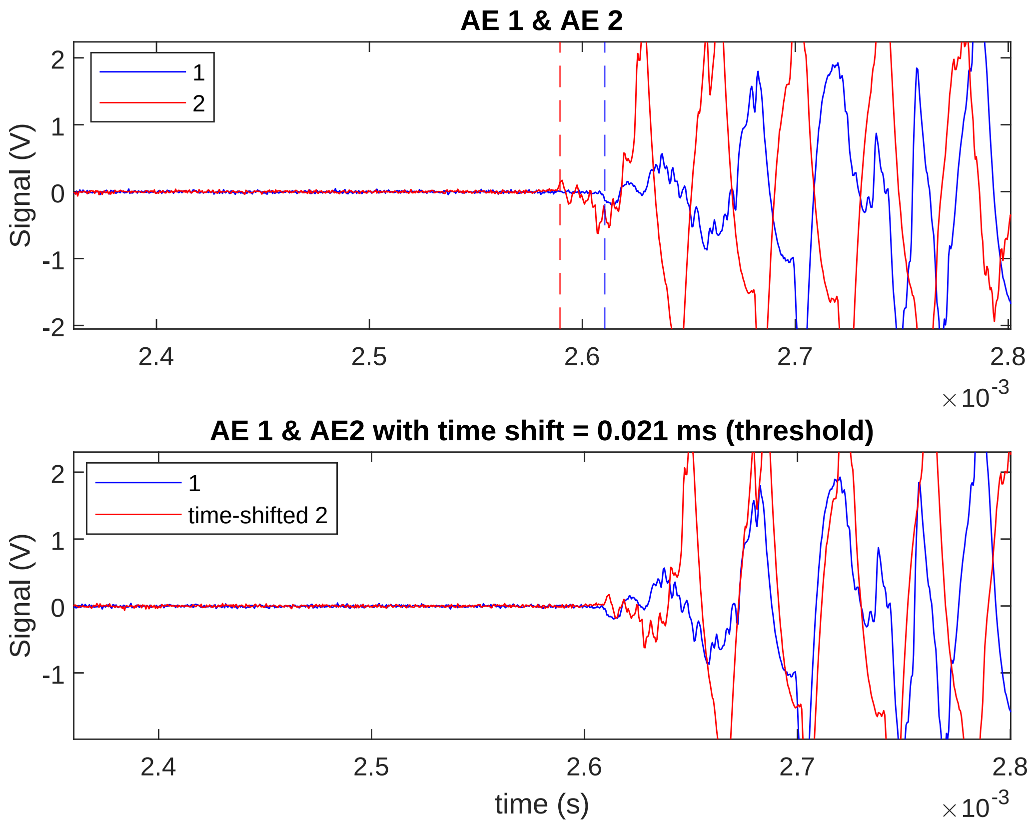

Figure IV.57. *RUPTUBE - 2nd campaign, HF amplifiers test: verification of the TDOA obtained by threshold crossing method on AE 1 and AE 2 signals.*

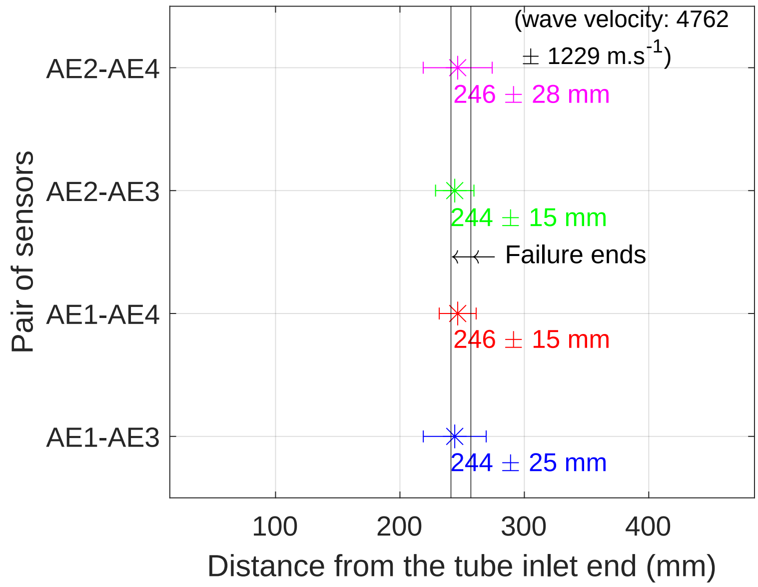

Figure IV.58. *RUPTUBE - 2nd campaign, HF amplifiers test: source positions obtained by threshold crossing method, considering the wave velocity estimated from AE 1 and AE 2. Indicated failure ends are observed after the test.*

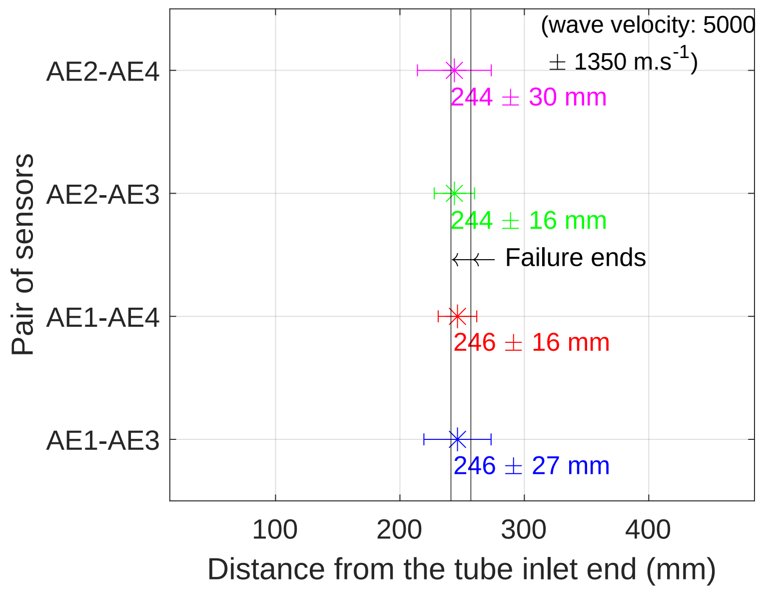

Figure IV.59. *RUPTUBE - 2nd campaign, HF amplifiers test: source positions obtained by threshold crossing method, considering the wave velocity estimated from AE 3 and AE 4. Indicated failure ends are observed after the test.*

Since the threshold crossing technique on raw signals provides relatively good results with the AE signals obtained with HF amplifiers, the other methods, which are more complex, were not tested on this data.

IV.4.2.3. Strain gauges

Only one test with strain gauges was carried out with the RUPTUBE device. The objectives of this test was to check the ability of strain gauges to detect a failure, to compare the response of 6 mm and 0.8 mm grid length gauges and to identify the kind of waves that have the most significant contribution in the measured signal.

One gauge of each type (6 mm and 0.8 mm grid length) was mounted on the tube. The failure was expected to occur at the middle of the tube and gauges were placed on each side of the failure. Gauges were instrumented with built-in Wheatstone bridges of the SIRIUS DeweSoft system, providing a bandwidth up to 100 kHz (with a 200 kHz sampling frequency).

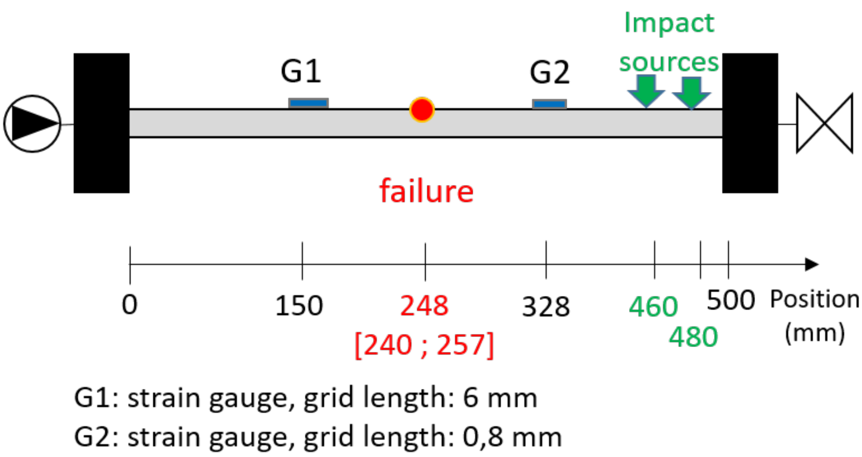

Figure IV.60. *RUPTUBE - 2nd campaign, gauges test: configuration.*

Before using the measured signals, they are filtered with a high-pass filter in order to remove the quasi-static component before the failure that is due to the pressure-induced swelling of the tube, which is relatively slowly released when the failure happens. A 2nd order Butterworth filter is considered as a good compromise between the frequency response slope and the distortion in time-domain (especially the ringing effect). The cutoff frequency is set at 75 Hz, so it removes the potential 50 Hz component generated by the electric supply network too. Signals are also denoised by discrete wavelet coefficients thresholding because the electromagnetic noise is quite high and, as shown by the DWT presented in Fig. IV.61, first coefficients mostly contain noise. Fig. IV.62 and Fig. IV.63 show respectively the raw signals and the HP filtered and denoised signals.

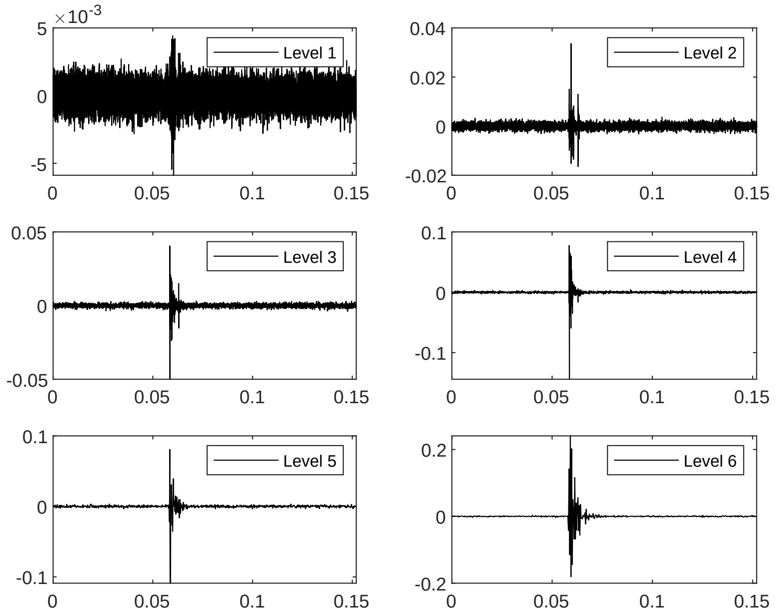

Figure IV.61. *RUPTUBE - 2nd campaign, gauges test: first detail coefficients of G1 signal DWT.*

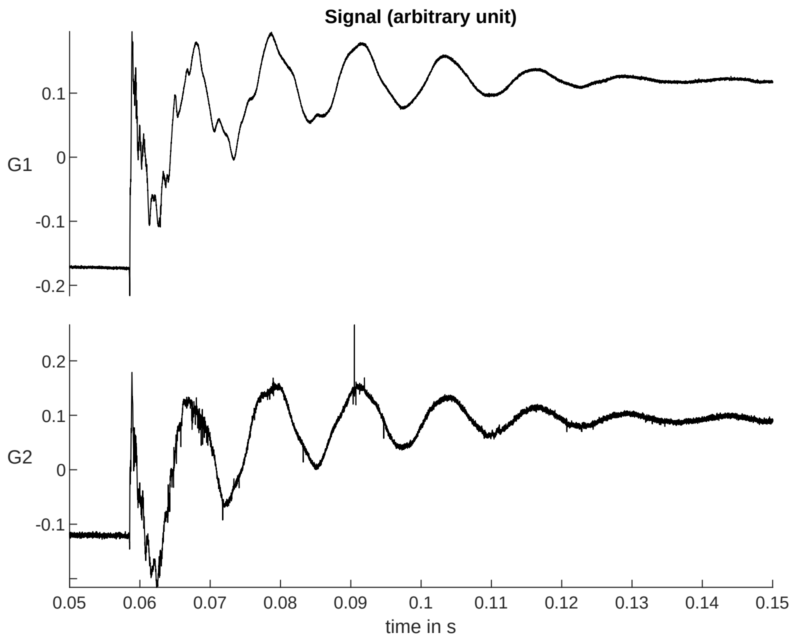

Figure IV.62. *RUPTUBE - 2nd campaign, gauges test: failure-induced raw signals.*

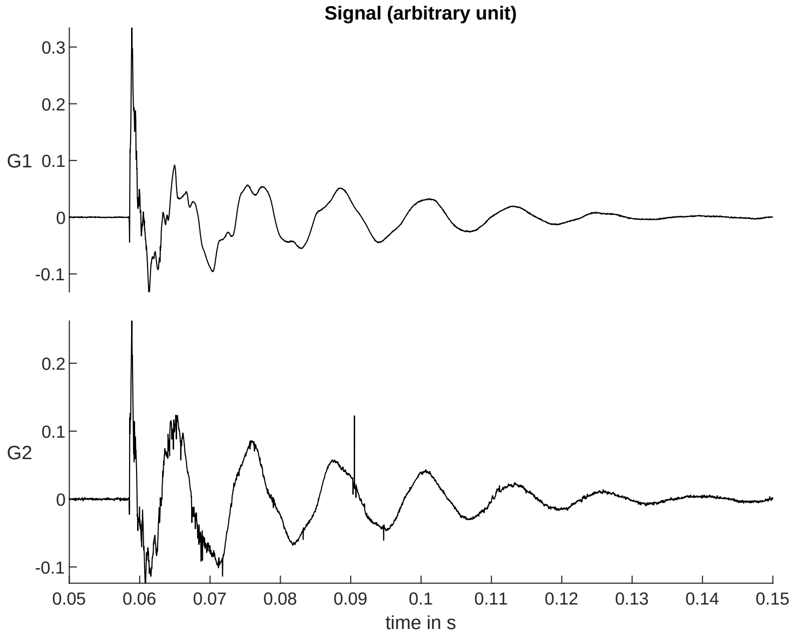

Figure IV.63. *RUPTUBE - 2^{nd} campaign, gauges test: failure-induced processed signals (HP filter at 75 Hz and DWT thresholding).*

Some hits can be observed after the failure on G2 signal (for instance, at 0.09 s). They are likely due to defects in the gauge mounting. Since their magnitude is significant, they are not removed by the wavelet thresholding. Since they do not affect the time localization of the studied event, it was not attempted to remove them.

In the first step of the analysis, the source position is considered as unknown. It is only assumed that the source is between the two sensors. In such a situation, it is impossible to determine the wave velocity (since the time of emission of the source signal is also unknown). Therefore, the wave velocity was estimated with an artificial impact source prior to the failure test. This artificial source was generated near an end of the tube. Two tests were done with different source positions, as shown in Fig. IV.60. In those configurations, wave velocity can be estimated with the two sensors independently from the source position. Signals obtained with one of the impacts (at 460 mm from the tube's end) are shown in Fig. IV.64. Those signals are processed in the same way as the failure-induced signals (HP filter at 75 Hz and denoising by wavelet coefficient thresholding). The TDOA is estimated with the threshold method and yields a wave velocity of 1271 $\pm$210 m.s^{-1}. The resulting wave velocity obtained with the impact at another position is exactly the same. Therefore, although the threshold is adjusted so that it detects the very first oscillations, resulting velocities are closer to the values obtained with AE sensor when the threshold is adjusted to locate the first high magnitude peak appearing after the first oscillations. Actually, contrary to AE sensors signals, gauge signals do not exhibit small oscillations before the high peak. Thus, whatever the threshold adjustment, it always detects the high peak. As previously explained, this peak is assumed to be related to first flexural guided waves mode. Although the gauges are mounted in the axial direction and should therefore especially detect longitudinal waves, it is not surprising that they are sensitive to flexural modes. Flexural guided waves modes, according to the terminology considered in the current document (introduced in Sec. II.1), consist in combinations of transverse and axial motions. It is however uncertain that the artificial impact source involves the same guided waves modes as the failure.

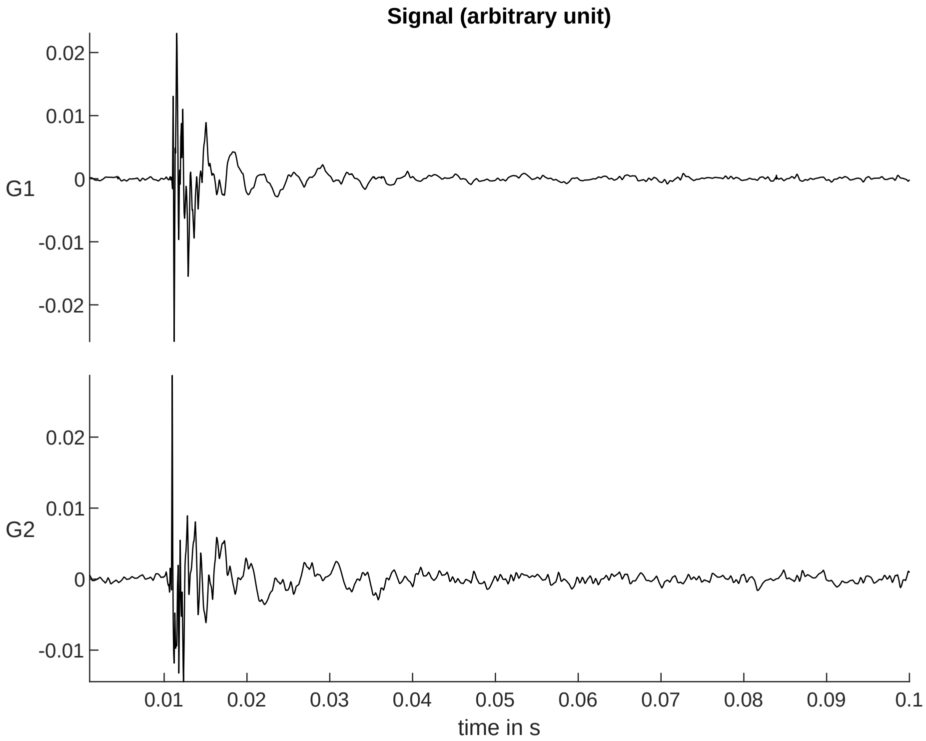

Figure IV.64. *RUPTUBE - 2^{nd} campaign, gauges test: signals obtained with an impact source at 460 mm from the tube's end.*

Finally, by assuming a wave velocity of $1271 \pm 210\,\mathrm{m.s^{-1}}$ and applying the threshold crossing method to the filtered failure-induced signals, the source position is estimated at 239 ± 17 mm from the tube end. The final failure observed after the test stretches from 240 to 257 mm from the tube end. Therefore, source localization with the strain gauges signals sampled at 200 kHz are relatively satisfactory. It is however recommended to use shorter and totally shielded wires, which was not the case in the presented test (wires were only partially shielded), to reduce the electromagnetic noise.

It can be noticed that a clear resonance appears on the measured signals (on test failure and impact source). Frequency of the oscillations are 76 Hz on the failure test signals, and 275 Hz on signals from the impact test. They are therefore related to different structural vibration modes. That was expected, since the source position is significantly different between the two tests (on the middle of the tube in the failure test, near an end in the impact test). By comparing their frequencies to the theoretical eigenfrequencies, it can be assumed that the 76 Hz oscillations are related to the first flexural vibration mode and the 275 Hz to the second flexural vibration mode. Moreover, this is consistent with the source position in relation to the corresponding mode shapes. This assumption can be more deeply confirmed if the travel velocity of those waves can be estimated and compared to the theoretical flexural wave speed, calculated in Sec. II.2. To this aim, the signal components corresponding to those resonances should be extracted in order to determine the TDOA, which is necessary to deduce the velocity. This time, TDOA can be determined by cross-correlation between the extracted component from the different signals. This technique is expected to work because the extracted components' spectra are concentrated around a single frequency. Therefore, the effects of the distortion due to small material defects and dispersion along the tubes are assumed to be small, and the signals should have similar aspects.

Firstly, the component extraction is attempted by an EMD of each signal. The EMD were computed after the filtering and denoising process described above. IMF obtained from the signals of the failure test are presented in App. H. It seems that IMF n°7 and n°8 are related to the 76 Hz resonance, on both G1 and G2 signals. Therefore, the sum of those two IMF is considered as the resonance-related component to extract.

Then, a velocity estimation can be attempted by determining the TDOA between the extracted components. In the failure test configuration, since there are only two sensors and the failure is between them, it is not possible to estimate the velocity without knowing the source position. The velocity can be estimated independently from the source position in the impact test configuration, but the result cannot be used for the failure test, since it is associated to another flexural vibration mode, hence a different velocity. Nevertheless, the velocity of the oscillations appearing in the failure test signals can be estimated by assuming a source position and using Eq. (IV.11) to express c as a function of x_s, Δt, x_i and x_j. To this aim, the source is assumed to be at the center of the observed final crack, *i.e.* 248 mm from the tube's end. Thus, the velocity is given by:

$$c = \frac{x_i + x_j - 2x_s}{\Delta t}, \tag{IV.12}$$

where $x_s = 248 \cdot 10^{-3}$ m is the source position, $x_i = 150 \cdot 10^{-3}$ m and $x_j = 328 \cdot 10^{-3}$ m are the positions of sensors G1 and G2, and Δt is the TDOA determined from the position of the maximum of the cross-correlation between G1 and G2 signals. With that formula, the uncertainty on c is: $\delta c = |\frac{1}{\Delta t}|\delta x_i + |\frac{1}{\Delta t}|\delta x_j + |\frac{2}{\Delta t}\delta x_s + \frac{x_i+x_j-2x_s}{\Delta t^2}|\delta(\Delta t)$. The uncertainty on the source position is based on the final crack length, so $\delta x_s = \pm 10$ mm and the uncertainty on Δt when deduced by cross-correlation is the sampling period, *i.e.* $\delta(\Delta t) = \pm 1/(200 \cdot 10^3) = \pm 10^{-5}$ s. Like previously, uncertainty on the sensor position is ± 2 mm. Fig. IV.65 shows the cross-correlation computed between the extracted components (sums of IMF 7 and 8) of G1 and G2 signals from the failure-test. Time-shifts equal to the first local maxima of the cross-correlation are applied to G2 signal, which is superimposed to G1 on Fig. IV.66. It yields a velocity of 95 ± 121m.s^{-1}. There is 35 % of error compared to the theoretical velocity of flexural vibration waves at 76 Hz, about 71m.s^{-1}. Moreover, the uncertainty is very large. It is a consequence of the fact that the source is near the exact middle point between the two sensors and, therefore, the TDOA is very small. It is clearly depicted on Fig. IV.66 by the fact that the signals overlay quite well to each other even without time-shift.

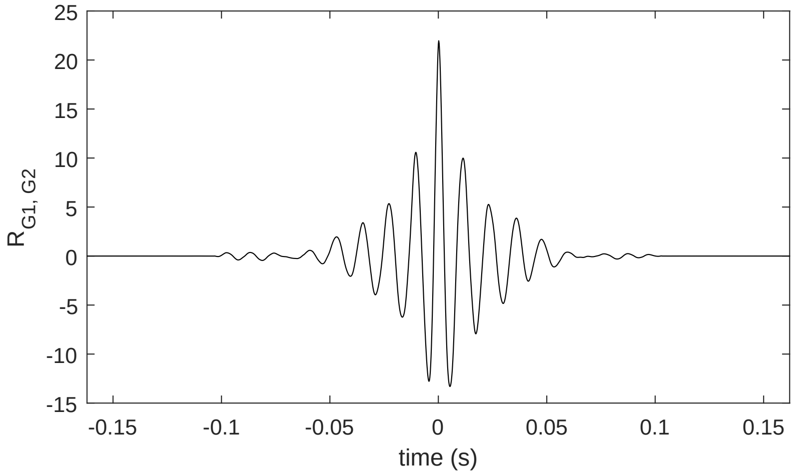

Figure IV.65. *RUPTUBE - 2nd campaign, gauges test: cross-correlation between the extracted components of G1 and G2 signal from the failure test.*

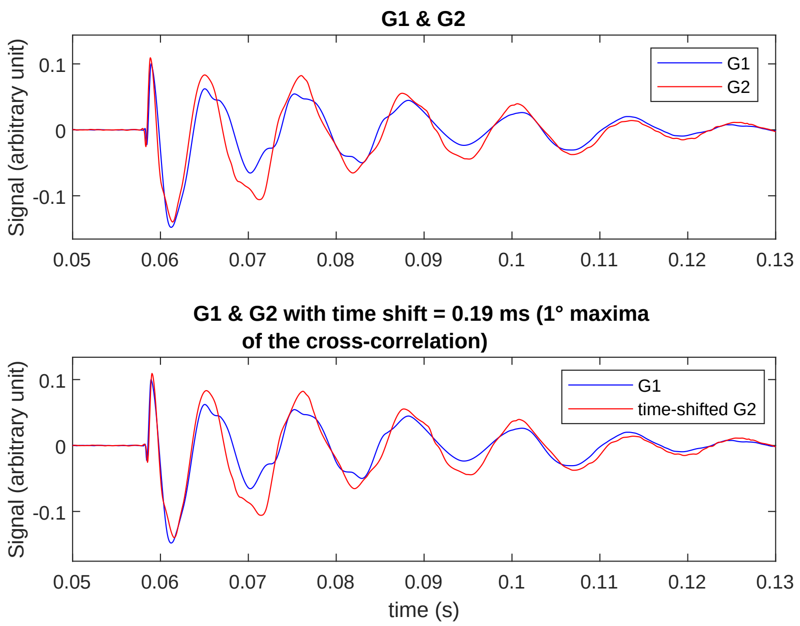

Figure IV.66. *RUPTUBE - 2nd campaign, gauges test: superimposition of G1 and G2 extracted components from the failure test.*

Concerning the oscillations appearing in the impact test, their velocity can be deduced independently from the source position, as explained in Sec. IV.4.2.2. Although the kind of waves studied in the mentioned section (high frequency quasi-longitudinal waves) is different from the low frequency structural vibrations that are currently studied, the expression of wave velocity is the same. After the extraction of the relevant IMF (results of the EMD are given in App. I, the extracted component is shown in Fig. IV.67), the TDOA was estimated in the same way as for the failure test signals. It finally yields a velocity of

$106 \pm 4 m.s^{-1}$, which means a 21 % error compared to the theoretical velocity of flexural vibration waves at 275 Hz, estimated at 135 $m.s^{-1}$.

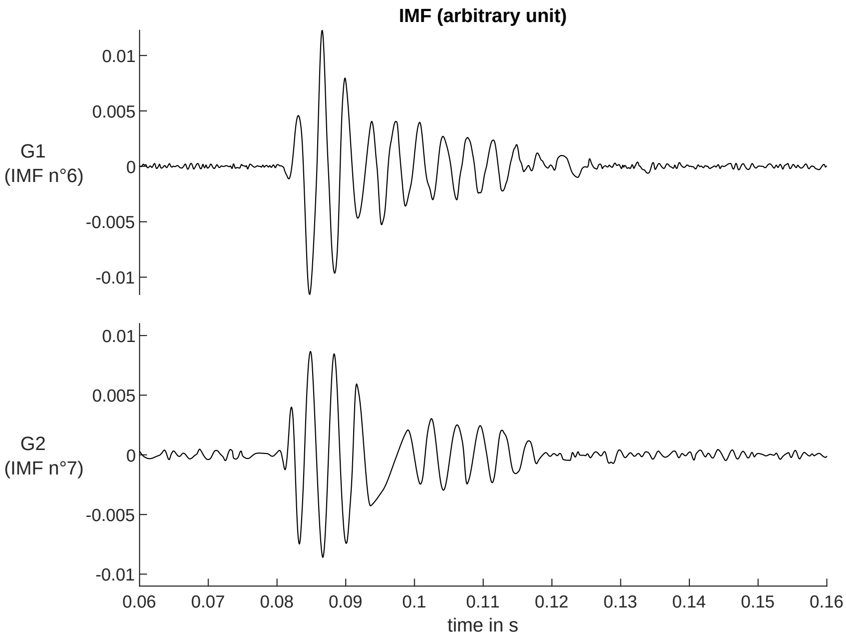

Figure IV.67. *RUPTUBE - 2^{nd} campaign, gauges test: IMF n°6 from the G1 signal EMD and IMF n°6 + IMF n°7 from the G2 signal EMD. Signals measured with an impact at 460 mm from the tube's end.*

As a conclusion, tests with strain gauges showed that those sensors are sensitive to flexural guided waves. Pure longitudinal waves did not appear on the measured signals. However, the threshold crossing method can work on first detected waves whatever the associated type of guided waves (longitudinal, torsional or flexural). In lower frequency range (about some hundreds Hz), the measured signals exhibit a relatively long resonance following the transient stage. Based on the frequency of the resonance, it seems to be mostly related to first flexural vibration modes, whether the source is a failure or an impact. This assumption could be confirmed by the extraction of the components associated to the resonance and the estimation of their travel velocity by cross-correlation technique. Resulting values are rather close to theoretical flexural vibration wave velocities at the same frequency. As assumed in Sec. IV.3.5.2, the relative contribution of each mode depends on the source position in relation to the mode shape. However the specific configuration of the failure test was not optimal for TDOA estimation, since the failure occurred almost perfectly between the two sensors, implying a small time difference.

In the studied bandwidth (50 Hz - 100 kHz), the small gauge (0.8 mm grid length) did not show any benefit compared to the longer one (6 mm). Actually, the small gauge seems even less relevant because its output exhibits higher noise level. Moreover, from a practical point of view, small gauges are more difficult to apply than longer ones, which results in higher risk of mounting defects.

Finally, strain gauges signals can be used to estimate velocity or source position either by threshold crossing method on the beginning of the event, or by cross-correlation on specific components related to structural vibration modes, whose spectrum is concentrated around a single frequency (otherwise, dispersion affects the results). Good results can be achieved within a frequency range of 50 Hz to 100 kHz, and 6 mm long gauges are suitable for such a range.

IV.4.2.4. High-speed camera

Initially, the high-speed camera was intended to capture the tube motion over a significant part of its length, in order to have vibration measurements at distant points. The measurements should be complementary to accelerometers' ones for in-air experiments and should make vibration measurements possible when tubes are in water without immersing accelerometers. However, a compromise between picture shape, dimension and sample rate is imposed by the specifications of the device. As a consequence, it is actually not possible to get, at the same time, a high enough sampling rate (20 kHz would be necessary to cover the accelerometer bandwidth, but the device is limited to 15 kHz), a spatial accuracy and an appropriate angle of view to capture the wanted part of the tube.

However, this tool could be used to determine what is the most significant motion in term of magnitude and to confirm that the oscillations observed after accelerometers' saturation correspond to actual flexural vibrations. To this aim, a small part of the tube was filmed and a specific point was selected on the first picture of the movie and automatically tracked on the following pictures (with a suitable software). Thus, two-dimension displacement of the selected point is obtained. The displacement in each direction can be plotted. Fig. IV.68 shows, as example, three frames extracted from the movie recorded during the failure test 6. The tracked point is indicated by a yellow mark (the mark is bigger than the actual tracked point). Fig. IV.69 shows the displacement of this point in the direction perpendicular to the tube axis. Parameters of the camera were a sampling rate of 8 kHz (*i.e.* 8 000 frames per second) and a dimension of 1024x56 pixels. The focus was adjusted so that one pixel corresponds to 0.25 mm on the tube, hence a captured area of about 256x14 mm² and a spatial resolution of 0.25 mm. The selected point is located at 180 mm from the tube's end (at the expected position for the failure). The graph exhibits important oscillations with a frequency of 89 ± 10 Hz. It shows that the first flexural mode contribution is significant. Because of the direction of the motion, those oscillations are obviously related to flexural vibrations, and the comparison of their frequency to the theoretical eigenfrequencies indicate that they are related to the first flexural mode.

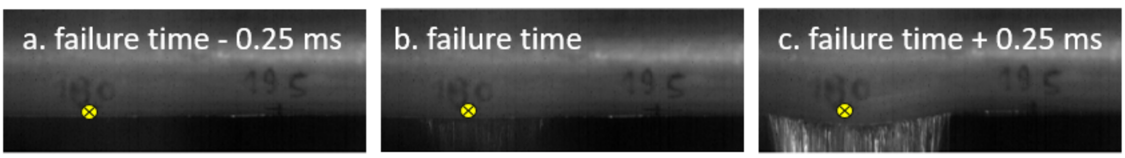

Figure IV.68. *RUPTUBE - 2nd campaign, high-speed camera test (failure test 6): three frames extracted from the movie, a: about 0.25 ms before the failure, b: first frame where the failure is visible, c: about 0.25 ms after the failure.*

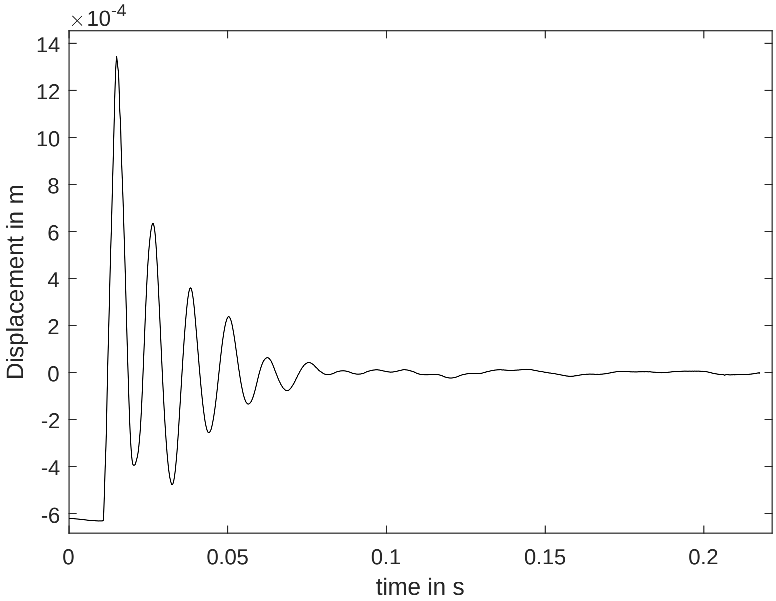

Figure IV.69. *RUPTUBE - 2^{nd} campaign, high-speed camera test (failure test 6): transversal displacement of a point on the tube.*

A test was performed to compare a saturated accelerometer signal with a tracked point motion, in order to determine the origin of the oscillations following the accelerometer's saturation. The source was an impact at 240 mm from the tube's end, strong enough to bring the accelerometer to saturate. The camera filmed the accelerometer, placed at 260 mm from the tube's end, and the tracked point was located on the accelerometer. Fig. IV.70 shows the superimposition of the tracked point's displacement and the signal of the accelerometer, which saturated. Acceleration of the tracked point that could be, theoretically, determined by a double-differentiation of the displacement is not shown because, some errors in the point tracking induce small non-physical variation in the computed displacements, which are slightly visible on the displacement history but result in significant errors in the acceleration.

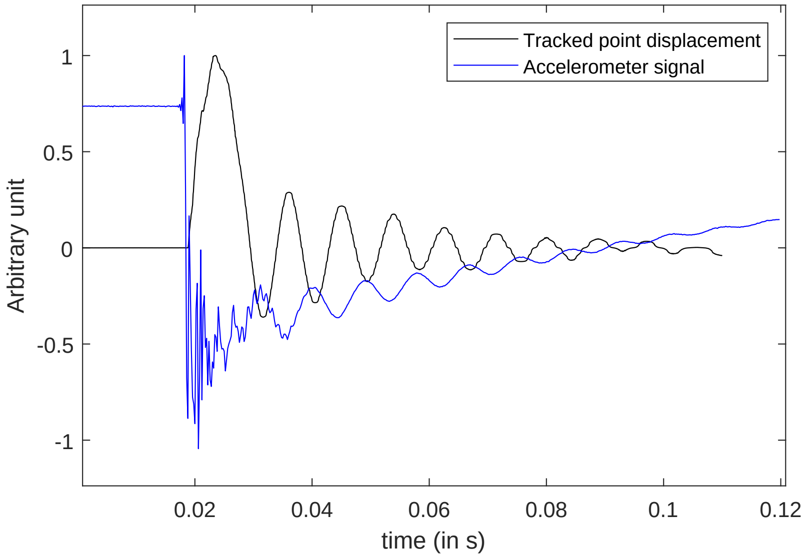

Figure IV.70. *RUPTUBE - 2nd campaign, camera test: comparison between accelerometer signal and tracked point displacement from high-speed camera pictures.*

Once again, the contribution of the first flexural mode is clearly visible on the tracked point motion. Moreover, it shows that the oscillations following the accelerometer's saturation overlays well with the filmed point motion. Thus, it can be reasonably concluded that the oscillations in the accelerometer's signal correspond to actual flexural vibrations. Several similar tests were performed (with other source's and sensor's positions) and led to the same conclusion.

As a conclusion, high-speed camera allowed to determine that the low-frequency oscillations that follow the saturation in the accelerometers' signals are related to actual physical vibrations, and are not due to electronic components' failure.

IV.4.3. Synthesis of the results of failure tests

The analysis of all the failure tests are described in App. J. In the current section, only a synthesis of the source localization results is presented. Since the accelerometer signals are eventually not usable for source localization (because of saturation), the tests 2, 3, 4 and 5 are not considered here. Table IV.9 shows for each test the value of the estimated velocity and the error on the resulting source position. The error on the source position is taken as the difference between the estimated position and the point between the final failure edges observed after the test. For each test, the half length of the final failure is also given. Thus, if the error on the estimated source position is less than the half failure length, it means that the estimated position lies between the edges of the real failure, hence in the range of the possible source position.

Test	Method for the TDOA estimation	Sensor pair for the velocity estimation	Estimated velocity (m.s^{-1})	Sensor pair for the failure position estimation	Error on the failure position (mm)	Uncertainty on the estimated failure position (mm)	Half-length of the real failure (mm)
1	Threshold crossing	AE1 - AE2	2941 ± 550	AE1 - AE 3	8	± 23	8
				AE1 - AE 4	7	± 13	8
				AE2 - AE 3	8	± 13	8
				AE2 - AE 4	7	± 13	8
		AE3 - AE4	2985 ± 565	AE1 - AE 3	7	± 23	8
				AE1 - AE 4	7	± 14	8
				AE2 - AE 3	8	± 13	8
				AE2 - AE 4	8	± 19	8
6	Threshold crossing	AE3 - AE4	4865 ± 603	AE2 - AE 1	15	± 21	7
				AE2 - AE 3	8	± 18	7
				AE2 - AE 4	8	± 7	7
	EMD + cross-corr.	AE3 - AE4	1241 ± 57	AE2 - AE 3	20	± 6	7
				AE2 - AE 4	29	± 6	7
	DWT + cross-corr.	AE3 - AE4	1276 ± 581	AE2 - AE 3	18	± 51	7
				AE2 - AE 4	13	± 60	7
	BP filter + cross-corr.	AE3 - AE4	1246 ± 57	AE2 - AE 3	7	± 6	7
				AE2 - AE 4	7	± 8	7
7	Threshold crossing	AE3 - AE4	5171 ± 682	AE2 - AE 1	7	± 24	7
				AE2 - AE 3	1	± 25	7
				AE2 - AE 4	1	± 37	7
HF amplif. test	Threshold crossing	AE1 - AE2	4762 ± 1229	AE1 - AE 3	5	± 25	8
				AE1 - AE 4	3	± 15	8
				AE2 - AE 3	5	± 15	8
				AE2 - AE 4	3	± 28	8
		AE3 - AE4	5000 ± 1350	AE1 - AE 3	3	± 27	8
				AE1 - AE 4	3	± 16	8
				AE2 - AE 3	5	± 16	8
				AE2 - AE 4	5	± 30	8
Gauges test	Threshold crossing	G1 - G2	1271 ± 210	AE2 - AE 1	9	± 17	8
	EMD + cross-corr.	G1 - G2	95 ± 121	No source localization			

Table IV.9. *Synthesis of failure tests results regarding velocity and failure position estimations.*

Concerning the estimated velocities, it can be noticed that they are globally distributed around three values: around 1250 m.s^{-1}, around 4950 m.s^{-1}, and around 2960 m.s^{-1}.

The first value is close to both the velocity of the first flexural guided wave modes, referred as F(1,1), around 25 kHz (1500 m.s^{-1}, see Sec. IV.3.4), and the sound velocity in water (additional experiments would be necessary to discriminate those two propagation phenomena). This value is obtained either by the threshold crossing method applied to the strain gauges' signals, or the methods that involve the components corresponding to the significant peak observed around 25 kHz applied to the AE sensors' signals. The response of the strain gauges is assumed to be relatively flat, and they were mounted on the tube in a way that they are especially sensitive to longitudinal waves. Therefore, the fact that they actually detected the F(1,1) mode and not the quasi-longitudinal waves that arrived before this mode (as it is proved by the AE sensors' signals) shows that, on the acquisition frequency range of the strain gauges, the flexural guided waves have a more significant contribution than the quasi-longitudinal ones. It can be noticed that it was also the case in the simulation presented in Sec. IV.3.4, despite the simulated source parameters were chosen arbitrarily since no information was available about the actual failure-related source.

The second value (4950 $m.s^{-1}$) is close to the theoretical quasi-longitudinal wave velocity in an aluminium beam or tube (5090 $m.s^{-1}$ according to the formula given in Sec. II.1). It is the highest possible velocity in such a tube. In the experimental signals, it corresponds to the first detected waves in the AE sensors' signals, found by the threshold crossing method.

The third value (2960 $m.s^{-1}$) was obtained by the threshold crossing method applied to AE sensors signals of Test 1, while the same method applied to the other tests provided the second value, mentioned above. That velocity is likely related to the first torsional guided wave modes, which corresponds to transversal waves, whose theoretical velocity is about 3100 $m.s^{-1}$. However, it could not be explained why the first test only leads to detect those waves instead of the quasi-longitudinal waves that are supposed to arrive before transversal ones and, thus, hide them. Quasi-longitudinal waves in that test might have very low amplitude, which could explain why transversal waves were detected, but the reason for that remains unknown.

It can be noticed that all those three values tend to be slightly lower than the theoretical corresponding velocities. It may be due to an actual Young modulus lower than the value considered in the calculations, or an higher actual density. The average density of the actual tubes was experimentally estimated and was found to be 2781 $\pm$ 154 $kg.m^{-3}$, while the value considered in the calculation is 2700 $kg.m^{-3}$. The Young modulus could not be experimentally estimated. In any case, the problem of the lack of information about the tube material properties should be solved before any attempt of an accurate investigation of the differences between experiments and theory.

IV.4.4. Conclusion of RUPTUBE experiments

Regarding the feasibility of the technical solution designed for tube failure generations, and to the tests of various kinds of acoustic and vibration instrumentation, RUPTUBE experiments' objectives are reached. The pressurization system worked and its specifications ensured its tightness. Therefore, similar specifications can be used for the final mockup.

The objective of a reliable failure pressure estimation method is not achieved. The analytical model was not validated, and no reliable trend could be inferred from experimental results. Nevertheless, they show that a failure can be easily reached under 100 bar with 0.5 mm thick aluminium tubes. For a better repeatability regarding failure pressure, it is wise to make initial cracks by electro-discharge technique, as it was done for the first RUPTUBE campaign. Such a technique offers a crack dimension accuracy of about 20 μm ([138]). However, because of time and budget concerns, all the cracks after the first RUPTUBE campaign were machined with classical hand-held tool. That way is time and cost saving but it implies low accuracy on the crack dimension (about 0.25 mm), hence a low predictability in the failure pressure.

Instrumentation tests proved that AE sensors and strain gauges are efficient tools to detect and localize the failure. However, some uncertainties remain because it was not possible to separate dispersion effects from the imperfection of sensors mountings and the unreliability of tube properties. Indeed, the supplied aluminium tested tubes exhibit geometrical inconsistency (some 10^{-2} mm variations in diameter and thickness along the tube), and might have heterogeneity in material properties too. Two different suppliers were resorted to, but both supplied such low quality tubes. The remaining possibility would be to order custom-made tubes, but it would imply much higher costs. Despite the low quality of the test samples, measurements enable to localize the failure with acceptable reliability and accuracy (about one or two centimeters, along 50 cm tubes). It was possible to test different methods (TDOA estimation based on threshold crossing detection on raw signals, or on cross-correlation between signals processed with various tools, such as band-pass filters, DWT or EMD). If dispersion effects could be isolated and properly estimated, thanks to fully controlled properties of the tubes, it would be possible to apply inverse problem methods to get more information about the failure. The possibilities of inverse problems would not only consist in a better source localization, but also in a reconstruction of the source signal (examples of inverse methods applied to pulse-like source identification are presented in [139] and [140]).

Concerning the study of first structure vibration modes with accelerometers, the chosen sensor model was eventually ill-suited to study such failures because of a too narrow full scale range, but the general idea of using accelerometers should still be considered. Despite the saturation of the chosen accelerometers, it proved that information about the excitation source and boundary conditions can be obtained by frequency domains analysis of accelerometer signals. It also showed a design mistake in the RUPTUBE device, which implies uncontrollable variations in the properties of the tube supports. Thus, this mistake was corrected for the next experimental device. Moreover, it is still assumed that accelerometers can provide information about FIV in case of an external flow, like in a real reactor or in the next experimental device. For further studies, it is however recommended to use charge-mode accelerometers or less sensitive IEPE in order to maximize the sensor's full scale range and avoid limits due to integrated electronics.

IV.5. Second experimental campaign: MAQAC

RUPTUBE was intended to be a preliminary test bench to help the design of the final experimental device, called MAQAC (*MAQuette pour l'étude du comportement Acoustique d'un Crayon combustible*, in english: "Mockup for the study of the acoustical behavior of a fuel rod").

The final experimental device consists of the tested tube and the same pressurization system than RUPTUBE's, inserted in a test section connected to a water loop. As a consequence, in addition to RUPTUBE's features, MAQAC enables the reproduction of a fluid flow around the fake rod (*i.e.* the tested tube). As the device was eventually delivered later than expected, the experiments could not be carried out before the writing of the current document but are currently in progress. The design of the device is presented in Sec. IV.5.1.1, and the experimental plan is introduced in Sec. IV.5.2.

IV.5.1. The device

The objectives defining specifications of the device correspond the global objectives of the experimental approach, given in Sec. IV.1.

IV.5.1.1. Specifications of the device

Technical functions

From those objectives, technical functions of the device are defined :

- Holding of the fake rod (*i.e.* the test tube) and possibility to remove it for replacement,
- Failure of the rod at a chosen location,
- Fluid flow around the rod, with a variable velocity from 0 to 4 m.s^{-1},
- Vibration and pressure measurements close to the source and upstream and downstream from the source,
- Several simultaneous measurement points distributed along the rod and in the surrounding fluid,
- Measurement points in the inlet and the outlet sections, for both fluid pressure waves and structural waves.

Technical constraints

The test section has to contain two different water systems: the first one, referred to as "circulation system", to generate the flow around the rod, the second one, referred to as "pressurization system", to increase the pressure inside the rod and generate the failure. Both system are filled with water.

Fluid flow around the rod requires the circulation system to be tight up to 5 bar of relative pressure, and the sensors to withstand water. Moreover, it is necessary to place the rod in an external transparent tube (in PMMA, with a thickness not larger than 40 mm), to make optical measurements possible. The narrow space between the rod and the inner wall of the external tube, which is intended to be representative of a real device, restricts the size of the sensors that are mounted on the tube.

The parts containing the pressurization system have to withstand 100 bar of relative pressure. Finally, constraints on the global design of the device are:

- The circulation system inside the device has to allow water flow at a velocity from 0 to 4 m.s^{-1} and with an absolute pressure of 1 to 6 bar,
- The pressurization system has to withstand an absolute pressure up to 106 bar (6 bar absolute pressure in the circulation system + 100 bar relative pressure inside the tube needed for failure generation),
- Independent degassing of the circulation and the pressurization systems must be possible,
- Replacement of the test tube must be possible,
- Wall pressure measurement must be possible at several points - at least 6 - in the main section and at one point in the lower section (inlet) and the upper section (outlet),
- Mounting contact sensors on the test tube inside the circulation system must be possible. Thus, it requires watertight feedthrough for the wires and enough space for the sensors,
- Optical measurement on the test tube must be possible. Thus, a transparent external tube is necessary.

Constraints on the instrumentation system are:

- Sensors have to withstand water flowing at a velocity up to 4 m.s^{-1},
- Measurements should not be troubled by the mean pressure in water (4 bar),
- Measurements should be lightly troubled by the flow,
- Sensors and wires have to be compatible with the tightness of the water system and the narrow available space.

Since the device will be connected to an already existing water loop, specifications related to the circulation system part outside the device are imposed and are therefore not defined in the present work. Characteristics of the water loop were given in Sec IV.1.1.

IV.5.1.2. Geometry of the device

Geometry of the test section has to meet three specifications. Firstly, it has to be representative of a real device's geometry. At least, it should allow to produce FSI phenomena similar to those observed during tests in a real facility. To this end, a dimensional analysis was carried out, as described in Sec. IV.1.1. Secondly, the device has to offer the space to place the sensors according to the objectives defined in Sec. IV.5.1.1. That specification requires a minimal distance between the outer surface of the test tube and the channel wall (*i.e.* inner wall of the transparent tube) of 7 mm. Thirdly, it has to be suitable for the use of tubes that are easily supplied regarding the market. Among different suppliers, the most common length for 10 mm diameter aluminium tube is 1 m. The device has therefore to allow the use of 1 m long test tubes.

In order to make the filling and the degassing of the test tube easier, it was decided not to fix extensions to the ends of the tube, contrary to a real reactor's configuration. That would have required at least one hollow extension connected to both a vacuum pump (for degassing before filling) and the pressurization pump. It seems preferable to use a system similar to RUPTUBE, which consists of filling at one end and degassing at the other end with a valve that is open during filling phase and closed after degassing. Consequently, the inlet end of the test tube is inserted in the lower section's flange, in which a channel connects the inner volume of the tube to the pressurization pump. The outlet end is outside the circulation system and covered by a flange (referred as pressurization system's flange) with a degassing valve. That flange is the same as the outlet flange in the RUPTUBE device.

An overview of the device is shown in Fig. IV.71. Such a design implies differences with a real device, but it ensures a reliable degassing and avoid a long and intricate preparation of the test tubes and a necessary custom-manufacturing of the extensions.

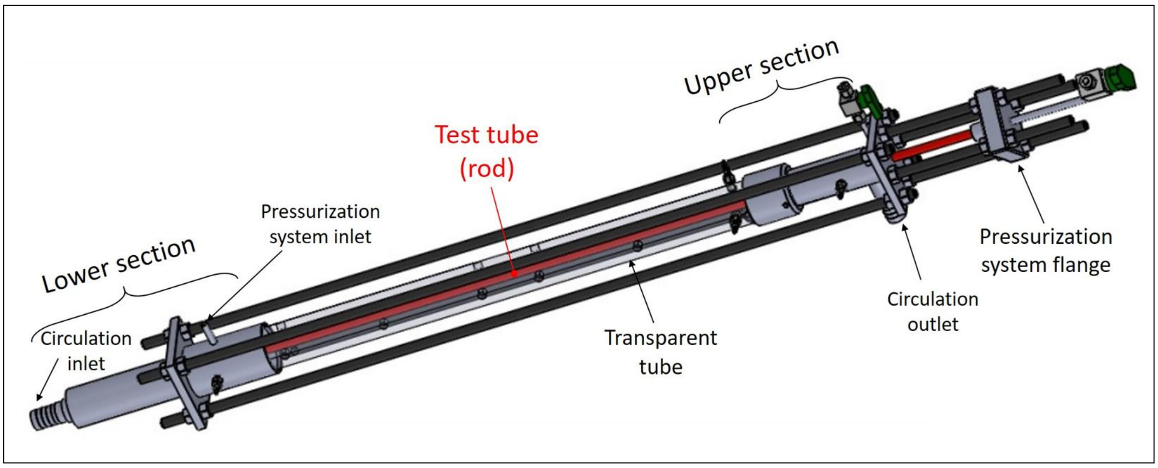

Figure IV.71. *MAQAC - Overview of the device.*

Because of that design, overall length of the test section must be smaller than the test tube length, *i.e.* 1 m. Moreover, to offer the necessary space for threaded rods' nuts and the tube adaptor, the length of the tube that is outside the circulation system must be more than 130 mm. Dimensions imposed by those specifications are presented in Fig. IV.72. These dimensions imply a Reynolds number in the mockup of the same order of magnitude of the one in a real device. In both cases, this Reynolds number depicts a turbulent flow. The dimensional analysis is more accurately described in Sec. IV.1.1.

	Real case	MAQAC
Rod outer diameter	9.5 mm	10 mm
Channel inner diameter	15 mm	25 mm
Distance between the rod supports		1047 mm
Length of the transparent section		940 mm
Minimal rod length		1300 mm
Reynolds number	$2.33 \cdot 10^5$	$5.05 \cdot 10^5$
Fluid added mass on the rod	0.124 $kg.m^{-1}$	0.108 $kg.m^{-1}$

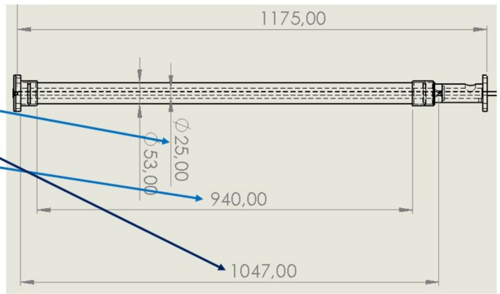

Figure IV.72. *MAQAC - Comparison of significant dimensions and parameters between a real case and the MAQAC device.*

IV.5.1.3. Materials

Test tube material has to be chosen according to the pressure needed to generate tube failure. Failure pressure strongly depends on the tube's material and, for technical and safety reasons, it should be lower than 100 bar. As shown in Sec. IV.4, RUPTUBE tests proved that failures under 100 bar are possible with aluminium tubes with 10 mm of diameter and 0.5 mm of thickness. Moreover, such tubes can be easily purchased and machined, which is a significant advantage.

The lower and upper sections' structures are made of stainless steel (304L), which can withstand water and high pressure and is easy to procure, to machine and to weld, and whose mechanical properties are known and close to a real device's ones. External tube of the main section is made of transparent PMMA (polymethyl methacrylate), so that test tube motion measurements with a laser vibrometer or a high speed camera are possible. That material is very different than Zr-4, which is used in the corresponding part of a real device. Nevertheless, no existing material offers both transparency and mechanical properties close to Zr-4's.

IV.5.1.4. Pressurization system

The pressurization system consists of the inner volume of the test tube, the degassing valve, external pipes and fittings and the pressurization pump. The pump is the same than the one used with RUPTUBE device, *i.e.* a hydraulic hand pump with a maximal absolute pressure of 100 bar. The pump is connected to a channel inside the lower section of the device. Lower end of the test tube is inserted in the lower section's flange and connected to that channel (Fig. IV.73). Tightness between pressurization and circulation systems is ensured by an O-ring around the part of the rod that is inserted in the flange. An adaptor and the pressurization system's flange with a degassing valve are placed on the upper end of the test tube. That flange is fixed to the upper section of the device by threaded rods (Fig. IV.74).

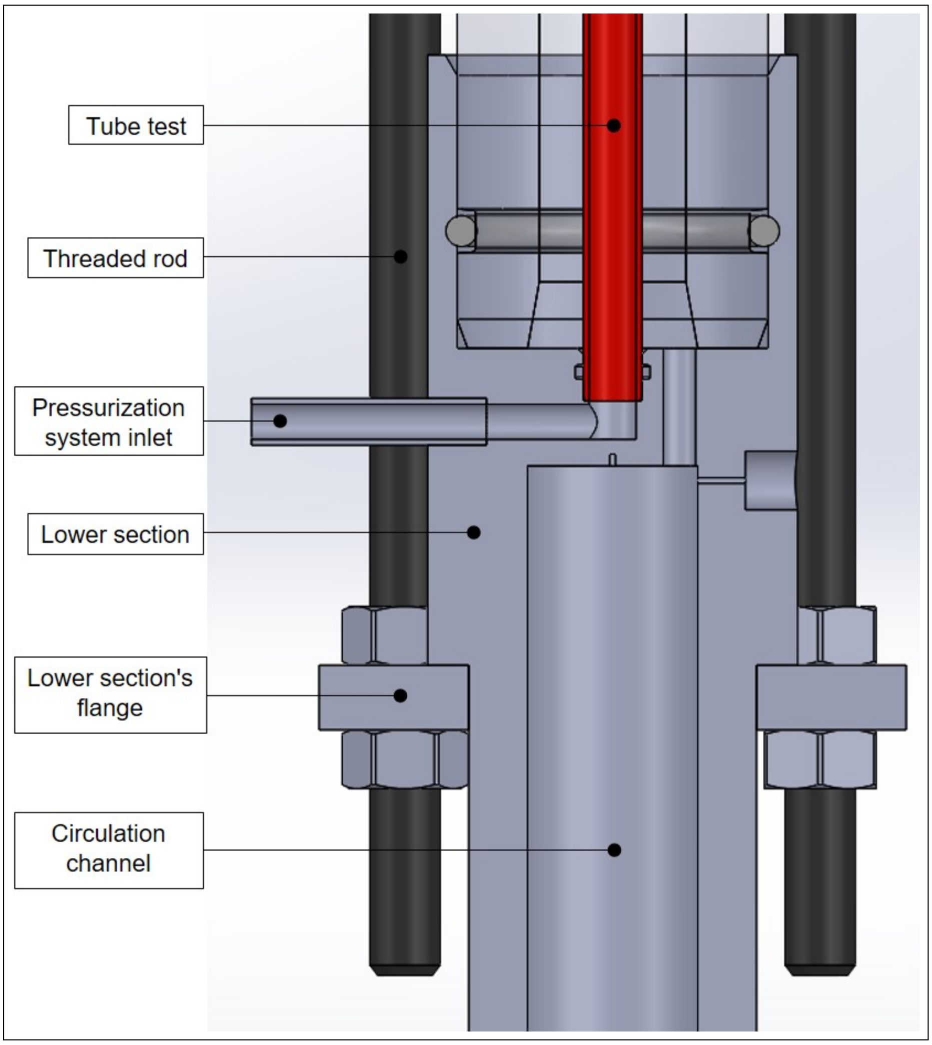

Figure IV.73. *MAQAC - Cutaway view of the lower section.*

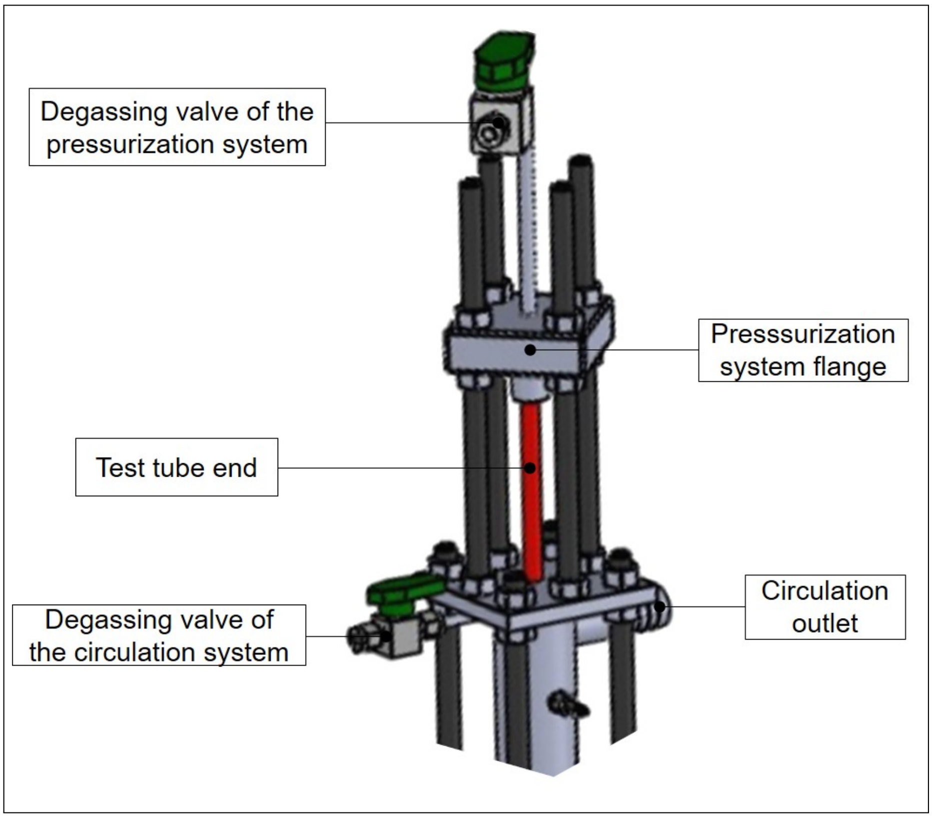

Figure IV.74. *MAQAC - Details of the upper section and the pressurization system's flange (same than the outlet flange of RUPTUBE device).*

Technical drawings of every part of the device can be found in App. L. A complete technical description of the device are given in the specifications [141] (in french).

IV.5.2. Experimental plan

The MAQAC device, whose a picture is shown in Fig. IV.75, was eventually delivered later than expected. Therefore, the experiments introduced below are currently in progress.

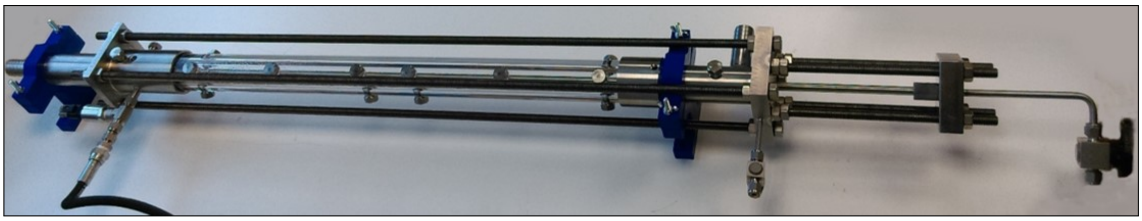

Figure IV.75. *MAQAC - Picture of the device before its installation.*

The MAQAC experimental campaign consists of four tests, described in the current section. Before the first test, experimental modal analyses will be carried out to characterize the system. Firstly, three modal analyses will be carried out with three different tubes mounted in the device. If the measured natural frequencies are consistent, it will be considered that all the tubes are similar and that the solution designed to insure the clamping of both ends of the tested tubes are reliable. In this case, it will not be necessary to repeat a modal analysis before each test. Otherwise, an inconsistency in the natural frequencies would indicate that either the tube properties or the boundary conditions differ between the tests. It will be therefore necessary to carry out a modal analysis for each test.

The configuration (positions of the sensors and the failure) associated to each test is depicted in Fig. IV.76 and IV.77. In the first tests, structural sensors will be mounted outside of the system, either on the outer structure or on the external part of the tested tube. In Test 4, AE sensors will be mounted on the immersed part of the tested tube. This choice aims at taking the risk to deteriorate sensors (because of immersion[7]) during the last test only. The objectives of Tests 1 and 2 are to study the propagation of the pressure wavefront (with pressure sensors distributed along the main section) and the associated vibration of the outer tube (with accelerometers placed near the pressure sensors). It will also allow for the assessment of the effects of the transmission between the main and the inlet and outlet sections on the pressure waves. With this data, it will be possible to assess the feasibility of the failure detection and localization with pressure sensors in the main section or in the inlet and outlet sections. Moreover, AE sensors will be mounted on the outer structure in order to assess the failure detection possibility with these sensors, and estimate the types of waves to consider to achieve the failure localization (vibration of the tube directly induced by the failure and propagating through the structure, or water-hammer related waves induced by the pressure release in the fluid). The objectives of Test 3 are to experimentally verify the plane wave assumption (with pressure sensors at the same axial position and distributed along the circumference), and to assess the feasibility of detection and localization with strain gauges, accelerometers, and AE sensors on the outer structure. Additional accelerometers and an AE sensor will be mounted on the tested tube to compare its own vibration with the vibration of the outer structure. Then, Test 4 should allow AE measurement to be performed with sensors on the immersed part of the tube, in order to study the FSI between the tube and the the pressure wavefront induced by the failure. Moreover, it will show if designing new sensors to perform vibration or AE measurement inside the fluid volume of such a system is relevant.

[7] Some models of AE sensors or accelerometers are specifically designed to be immersed. However, those models did not meet the size and bandwidth requirements for the current study. Therefore, it will be attempted to immerse AE sensors that are initially not intended to be immersed, after protecting them with a suitable coating

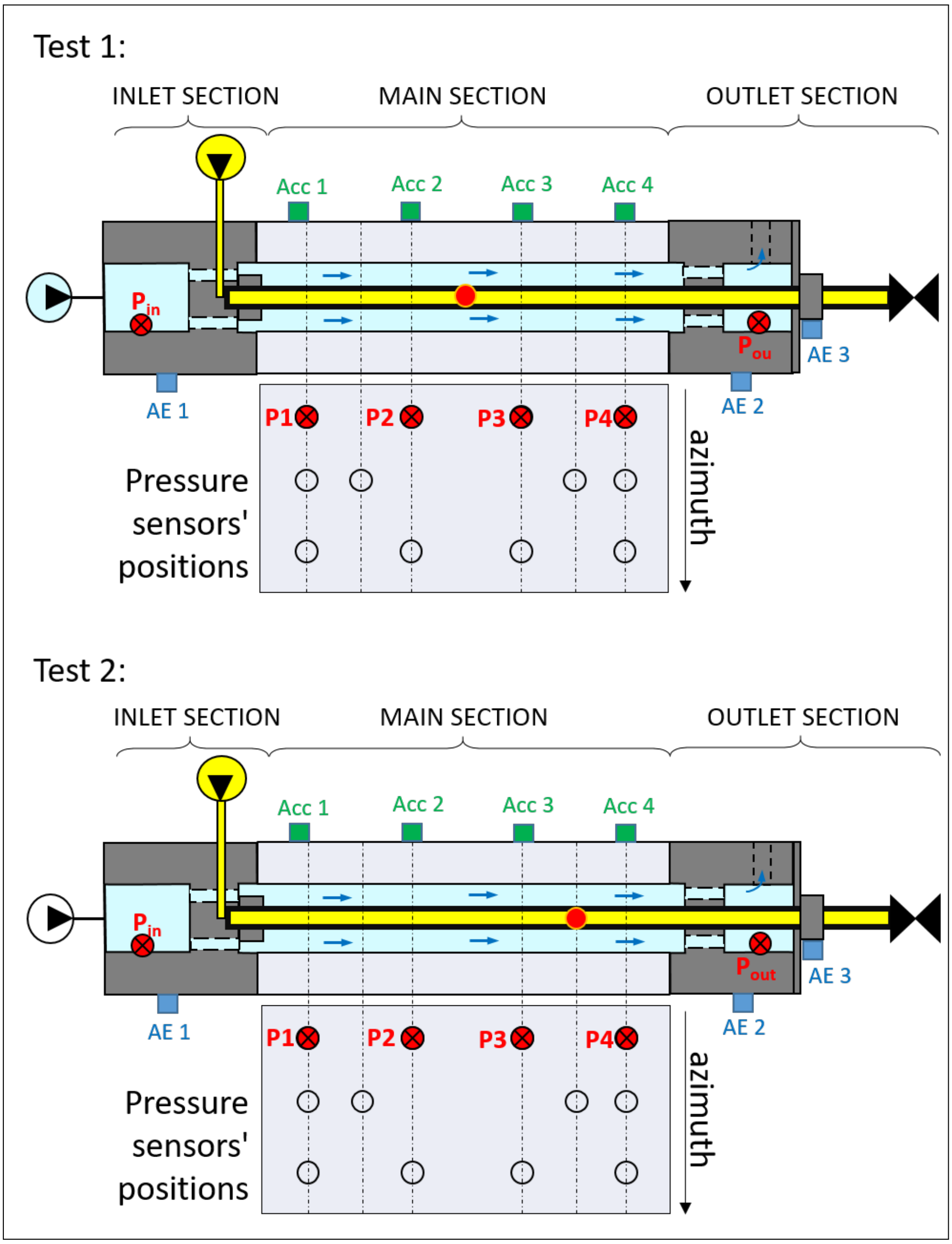

Figure IV.76. *MAQAC - Configuration of Test 1 and Test 2.*

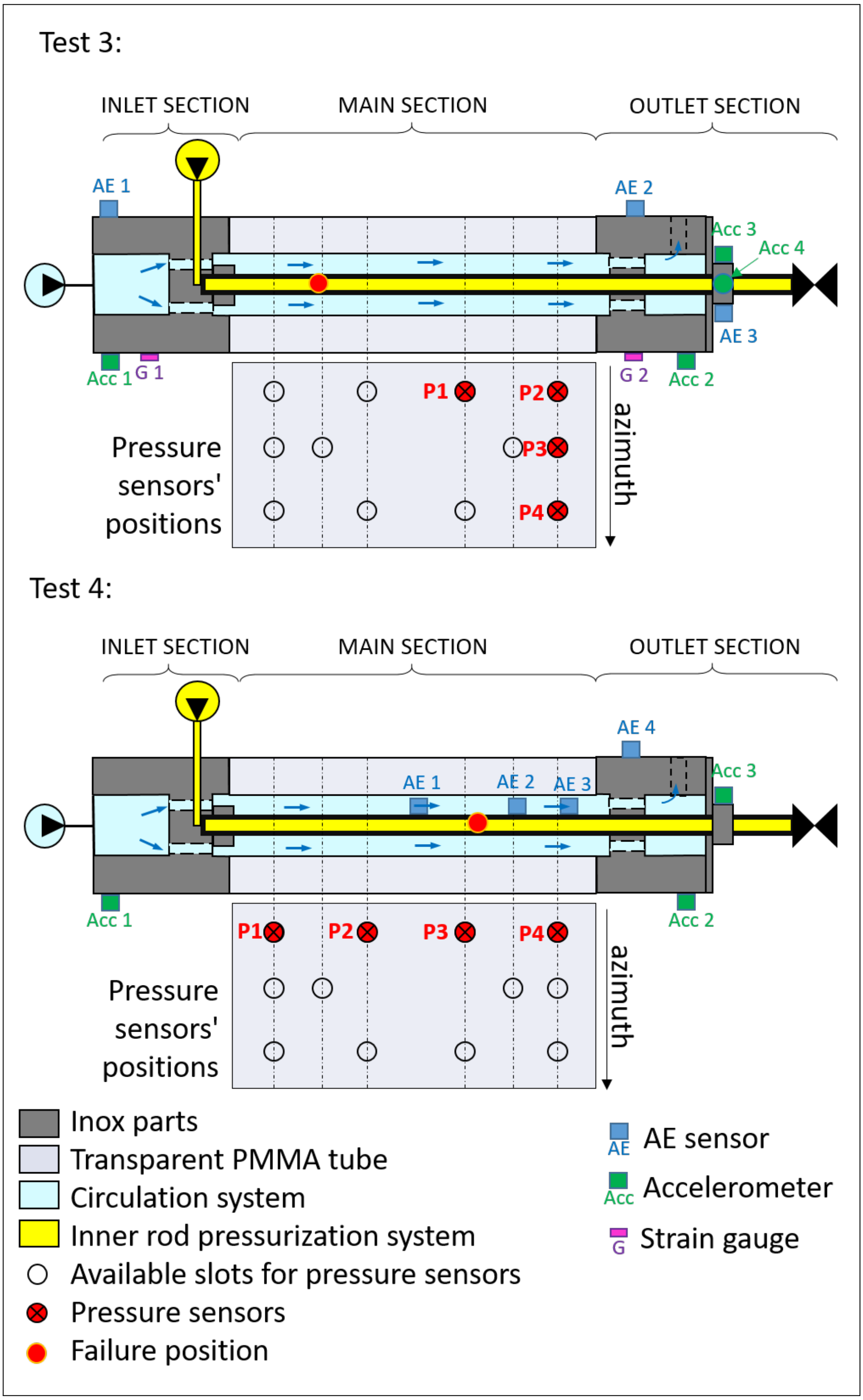

Figure IV.77. *MAQAC - Configuration of Test 3 and Test 4.*

Conclusions & Perspectives

The work presented in this document consists of theoretical, numerical and experimental studies of fluid and structural dynamic phenomena induced by the failure of nuclear fuel rod cladding. The primary aim was to design or improve methods to detect and locate such a failure with fluid pressure and structural vibration measurements. Such methods are considered to be of interest for the detection and localization of fuel cladding failures, as the propagation of waves (either pressure waves in the coolant fluid or elastic waves in the structure) generated by the failure enables information about this event to be recorded with sensors that are mounted relatively far from its position. This is an advantage of these methods because, as failures occur in the reactor core, where there is high temperature, radiation, and little available space, most of existing measuring devices can not be installed close to the rods. However, some information about wave propagation and fluid-structure phenomena was missing. This information was needed to identify the most efficient measurement methods and to properly interpret the signals that can be measured by pressure and vibration sensors.

Preliminary investigations about effects of a cladding failure and about existing passive acoustic and vibration methods for fluid system monitoring allowed for the identification of the phenomena of interest and a comprehensive definition of the objectives of this work, as shown in Chap. I. The objectives can be summarized as the study of fluid-structure interaction phenomena induced by the cladding failure, with the aim of detecting and locating the failure with distant sensors, as the conditions inside a reactor core prevent sensors to be mounted near the area where a failure may occur. Such a study was achieved by a numerical and an experimental approach.

The numerical approach, presented in Chap. III, allowed numerical simulations to be carried out on a three-dimensional model of the studied system (typical test device used in research reactors), using the finite-element and finite-volume code EUROPLEXUS. The results could be used to complement the experimental approach, both in the design of the experiments and in the interpretation of the results, either in experimental devices or in actual reactors. Furthermore, this model may be used for future experiments as well. The experimental approach, presented in Chap. IV, led to the design and the implementation of two experimental devices (*RUPTUBE* and *MAQAC*) and a modular and versatile instrumentation system. The purposes of the experimental devices were to induce the failure of a fake rod cladding and to generate a water flow, representing coolant fluid flow, around the cladding. Two constraints had to be taken into account. The first constraint was to design devices that are easy to use, intrinsically safe, and compliant with the regulations regarding pressure equipment, so that a person can use it alone and with limited safety obligations. The second constraint was to use tube samples that can be easily purchased. Moreover, the instrumentation system allowed the use of all the different types of sensors that were identified as suitable for failure monitoring: fluid pressure sensors, AE sensors, accelerometers, and strain gauges. Thus, such sensors could be tested when a failure was reproduced. Then, the measurements allowed some processing methods to be tested. In the future, this material will make it possible to carry out the necessary experiments to obtain the missing phenomenological and practical information for the final application in a real reactor.

The first objective of the PhD was to identify the methods and the phenomena to study and to provide both numerical and experimental resources that make such studies possible. In addition to the achievement of this objective, it was also possible to start to use those resources, which provided interesting results for the phenomenological understanding and the possible applications in actual reactors. Some of those results are related to the identification of wave propagation phenomena and the quantitative estimation of velocities of different types of waves. The numerical simulations and the experiments showed that pressure waves propagating through the fluid and elastic waves through the structure can be detected and used to obtain information about the failure, especially its position. Numerical simulations exhibited that precursor and primary waves are generated by the pressure surge induced in the coolant fluid by the failure. Those types of waves are defined in water-hammer theories, introduced in Chap. II. Precursor waves are due to structural axial waves that are generated by the load exerted by the fluid pressure on the structure walls, propagate through the structure at a velocity higher than the pressure wave velocity in the fluid, and radiate back into the fluid, resulting in small pressure fluctuations. The primary wave refers to the pressure wave that is directly related to the initial pressure surge and propagates through the fluid. The numerical simulations also showed that the one-dimensional plane wave assumption, which is commonly accepted for water-hammer models, is valid for the current case. Moreover, those simulations allowed the assessment of the effects of geometrical singularities on the distortion and attenuation of the pressure wavefront between the source and measurement points. It showed that a significant loss in the pressure signal is induced by the necessary geometrical singularities at the ends of the rod (reduction in the hydraulic diameter due to mechanical supports of the rod).

Some other results consist of practical information about the suitability of various types of measuring devices and processing methods. Based on numerical results, it can be expected that fluid pressure measurements near the rod or at distant upstream or downstream positions make the failure detection and localization possible. RUPTUBE experiments showed that the failure can be studied by structural vibration measurements. Good results were obtained with AE sensors and strain gauges. On the other hand, accelerometers and fast camera did not provide relevant results. It is, however, assumed that better results could be obtained with a better choice of accelerometer (either charge mode accelerometers, or IEPE accelerometers with a lower sensitivity) and a more powerful camera. Different processing methods were applied to the signals of various sensors, such as transient detection by threshold crossing method, wavelet time frequency analysis, and empirical mode decomposition. Those methods allowed the identification of the types of waves that were measured and finally made it possible to localize the failure. Such tools and methods should be applied now to the MAQAC experiments, where external fluid flow will be added to the cladding failure.

Now, relevant investigation paths have been identified and computational and experimental resources are available to study failure-related FSI phenomena more deeply before applying the associated measurement methods to the monitoring of rod cladding in actual reactors.

Some perspectives that should follow the presented work have been identified. Firstly, the theoretical background should be developed. Adapting existing water-hammer models to the specific studied system and the phenomenon of cladding failure could be attempted. This would allow for simulations of the failure-induced pressure surge and its effects with lower computation costs than three-dimensional FEM simulations. In parallel, the relatively simple beam model used to describe RUPTUBE experiments could be completed to take into account the surrounding fluid (to represent either the MAQAC device or a rod in an actual reactor), and the appropriate initial conditions to represent the failure-induced excitation should be estimated. This would result in improvements in the possibilities of modeling the failure phenomenon or its direct effects on fluid and structure dynamics. It may be therefore possible to assess the significance of the coolant fluid flow's effects in the measurements. Then, the numerical FEM model should be improved, by adding the fluid flow (if its effects are assessed to be significant) and estimating the failure-related parameters with more accuracy. In parallel with theoretical and numerical developments, the experimental approach should be continued. It seems to be relevant to test other models of accelerometers, as the tested ones failed at recording the tested tubes' response to the failure. Regarding signal processing, some methods that were identified (such as Akaike Information Criterion, Shannon's entropy, semblance) could be applied to the results of either RUPTUBE or MAQAC experiments. Moreover, further tests on MAQAC have to be carried out.

Such additional works should lead to a significant improvement of the results of the studied methods. After that, it will be possible to think about further applications in industrial environments, such as nuclear power plants, or any other duct systems involving transient phenomena with fluid-structure interaction.

Bibliography

[1] IAEA. *On-line Monitoring for Improving Performance of Nuclear Power Plants - Part 2: Process and Component Condition Monitoring and Diagnostics.* Version No NP-T-1.2. 2008. URL: https://www-pub.iaea.org/MTCD/Publications/PDF/Pub1323_web.pdf (visited on 01/03/2022).

[2] T. Stepinski. *Structural Health Monitoring of Piping in Nuclear Power Plants - A Review of Efficiency of Existing Methods, report n°2011:17.* Swedish Radiation Safety Authority, 2011.

[3] J. Papin et al. *Synthesis of CABRI-RIA tests interpretation.* Tech. rep. Institut de Radioprotection et Sûreté Nucléaire (IRSN), 2003.

[4] CEA, Nuclear Energy Directorate. *OSIRIS - Nuclear reactors and services department.* URL: http://www-rjh.cea.fr/Add-On/osiris_gb.pdf.

[5] M.P. Ferroud-Platter. *The Irradiation Devices.* CEA, Accessed 27/11/2021. URL: http://www-rjh.cea.fr/irradiation-devices.html.

[6] IAEA. *Review of Fuel Failures in Water Cooled Reactors.* Version No FT-T-2.1. 2010. URL: https://www-pub.iaea.org/MTCD/Publications/PDF/Pub1445_web.pdf (visited on 01/03/2022).

[7] F. Boldt and H.G. Sonnenburg. *Brennstabverhaltenim Betrieb undbei Störfällen.* Tech. rep. Gesellschaft für Anlagen-und Reaktorsicherheit, 2020.

[8] T. Fuketa T. ; Fujishiro. “Generation of destructive forces during fuel/coolant interactions under severe reactivity initiated accident conditions”. In: *Nuclear Engineering and Design* 146 (1994), pp. 181–194.

[9] J. Bernaudat C. ; Delplace. “Consequences of leaking fuel rod failure during RIA transients”. In: *TopFuel 2018.* 2018.

[10] J. David and N. Cheeke. *Fundamentals and Applications of Ultrasonic Waves.* 2nd ed. CRC Press, 2012.

[11] *ASTM E1316 Standard Terminology for Nondestructive Examinations.* ASTM international, 2014.

[12] S. Gholizadeh, Z. Leman, and Baharudin B.T.H.T. “A review of the application of acoustic emission technique in engineering”. In: *Structural Engineering and Mechanics* 54 (6) (2015), pp. 1075–1095. DOI: 10.12989/sem.2015.54.6.1075.

[13] A.A. Pollock. *Acoustic Emission Inspection.* Tech. rep. Physical Acoustics Corporation, Technical Report TR103-96-12/98, 1989.

[14] A. Nair and C. S. Cai. “Acoustic emission monitoring of bridges: Review and case studies”. In: *Engineering structures* 32.6 (2010), pp. 1704–1714.

[15] H.N.G Wadley and R Mehrabian. "Acoustic emission for materials processing: a review". In: *Materials Science and Engineering* 65 (2) (1984), pp. 245–263. DOI: 10.1016/0025-5416(84)90086-7.

[16] N. Nazarchuk, V. Skalskyi, and O. Serhiyenko. *Acoustic Emission - Methodology and Application*. Foundations of Engineering Mechanics. Springer, 2017.

[17] G. Shen, J. Zhang, and Z. Wu, eds. *Advances in Acoustic Emission Technology - Proceedings of the World Conference on Acoustic Emission*. 2017. Springer.

[18] W. Fan and P. Qiao. "Vibration-based Damage Identification Methods: A Review and Comparative Study". In: *Structural Health Monitoring* 10 (1 2010), pp. 83–111. DOI: 10.1177%2F1475921710365419.

[19] J. Antoni and M. Sidahmed. "Controle et diagnostic à partir des signaux acoustiques et vibratoires". In: *Acoustique & Techniques* 38 (2004).

[20] S. Chapain and A.M. Aly. "Vibration attenuation in high-rise buildings to achieve system-levelperformance under multiple hazards". In: *Engineering Structures* 197 (2019). DOI: 10.1016/j.engstruct.2019.109352.

[21] F. Gao, Y. Fah Yap, and Y. Yan. "Modeling of hard disk drives for vibration analysis using a flexible multibody dynamics formulation". Version 2. In: *IEEE Transactions on Magnetics* 41 (2005), pp. 744–749. DOI: 10.1109/TMAG.2004.840329.

[22] P.L. Walter. *How High in Frequency AreAccelerometer Measurements Meaningful - TN25*. Tech. rep. PCB PIEZOTRONICS, 2008.

[23] Y.A. Khulief and A. Khalifa. "On the In-Pipe Measurements of Acoustic Signature of Leaks in Water Pipelines". In: *Proceedings of IMECE2012*. 2012.

[24] D. Chatzigeorgiou, K. Youcef-Toumi, and R. Ben-Mansour. "Design of a Novel In-Pipe Reliable Leak Detector". In: *IEEE/ASME Transactions on Mechatronics* 20 (2 2015), pp. 824–833. DOI: 10.1109/TMECH.2014.2308145.

[25] American Petroleum Institute. *API RP 1130 Computational Pipeline Monitoring for Liquids*. American Petroleum Institute, 2007.

[26] A. Keramat et al. "Transient-based leak detection in the frequency domain considering fluid–structure interaction and viscoelasticity". In: *Mechanical Systems and Signal Processing* (2020).

[27] B. Brunone and M. Ferrante. "Detecting leaks in pressurised pipes by means of transients". In: *Journal of Hydraulic Research* 39 (5 2000), pp. 539–547. DOI: 10.1080/00221686.2001.9628278.

[28] S. Sewerin, J. Montero, and S. Ziemendorff. "Detection of illegal drinking water installations with the use of water hammers". Version 30. In: *Campus* 25 (2020), pp. 361–372.

[29] W.W. Reinhardt. *Acoustic-Emission monitoring of LOFT fuel-cladding-burst tests*. Tech. rep. U.S. Department of Energy, Idaho Operations Office, 1982.

[30] A.J. Regueiro. "Acoustic emission in Zircaloy-4 tubes". In: *NDT.net* (2002).

[31] S.H. Baek et al. "Acoustic emission monitoring of water boiling on fuel cladding surface at 1 bar and 130 bar". In: *Measurement* 109 (2017), pp. 18–26.

[32] M.S. Choi, M.S. Yang, and H.C. Kim. "Detection of leak-defective fuel rods using the circumferential Lamb waves excited by theresonance backscattering of ultrasonic pulses". In: *Ultrasonics* 30 No 4 (1991), pp. 221–223.

[33] H. Kwun, E. Mader, and K. Krzywosz. "Guided Wave Inspection of Nuclear Fuel Rods". In: *7th International Conference on NDE in Relation to Structural Integrity for Nuclear and Pressurized Components*.

[34] D. Fourmentel et al. "Acoustic Sensor for In-Pile Fuel Rod Fission Gas Release Measurement". In: *IEEE Transactions on nuclear science* 50 (2011), pp. 151–155.

[35] V. Prakash et al. "Experimental qualification of subassembly design for Prototype-Fast Breeder Reactor". In: *Nuclear ENgineering and Design* (2011), 3325– 3332. DOI: 10.1016/j.nucengdes.2011.04.040.

[36] V. D'Ambrosi. *IMPIGRITIA experimental set-up to characterize PCI impact on rod vibration: Conception and planning of the experience*. Tech. rep. Commissariat à l'énergie atomique et aux énergies alternatives, 2019.

[37] A. Lhemery et al. "Emission acoustique : simulation des contrôles – le projet ANR MACSIM". In: *Actes du congrès COFREND, Dunkerque*. 2011.

[38] D. C. Gazis. "Exact Analysis of the Plane-Strain Vibrations of Thick-Walled Hollow Cylinders". In: *The Journal of the Acoustical Society of America* 30.8 (1958), pp. 786–794.

[39] H. Nishino et al. "Modal Analysis of Hollow Cylindrical Guided Waves and Applications". In: *The Japan Society of Applied Physics* (2000).

[40] V. Baronian. "Couplage des méthodes modale et éléments finis pour la diffraction des ondes élastiques guidées : Application au Contrôle Non Destructif". PhD thesis. Ecole Polytechnique, 2009.

[41] I. Bartoli et al. "Modeling wave propagation in damped waveguidesof arbitrary cross-section". In: *Journal of Sound and Vibration* 295 (2006), pp. 685–707. DOI: 10.1016/j.jsv.2006.01.021.

[42] L. Bergman and H. Hatfield. *Ultrasonics and their Scientific and Technical Applications*. Wiley, New-York, 1938.

[43] A. Tarasenko, R. Ctvrtlik, and Kudelka R. *Theoretical and experimentalrevision of surface acoustic waveson the (100) plane of silicon*. Scientific Report. Nature, 2021.

[44] T. Haukaas. *Euler-Bernoulli Beams*. Ed. by University of Bristish Columbia, Vancouver. 2020. URL: https://civil-terje.sites.olt.ubc.ca/files/2020/02/Euler-Bernoulli-Beams.pdf.

[45] Blevins R.D. "Flow-Induced Vibration in nuclear reactors: a review". In: *Progress in Nuclear Energy* 4 (1979), pp. 25–49.

[46] T.L. Schmitz and Smith S.S. "Continuous Beam Modeling". In: *Mechanical Vibrations - Modeling and Measurement*. Springer, 2012. Chap. 8, pp. 279–319.

[47] G. Szeidl and L.P. Kiss. "Systems with Infinite Degrees of Freedom". In: *Mechanical Vibrations - An Introduction*. Springer, 2020. Chap. 7, pp. 201–241.

[48] R.D. Blevins. *Formulas for Dynamics, Acoustics and Vibration.* 2016.

[49] J.C. Pascal. *Vibrations et Acoustiques 2.* Ed. by Ecole Nationale Superieure d'Ingenieurs du Mans. 2008, pp. 49–50.

[50] A.S. Tijsseling. "Fluid-Structure Interaction in Liquid-filled Pipe Systems: A Review". In: *Journal of Fluids and Structures* 10 (1996), pp. 109–146.

[51] J. Montgolfier. "Note sur le bélier hydraulique et sur la manière d'en calculer les effets". In: *Journal des Mines* 13 (1803).

[52] A.S. Tijsseling and A. Anderson. "Thomas Young's research on fluid transients : 200 years on". In: *Proc. of the 10th Int. Conf. on Pressure Surges, Edinburgh, United Kingdom,* 2008, pp. 21–33.

[53] L.F. Menabrea. "Note sur les effets du choc de l'eau dans les conduites". In: *Extrait des Comptes rendus des séances de l'Académie des Sciences, T. 47.* 1858.

[54] J. Michaud. "Coups de bélier dans les conduites, étude des moyens employés pour en atténuer les effets". In: *Bulletin de la Société Vaudoise des ingénieurs et architectes* 4 (1878), pp. 56–77.

[55] A.S. Tijsseling and A. Anderson. "Johannes von Kries and the History of Water Hammer". In: *Journal of Hydraulic Engineering* (2007).

[56] N. Joukowksy. "Über des hydraulischen Stoss in Wasserleitungsröhren". In: *Mémoires de l'Académie Impériale des Sciences de St. Pérersbourg* 9 (1898), pp. 1–71.

[57] H. Lamb. "On the velocity of sound in a tube, as affected by the elasticity of the walls". In: *Memoirs of the Manchester Literary and Philosophical Society* 42 (9 1898), pp. 1–16.

[58] R. Skalak. *An extension of the theory of water hammer.* Tech. rep. The American Society of Mechanical Engineers, 1956.

[59] M.H. Chaudry. "Charactertics and Finite-Difference Methods". In: *Applied Hydraulic Transients.* 3rd ed. 2014. Chap. 3, pp. 80–92.

[60] P. Susovan, P.R. Hanmaiahgari, and B.W. Karney. "An Overview of the Numerical Approaches to Water Hammer Modelling: The Ongoing Quest for Practical and Accurate Numerical Approaches". In: *Water* 13 (2021). DOI: 10.3390/w13111597.

[61] T. Neuhaus, A. Dudik, and A.S. Tijsseling. *Experiments and corresponding calculations onthermohydraulic pressure surges in pipes (CASA-report; Vol. 0545).* Technische Universiteit Eindhoven, 2006.

[62] A.K. Soares, D.I. Covas, and L.F. Reis. "Analysis of PVC Pipe-Wall Viscoelasticity during Water Hammer". In: *Journal of Hydraulic Engineering* 134 (9 2008). DOI: 10.1061/(ASCE)0733-9429(2008)134:9(1389).

[63] H.A. Warda and Y. Elashry. "Towards an Improved Understanding of Water-Hammer Column-Separation Due to Rapid Valve Closure". In: *ASME 2010 Pressure Vessels and Piping Division/K-PVP Conference.* 2010. DOI: 10.1115/PVP2010-26146.

[64] A. Keramat et al. "Fluid–structure interaction with pipe-wall viscoelasticity during water hammer". In: *Journal of Fluids and Structures* 28 (2011), pp. 434–455. DOI: 10.1016/j.jfluidstructs.2011.11.001.

[65] P. Cesana and N. Bitter. "Modeling and analysis of water-hammer in coaxial pipes". In: *Journal of Fluids and Structures* (2014). URL: http://dx.doi.org/10.1016/j.jfluidstructs.2014.08.011i.

[66] A.S. Tijsseling. "Exact solution of the FSI four-equation model". In: *Journal of Fluids and Structures* (2003), pp. 179–196.

[67] A.S. Tijsseling. "Water hammer with fluid-structure interaction in thick-walled pipes". In: *Computers & Structures* 85 (2007), pp. 844–851. DOI: 10.1016/j.compstruc.2007.01.008.

[68] A.E. Vardy and A.S. Tijsseling. "Method of characteristics: (Why) is it so good ?" In: *12th International Conference on Pressure Surges*. 2015.

[69] A.S. Tijsseling and A.E. Vardy. "What is wave speed ?" In: *12th International Conference on pressure Surges*. 2015.

[70] A.S. Tijsseling. "Fluid-structure interaction in case of waterhammer with cavitation". PhD thesis. Technische Universiteit Delft, 1993.

[71] Korteweg, D. J. "Über die Fortpflanzungsgeschwindigkeit des Schalles in elastischen Röhren". In: *Annalen der Physik und Chemie* Vol. 5.12 (1878).

[72] L. Zhang, A.S Tijsseling, and A.E Vardy. "FSI Analysis of liquid-filled pipes". In: *Journal of Sound and Vibration* (1999).

[73] T. Catterou. "Étude numérique et expérimentale du comportement dynamique nonlinéaire d'un réseau de tubes avec jeux - application aux faisceauxd'aiguilles combustibles RNR". PhD thesis. Aix-Marseille Université, 2018.

[74] V. D'Ambrosi et al. "Fuel rod nonlinear vibrations to detect and characterize Pellet-Cladding Interaction". In: *Nuclear Engineering and Design* 379 (3 2021). DOI: 10.1016/j.nucengdes.2021.111214.

[75] V. Faucher, M. Bulik, and P. Galon. "Updated VOFIRE algorithm for fast fluid–structure transient dynamics with multi-component stiffened gas flows implementing anti-dissipation on unstructured grids". In: *Journal of Fluids and Structure* 74 (2017), pp. 64–89. DOI: 10.1016/j.jfluidstructs.2017.07.001.

[76] O. Le Metayer, J. Massoni, and J. Saurel. "Elaborating equations of state of a liquid and its vapor for two-phase flow models". In: *International Journal of Thermal Sciences* 43 (2003), pp. 265–276. DOI: 10.1016/j.ijthermalsci.2003.09.002.

[77] F. H. Harlow and A. A. Amsden. *Fluid Dynamics - Monography*. Los Alamos Scientific Laboratory of the University of California, 1971.

[78] Z. Gao, P. Galon, and F. Daude. *Introduction and Validation of Three Different Multiphase Flows Models in the Fast Transient Dynamic Code EUROPLEXUS*. Tech. rep. 2010. DOI: 10.13140/RG.2.1.4029.0408.

[79] V. Faucher. "Advanced parallel strategy for strongly coupled fast transient fluid-structure dynamics with dual management of kinematic constraints". In: *Advances in Engineering Software* 67 (2014), pp. 70–89. DOI: 10.1016/j.advengsoft.2013.08.002.

[80] F. Casadei et al. "Transient fluid-structure interaction algorithms for large industrial applications". In: *Computer methods in applied mechanics and engineering* 190 (2001), pp. 3081–3110.

[81] F. Casadei and S. Potapov. "Permanent fluid–structure interaction with non-conforming interfaces in fast transient dynamics". In: *Computer methods in applied mechanics and engineering* 193 (2004), pp. 4157–4194. DOI: 10.1016/j.cma.2003.06.002.

[82] CEA. *Europlexus website*. Accessed 06/09/2021. URL: http://www-epx.cea.fr/.

[83] J. Von Neumann and R.D. Richtmyer. "A Method for the Numerical Calculation of Hydrodynamic Schocks". In: *Journal of Applied Physics, Vol. 21* (1950).

[84] J. Batoz and G. Dhatt. *Modélisation des structures par éléments finis*. Vol. 3. Hermes, 1990.

[85] EPX Manual. *EUROPLEXUS user's manual*. Commissariat à l'énergie atomique and European Commission. 2019.

[86] K. Ono. "Calibration Methods of Acoustic Emission Sensors". In: *Materials* (2016). DOI: 10.3390/ma9070508.

[87] G. Manthei. "Characterisation of Acoustic Emission Sensors". In: *European Working Group on Acoustic Emission*. September 2010.

[88] J. Kober, J. Prevrovsky, and M. Chlada. "In situ calibration of acoustic emission transducers by time reversal method". In: *Sensors and Actuators* 240 (2016), pp. 50–56. DOI: 10.1016/j.sna.2016.01.033.

[89] "Directive 2014/68/EU of the European Parliament and of the Council of 15 May 2014 on the harmonisation of the laws of the Member States relating to the making available on the market of pressure equipment". In: *Officiel Journal of the European Union* (2014).

[90] C. Herer. "Thermohydraulique des réacteurs à eau sous pression". In: *Techniques de l'Ingénieur* (2018).

[91] B. Le Neindre. "Viscosité". In: *Techniques de l'Ingénieur* (1988).

[92] W.E. Baker, P.S. Westine, and F.T. Dodge. *Similarity Methods in Engineering Dynamics, revised edition*. Elsevier, 1991.

[93] S. Candel. *Mécanique des fluides*. Dunod, 1995.

[94] F. Moreno. *ASTRID - Essais en eau des (DCS-P)-H Définition des conditions de similitudes sodium-eau*. Tech. rep. Note technique CEA/DEN, 2014.

[95] P. Testud et al. "The whistling potentiality of an orifice in a confined flow using an energetic criterion". In: *Journal of Sound and Vibration* 325 (2009), pp. 769–780. DOI: 10.1016/j.jsv.2009.03.046.

[96] R.D. Blevins. *Flow-Induced Vibration*. 2nd ed. Krieger Publishing Company, Malabar, Florida, 2001.

[97] M.P. Paidoussis. "Fluidelastic Vibration of cylinder arrays in axial and cross flow: State of the art". In: *Journal of Sound and Vibration* 76 (3) (1980), pp. 329–360.

[98] D. Burgreen. "Vibrations of rods in parallel flow". In: *Trans. ASME* 17 (8) (1965).

[99] B. De Pauw. “Operational modal analysis of flow-induced vibration of nuclear fuelrods in a turbulent axial flow”. In: *Nuclear Engineering and Design* (2015).

[100] F. Axisa. *Modélisation des systèmes mécaniques. Tome 4, Vibrations sous écoulements.* Hermes Science Publications, 2000, pp. 356–361.

[101] P. Defrasne and E. Pluyette. *Compte rendu des essais Squat T91 - 1ere partie - DEN/-CAD/DTN/STPA/LIET/NT 2012-071.* Tech. rep. Commissariat à l’énergie atomique et aux énergies alternatives, 2012.

[102] M. Le Saux. “High Temperature Expansion Due to Compression Test for the Determination of a Cladding Material Failure Criterion under RIA Loading Conditions”. In: *International Topical Meeting on Light Water Reactor Fuel Performance, San Francisco, USA.*

[103] M. Akyurt, A.N.A. Aljawi, and S. Aldousari. “Ice-Based Technique for Burst Testing of Tubular Elements”. In: *Journal of King Saud University - Engineering Sciences* 16 (2005), pp. 103–130.

[104] K.H. Eom et al. “Failure Behavior of Multiple-Axial Part-Through-Wall Flaws in Alloy 690TT Steam Generator Tubes”. In: *Journal of Pressure Vessel Technology* 138 (2) (2015). DOI: 10.1115/1.4031663.

[105] D. Qingquan et al. “Hydrostatic burst test of X80 grade steel pipe”. In: *Journal of Loss Prevention in the Process Industries* 22 (2009), pp. 897–900. DOI: 10.1016/j.jlp.2009.09.003.

[106] T.B. Quy and J.M. Kim. “Crack detection and localization in a fluid pipeline based on acoustic emission signals”. In: *Mechanical Systems and SIgnal Processing* 150 (2020). DOI: 10.1016/j.ymssp.2020.107254.

[107] G.A. Pantazopoulos. “A Short Review on Fracture Mechanisms of Mechanical Components Operated under Industrial Process Conditions: Fractographic Analysis and Selected Prevention Strategies”. In: *Metals* 9, 148 (2019). DOI: 10.3390/met9020148.

[108] M. El-Sayed, A. Ek Domiaty, and A-H.I Mourad. “Fracture Assessment of Axial Crack in Steel Pipe under Internal Pressure”. In: *Procedia Engineering 130 1273-1287.* 2015.

[109] Cambridge University Engineering Department. *Materials Data Book.* 2003, p. 6.

[110] J. Fraden. *Handbook of Modern Sensors: Velocity and Acceleration.* Springer, 2010. Chap. 8, pp. 353–373.

[111] DJB Instruments. *A/128/V1 Miniature IEPE Accelerometer, datasheet.* URL: https://www.djbinstruments.com/app/djb/files-module/local/datasheets/A-128-V1.pdf (visited on 10/01/2021).

[112] G. Gautschi. *Piezoelectric Sensorics: Acoustic Emission Sensors.* Springer, 2002, pp. 199–207.

[113] ASTM. *Standard test method for primary calibration Acoustic Emission sensors.* ASTM international, 2012.

[114] Physical Acoustics. *PICO Acoustic Emission sensor, datasheet*. URL: https://www.physicalacoustics.com/by-product/sensors/PICO-200-750-kHz-Lightweight-Miniature-AE-Sensor-with-Integral-Coaxial-Cable (visited on 10/01/2021).

[115] Physical Acoustics. *D9215 Acoustic Emission sensor, datasheet*. URL: https://www.physicalacoustics.com/by-product/sensors/D9215-50-650-kHz-Very-High-Temperature-AE-Sensor-with-Hardline-Softline-Cable (visited on 10/01/2021).

[116] H.L. Dunegan. *Modal analysis of Acoustic Emission signals*. Tech. rep. Dunegan Engineerinc Company, 1997.

[117] Physical Acoustics. *246 preamplifier, datasheet*. URL: https://www.physicalacoustics.com/by-product/2-4-6/ (visited on 10/01/2021).

[118] Alligator Technologies. *USBPBP S1 instrumentation amplifier*. URL: https://www.alligatortech.com/USBPBPS1_USB_programmable_instrumentation_amplifier_band_pass_filter.html (visited on 10/01/2021).

[119] J. Fraden. *Handbook of Modern Sensors: Force, Strain and Tactile Sensors*. Springer, 2010. Chap. 9, pp. 327–352.

[120] J. Carlsson. "Water Hammer Phenomenon Analysisusing the Method of Characteristics and Direct Measurements using a "stripped" Electromagnetic Flow Meter". MA thesis. KTH Royal Institute of Technology.

[121] N.P. Bitter and J.E. Shepherd. "Dynamic Buckling and Fluid–Structure Interaction of Submerged Tubular Structures". In: *Blast Mitigation: Experimental and Numerical Studies* (2014), pp. 189–227. DOI: 0.1007/978-1-4614-7267-4_7.

[122] K. Ueda and A. Umeda. "Dynamic Response of Strain Gages up to 300 kHz". In: *Experimental Mechanics 38* (1998).

[123] PCB Piezotronics. *Pressure fundamentals*. URL: http://www.pcb.com/contentstore/mktgcontent/linkeddocuments/Pressure/TM-PRS-PosterBook_Lowres.pdf (visited on 10/01/2021).

[124] NI. *Fundamentals, System Design, and Setup for the 4 to 20 mA Current Loop*. URL: https://www.ni.com/fr-fr/innovations/white-papers/08/fundamentals--system-design--and-setup-for-the-4-to-20-ma-curren.html (visited on 10/01/2021).

[125] T. Julien. *Cahier des Spécifications Techniques Particulières - DISPOSITIF EXPERIMENTAL RUPTUBE*. Tech. rep. Commissariat à l'énergie atomique et aux énergies alternatives.

[126] G.S.I.A. Aldeia et al. "A semblance based TDOA algorithm for sound source localization". In: *XXXVII SIMPOSIO BRASILEIRO DE TELECOMUNICACOES E PROCESSAMENTO DE SINAIS*.

[127] F. Sagasta, K.F Tee, and R. Piotrowski. "Lamb Modes Detection Using Cumulative Shannon Entropy with Improved Estimation of Arrival Time". In: *Journal of Nondestructive Evaluation* 38:27 (2019). DOI: 10.1007/s10921-019-0561-1.

[128] G. Kitagawa and H. Akaike. “A procedure for the modelling of nonstationary time series”. In: *Annals of the Institute of StatisticalMathematics* 30 (1978), pp. 351–363.

[129] R.B. Randall. *Handbook of Signal Processing in Acoustics*. Ed. by D. Havelock. Ed. by S. Kuwano. Ed. by M. Vorlaender. Vol. 1. Springer, 2008.

[130] D. Havelock, S. Kuwano, and M. Vorlaender. *Handbook of Signal Processing in Acoustics*. Ed. by D. Havelock. Ed. by S. Kuwano. Ed. by M. Vorlaender. Vol. 1. Springer, 2008, pp. 33–52.

[131] MathWorks. *Documentation - cwt function - Continous 1-D wavelet transform*. URL: https://fr.mathworks.com/help/wavelet/ref/cwt.html (visited on 11/17/2021).

[132] N.E. Huang et al. “The empirical mode decomposition and the Hilbert spectrum for nonlinear and non-stationary time series analysis”. In: *Proc. R. Soc. Lond. A* 454 (1971 1998), pp. 903–995.

[133] EXTENDE S.A. *Civa software website*. URL: https://www.extende.com/ (visited on 11/17/2021).

[134] AFNOR. *NF EN 1330-9 Non-destructive testing - Terminology - Part 9: termis used in acoustic emission testing*. AFNOR, 2017.

[135] C. Rainieri and G. Fabbrocino. *Operational Modal Analysis of Civil Engineering Structures*. Springer, 2014.

[136] MathWorks. *Matlab documentation - fft function - Fast Fourier transform*. URL: https://fr.mathworks.com/help/matlab/ref/fft.html (visited on 11/17/2021).

[137] M. Frigo and S.G. Johnson. *FFTW Library website*. 2014. URL: http://www.fftw.org/ (visited on 11/17/2021).

[138] M.P. Jahan, M Rahman, and Y.S Wong. “Micro-Electrical Discharge Machining (Micro-EDM): Processes, Varieties, and Applications”. In: *Comprehensive Materials Processing*. Vol. 11. Elsevier, 2014, pp. 333–371.

[139] E. Jacquelin, A. Bennani, and P. Hamelin. “Force reconstruction: analysis and regularization of a deconvolution problem”. In: *Journal of Sound and Vibration* 265 (2002), pp. 81–107. DOI: 10.1016/S0022-460X(02)01441-4.

[140] D. Goutaudier et al. “Impulse identification technique by estimating specific modal ponderation from vibration measurements”. In: *Journal of Sound and Vibration* 474 (2020). DOI: 10.1016/j.jsv.2020.115263.

[141] T. Julien. *Cahier des spécifications techniques particulières - section d’essai MAQAC*. Tech. rep. Commissariat à l’énergie atomique et aux énergies alternatives, 12–2020.

[142] C. Torrence and G.P. Compo. “A Practical Guide to Wavelet Analysis”. In: *Bulletin of the American Meteorological Society* 79 (1 1998), pp. 61–78.

[143] F.C. Tenoudji. “Analog and Digital Signal Analysis”. In: ed. by W.M. Hartmann. Springer, 2012. Chap. 12, 19, pp. 218–226, 337–374.

[144] L. Debnath. *Wavelet Transforms & Time-Frequency Analysis*. Springer, 2001.

[145] J.C. Newman. “Fracture Analysis of Surface and Through-Cracked Sheets and Plates”. In: *Engineering Fracture Mechanics, Vol.5, No.3, pp. 667-689.* 1973.

[146] G. Avakian. *Logiciel TDO (version zéro) - Note de présentation et notice d’utilisation.* Tech. rep. CEA, 1992.

[147] M. Pillet. *Introduction aux plans d’expériences par la méthode Taguchi.* 1994.

APPENDICES

Appendix A. Introduction to the Empirical Mode Decomposition

Empirical Mode Decomposition (EMD) is a data analysis method proposed in [132]. It aims at decomposing data (possibly nonlinear and non stationary) into a finite number of components, called Intrinsic Mode Functions (IMF). IMF are defined as functions whose upper and lower envelopes are symmetric and whose number of extrema and number of zero-crossing are equal or differ at most by one. The idea behind the method is that each IMF represents oscillations at a specific time scale, but with a potentially varying frequency. Moreover, considering that the initial data (or signal) is in time domain, IMF are in time domain as well and have the same size than the initial signal. As a result, in some situations, an IMF can be considered as a part of the signal associated to a specific physical phenomena. For instance, in acoustic or vibration signals, an IMF can be related to a specific source, or a specific wave propagation mode. However, it is not always the case and the results of an EMD must be carefully analyzed to validate such a physical interpretation.

The decomposition is achieved by the algorithm presented below, for an arbitrary signal $Y(t)$:

1. The local extrema of the signal $Y(t)$ are identified,
2. The local maxima are connected together by a cubic spline line, which gives the upper envelope. The same is done with local minima, which gives the lower envelope,
3. The mean $m1$ of the lower and upper envelopes is computed, and the difference h_1 between $m1$ and the initial signal Y is computed: $h_1(t) = Y(t) - m_1(t)$,
4. If h_1 satisfies the definition of IMF, its value is stored and will be referred as c_1, otherwise, all the previous steps are repeated by taking h_1 instead of the initial signal Y. Then, the mean of the new envelopes is referred as m_{11} and the difference between the signal and the mean is: $h_{11}(t) = h_1(t) - m_{11}(t)$,
5. The previous step is repeated k times, until h_{k1} is an IMF. Thus, at the last iteration, it yields: $c_1(t) = h_{1k}(t) = h_{1\ k-1}(t) - m_{1k}(t)$,
6. The first residue is defined as $r_1(t) = Y(t) - c_1(t)$,
7. All the previous steps are repeated by taking r_1 instead of Y. Then, the previous steps are repeated with r_2, r_3... r_n until the stopping criteria is satisfied.

Different stopping criteria can be chosen: minimal amplitude of c_n or r_n, or when no more IMF can be extracted from r_n.

At the end, it yields:

$$X(t) = r_n(t) + \sum_{j=1}^{n} c_j(t). \tag{A.1}$$

The first step of the process is depicted in Fig. A.1.

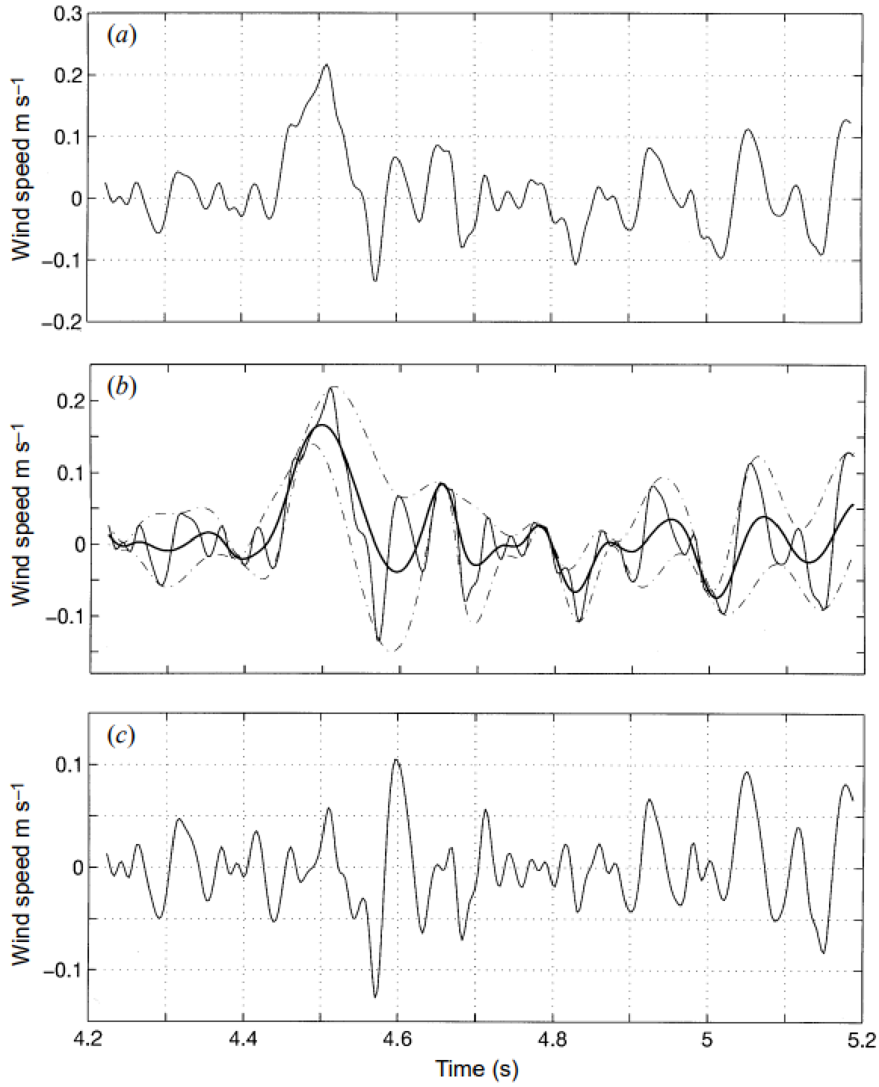

Figure A.1. *First step of the EMD algorithm: (a) initial signal; (b) upper and lower envelope in dot-dashed lines and the mean in thick line; (c) difference between the initial signal and the enveloppes' mean [132].*

Appendix B. Introduction to wavelet transforms

The current appendix aims at providing a short introduction to wavelet transforms and should not be considered as a complete presentation of the topic. For more accurate descriptions of wavelet functions or wavelet transforms, and their applications in signal processing, the reader may refer to [142] (continuous wavelet transform only), [143] (continuous and discrete wavelet transforms), [144] (exhaustive presentation of wavelet transforms applied to time-frequency analysis).

Wavelet transform is a signal analysis tool mainly used to decompose a signal into components that are located in both time and frequency (or scale). Most classical application are time-frequency (or time-scale) analysis, filtering, component extraction or data compression. The latter is not used in the current work. Wavelet transform can be applied to multi-dimensional data, but the current introduction is restricted to one-dimensional data, like the pressure or vibration signals studied in this work.

Wavelet transform can be understood as a convolution between the signal to be analyzed and a set of functions, called wavelets. All the wavelets constituting the set are obtained by translation and dilation of a fundamental one, called the *mother wavelet*.

A mother wavelet $\psi(\tau)$ is chosen as a function that depends on a time parameter τ, has a zero mean and is localized in time and frequency space [142]. The set of wavelets is built by a dilation with the scale parameter s and a time translation t of the mother wavelet as follows:

$$\psi_{st}(\tau) = \frac{1}{\sqrt{s}}\psi\left(\frac{\tau - t}{s}\right). \tag{B.2}$$

The purpose of the factor $\frac{1}{\sqrt{s}}$ is to normalize each wavelet to make it comparable to each other.

Then, the wavelet transform of the signal Y can be defined as a function of the scale s and the time t as:

$$W(s,t) = \frac{1}{\sqrt{s}}\int_{-\infty}^{+\infty} Y(\tau)\psi^*\left(\frac{\tau - t}{s}\right)d\tau, \tag{B.3}$$

where s is the scale parameter (which is related to the frequency), t the time position and "$*$" denotes the conjugate. As all the signals treated in this PhD are numerical signals, a discrete form of Eq. (B.3) can be of interest:

$$W_n(s,t_n) = \frac{\Delta t}{\sqrt{s}}\sum_{k=0}^{N-1} Y(t_k)\psi^*\left(\frac{t_k - t_n}{s}\right), \tag{B.4}$$

where n and k are two integers referring to two time samples, N is the size of the signal, and Δt is the time step.

Many methods and many kinds of wavelets exist, but they can be divided into two main categories that are introduced below: Continuous Wavelet Transform (CWT) and Discrete Wavelet Transfrom (DWT).

B.1. Continuous Wavelet Transform

CWT and DWT differ mainly in the way the set of wavelets is built, and, consequently, in the kind of function that can be chosen for each method.

In CWT, the wavelets are chosen to have a zero mean (*i.e.* $\int_{-\infty}^{+\infty} \psi(t)dt = 0$) and to be localized in time and frequency. It results in a redundancy in the information contained in the transform; it can be considered that the information contained in consecutive scales of the transform overlap. Thus, CWT is rather aimed at signal analyses when data size and computation cost are not of concern. One of the advantages of CWT analysis is that it provides an accurate time-frequency analysis with a variable time-frequency resolution.

In this work, CWT were computed with Maltab, using the function "cwt". For this function, the scale parameter is discretized so that $s = 2^{j/v}$, where v is a parameter to be chosen, referred as the number of voices per octave and $j = 1, 2...N$, with N an integer automatically estimated according to v and the type of wavelets. Therefore, the wavelet at scale s and translated by a shift t_n is given by:

$$\psi_{j,t_n}(t_k) = \frac{1}{\sqrt{2^{j/v}}}\psi\left(\frac{t_k - t_n}{2^{j/v}}\right). \tag{B.5}$$

Morse wavelets were used to build the wavelet set. In Matlab, the adjustable parameters for such wavelets are the Time-Bandwidth product P, and the symmetry factor γ. Considering these parameters, the Morse wavelet is defined in the frequency domain (the actual computation of the CWT is carried out in the frequency domain) as:

$$\Psi_{P,\gamma}(\omega) = U(\omega)a\omega^{P^2/\gamma}e^{-\omega^\gamma}, \tag{B.6}$$

where $U(\omega)$ is the unit step function and a is a normalization constant. Both P and γ parameters have simultaneous effects on the width in time and in frequency of the wavelet. These effects are shown for some examples in Matlab's documentation [131].

B.2. Discrete Wavelet Transform

In DWT, the wavelets are chosen to satisfy the previous conditions and, in addition, to be orthogonal. Therefore, the signal can be projected on an orthogonal basis constituted by those functions, which provides non-redundant information.

In this work, DWT were used for filtering and for the extraction of some components of the signals. DWT were preferred to CWT as it is faster to compute and it provides a more convenient way to select the set of wavelet coefficients containing the desired feature.

DWT were computed with the Matlab function "wavedec". In this function, the scale parameter is discretized differently than in the CWT function. At level j, the scale parameter is defined by $s = \sqrt{2^j}$. Moreover, as the DWT process includes decimation of the signals at each scale or level, the shift parameter t_n is discretized according to j: $t_n = 2^j n$. Thus, the wavelet at level j and translated by t_n reads:

$$\psi_{j,t_n}(t_k) = \frac{1}{\sqrt{2^j}}\psi\left(\frac{t_k - 2^j n}{2^j}\right). \tag{B.7}$$

It results in a coarser decomposition along the scale or frequency axis with the DWT than with the CWT.

Appendix C. Analytical calculation of the failure pressure of an initially cracked tube

The analytical method to calculate failure stress in a cracked tube is introduced in [145]. It was later improved in [108]. This latter improvement is used in the present work.

The aim of this method is to express the stress intensity factor around the tip of a crack on the outer surface of a metal tube under internal pressure, as a function of the applied stress and crack dimensions. Once such an expression is defined, it can be rewritten to express the applied stress as a function of the stress intensity factor and crack dimensions. Then, the stress intensity factor can be replaced by the value of the critical stress intensity factor (usually referred as "fracture toughness"), over which a failure occurs, to give the critical applied stress as a function of crack dimensions.

The initial form of the expression is:

$$K_I = F(a, c, t, R_m, \nu) \cdot \sigma_\phi \tag{C.8}$$

Where K_I is the stress intensity factor, a is the crack depth, c is the crack half-length (in the tube axis direction), tt is the wall thickess of the tube, R_m is the mean radius of the tube, ν is the Poisson coefficient and F is a function defined below.

$$F(a, c, t, R_m, \nu) = \left(M_F + (E_{(k)}\sqrt{\frac{c}{a}} - M_F)(\frac{a}{t})^s\right)^{-1} \frac{E_{(k)}}{M_{TM}\sqrt{\pi a}}\,, \tag{C.9}$$

where:

- $M_F = \begin{cases} \sqrt{\frac{c}{a}}(1+0.03\frac{c}{a})\,,\ si\ \frac{a}{c} > 1 \\ 1,13 - 0,1\frac{a}{c}\,,\ si\ 0,02 < \frac{a}{c} < 1 \end{cases}$
- $E_k = \int_0^{n/2} \sqrt{1 - k^2 sin^2\Theta\ d\Theta} = 1 + 1.464\left(\frac{a}{c}\right)^{1.65}$
- $s = 2 + 8\left(\frac{a}{c}\right)^3$
- $M_{TM} = \frac{1 - \frac{a/t}{\sqrt{1+1,255\lambda^2 - 0,0135\lambda^4}}}{1 - a/t}$, où $\lambda = \frac{c}{\sqrt{R_m t}}$.

After replacing K_I by the critical intensity factor (also called fracture toughness) K_c:

$$(C.8) \Rightarrow \sigma_c = \frac{K_c}{F(a, c, t, R_m, \nu)} \tag{C.10}$$

It should be noticed that this model is valid for cracks whose the ratio between depth and length ($c/2a$) is at least 0.02.

Appendix D. Feasibility study of water boiling reproduction in the experimental device

The reproduction of a boiling crisis requires high enough temperature on the rod walls in an area of the test section. However, the external tube, which is in PMMA, limits the maximum temperature on the channel outer wall. Calculations are necessary to determine if both conditions can be satisfied.

D.1. Issue

To be representative of the real situation, the fluid as to be heated by the rod. It is possible to use Joule effect, like in several existing experimental facilities, in order to generate an nucleate boiling around the rod. At atmospheric pressure, it is assumed that 110 °C in the test section is enough to produce a nucleare boiling. However, the PMMA outer tube can withstand a temperature up to 70 °C (a steel or glass outer tube could withstand a higher temperature, but steel would prevent optical vibration measurements and glass is too expensive and fragile). Calculations were carried out to estimate if it is possible to have 110 °C water near the rod surface and less than 70 °C on the outer channel wall made of PMMA. The following variables are used:

- T_{inlet}: inlet fluid temperature in the test section température d'entrée dans la section d'essai,
- $T_1(x)$: fluid temperature on the rod wall,
- $T_{mean}(x)$: average temperature in the fluid température moyenne du fluide, out from the boundary layers next to the walls,
- $T_2(x)$: fluid temperature on the PMMA wall,
- Φ: heat flux coming from the rod (in W), assumed to be constant along the heating section,
- P: average static pressure in the test section, set at 1 bar,
- v: average flow velocity (in m.s^{-1}),
- D_1: rod diameter (equal to the inner channel diameter),
- D_2: outer channel diameter diamètre du canal de confinement (diamètre extérieur de la section de passage du fluide),
- D_h: hydraulic diameter, in the current case of an annular channel, $D_h = D_2 - D_1$,
- Q: flow rate, $Q = v\pi\frac{D_2^2-D_1^2}{4}$ (in m^3.s^{-1})
- L: total length of the channel, about 810 mm,
- L_C: length of the heating section (assuming that the rod does not heat along its entire length),

- ρ: water density, 965 kg.m^{-3},
- λ: water thermal conductivity, 0.67 W.m^{-1}.K^{-1},
- μ: dynamic water viscosity, 3.45.10^{-4} Pa.s.
- C_p: thermal water capacity, 4.2.10^3 J.kg^{-1}

Temperatures are in °C. Water properties are considered for an average temperature of 90°C (mean value between the needed temperature around the rod and the maximum value near the PMMA wall).

The studied situation is depicted by Fig.D.2.

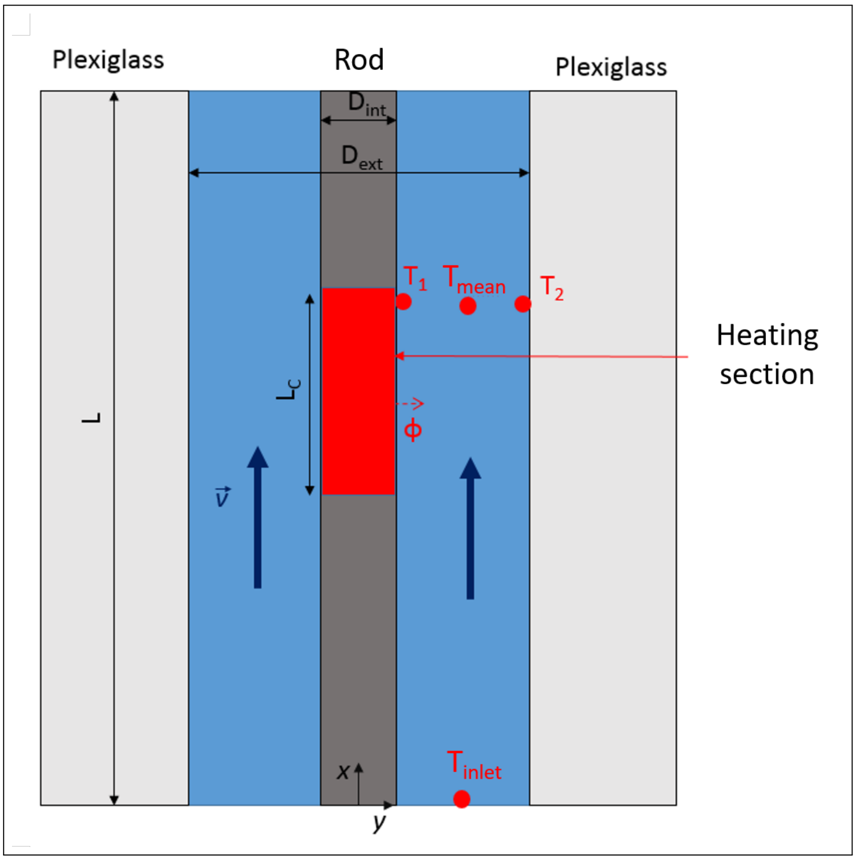

Figure D.2. *Studied situation for heat transfer calculation.*

Unscaled temperature profile is presented in Fig. D.3. This profile shows a decrease in the temperature near the outer wall. It is due to the heat transfer through the outer wall. Outer air is colder than the inner fluid. Therefore, fluid heat is partially absorbed by the PMMA wall and then by outer air. As a consequence $T_2 < T_{mean}$. For design calculations, we want $T_2 \leq 70\,°C$. At a first step, in order to avoid to take into acount the heat transfer to the outer air and, thus, to limit the number of model parameters, T_2 is bounded under T_{mean}. Indeed, if $T_{mean} \leq 70°C$, so $T_2 < 70°C$.

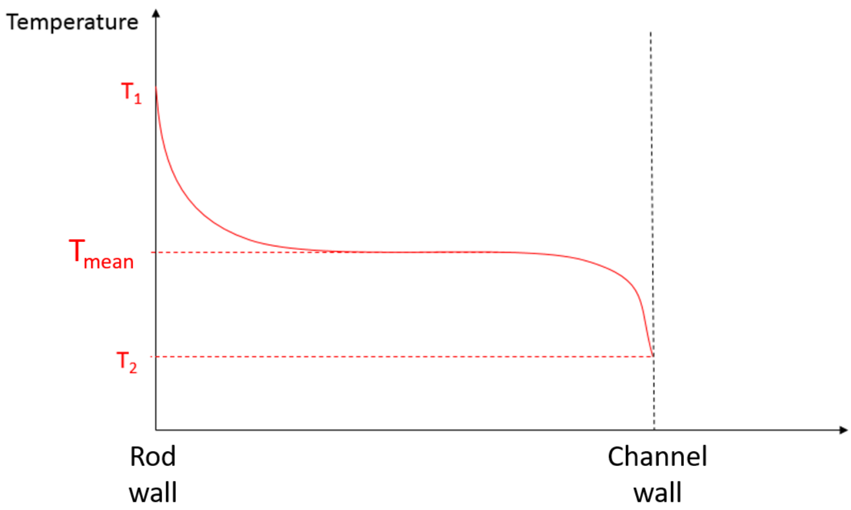

Figure D.3. *Temperature profil in the channel*

The aim of the calculation is to determine $T_2(x)$ and $T_{mean}(x)$ when $T_1(x)$ is imposed. Parameters that are not fixed at the current step are presented in Tab. D.1.

Parameter	Range	Ease of modification during operation
Channel diameter	[15; 60] mm	- - -
Heat flux	[0; 1] kW	+++
Heating section length	[0; 810] mm	- - -
Flow rate	[0; 200] $m^3.h^{-1}$	+
Inlet temperature	[50; 70] °C	+

Table D.1. *Variable parameters*

In order to find the optimal combination of heating flux and heating section's length that provides 110 °C around the rod without having more than 70 °C on the outer wall, the algorithm introduced in D.4 is applied.

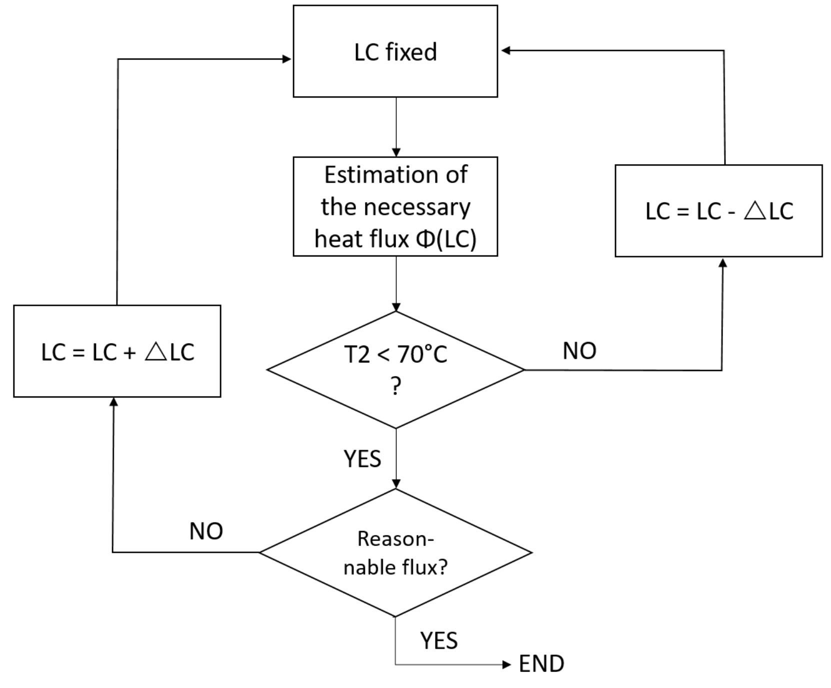

Figure D.4. *Approach for the estimation of the required heat flux.*

D.2. Calculation

Let an elementary fluid slice between axial coordinates x and $x+dx$. Downstream of this slice, at $x+dx$, the average temperature and the temperature next to the heating wall are given by [146]:

$$\begin{cases} T_{mean}(x+dx) = T_{mean}(x) + \frac{\Phi \pi D_1}{QC_p} dx \\ T_2(x+dx) = T_{mean}(x+dx) + \frac{\Phi}{h} \end{cases} \tag{D.11}$$

($T_{mean}(x)$ can be considered as the average temperature entering the elementary slice.)

Firstly, the necessary heat flux,Φ_c , to get 110°C on the rod wall is expressed as a function of the heating length, the inlet temperature, the flow rate and the outer diameter. The last two parameters are taken into account by the Reynolds number, which is included in the heat transfer coefficient h. This coefficient can be approximated by Dittus-Boelter's correlation (with a corrective term to take into account the small length that does not provide a fully stationary turbulent flow) :

$$h = 0,023 * \mathrm{Re}^{0,8}\, \mathrm{Pr}^{0,4}\, (1 + \frac{D_h}{L}^{0,7}), \tag{D.12}$$

where $Re = \frac{v D_h}{\mu}$ (Reynolds number) and $Pr = \mu \frac{C_p}{\lambda}$ (Prandtl number).

From eq. D.11 applied at the upper point of the heating length, and by considering a constant heat flux along this section, it yields:

$$\Phi_c = (110 - T_{inlet}) \frac{hQC_p}{QC_p + hP_c L_c} \tag{D.13}$$

That expression is used in the mentioned approach (Fig. D.4) to determine the necessary flux for an imposed heating length. Then, temperatures T_{mean} and T_2 are estimated with eq. D.11, which is solved for the entire length of the rod (considered as an interval [0;L], discretized by a step dx). Outside of the heating length ($0 < x < x_c$ and $x_c + L_c < x < L$), $\Phi(x) = 0$ (there is no heat flux) and in the heating length ($x_c \leq x \leq x_c + L_c$), the heat flux is imposed so that $\Phi(x) = \Phi_c$.

D.3. Conclusion about water boiling reproduction feasibility

Calculations showed that it is not possible to obtain 110 °C on the inner wall while keeping the average temperature below 70 °C, unless with a small heating length (about some centimeters) and a very high heat flux (about several hundreds Watt). Generating such a flux is not realistic. Reducing the heating length would allow a reduction in the necessary heat flux to obtain 110 °C on the inner wall, but the average temperature would be higher than 70°C.

Two solutions are however possible:

- Decrease the pressure in the water loop, in order to decrease the boiling point and, thus, to decrease the necessary temperature on the inner wall. Nevertheless, such a solution implies significant technical constraints in the design and the use of the water loop.
- Use an external tube made of a more heat-resistant material, such as glass or steel. A glass external tube would still allow optical vibration measurements, but it would be far more expensive and less resistant to mechanical shocks. A steel external tube would be relatively cheap and resistant, but it would make optical measurement impossible.

Despite those solutions, it was finally decided not to reproduce boiling crisis and to focus the study on the cladding failure.

Appendix E. RUPTUBE: First design of experiments

The objective of the first RUPTUBE tests series was to experimentally estimate tube failure pressure. Experimental results were intended to check the validity of the calculation method, presented in App. C, which gave the failure stress of an initially cracked tube as a function of the tube geometry (diameter and thickness), the tube material properties (fracture toughness and Poisson coefficient) and the size dimensions (length and depth). A design of experiments was established following the method presented in [147], based on Taguchi's method. Firstly, an ideal design of experiment is introduced. Some tests defined in this design are not possible because the required tubes are not commercially available. Then, an altered design of experiments that takes in acount commercial availability is presented.

E.1. Ideal experimental design

Generally, design of experiments methods are intended to identify the tests that are necessary to estimate the influence of various factors on the phenomena of interest, referred to as the "responses" of the studied system. In other words, design of experiments methods provide the way to define or validate a model whose inputs are the factors and the outputs are the responses. The factors are variables that are assumed to have effects on the studied systems and must be, in most of methods, identified beforehand. However, experimental results might show that some considered factors are actually negligible, or that some significant factors are missing. There can be interactions between factors, which means that the effect of a factor on the response can depend on the level of another factor. Most of the experimental design methods, including Taguchi's one, allow to estimate interactions.

Firstly, according to Taguchi's method, a model of the following form is considered:

$$\begin{aligned}\sigma_r = M + [k_1\ k_2\ k_3\ k_4]K + [d_1\ d_2\ d_3\ d_4]D + [t_1\ t_2]T + [a_1\ a_2]A + [c_1\ c_2]C \\ + A^T \begin{bmatrix} I_{A1T1} & I_{A1T2} \\ I_{A2T1} & I_{A2T2} \end{bmatrix} T + A^T \begin{bmatrix} I_{A1C1} & I_{A1C2} \\ I_{A2C1} & I_{A2C2} \end{bmatrix} C\text{'}\end{aligned} \tag{E.14}$$

where :

- σ_r is the failure stress, which is the response of the system,
- M is the average of the measured response values,
- K is the material parameter, represented by its fracture toughness,
- D is the outer diameter of the tube,
- T is the wall thickness of the tube,
- A is the depth of the initial crack,
- C is the length of the initial crack (in the tube axis' direction),

- k_i, r_i, t_i, a_i, c_i are the respective effects of parameters K, R, T, A ou C while the parameters are at level i,
- I_{AiTj} is the interaction between A and T while A is at level i and T at level j,
- I_{AiCj} is the interaction between A and C while A is at level i and C at level j.

Levels of each parameter and interactions are described in Tab. E.2 , as well as their number of degrees of freedom (DOF).

	M	K	D	T	A	C	IAT	IAC
Levels		Steel ; Aluminium ; Magnesium ; PVC	6 ; 8 ; 9.5 ; 12 mm	0.6 ; 1 mm	1/4 ; 3/4 T	15 ; 25 mm		
Number of levels		4	4	2	2	2	4	4
Number of DOF	1	3	3	1	1	1	1	1

Table E.2. *Levels and degrees of freedom of each parameter*

The number of tests required to estimate the model has to fulfil two conditions:

- It must be greater or equal to the summ of the DOF of each factor and interaction„
- Independant factor and interaction must be orthogonal to each other. It implies that the number of tests must be greater or equal to the smallest common multiple of the products of numbers of levels of each pair of independant factors and interactions.

In the current case, the condition related to the DOF implies a number of tests superior or equal to 12, and the orthogonality condition a number superior or equal to 16. Therefore, 16 tests are necessary.

To design the experimental plan, we use Tahuchi's table $L_{16}(2^15)$, defined in Tab. E.5. This table is initially intended for a system of 15 factors that all have two levels. It can be transformed to make it suited to a systrm containing two factors with four levels and three factors with two levels. To this end, on of the graphs associated to the $L_{16}(2^15)$ table is used (every Taguchi's table is associated with one or several graphs that represent factors and their interactions) and presented in Fig. E.6. On this graph, each black dot is a factor and the lines represent interactions between the factors. A row, whose number is shown in the graph, are associated to each factor and each interaction. It is possible to gather two rows associated to two two-levels factors in order to study one four-levels factor. Graphically, it can be seen as associating two points to a single factor. After gathering two factors, the row that represents the interaction between the gathered factors can not be associated to another facor or interaction in the new table.

In the current case, rows 2 and 4 are associated to the factor R and rows 8 and 15 to factor K. Thus, rows 7 and 6 can not be considered anymore. Then, row 1 is associated to the factor A, row 10 to the factor C and row 12 to the factor T. Row 11 can therefore be associated to the AC interaction and row 13 to the AT interaction. The resulting experimental design is presented in Tab. E.7.

Run	Columns														
	1	2	3	4	5	6	7	8	9	10	11	12	13	14	15
1	1	1	1	1	1	1	1	1	1	1	1	1	1	1	1
2	1	1	1	1	1	1	1	2	2	2	2	2	2	2	2
3	1	1	1	2	2	2	2	1	1	1	1	2	2	2	2
4	1	1	1	2	2	2	2	2	2	2	2	1	1	1	1
5	1	2	2	1	1	2	2	1	1	2	2	1	1	2	2
6	1	2	2	1	1	2	2	2	2	1	1	2	2	1	1
7	1	2	2	2	2	1	1	1	1	2	2	2	2	1	1
8	1	2	2	2	2	1	1	2	2	1	1	1	1	2	2
9	2	1	2	1	2	1	2	1	2	1	2	1	2	1	2
10	2	1	2	1	2	1	2	2	1	2	1	2	1	2	1
11	2	1	2	2	1	2	1	1	2	1	2	2	1	2	1
12	2	1	2	2	1	2	1	2	1	2	1	1	2	1	2
13	2	2	1	1	2	2	1	1	2	2	1	1	2	2	1
14	2	2	1	1	2	2	1	2	1	1	2	2	1	1	2
15	2	2	1	2	1	1	2	1	2	2	1	2	1	1	2
16	2	2	1	2	1	1	2	2	1	1	2	1	2	2	1

Figure E.5. *Taguchi's table* $L_{16}(2^{15})$

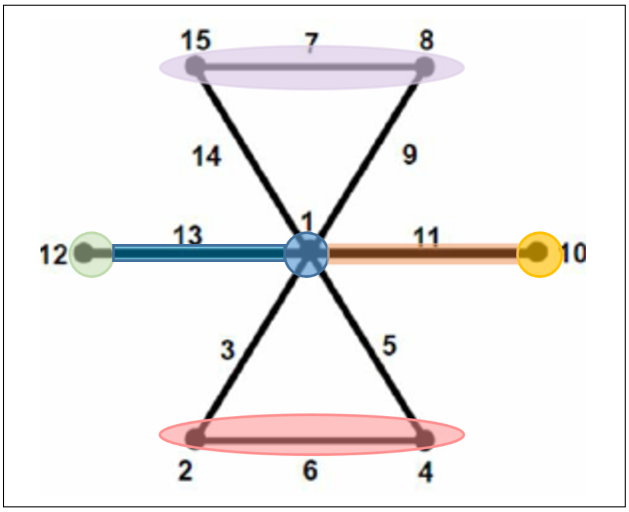

Figure E.6. *Diagramm of table* $L_{16}(2^{15})$

Essai	R	K	A	C	AC	T	AT
1	1	1	1	1	1	1	1
2	1	4	1	2	2	2	2
3	2	2	1	1	1	2	2
4	2	3	1	2	2	1	1
5	3	2	1	2	2	1	1
6	3	3	1	1	1	2	2
7	4	1	1	2	2	2	2
8	4	4	1	1	1	1	1
9	1	2	2	1	2	1	2
10	1	3	2	2	1	2	1
11	2	1	2	1	2	2	1
12	2	4	2	2	1	1	2
13	3	1	2	2	1	1	2
14	3	4	2	1	2	2	1
15	4	2	2	2	1	2	1
16	4	3	2	1	2	1	2

Figure E.7. *Table* $L_{16(4^2,2^5)}$, *from table* $L_{16}(2^{15})$

Tab. E.3 describes the experimental descign with the levels of every factor for each test. In the table are also given the expecred failure pressures, estimated by the model presented in C.

Test	Outer diam. (mm)	Material	a/t	C (mm)	T (mm)	Expected failure pressure (relative pressure, bar)
1	6	1	1/4	15	0,6	282
2	6	4	1/4	25	1	3
3	8	2	1/4	15	1	44
4	8	3	1/4	25	0,6	18
5	9.5	2	1/4	25	0,6	22
6	9.5	3	1/4	15	1	25
7	12	1	1/4	25	1	173
8	12	4	1/4	15	0,6	1
9	6	2	3/4	15	0,6	5
10	6	3	3/4	25	1	4
11	8	1	3/4	15	1	5
12	8	4	3/4	25	0,6	0.1
13	9.5	1	3/4	25	0,6	16
14	9.5	4	3/4	15	1	0.3
15	12	2	3/4	25	1	3
16	12	3	3/4	15	0,6	2

Table E.3. *Factor levels for each test*

In the table, materials are referred by the following numbers Dans ce tableau, les matériaux sont désignés par les numéros suivants :

1. Stainless steel (316 or 304),
2. Aluminium,

3. Magnesium,
4. PMMA (Poly Methyl Metacrylate) or ABS (Acrylonitrile Butadiene Styrene).

Materials were choosen based on their fracture toughness and their cost. On one hand, materials with low fracture-toughness are wanted to have a low fracture failure. A limit of 150 MPa/$\sqrt{\text{m}}$ is fixed. On another hand, fracture toughness of the different materials should be regularly distributed on the interval from 1 to 150 MPa/$\sqrt{\text{m}}$.

Zircalloy, although it is the materials of most of real fuel rod claddings, is not considered because of its high cost and the difficulty to supply. Moreover, no reliable data about its fracture toughness could be found.

According to the calculation with the method presented in C applied to the test parameters, the expected failure pressures are presented in Tab. E.3.

E.2. Possible experimental design

After looking at the tubes available in the market, it came out that some tubes required by the initial experimental design would be supplied with extreme difficulty. Some of those tubes are not mass-produced and must be custom made, but, given the small numbers that were required, the unit price proposed by requested producers were too high. As a consequence, the experimental design was adjusted to match with market possibilities. Tab. E.4 shows the tubes that are easily available.

Material	Outer diam. (mm)	Thickness (mm)
Steel (316L)	12	1.5
Steel (316L)	12	1
Steel (316L)	10	1.5
Steel (316L)	8	1.5
Steel (316L)	8	0.5
Steel (Parker A-LOK)	6	1
Steel (316L)	6	0,6
Aluminium	12	1
Aluminium	12	0.5
Aluminium	10	1
Aluminium	10	0.5
Aluminium	8	1
Aluminium	8	0.5
Aluminium	6	1
Aluminium	6	0.5
PMMA	12	2
ABS	12.7	0.7
ABS	12.7	0.7
ABS	10	2
ABS	7.9	1.7
ABS	8.7	0.7
ABS	6.4	1.5
ABS	6	0.5

Table E.4. *Commercially available tubes*

To meet these additional constraints, the study is divided in three series of experiments:

1. Experiments on aluminium and steel tubes, to determine if it is actually possible to generate failures under 50 bar, and to study effects of the tube diameter and the crack size, with a constant tube thickness. This series consists of eight tests,
2. If the first series proves that failures can be obtained under 50 bar with metal tubes, a second series is carried out with aluminium and steel tubes to study the effects of the tube thickness and crack size, with two different tube diameters. This series consists of eight test, one is common with the previous series,
3. If the first series shows that failures of metal tubes are not possible under 50 bar, a second series will be carried out with plastic tubes. This series requires twelve tests.

Factors that are considered in each series are presented in Tab. E.5, E.6, and E.7.

	M	K	D	T	A	C
Levels	/	Steel ; Alu	6 ; 8 ; 10 ; 12 mm	1 mm	1/4 ; 3/4 T	15 ; 25 mm
Number of levels	/	2	4	1	2	2
Number of DOF	1	1	3	1	1	1

Table E.5. *Levels and DOF of factors for the first tests series*

	M	K	D	T	A	C	IAT	IAC
Levels	/	Steel ; Alu	6 ; 8	0.6 ; 1 mm	1/4 ; 3/4 T	15 ; 25 mm	/	/
Number of levels	/	2	2	2	2	2	4	4
Number of DOF	1	2	2	1	1	1	1	1

Table E.6. *Levels and DOF of factors and interactions for the second test series with metal tubes*

	M	K	G=D/T	T	A	C	IAC	IAG
Levels	/	ABS	/	0,6 ; 1 mm	1/4 ; 3/4 T	15 ; 25 mm	/	/
Number of levels	/	1	3	2	2	2	4	6
Number of DOF	1	0	2	1	1	1	1	2

Table E.7. *Levels and DOF of factors and interactions for the second test series with plastic tubes*

Remark: For the plastic tubes series, the factor G=D/T (diameter/thickness) is considered instead of the two different diameter and thickness factors, because of constraints caused by commercial availability of the tubes. Among the available tubes, only one specific thickness is available for each diameter.

Appendix F. IMF computed by the EMD of signal AE 3 from test 6

Successive IMF resulting from the EMD of signal AE 3 measured during the tube failure of test 6.

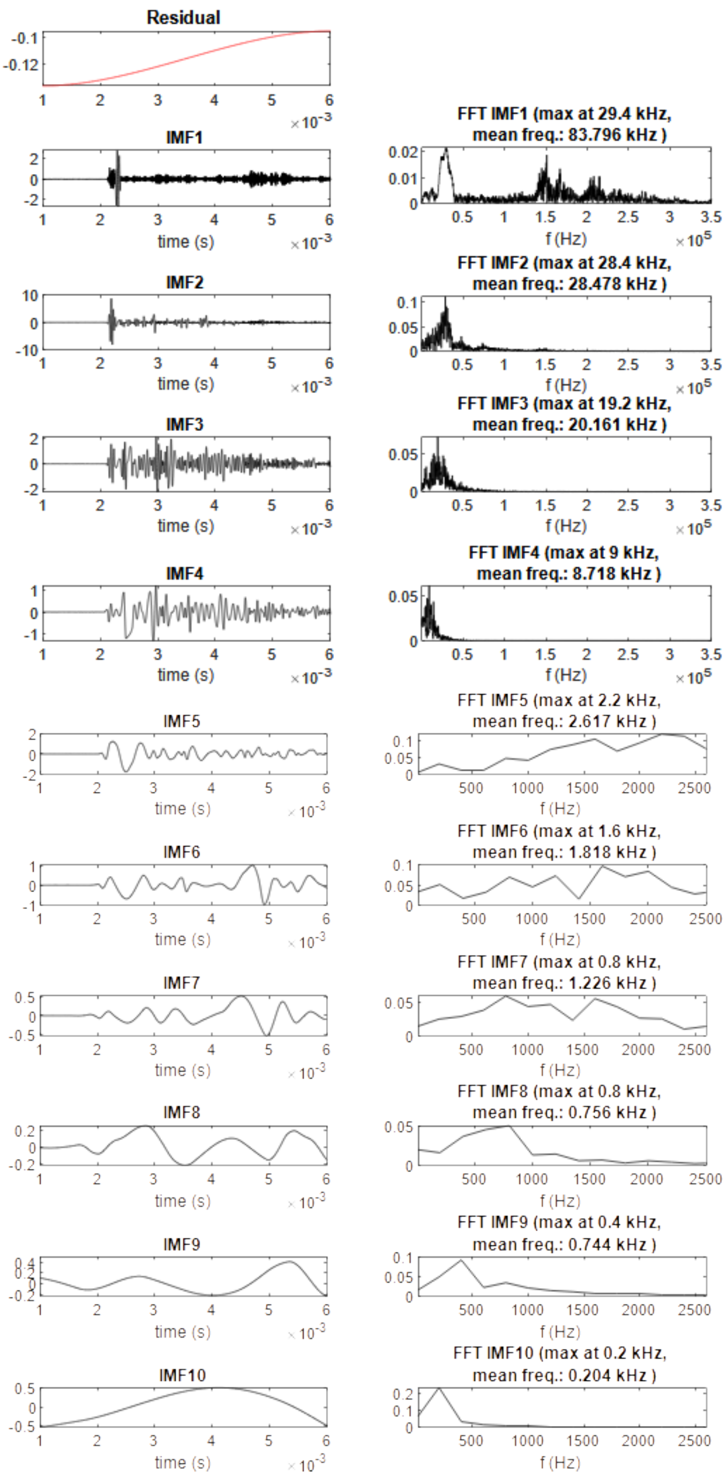

Figure F.8. *RUPTUBE - 2nd campaign, Test 6: IMF from the EMD of signal AE 3.*

Appendix G. IMF computed by the EMD of signal AE 4 from test 6

Successive IMF resulting from the EMD of signal AE 4 measured during the tube failure of test 6.

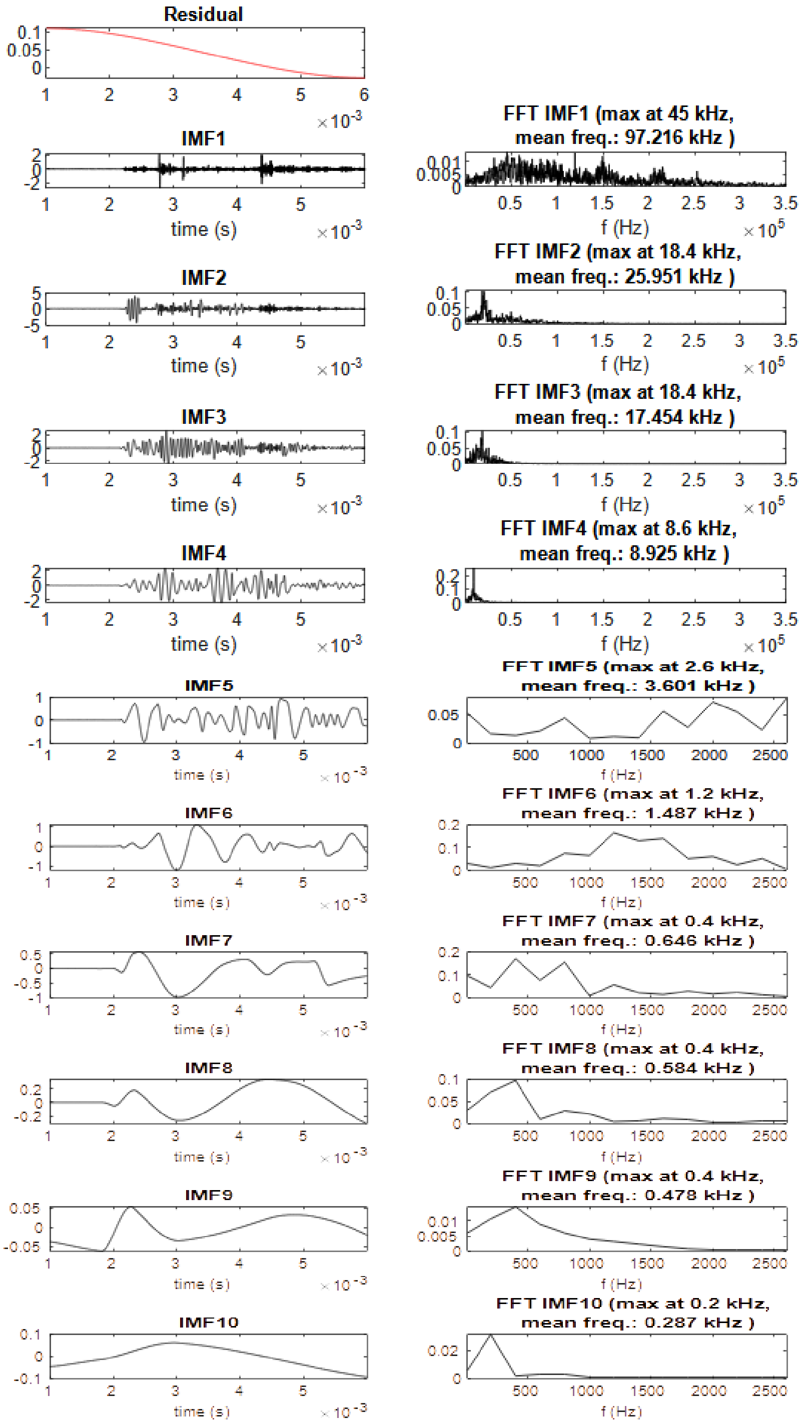

Figure G.9. *RUPTUBE - 2nd campaign, Test 6: IMF from the EMD of signal AE 4.*

Appendix H. IMF computed by EMD of strain gauges signals from the failure test

Successive IMF resulting from the EMD of the strain gauges signals measured during the failure test are presented in Fig. H.10 and H.11. Each EMD is presented with its Fourier Transform computed by FFT. For low frequency IMF (from the 5th to the 10th) the spectra are displayed over a reduced frequency range for the sake of readability.

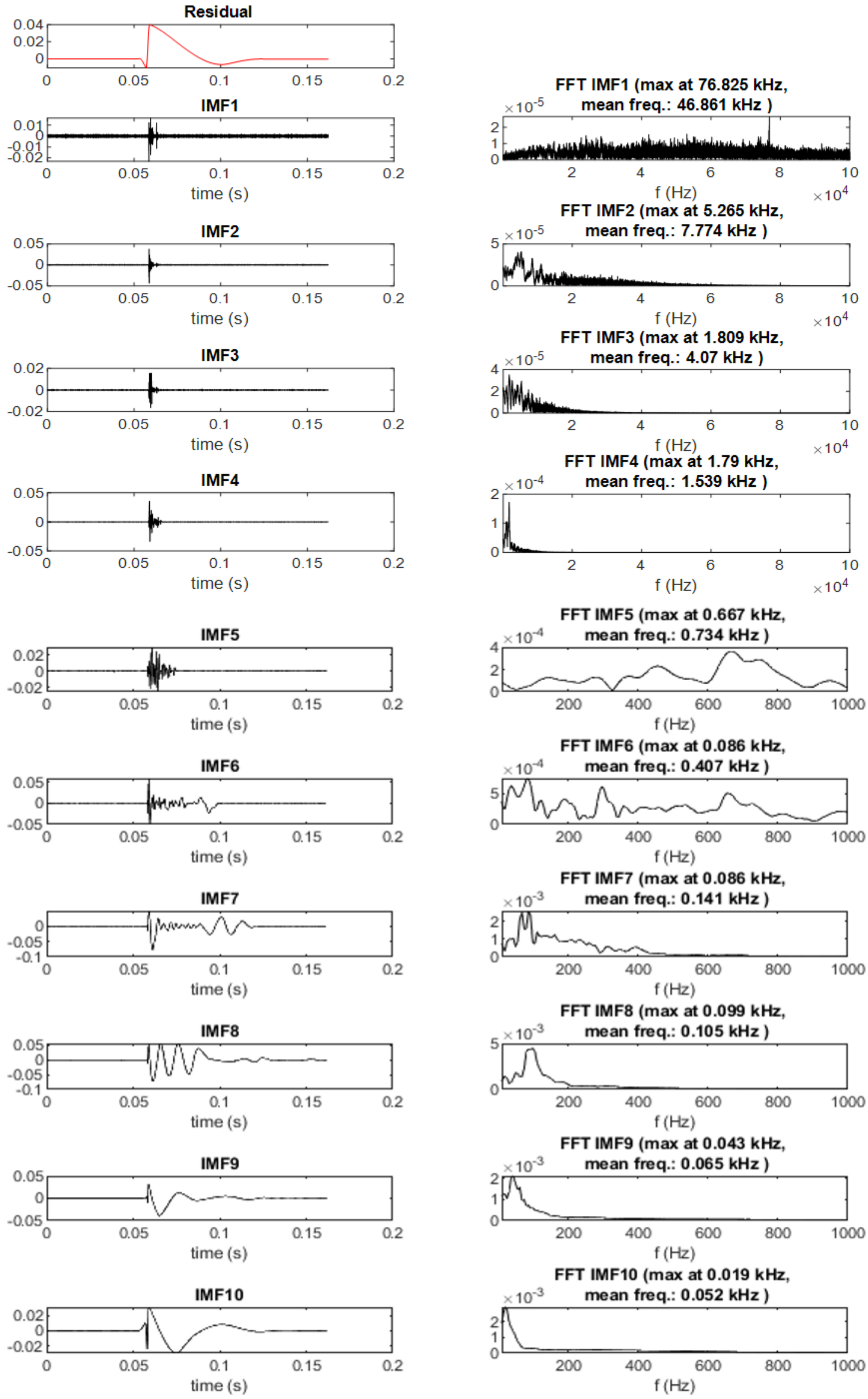

Figure H.10. *RUPTUBE - 2nd campaign, gauges test: IMF from the EMD of G1 signal during the failure test.*

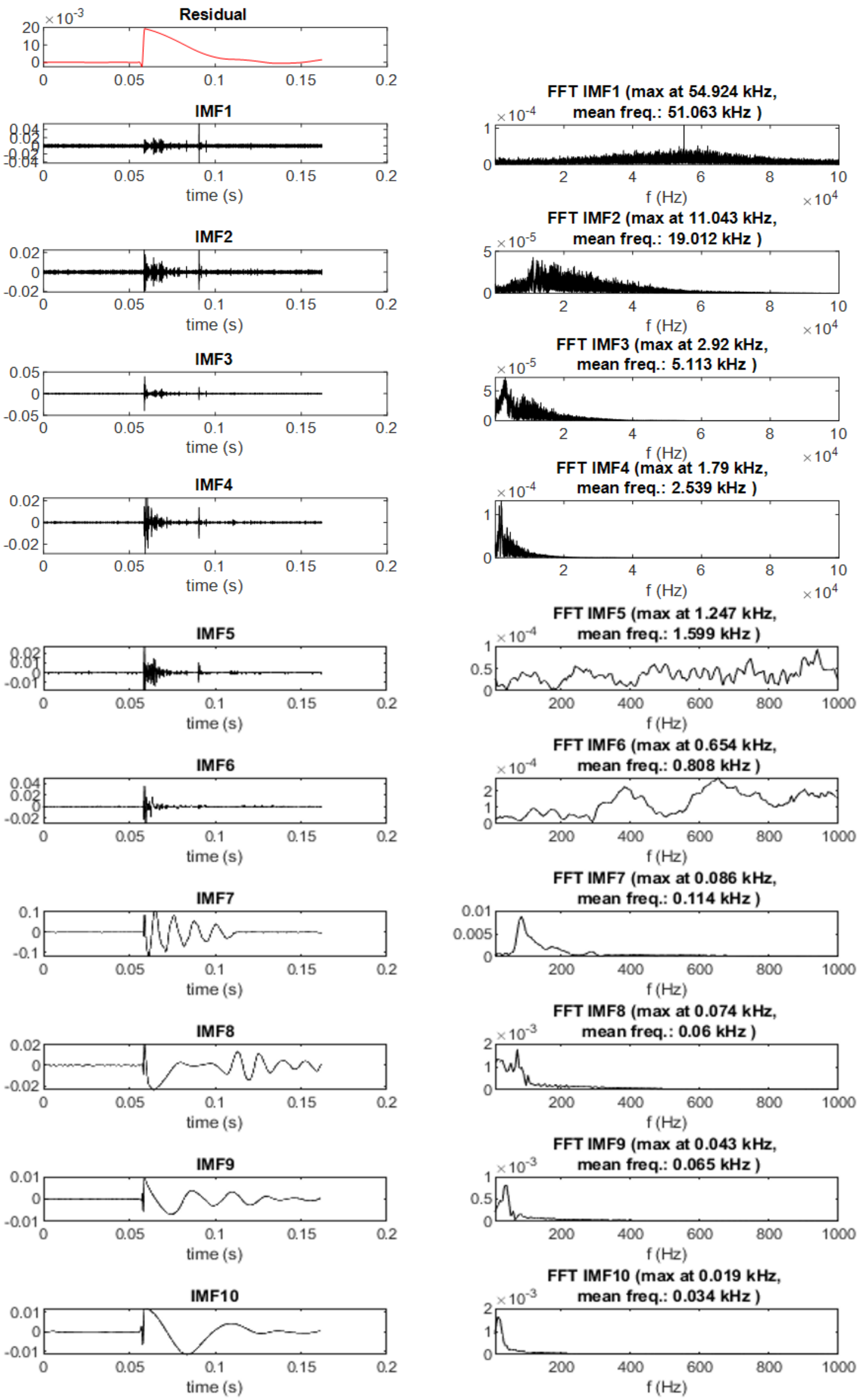

Figure H.11. *RUPTUBE - 2nd campaign, gauges test: IMF from the EMD of G2 signal measured during the failure test.*

Appendix I. IMF computed by EMD of strain gauges signals from tests with an impact source

Successive IMF resulting from the EMD of the strain gauges signals measured during the test with an impact at 460 mm from the tube inlet's end are presented in Fig. I.12 and I.13. Each EMD is presented with its Fourier Transform computed by FFT. For low frequency IMF (from the 5th to the 10th) the spectra are displayed over a reduced frequency range for the sake of readability.

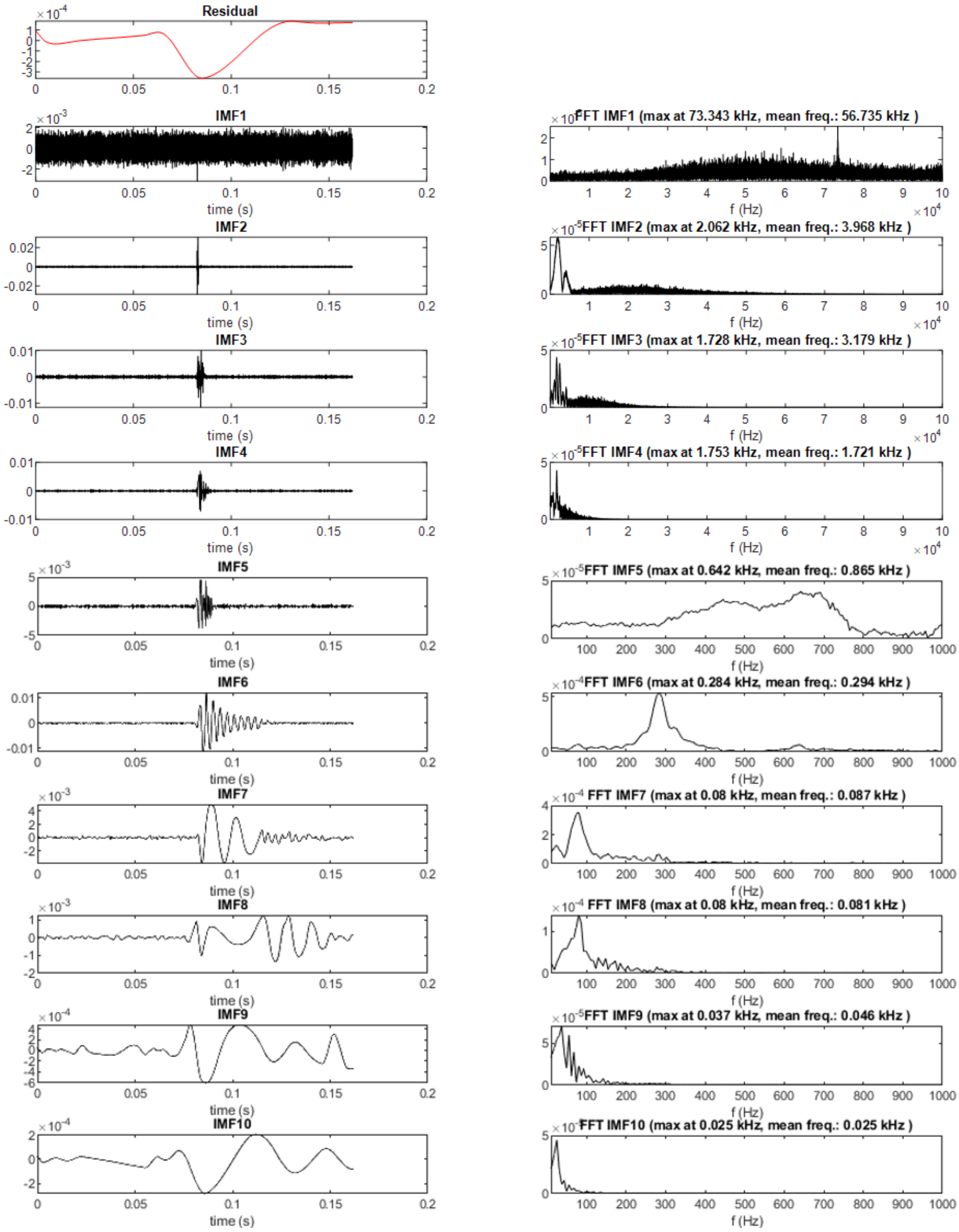

Figure I.12. *RUPTUBE - 2nd campaign, gauges test: IMF from the EMD of G1 signal with an impact at 460 mm from the tube inlet's end.*

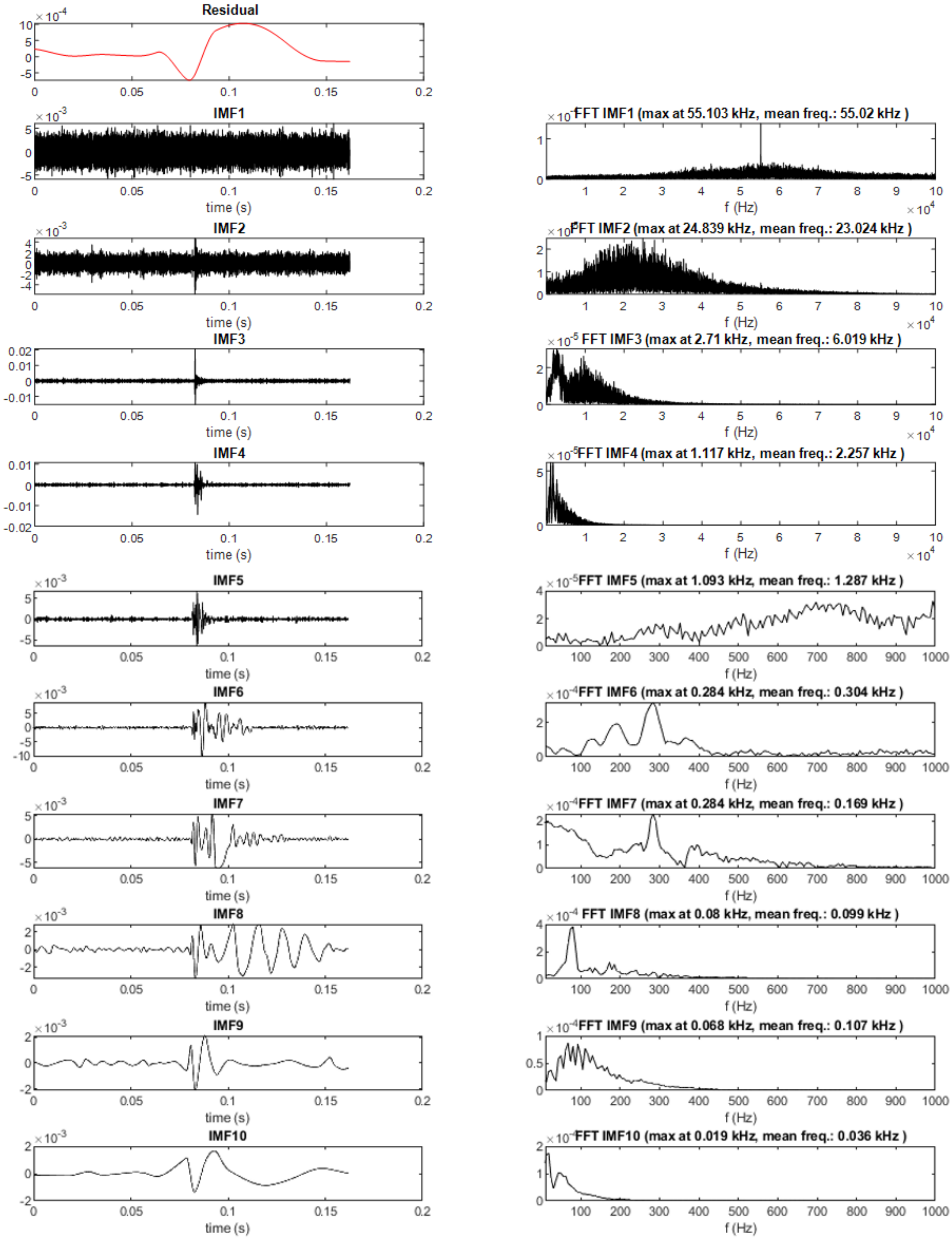

Figure I.13. *RUPTUBE - 2nd campaign, gauges test: IMF from the EMD of G2 signal measured with an impact at 460 mm from the tube inlet's end.*

Appendix J. Complementary results of RUPTUBE experiments

J.1. Results of Test 1

Configuration of Test 1 is resumed in Fig. J.14.

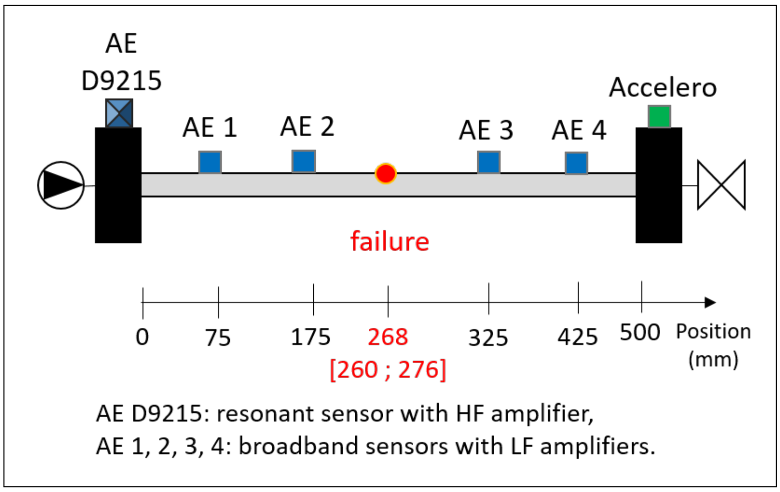

Figure J.14. *RUPTUBE - 2^{nd} campaign, test 1: configuration.*

Firstly, signals of the broadband AE sensors mounted on the tube are analyzed. Time-domain representation are given in Fig. J.15 and time-frequency representations, by CWT, in Fig. J.16. Those signals are processed following the method introduced in Sec. IV.4.2.2.

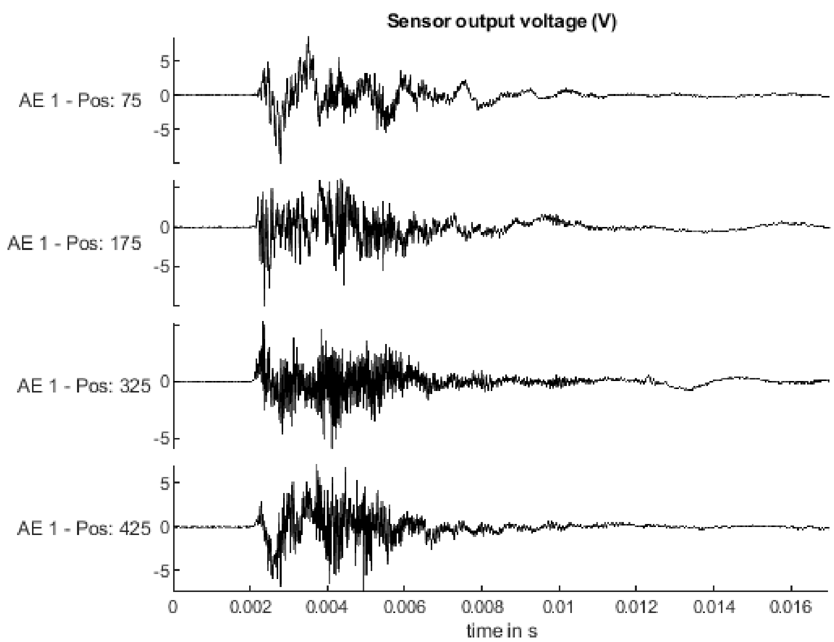

Figure J.15. *RUPTUBE - 2^{nd} campaign, test 1: Time domain view of the AE sensors' signals.*

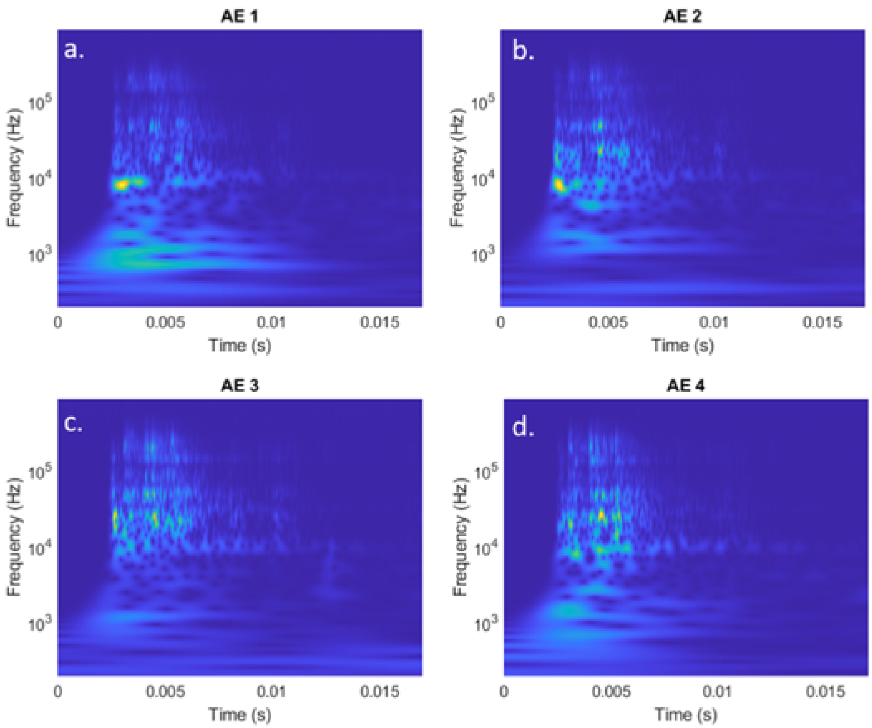

Figure J.16. *RUPTUBE - 2nd campaign, test 1: Time-frequency views of the AE sensors' signals. CWT by Morse wavelets. a.: Sensor 1, b.: Sensor 2, c.: Sensor 3, d.: Sensor 4.*

Fig. J.17 shows the 20 kHz HP filtered signals with a time magnification around the arrival of the failure-induced waves.

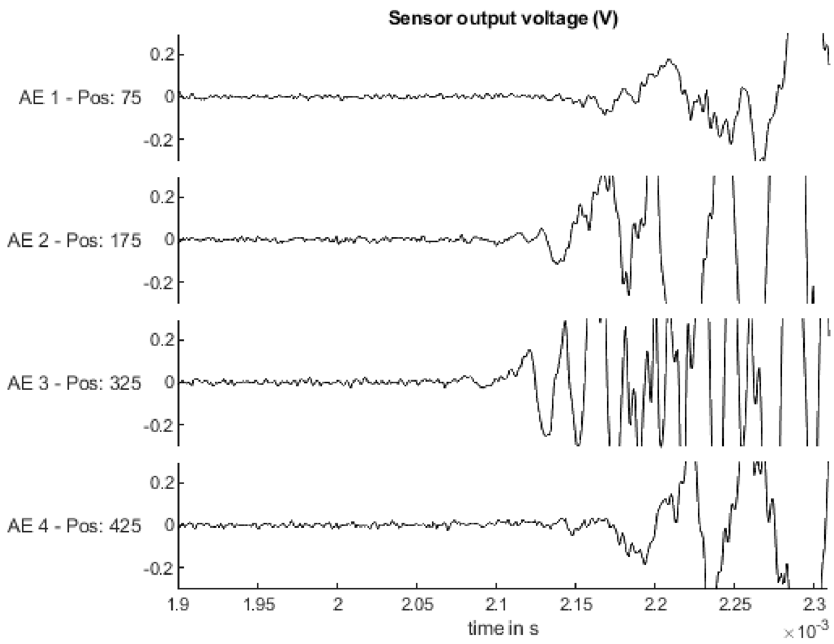

Figure J.17. *RUPTUBE - 2^{nd} campaign, test 1: Time and amplitude magnification around the beginning of the event on filtered signals (2^{nd} order Butterworth High-Pass filter at 20 kHz).*

The wave velocity can be estimated with the TDOA between AE 1 and AE 2 signals, which gives 2941 $\pm$550m.s^{-1}. It can also be estimated from AE 3 and AE 4 signals, which gives 2985 $\pm$565m.s^{-1}. Those values are lower than the theoretical velocity for quasi-longitudinal waves. They are actually closer to the transverse wave and Rayleigh wave velocities (respectively 3100 and 2900 m.s^{-1}, according to Eq. (II.6) and Eq. (II.14) given in Sec. II.1). The available experimental data do not enable us to determine why the first detected waves in the current test seem to be transverse waves while the detected waves in the other tests are likely related to quasi-longitudinal waves.

The resulting source positions obtained with the experimental velocities are shown in Fig. J.18 and Fig. J.19. The relatively good consistency with the actual observed failure position might indicate that the estimated velocities are correct and that first detected waves are actually transverse waves.

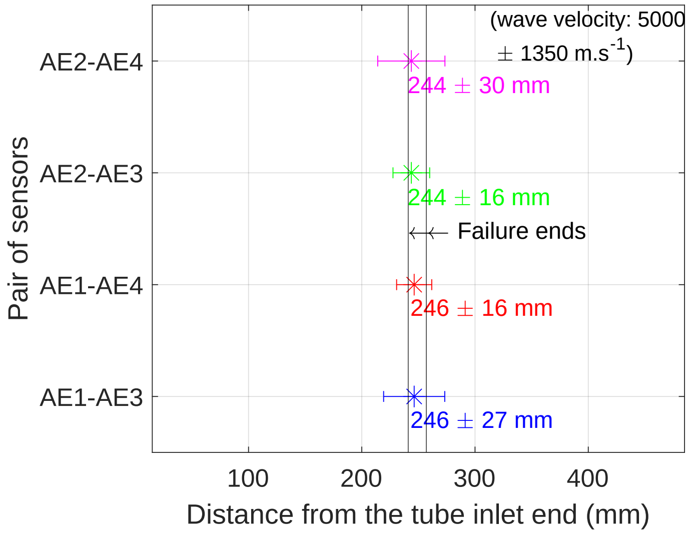

Figure J.18. *RUPTUBE - 2nd campaign, test 1: Source positions obtained by threshold crossing method with 20 kHz LP filtered signals, considering the wave velocity estimated from AE 1 and AE 2. Indicated failure ends are observed after the test.*

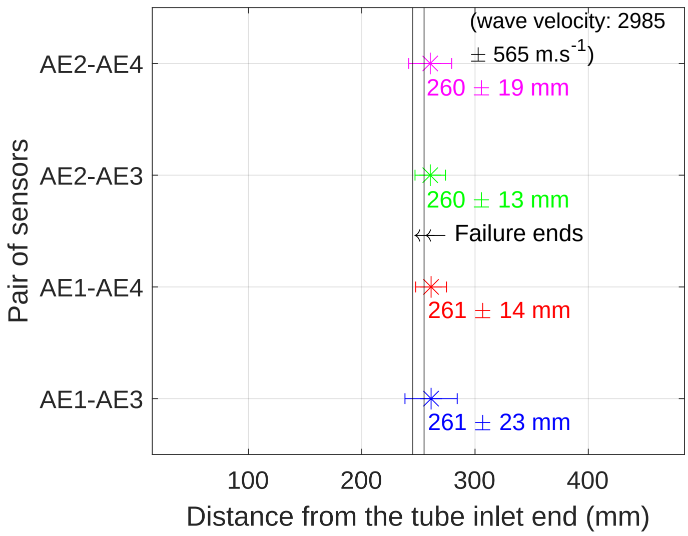

Figure J.19. *RUPTUBE - 2nd campaign, test 1: Source positions obtained by threshold crossing method with 20 kHz LP filtered signals, considering the wave velocity estimated from AE 3 and AE 4. Indicated failure ends are observed after the test.*

Fig. J.20 and J.21 show respectively the time-domain and the time-frequency representation, by CWT, of the resonant AE sensor signal. The CWT, computed with Morse wavelets like previously, was focused on the frequency range of the sensor (20 kHz-1 MHz) and the Time-Bandwidth product of the wavelets was enlarged (up to 120) in order to improve the frequency resolution, the time resolution being good enough.

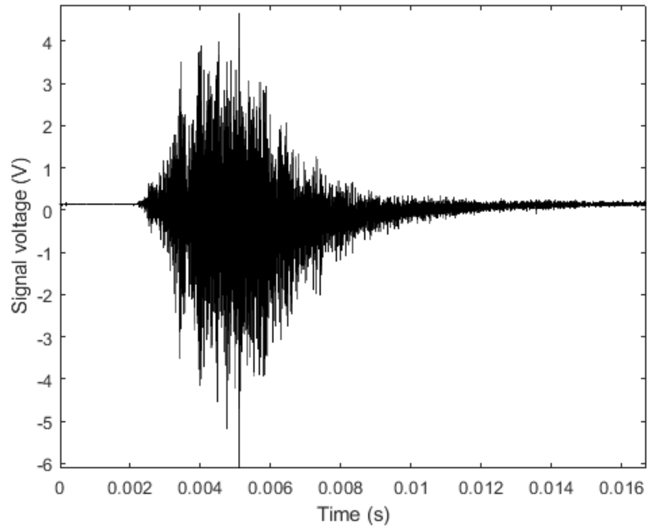

Figure J.20. *RUPTUBE - 2nd campaign, test 1: Signal of the resonant AE sensor mounted on the outer structure.*

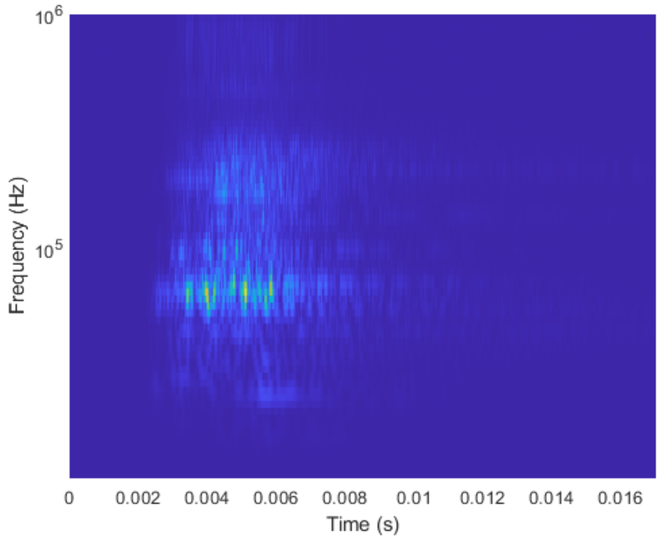

Figure J.21. *RUPTUBE - 2nd campaign, test 1: CWT of the signal of the resonant AE sensor mounted on the outer structure.*

The analysis of the resonant sensor signal simply shows that the failure can be detected without ambiguity when the sensor is mounted on the outer structure. Because of the significant effect of the resonance on the sensor's response, signals from this sensor can not be compared to broadband sensors mounted on the tube and does not provide accurate information about the spectrum of the actual physical waves.

Because of a mistake in the accelerometer conditioner setting, the signal of the accelerometer mounted on the outer structure is not usable.

J.2. Results of Test 2

Configuration of Test 2 is resumed in Fig. J.22.

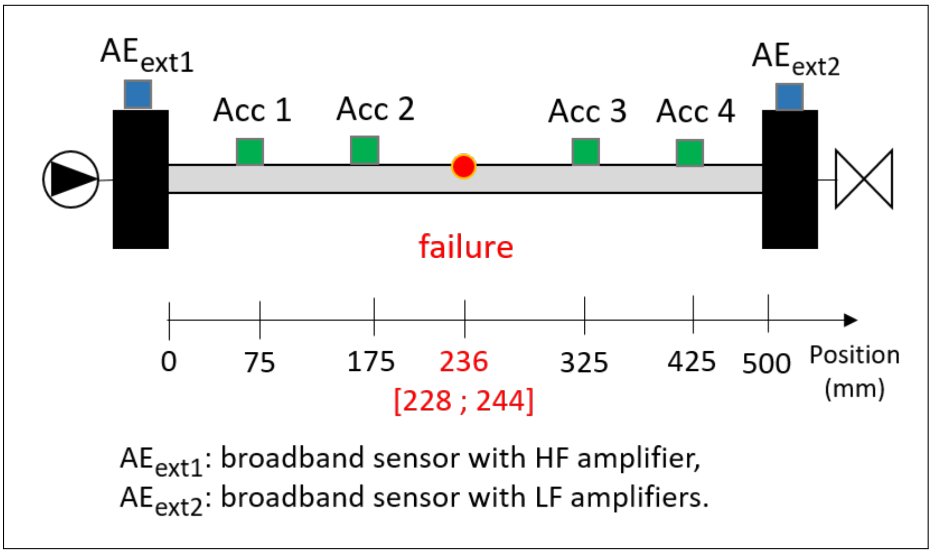

Figure J.22. *RUPTUBE - 2nd campaign, test 2: configuration.*

Because of saturation, accelerometer signals could not be used neither to localize the failure nor to study the tube response. The only usable information consists in the resonance of the first flexural mode exhibited by the STFT of Acc. 1 and Acc. 2 shown in Fig. J.23 and J.24, computed after decimation of the signals (final sampling frequency of 2500 kHz) to exhibit more clearly the low frequency resonance. Acc. 3 and Acc. 4 signals are too distorted to give any useful information.

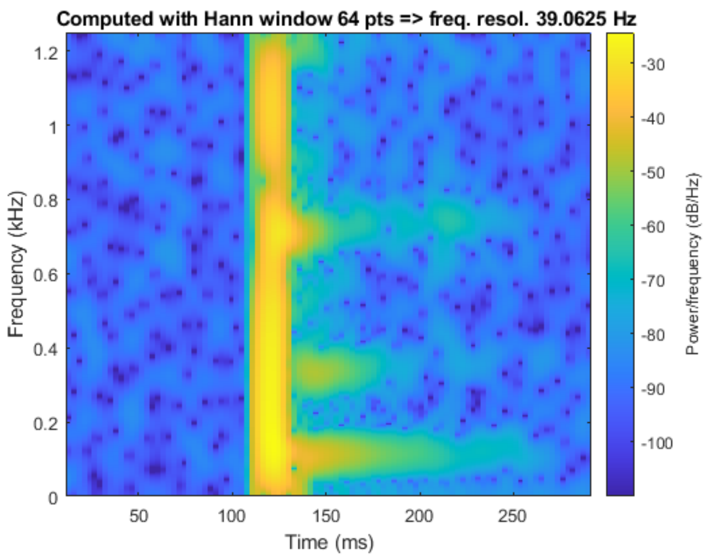

Figure J.23. *RUPTUBE - 2nd campaign, test 2: STFT of the Acc 1 signal.*

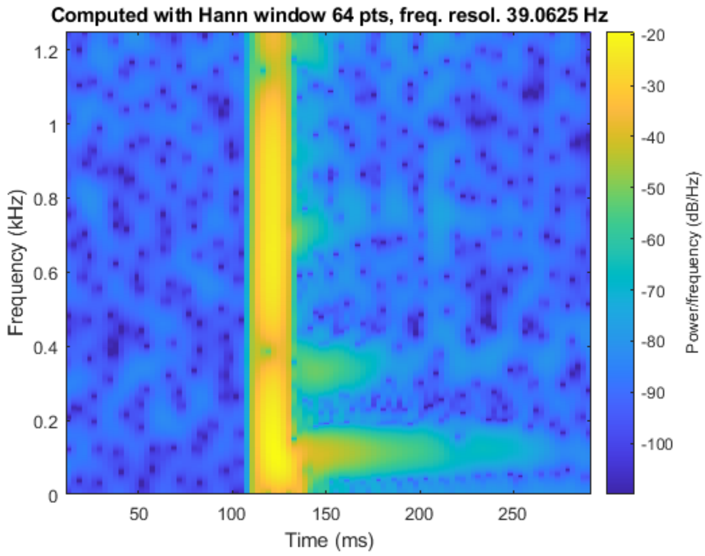

Figure J.24. *RUPTUBE - 2^{nd} campaign, test 2: STFT of the Acc 2 signal.*

The AE sensors mounted on the outer structures are instrumented with a HF amplifier for the sensor on the inlet flange and with a LF amplifier for the sensor mounted on the outlet flange. CWT of their signals (computed on a reduced time interval) are shown in Fig. J.25 and Fig. J.26. The HF amplifier saturated but both signals show that the failure can be detected without ambiguity with the two sensors.

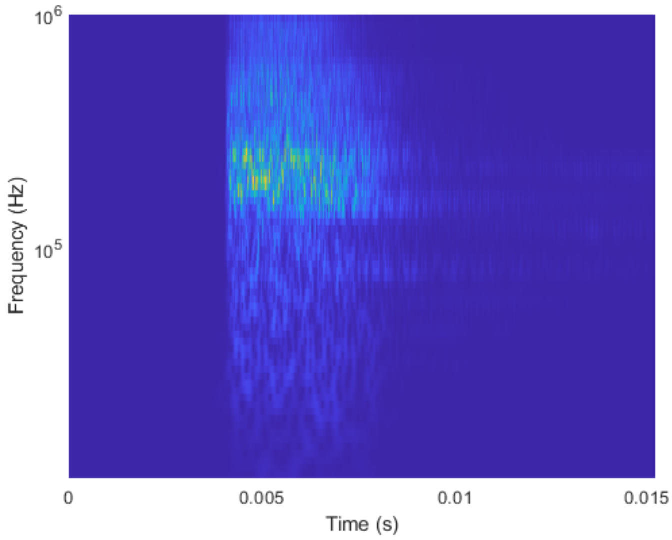

Figure J.25. *RUPTUBE - 2^{nd} campaign, test 1: CWT of the signal of the broadband AE sensor instrumented with a HF amplifier and mounted on the outer structure. The amplifier saturated.*

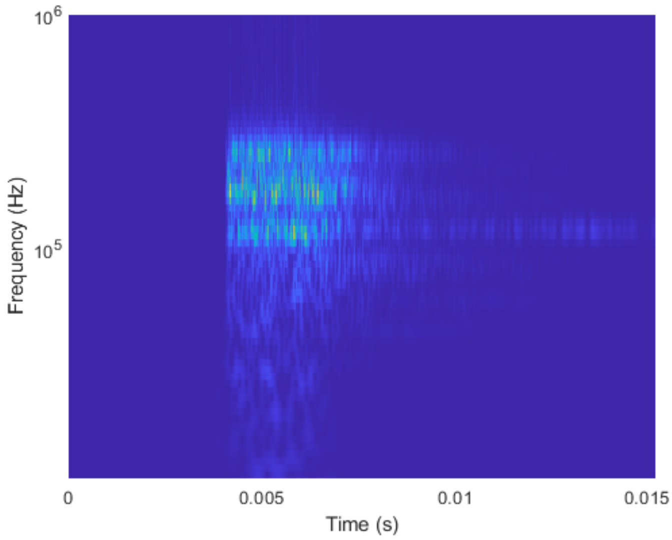

Figure J.26. *RUPTUBE - 2^{nd} campaign, test 1: CWT of the signal of the broadband AE sensor instrumented with a LF amplifier and mounted on the outer structure.*

J.3. Results of Test 3

Results of Test 3 are presented in Sec. IV.4.2.1.

J.4. Results of Test 4

Configuration of Test 4 is resumed in Fig. J.27.

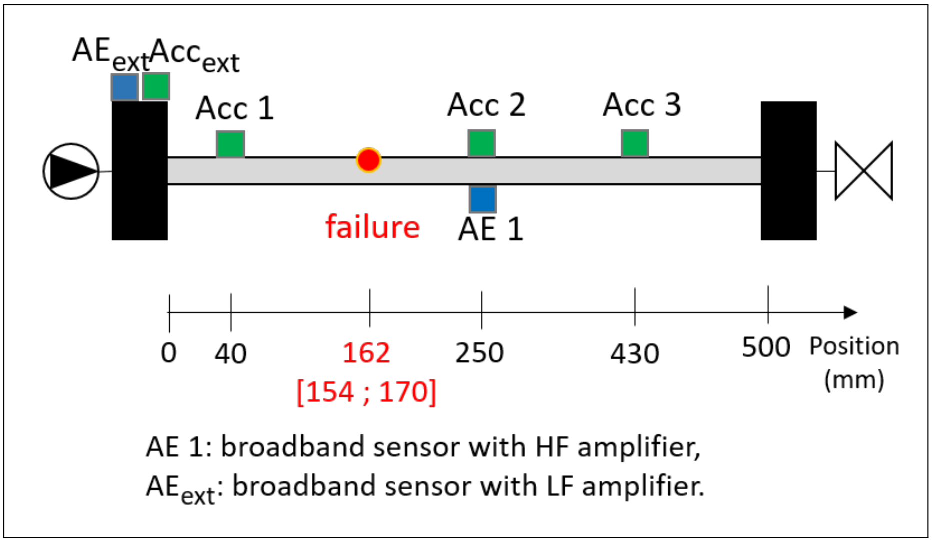

Figure J.27. *RUPTUBE - 2^{nd} campaign, test 4: configuration.*

The accelerometers mounted on the tube saturated. Only the accelerometer mounted on the outer structure is analyzed here. Fig. J.28 shows the time-frequency representation, by

CWT (with Morse wavelets), of the accelerometer signal. Fig. J.29 shows the STFT, which better exhibits the resonance, computed after decimation and plotted on a restricted frequency range for a better visibility of the first structural vibration modes. However, those modes are damped by the transmission from the tube to the outer structure and are eventually hardly visible. Fig. J.30 and Fig. J.31 show respectively the ESD and its magnification on the low frequency range. The purpose of frequency analysis of the accelerometer signal is the comparison with other tests instrumented with accelerometers (on the tube or on the outer structure). Regarding Test 4 only, since no signal measured on the tube are available, the outer accelerometer's signal simply shows that the failure is detected without ambiguity.

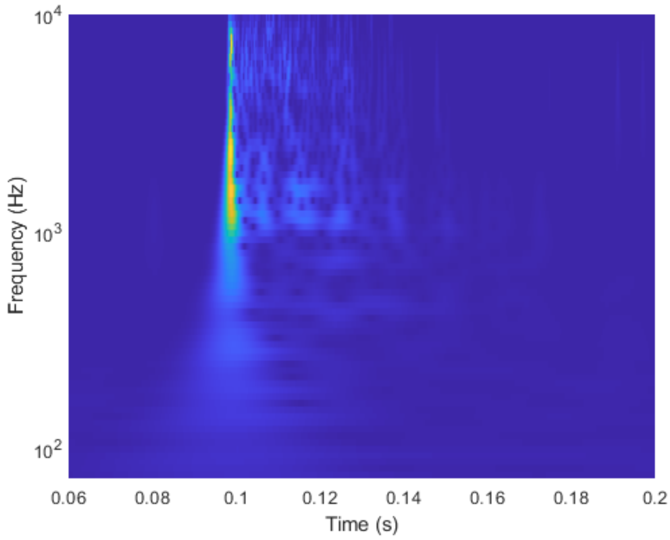

Figure J.28. *RUPTUBE - 2^{nd} campaign, test 4: CWT of the signal of the accelerometer mounted on the outer structure.*

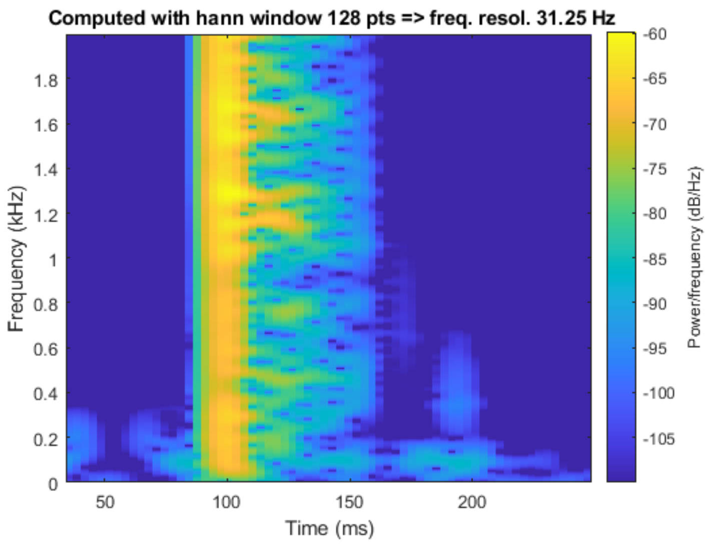

Figure J.29. *RUPTUBE - 2^{nd} campaign, test 4: STFT of the signal of the accelerometer mounted on the outer structure.*

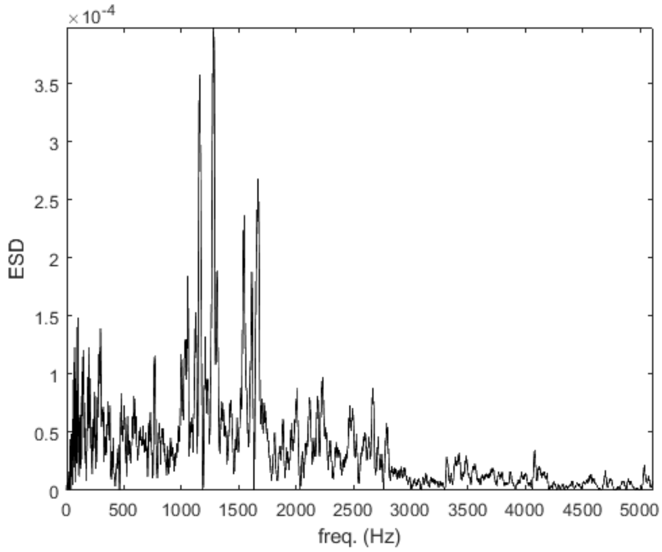

Figure J.30. *RUPTUBE - 2^{nd} campaign, test 4: ESD of the signal of the accelerometer mounted on the outer structure.*

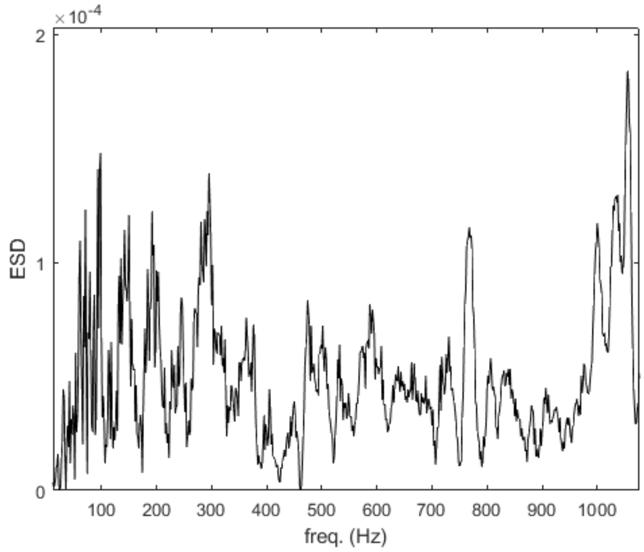

Figure J.31. *RUPTUBE - 2nd campaign, test 4: ESD of the signal of the accelerometer mounted on the outer structure, low frequency range.*

J.5. Results of Test 5

Configuration of Test 5 is resumed in Fig. J.32.

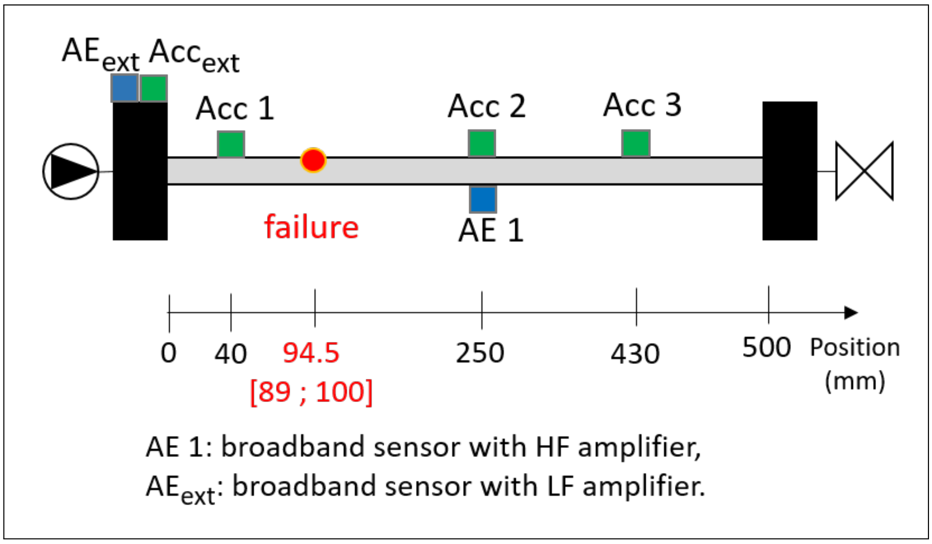

Figure J.32. *RUPTUBE - 2nd campaign, test 5: configuration.*

The accelerometers mounted on the tube saturated. External accelerometer and AE signals do not bring any interesting feature in addition to the ones presented in Sec. IV.4.2.2, Sec. IV.4.2.1, Sec. J.4. and Sec. J.7.

J.6. Results of Test 6

Regarding AE sensors signals, results of Test 6 are already presented in Sec. IV.4.2.2. The accelerometer mounted on the outer structure saturated and the signal is not usable.

J.7. Results of Test 7

Configuration of Test 7 is resumed in Fig. J.33.

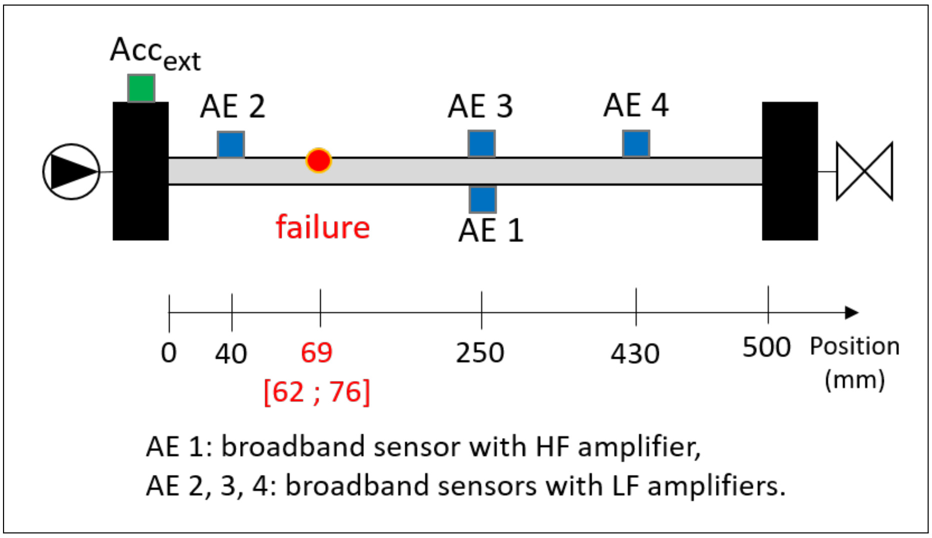

Figure J.33. *RUPTUBE - 2nd campaign, test 7: configuration.*

Signals of the four AE sensors are shown in Fig. J.34 (time domain view) and Fig. J.35 (time-frequency view by CWT).

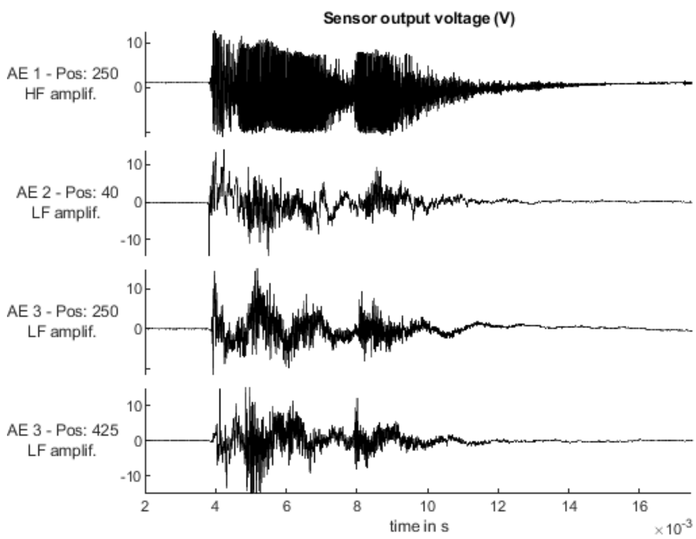

Figure J.34. *RUPTUBE - 2nd campaign, test 7: Time domain view of the AE sensors' signals.*

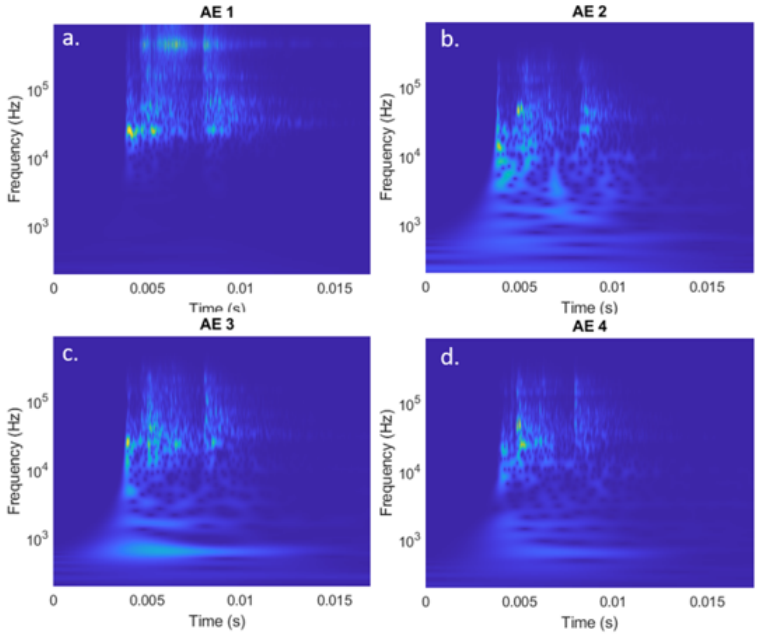

Figure J.35. *RUPTUBE - 2^{nd} campaign, test 7: Time-frequency views of the AE sensors' signals. CWT by Morse wavelets. a.: Sensor 1, b.: Sensor 2, c.: Sensor 3, d.: Sensor 4.*

Fig. J.36 shows the 20 kHz HP filtered signals with a time magnification around the arrival of the failure-induced waves.

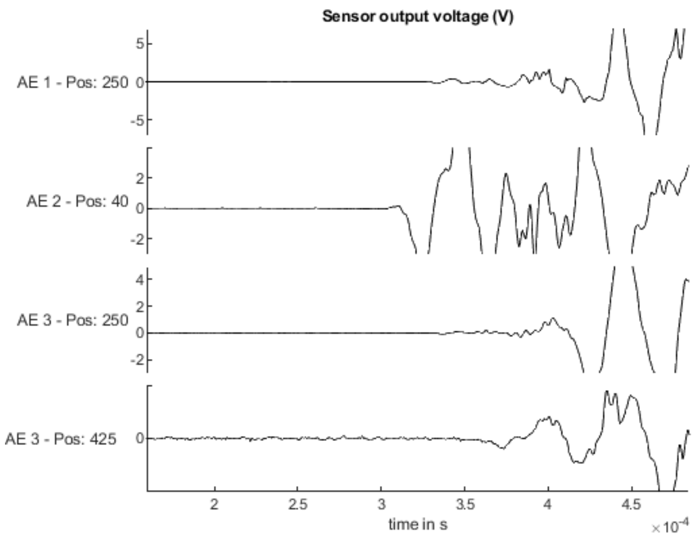

Figure J.36. *RUPTUBE - 2^{nd} campaign, test 7: Time and amplitude magnification around the beginning of the event on filtered signals (2^{nd} order Butterworth High-Pass filter at 20 kHz).*

Like for Test 6, the wave velocity is estimated with the TDOA between sensor AE 3 and AE 4, using the filtered signals. Considering the very first disruptions, which are assumed to be related to quasi-longitudinal waves, it yields a velocity of 5171 $\pm 682 m.s^{-1}$. The source positions estimated with the different pair of sensors are shown in Fig. J.37.

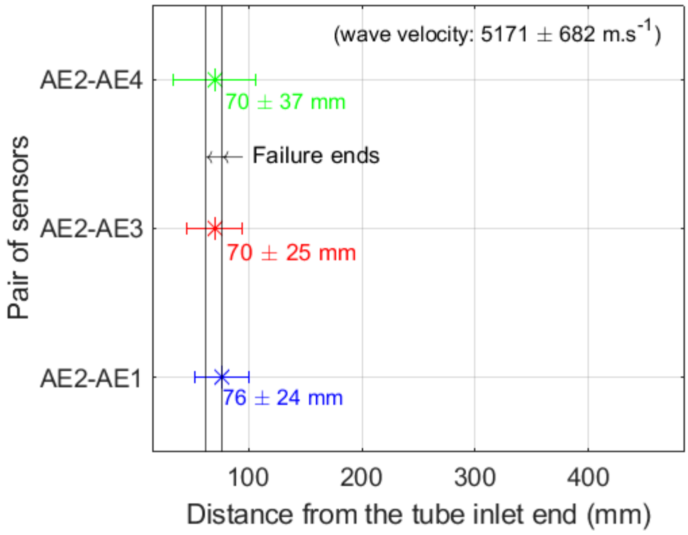

Figure J.37. *RUPTUBE - 2nd campaign, test 7: source positions obtained by threshold crossing method with 20 kHz LP filtered signals. Indicated failure ends are observed after the test.*

The accelerometer saturated and its signal is therefore not usable.

Appendix K. Drawings of the RUPTUBE device

Content:

- Drawing 1: general view,
- Drawing 2: exploded view,
- Drawing R3: inlet flange,
- Drawing R4: outlet flange.

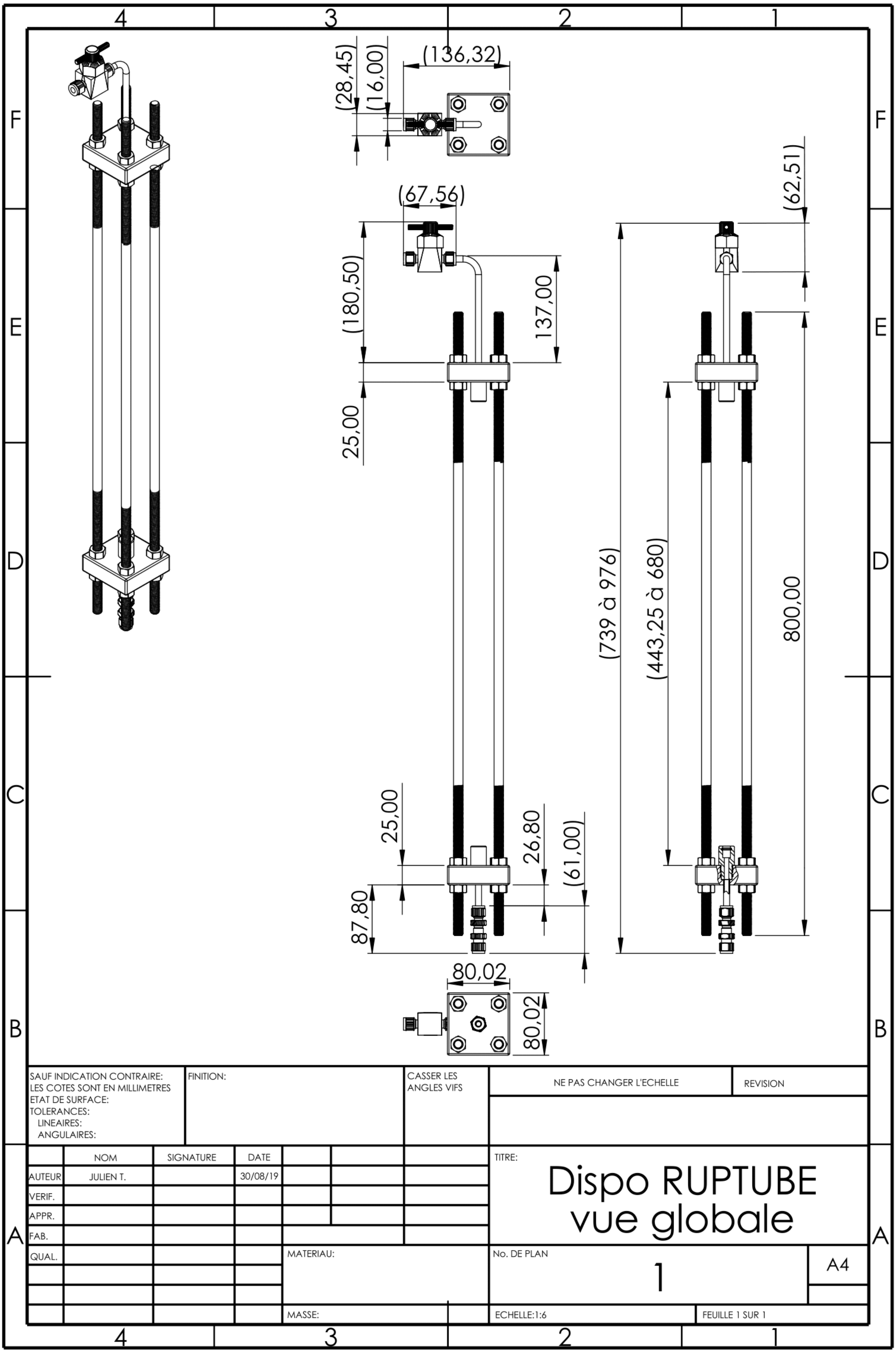
(136,32)
(28,45)
(16,00)
(67,56)
(62,51)
(180,50)
137,00
25,00
(739 à 976)
(443,25 à 680)
800,00
25,00
26,80
(61,00)
87,80
80,02
80,02
SAUF INDICATION CONTRAIRE:
LES COTES SONT EN MILLIMETRES
ETAT DE SURFACE:
TOLERANCES:
LINEAIRES:
ANGULAIRES:
FINITION:
CASSER LES ANGLES VIFS
NE PAS CHANGER L'ECHELLE
REVISION
NOM
SIGNATURE
DATE
AUTEUR
JULIEN T.
30/08/19
VERIF.
APPR.
FAB.
QUAL.
TITRE:
Dispo RUPTUBE vue globale
MATERIAU:
No. DE PLAN
1
A4
MASSE:
ECHELLE:1:6
FEUILLE 1 SUR 1

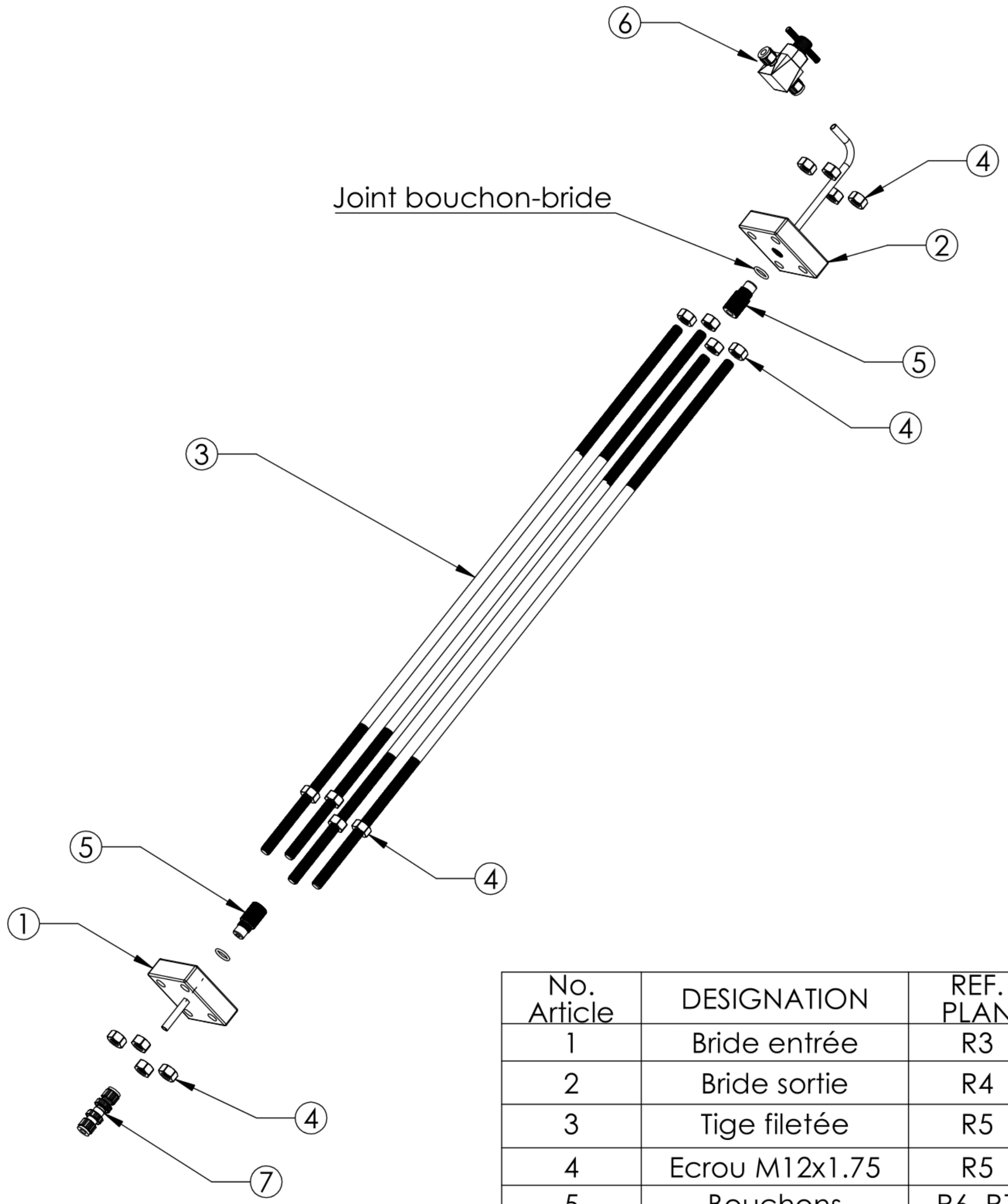

No. Article	DESIGNATION	REF. PLAN
1	Bride entrée	R3
2	Bride sortie	R4
3	Tige filetée	R5
4	Ecrou M12x1.75	R5
5	Bouchons	R6, R7
6	Vanne dégazage	/
7	Raccord 8-8	/

SAUF INDICATION CONTRAIRE:
LES COTES SONT EN MILLIMETRES
ETAT DE SURFACE:
TOLERANCES:
LINEAIRES:
ANGULAIRES:

FINITION:

CASSER LES ANGLES VIFS

NE PAS CHANGER L'ECHELLE

REVISION

	NOM	SIGNATURE	DATE
AUTEUR	JULIEN T.		30/08/19
VERIF.			
APPR.			
FAB.			
QUAL.			

TITRE: **Dispo RUPTUBE vue éclatée**

MATERIAU:

No. DE PLAN: 2

A4

MASSE:

ECHELLE:1:6

FEUILLE 1 SUR 1

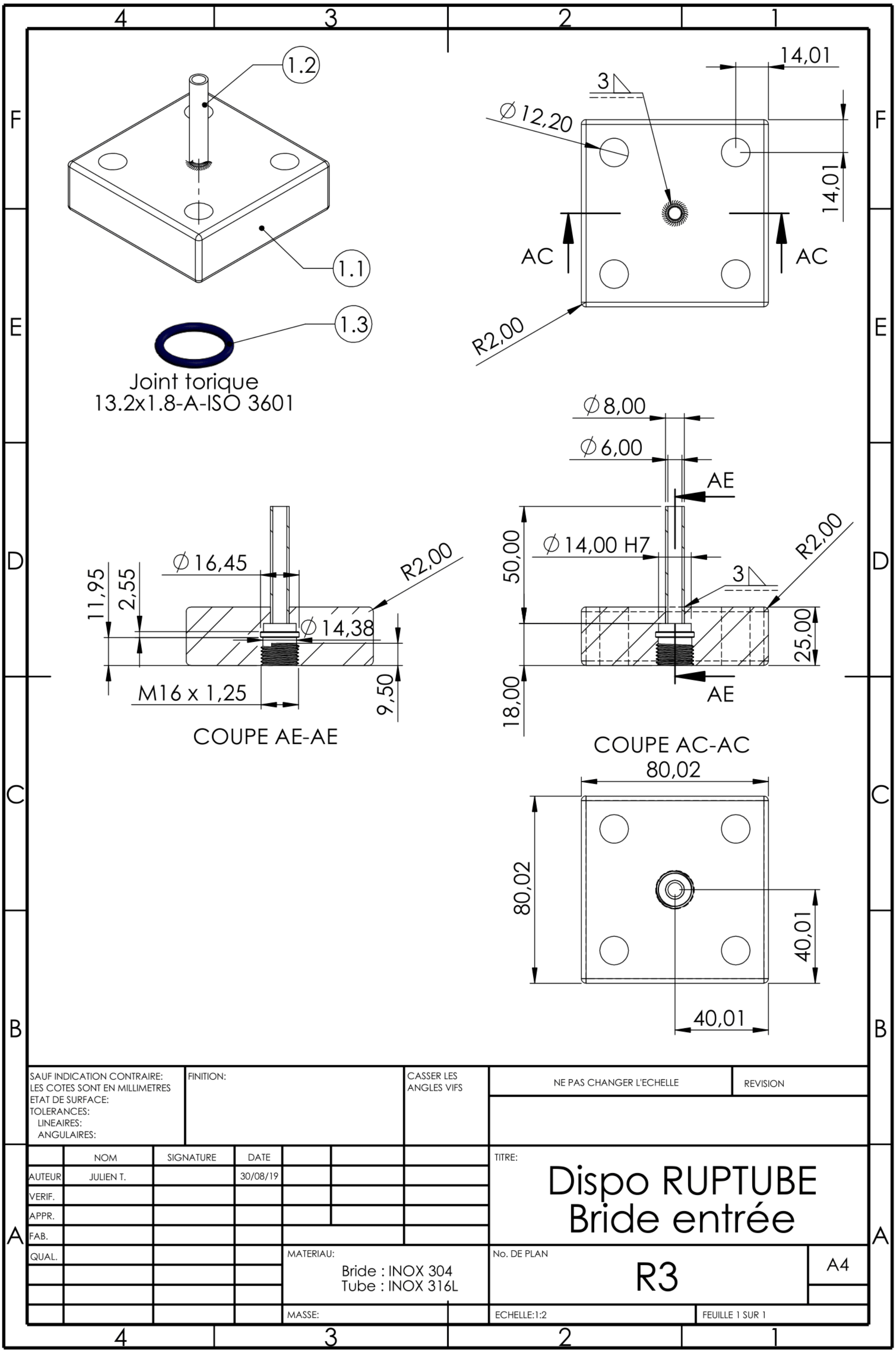

1.2
1.1
1.3
Joint torique
13.2x1.8-A-ISO 3601
3
Ø12,20
14,01
14,01
AC
AC
R2,00
Ø8,00
Ø6,00
AE
Ø16,45
R2,00
11,95
2,55
Ø14,38
M16 x 1,25
9,50
COUPE AE-AE
50,00
Ø14,00 H7
3
R2,00
25,00
18,00
AE
COUPE AC-AC
80,02
80,02
40,01
40,01
SAUF INDICATION CONTRAIRE:
LES COTES SONT EN MILLIMETRES
ETAT DE SURFACE:
TOLERANCES:
LINEAIRES:
ANGULAIRES:
FINITION:
CASSER LES ANGLES VIFS
NE PAS CHANGER L'ECHELLE
REVISION
NOM
SIGNATURE
DATE
AUTEUR
JULIEN T.
30/08/19
VERIF.
APPR.
FAB.
QUAL.
TITRE:
Dispo RUPTUBE
Bride entrée
MATERIAU:
Bride : INOX 304
Tube : INOX 316L
No. DE PLAN
R3
A4
MASSE:
ECHELLE:1:2
FEUILLE 1 SUR 1

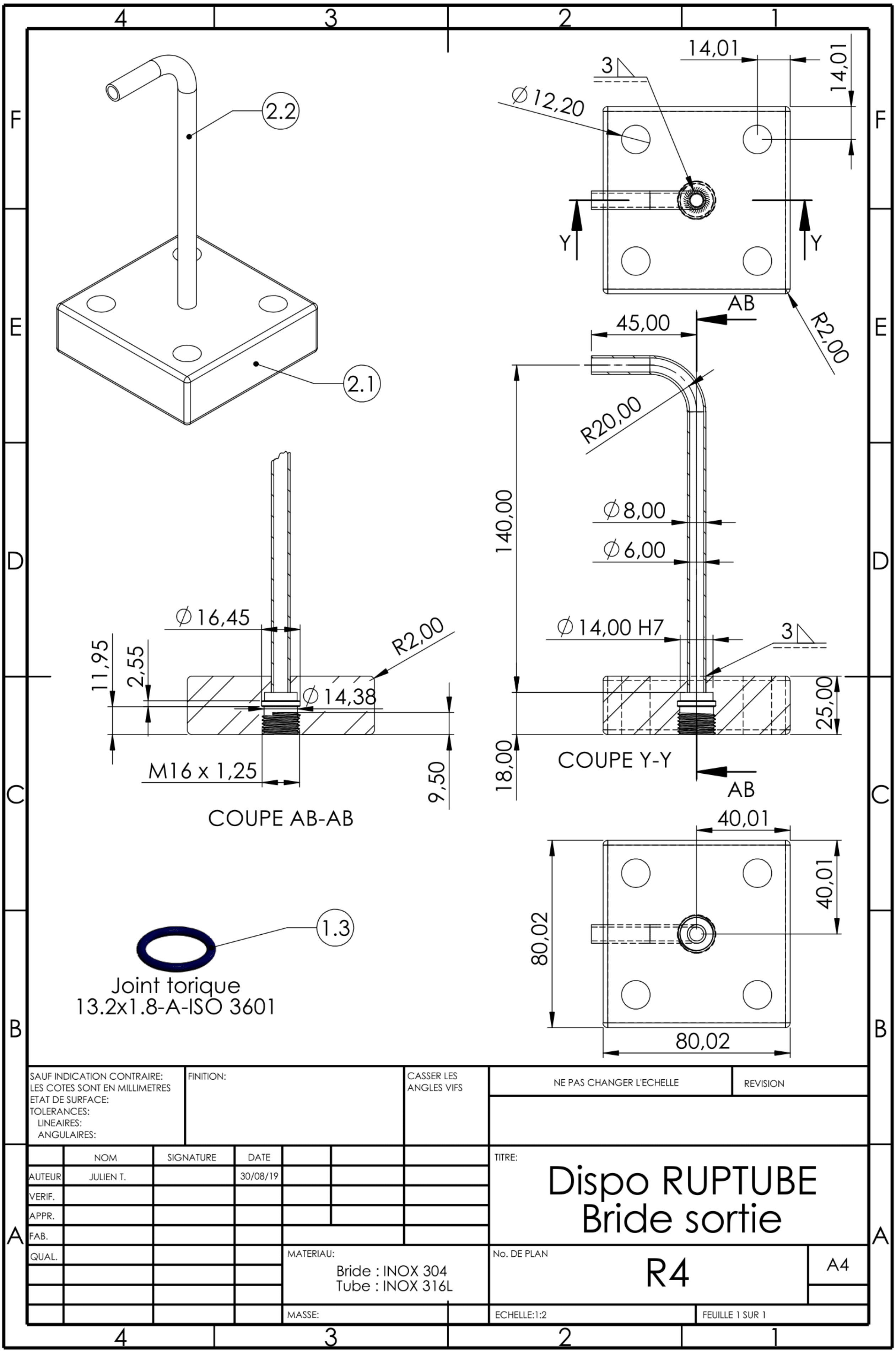
2.2
2.1
3
14,01
14,01
⌀12,20
Y
Y
AB
R2,00
45,00
R20,00
140,00
⌀8,00
⌀6,00
⌀16,45
R2,00
11,95
2,55
⌀14,38
M16 x 1,25
9,50
COUPE AB-AB
⌀14,00 H7
3
25,00
18,00
COUPE Y-Y
AB
40,01
40,01
80,02
80,02
1.3
Joint torique
13.2x1.8-A-ISO 3601
SAUF INDICATION CONTRAIRE:
LES COTES SONT EN MILLIMETRES
ETAT DE SURFACE:
TOLERANCES:
LINEAIRES:
ANGULAIRES:
FINITION:
CASSER LES ANGLES VIFS
NE PAS CHANGER L'ECHELLE
REVISION
NOM
SIGNATURE
DATE
AUTEUR
JULIEN T.
30/08/19
VERIF.
APPR.
FAB.
QUAL.
TITRE:
Dispo RUPTUBE
Bride sortie
MATERIAU:
Bride : INOX 304
Tube : INOX 316L
No. DE PLAN
R4
A4
MASSE:
ECHELLE:1:2
FEUILLE 1 SUR 1

Appendix L. Drawings of the MAQAC device

Content:

- Drawing 1-1: general view,
- Drawing 1-2: exploded view,
- Drawing 2-1: lower section,
- Drawing 3-1: upper section,
- Drawing 4: outer tube.

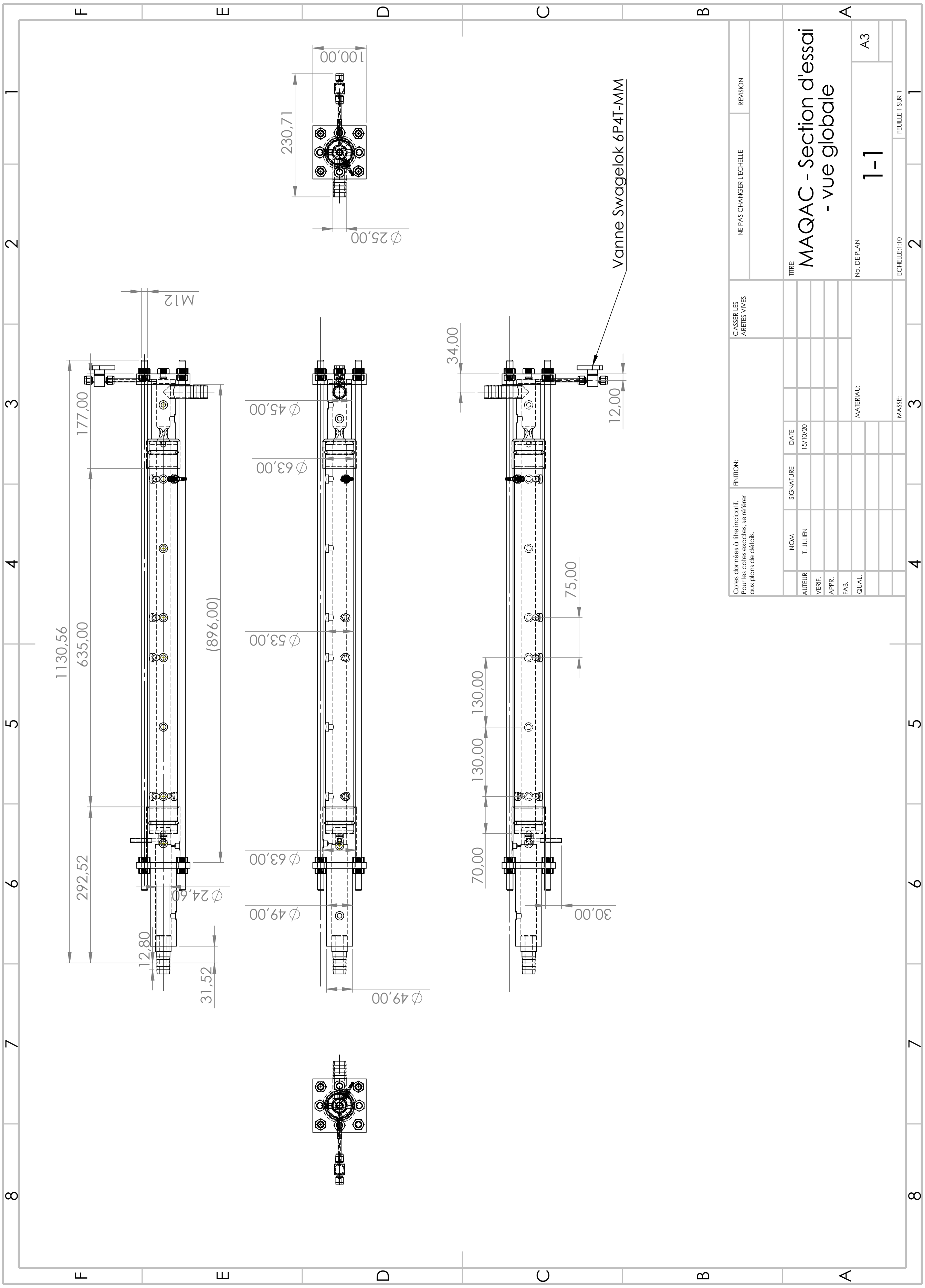
MAQAC - Section d'essai
- vue globale
Vanne Swagelok 6P4T-MM
1-1
A3
T. JULIEN
15/10/20
ECHELLE:1:10
FEUILLE 1 SUR 1

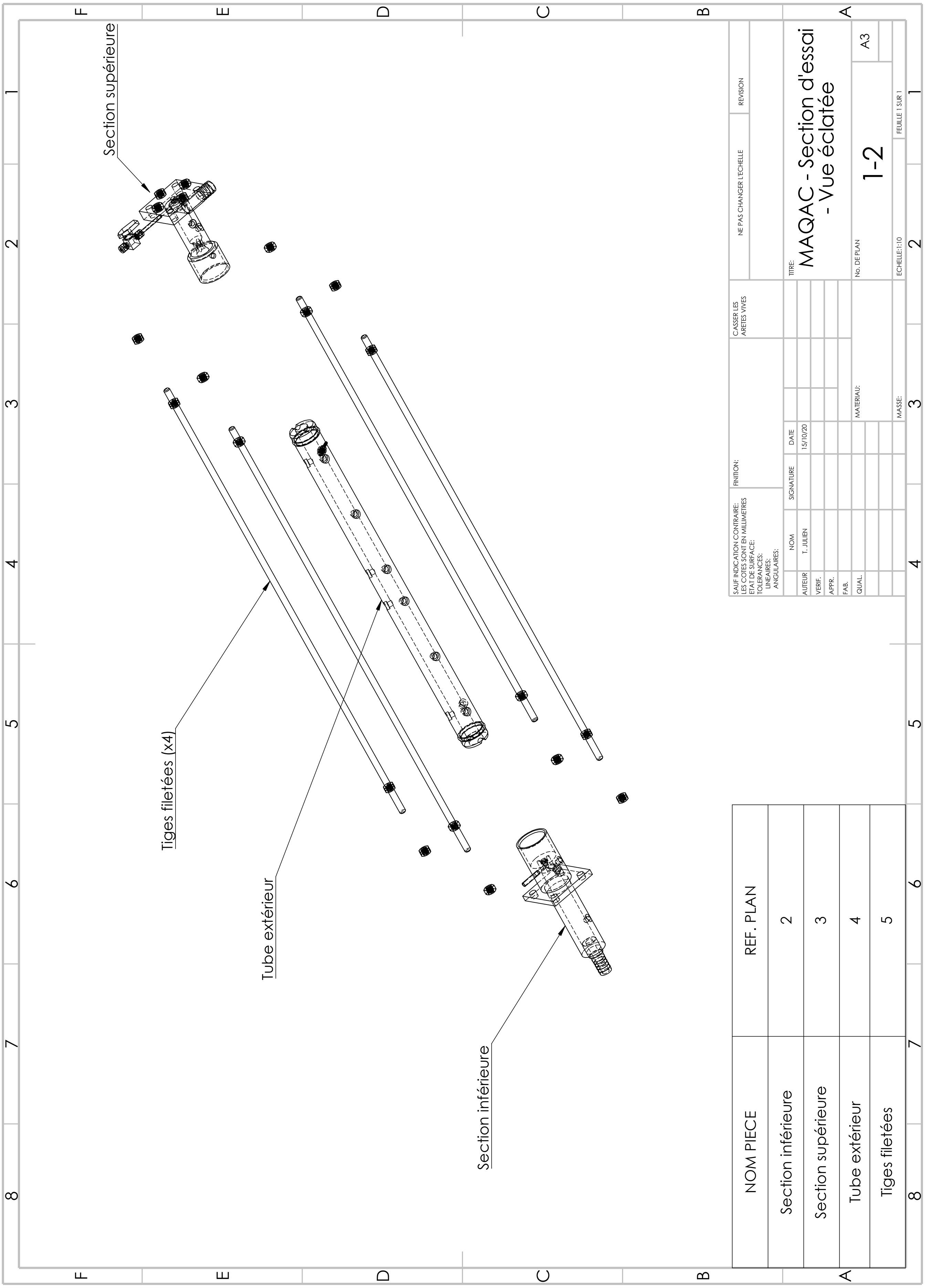
Section supérieure
Tiges filetées (x4)
Tube extérieur
Section inférieure
NOM PIECE
REF. PLAN
Section inférieure
2
Section supérieure
3
Tube extérieur
4
Tiges filetées
5
MAQAC - Section d'essai - Vue éclatée
1-2
A3
NE PAS CHANGER L'ECHELLE
REVISION
SAUF INDICATION CONTRAIRE: LES COTES SONT EN MILLIMETRES ETAT DE SURFACE: TOLERANCES: LINEAIRES: ANGULAIRES:
FINITION:
CASSER LES ARETES VIVES
NOM
SIGNATURE
DATE
AUTEUR
T. JULIEN
15/10/20
VERIF.
APPR.
FAB.
QUAL.
MATERIAU:
No. DE PLAN
TITRE:
ECHELLE:1:10
MASSE:
FEUILLE 1 SUR 1

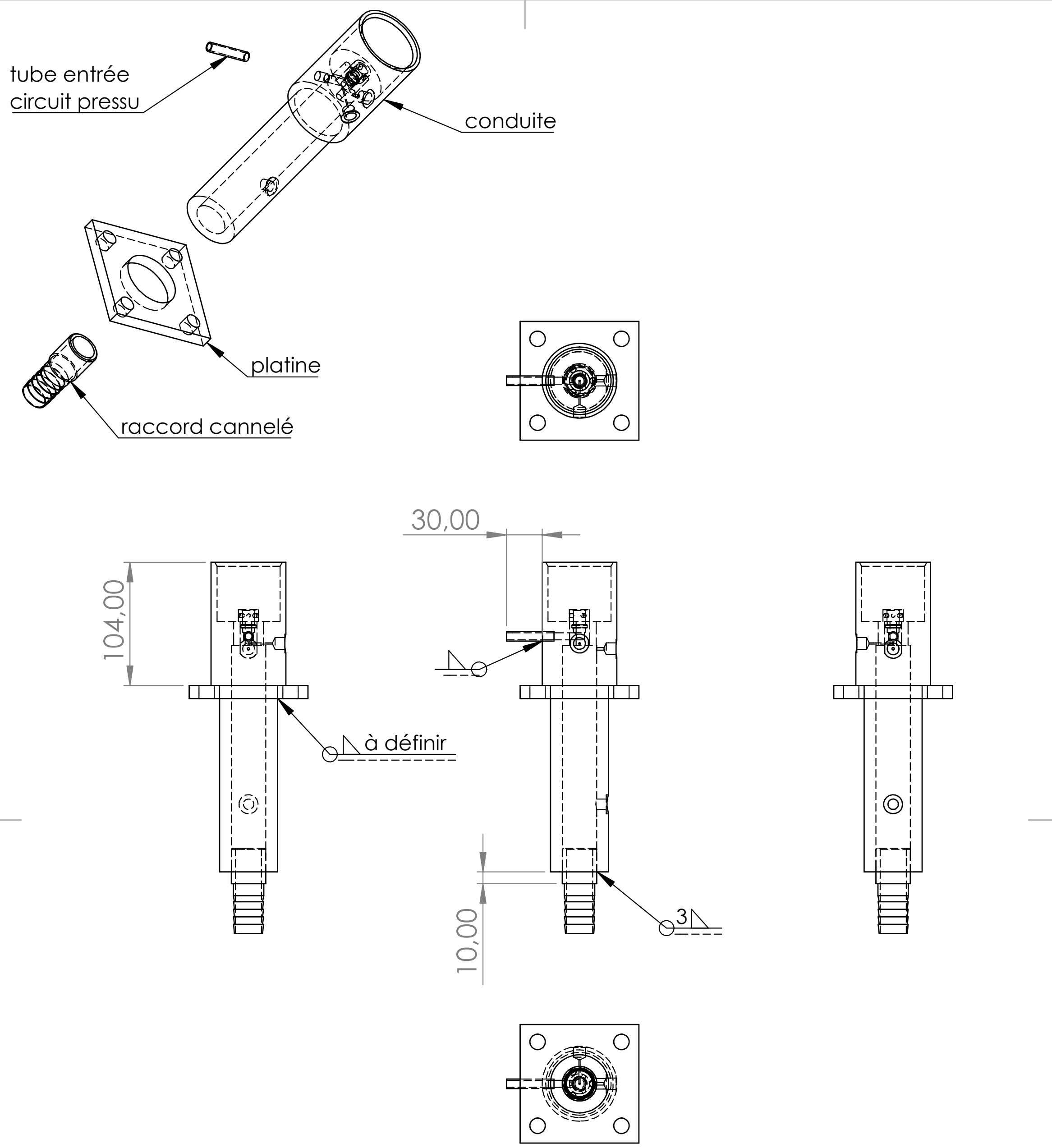

Les soudures entre tube d'entrée du circuit pressu et conduite, et entre raccord cannelé et conduite doivent être étanches.
La soudure entre platine et conduite peut être discontinue.

SAUF INDICATION CONTRAIRE:
LES COTES SONT EN MILLIMETRES
ETAT DE SURFACE:
TOLERANCES:
LINEAIRES:
ANGULAIRES:

FINITION:

CASSER LES ARETES VIVES

NE PAS CHANGER L'ECHELLE

REVISION N°2 - 27/07/21

	NOM	SIGNATURE	DATE
AUTEUR	T. JULIEN		27/07/21
VERIF.			
APPR.			
FAB.			
QUAL.			

TITRE: MAQAC - Bride inférieure

MATERIAU:

No. DE PLAN: 2-1

A4

MASSE:

ECHELLE:1:5

FEUILLE 1 SUR 1

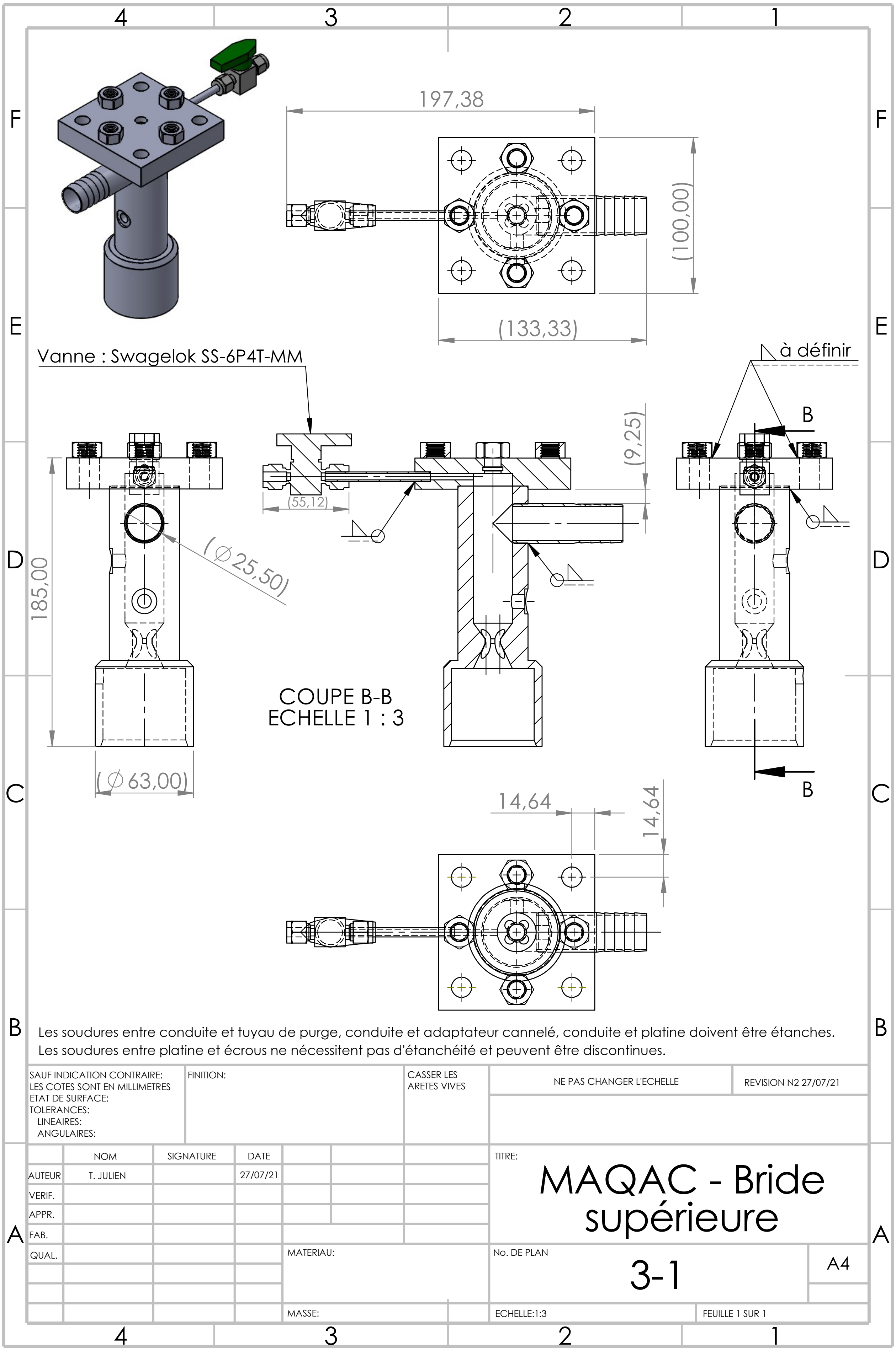
197,38
(100,00)
(133,33)
Vanne : Swagelok SS-6P4T-MM
à définir
B
(9,25)
(55,12)
185,00
(Ø25,50)
COUPE B-B
ECHELLE 1 : 3
(Ø63,00)
B
14,64
14,64
Les soudures entre conduite et tuyau de purge, conduite et adaptateur cannelé, conduite et platine doivent être étanches.
Les soudures entre platine et écrous ne nécessitent pas d'étanchéité et peuvent être discontinues.
SAUF INDICATION CONTRAIRE:
LES COTES SONT EN MILLIMETRES
ETAT DE SURFACE:
TOLERANCES:
LINEAIRES:
ANGULAIRES:
FINITION:
CASSER LES ARETES VIVES
NE PAS CHANGER L'ECHELLE
REVISION N2 27/07/21
NOM
SIGNATURE
DATE
AUTEUR
T. JULIEN
27/07/21
VERIF.
APPR.
FAB.
QUAL.
TITRE:
MAQAC - Bride supérieure
MATERIAU:
No. DE PLAN
3-1
A4
MASSE:
ECHELLE:1:3
FEUILLE 1 SUR 1

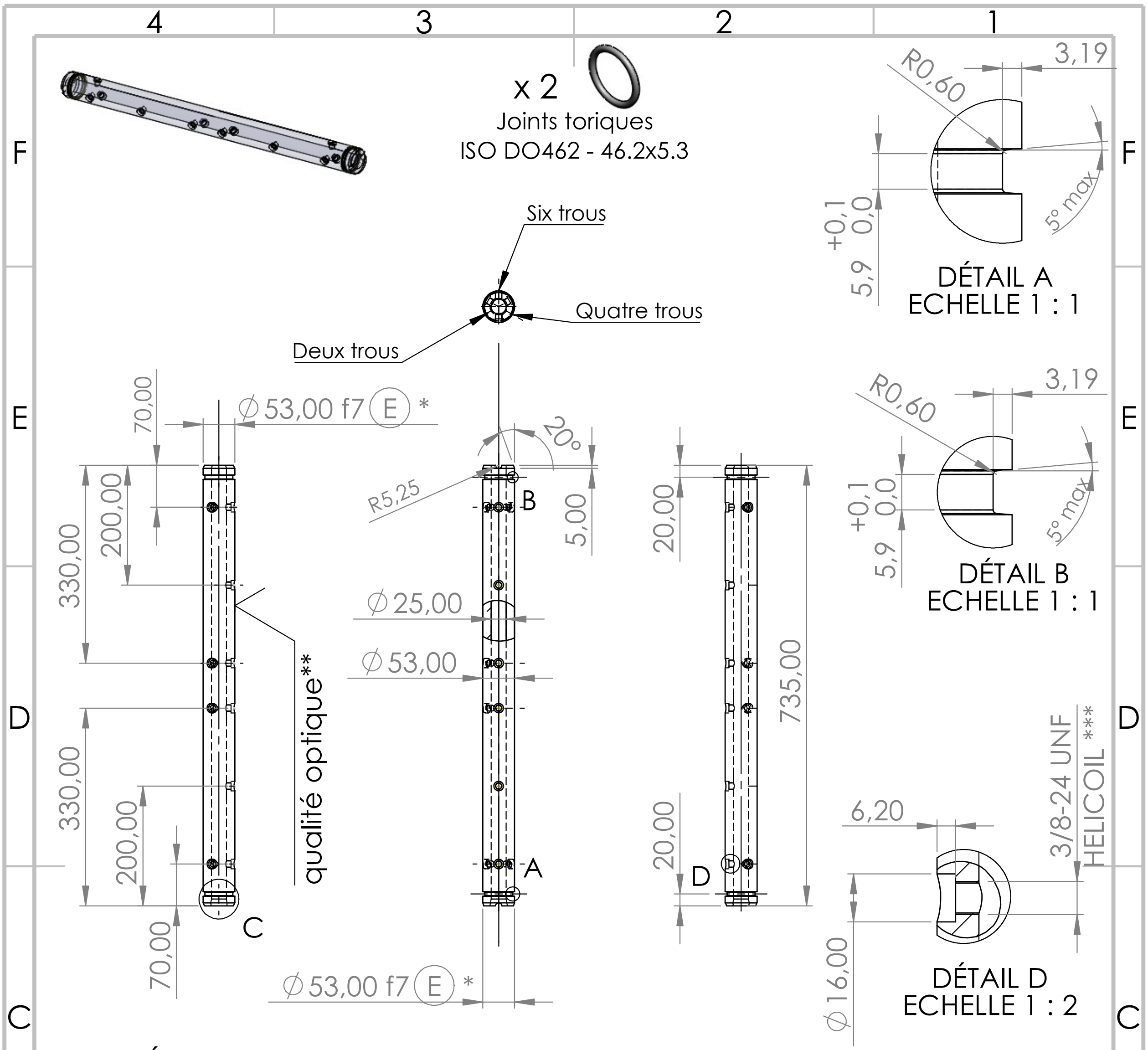

DÉTAIL C
ECHELLE 1 : 2

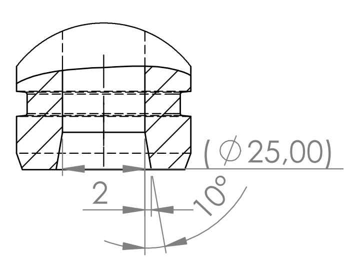

* Tolérance f7 sur diamètre extérieur : sur une longueur de 55 mm aux deux extrémités. Non nécessaire sur le reste du tube.
** La qualité optique doit être assurée sur les surfaces intérieure et extérieure. Elle n'est pas nécessaire sur les zones soumises à la tolérance f7 sur le diamètre extérieur (55 mm aux deux extrémités)
*** Prévoir étanchéité entre taraudage et insert (résine Loctite 577 ou équivalent)

SAUF INDICATION CONTRAIRE: LES COTES SONT EN MILLIMETRES ETAT DE SURFACE: TOLERANCES: LINEAIRES: ANGULAIRES:	FINITION:	CASSER LES ARETES VIVES	NE PAS CHANGER L'ECHELLE / REVISION

	NOM	SIGNATURE	DATE
AUTEUR	JULIEN T.		23/03/21
VERIF.			
APPR.			
FAB.			
QUAL.			

TITRE: **Tube extérieur MAQAC**

MATERIAU: Polycarbonate ou PMMA (à définir)

No. DE PLAN: 4 — A4

MASSE:

ECHELLE:1:10

FEUILLE 1 SUR 1